

Recent Advances in Neuroimaging Methodology

Guest Editors: Oury Monchi, Habib Benali, Julien Doyon,
and Antonio P. Strafella





Recent Advances in Neuroimaging Methodology

International Journal of Biomedical Imaging

Recent Advances in Neuroimaging Methodology

Guest Editors: Oury Monchi, Habib Benali,
Julien Doyon, and Antonio P. Strafella



Copyright © 2008 Hindawi Publishing Corporation. All rights reserved.

This is a special issue published in volume 2008 of "International Journal of Biomedical Imaging." All articles are open access articles distributed under the Creative Commons Attribution License, which permits unrestricted use, distribution, and reproduction in any medium, provided the original work is properly cited.

Editor-in-Chief

Ge Wang, Virginia Polytechnic Institute and State University, USA

Associate Editors

Haim Azhari, Israel
Kyongtae Bae, USA
Richard Bayford, UK
Freek Beekman, The Netherlands
Subhasis Chaudhuri, India
J.-C. Cheng Chen, Taiwan
Anne Clough, USA
Carl Crawford, USA
Min Gu, Australia
Eric Hoffman, USA
Jiang Hsieh, USA

M. Jiang, China
Marc Kachelrieß, Germany
Seung Wook Lee, South Korea
Alfred Karl Louis, Germany
E. Meijering, The Netherlands
Vasilis Ntziachristos, USA
Scott Pohlman, USA
Erik Ritman, USA
Jay Rubinstein, USA
Pete Santago, USA
Lizhi Sun, USA

Jie Tian, China
Michael Vannier, USA
Yue Wang, USA
Guowei Wei, USA
David L. Wilson, USA
Sun K. Yoo, South Korea
Habib Zaidi, Switzerland
Yantian Zhang, USA
Yibin Zheng, USA
Tiange Zhuang, China

Contents

Recent Advances in Neuroimaging Methods, Oury Monchi, Habib Benali, Julien Doyon, and Antonio P. Strafella

Volume 2008, Article ID 218582, 2 pages

The Connectivity of the Human Pulvinar: A Diffusion Tensor Imaging Tractography Study, Sandra E. Leh, M. Mallar Chakravarty, and Alain Ptito

Volume 2008, Article ID 789539, 5 pages

Exploring the Anatomical Basis of Effective Connectivity Models with DTI-Based Fiber Tractography, Hubert M. J. Fonteijn, David G. Norris, and Frans A. J. Verstraten

Volume 2008, Article ID 423192, 9 pages

Accurate Anisotropic Fast Marching for Diffusion-Based Geodesic Tractography, S. Jbabdi, P. Bellec, R. Toro, J. Daunizeau, M. Péligrini-Issac, and H. Benali

Volume 2008, Article ID 320195, 12 pages

Connectivity-Based Parcellation of the Cortical Mantle Using q -Ball Diffusion Imaging, Muriel Perrin, Yann Cointepas, Arnaud Cachia, Cyril Poupon, Bertrand Thirion, Denis Rivière, Pascal Cathier, Vincent El Kouby, André Constantinesco, Denis Le Bihan, and Jean-François Mangin

Volume 2008, Article ID 368406, 18 pages

Diffusion Maps Clustering for Magnetic Resonance Q-Ball Imaging Segmentation,

Demian Wassermann, Maxime Descoteaux, and Rachid Deriche

Volume 2008, Article ID 526906, 12 pages

Repetitive Transcranial Magnetic Stimulation of Dorsolateral Prefrontal Cortex Affects Performance of the Wisconsin Card Sorting Task during Provision of Feedback, Ji Hyun Ko,

Oury Monchi, Alain Ptito, Michael Petrides, and Antonio P. Strafella

Volume 2008, Article ID 143238, 7 pages

Dorsolateral Prefrontal Cortex: A Possible Target for Modulating Dyskinesias in Parkinson's Disease by Repetitive Transcranial Magnetic Stimulation, I. Rektorova, S. Sedlackova, S. Telecka,

A. Hlubocky, and I. Rektor

Volume 2008, Article ID 372125, 6 pages

BOLD-Perfusion Coupling during Monocular and Binocular Stimulation, Claudine Gauthier and Richard D. Hoge

Volume 2008, Article ID 628718, 6 pages

Contribution of Exploratory Methods to the Investigation of Extended Large-Scale Brain Networks in Functional MRI: Methodologies, Results, and Challenges, V. Perlberg and G. Marrelec

Volume 2008, Article ID 218519, 14 pages

Resurrecting Brinley Plots for a Novel Use: Meta-Analyses of Functional Brain Imaging Data in Older Adults, Ann M. Peiffer, Joseph A. Maldjian, and Paul J. Laurienti

Volume 2008, Article ID 167078, 7 pages

The Role of Noninvasive Techniques in Stroke Therapy, Daniel Maxwell Bernad and Julien Doyon

Volume 2008, Article ID 672582, 7 pages

Editorial

Recent Advances in Neuroimaging Methods

Oury Monchi,^{1,2} Habib Benali,^{1,3} Julien Doyon,^{1,4} and Antonio P. Strafella⁵

¹Functional Neuroimaging Unit, Montreal Geriatric's Institute, University of Montreal, Montreal, QC, Canada H3W 1W5

²Département de Radiologie, University of Montreal, Montreal, QC, Canada H3T 1J4

³Laboratoire d'Imagerie Fonctionnelle (UMR S678), INSERM-UPMC, CHU-Pitié-Salpêtrière, 75013 Paris, France

⁴Département de Psychologie, University of Montreal, Montreal, QC, Canada H2V 2S9

⁵Toronto Western Hospital and CAMH-PET Centre, University of Toronto, Toronto, ON, Canada M5T 1R81

Correspondence should be addressed to Oury Monchi, oury.monchi@umontreal.ca

Received 18 March 2008; Accepted 18 March 2008

Copyright © 2008 Oury Monchi et al. This is an open access article distributed under the Creative Commons Attribution License, which permits unrestricted use, distribution, and reproduction in any medium, provided the original work is properly cited.

Over the past decade, we have seen a large explosion of anatomical and functional neuroimaging techniques, allowing exciting investigation of new aspects of the human brain functions with respect to cognition, learning, and memory. These developments have occurred with respect to the machinery (diverse methods of acquisition), the methods for analysis, and the extent of clinical applications. This issue gives representative examples of these three avenues of development.

Recent advances in magnetic resonance imaging acquisition techniques have not only focused on functional sequences but also on anatomical ones. One important contribution to this field has been the recent development of diffusion weighted imaging magnetic resonance (MR) sequences in order to study the quality of white matter connectivity and importantly perform tractography in order to study for the first time anatomical connectivity in the human brain *in vivo*. Indeed, five articles in the present issue focus on such methods. Leh et al. use diffusion tensor imaging (DTI) tractography to study cortical and subcortical connectivity of the pulvinar in the living human brain. Their results are in accordance with those previously observed in monkeys and provide further support for an important role of the pulvinar in human visual information processing and spatial attention. One difficulty often encountered in performing analyses of effective connectivity (such as structural equations modeling or dynamical causal modeling) of fMRI data is that one usually has to provide an initial network model to be validated. This model should ideally be based on known anatomical connections between brain regions. However, such information in humans is still incomplete. In their article, Fonteijn et al. present a study that revisits existing functional networks using DTI. The obtained results

are of great interest for all researchers in the field. Information is provided about the likelihood of region connections via tractography. For a number of connections the authors find anatomical connectivity that corresponds to the proposed functional paths. They provide compelling examples showing that the use of DTI tractography is a valuable tool to define the anatomical networks required to perform good analysis of effective connectivity. From a more methodological viewpoint, Jbabdi et al. propose a model for the structure of the brain which considers anatomical connections between various cerebral regions as being geodesic with respect to a metric given by the inverse of the diffusion tensor. Using this geodesic method, they are able to construct a path connecting every pair of brain regions. However, the brain is obviously not fully connected, and consequently, they needed to determine whether a given geodesic really represents a white matter fiber tract or not. This is why they also propose an index for the probability of being a fiber, which combines a term that represents the data fit and another term that represents the data confidence. Their new algorithm is tested on simulated data and proves to be computationally fast as well as robust to local perturbation induced by fiber crossing. They also use it on real data to show its feasibility.

A new approach in studying diffusivity in the human brain has been the use of high angular resolution diffusion imaging (HARDI) as an alternative to DTI to overcome the latter method's limitation in complex fiber regions with crossing. Two articles propose novel methods to make the best use of such acquisition sequences. Probabilistic algorithms have been preferred to standard streamline techniques because they are robust to noise in the orientation distribution functions (ODFs) maps and because they can go through bundle crossings that are likely to happen

given the effective resolution of the voxels. Perrin et al. develop a new probabilistic algorithm based on the fiber ODF using a Monte Carlo random walk algorithm. Monte Carlo particles move inside the continuous field of q-ball diffusion ODF and are subject to a trajectory regularization scheme. Their new algorithm is tested on simulated data. Segmentation of white matter and subcortical structures from diffusion weighted magnetic resonance imaging, either DTI or HARDI, is fairly recent. Wassermann et al. use a region-based statistical active contour technique on these images of ODFs to find coherent white matter fiber bundles and a nonlinear spectral-clustering algorithm is presented in order to segment different fiber bundles.

The use of transcranial magnetic stimulation (TMS) has greatly increased during the last five years. While not being an imaging method per se, it does allow to perform “brain mapping” by studying change in behavior and performance when stimulating a specific cortical region. In combination with other brain imaging methods such as Positron emission tomography or functional MRI, it also allows for the study of functional connectivity. Finally, it is also being explored as a therapeutic tool for patients with neurological and psychiatric disorders. In their manuscript, Ko et al. applied rTMS to right dorsolateral prefrontal cortex (DLPFC) and the vertex during different temporal phases of the Wisconsin card sorting task (WCST), an extensively used neuropsychological task to assess executive processes. Performance on the WCST specifically deteriorated when applying rTMS to the DLPFC (and not the vertex) when it was applied during the feedback period (when the participant plans the next response) but not when it was applied during the matching period (when the response is executed). This selective impairment of the DLPFC is consistent with its proposed role in monitoring events in working memory. Rektorova et al., for their part, investigated whether rTMS can induce beneficial effects on L-Dopa induced dyskinesias in Parkinson’s disease. Their preliminary results indicate that rTMS of the DLPFC in these patients does have an improving effect on dyskinesias possibly by inducing a depression of motor cortex excitability, while stimulating the motor cortex directly does not provide the same effect.

One issue of great debate regarding blood oxygenated level dependant (BOLD) functional MRI is its relationship to cerebral blood flow and metabolism under different conditions. Previous studies have suggested that during selective activation of a subset of the zones comprising a columnar system in the visual cortex, perfusion increases uniformly in all columns in the system, while an increase in oxidative metabolism occurs predominantly in the activated column. If this were true, one would expect a disproportionately large BOLD increase compared with blood flow, for a highly localized response in the cortex as opposed to a more diffuse one. To address this issue, Gauthier and Hoge used arterial spin labeling in a group of young adults while performing a monocular and a binocular task. Their results show that the ratio of BOLD to cerebral blood flow effects do not differ significantly between the two stimulation conditions, indicating comparable coupling between flow and oxidative metabolism in V1, regardless of the columnar fraction that was activated.

The investigation of the patterns of connectivity in large-scale extended brain networks in the context of BOLD fMRI is a complex task that has also been the source of much attention during the last few years. In their article, Perlberg and Marrelec review the methods used so far, discuss some of the issues that have to be faced, and propose some avenues for more efficient exploration of such networks. They describe the early correlation approaches that have been used, so-called functional connectivity studies, but point out that the exploration of a whole network would require the successive computations of many functional connectivity maps, each map being used for the selection of the seed voxel, which does not prove very realistic. They also advocate that most methods developed so far for effective connectivity have been of restricted use for studying extended large-scale networks, as their intrinsic complexity prevents them from modeling systems with that many degrees of freedom. They propose that mathematical methods coming from graph and/or network theory may be well suited to deal with such problems, and stress the importance of comparing results coming from other imaging modalities to validate and better understand the large-scale network approach in fMRI.

Multiple methods have been developed recently to perform meta-analysis of functional neuroimaging data. Many of them have been task dependent. Peiffer et al. propose to extend to BOLD fMRI, a method that has been proposed in the mid-60’s to assess the relationship between response times in young and older adults across a variety of tasks called the Brinley plots. In the proposed method, a linear regression is performed over the average BOLD activity map taken over different scanning sessions (while performing different tasks) taken from each group to be compared (e.g., older versus younger adults). This provides a relatively easy method to perform a meta-analysis to evaluate two different groups that take into account between-task differences.

Finally, on the clinical side, Bernad and Doyon review the role of noninvasive neuroimaging techniques such as fMRI and TMS in understanding how the neural connections are altered as a consequence to cerebrovascular injury, the neural mechanisms that underlie neurorehabilitation in stroke, as well as motor memory consolidation in healthy adults. They argue that these methods have the potential to be used as clinical tools to promote and optimize individualized motor recovery in stroke patients.

Altogether, these papers constitute a representative sample of the state of the art in neuroimaging methodology and we hope they will be of great interest to a large number of scientists and clinicians in the field.

ACKNOWLEDGMENTS

We would like to express our sincere gratitude to all contributing authors, reviewers, as well as the Editor Dr. Ge Wang, for making this special issue possible and successful.

*Oury Monchi
Habib Benali
Julien Doyon
Antonio P. Strafella*

Research Article

The Connectivity of the Human Pulvinar: A Diffusion Tensor Imaging Tractography Study

Sandra E. Leh,¹ M. Mallar Chakravarty,² and Alain Ptito¹

¹ Cognitive Neuroscience Unit, Montreal Neurological Institute and Hospital, McGill University, Montreal, Canada H3A 2B4

² McConnell Brain Imaging Center, Montreal Neurological Institute and Hospital, McGill University, Montreal, Canada H3A 2B4

Correspondence should be addressed to Sandra E. Leh-Seal, sandra@bic.mni.mcgill.ca

Received 28 March 2007; Accepted 11 September 2007

Recommended by Antonio P. Strafella

Previous studies in nonhuman primates and cats have shown that the pulvinar receives input from various cortical and subcortical areas involved in vision. Although the contribution of the pulvinar to human vision remains to be established, anatomical tracer and electrophysiological animal studies on cortico-pulvinar circuits suggest an important role of this structure in visual spatial attention, visual integration, and higher-order visual processing. Because methodological constraints limit investigations of the human pulvinar's function, its role could, up to now, only be inferred from animal studies. In the present study, we used an innovative imaging technique, Diffusion Tensor Imaging (DTI) tractography, to determine cortical and subcortical connections of the human pulvinar. We were able to reconstruct pulvinar fiber tracts and compare variability across subjects *in vivo*. Here we demonstrate that the human pulvinar is interconnected with subcortical structures (superior colliculus, thalamus, and caudate nucleus) as well as with cortical regions (primary visual areas (area 17), secondary visual areas (area 18, 19), visual inferotemporal areas (area 20), posterior parietal association areas (area 7), frontal eye fields and prefrontal areas). These results are consistent with the connectivity reported in animal anatomical studies.

Copyright © 2008 Sandra E. Leh et al. This is an open access article distributed under the Creative Commons Attribution License, which permits unrestricted use, distribution, and reproduction in any medium, provided the original work is properly cited.

1. INTRODUCTION

Previous studies in nonhuman primates and cats have shown that the pulvinar is interconnected with various subcortical and cortical areas. Neuroanatomical tracer studies demonstrated, for example, connections between the pulvinar and the amygdala, the pons, the superior colliculus, the caudate nucleus, the putamen, as well as with areas V3, V4, and V5 (MT) [1, 2]. In humans, however, the connections of the pulvinar are less well known because the number of anatomical studies is limited by methodological constraints and access only to postmortem samples.

The major retinal-cortical pathway is known to connect directly via the Lateral Geniculate Nucleus (LGN) to visual cortical areas; however, extensive cortico-pulvinar connections exist (e.g., [2–4]) and suggest an important role of the pulvinar in vision, although its precise function remains unknown. Some studies have proposed an important role of the pulvinar in visual spatial attention, attention shifting, and visual integration [4–8] while others have suggested a contribution to sleep/wakefulness mechanisms and senso-

rimotor integration [9]. Electrophysiological studies in cats [6, 10, 11] as well as a recent fMRI study have further proposed an involvement of the pulvinar in higher-order visual processing [12]. With regard to the human pulvinar, its function and anatomical connections remain speculative and are based mainly on nonhuman primate research [7, 13].

The goal of the present study was to investigate human pulvinar connections *in vivo*. We used Diffusion Tensor Imaging (DTI) tractography, an innovative imaging technique that allows fiber tracking *in vivo*, to determine cortical and subcortical connections of the human pulvinar and to compare variability across normal subjects. DTI measures the random microscopic motion (diffusion) of water molecules in the brain, which allows the reconstruction of cortical fiber structures [14] by determining the diffusion direction. The preferred diffusion direction is known to be parallel to axons and can be visualized. Fiber tracking between grey matter structures can be achieved by using a probabilistic diffusion tractography algorithm and further computational analysis to reconstruct white matter fiber tracts in 3D (for further details see also [15–17]

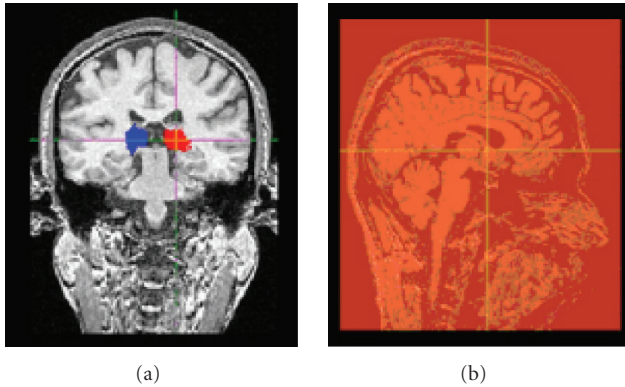


FIGURE 1: *Seedmask and exclusion mask.* An atlas-to-subject transformation was estimated to match the high-resolution MRI template to the subject data. The subsequent transformation was applied to the atlas definition of the pulvinar in order to properly customize to each individual subject. An example of the obtained right (red) and left (blue) pulvinar seedmask is shown in (a). A single sagittal slice along the midline was created on the T_1 -image of each subject to obtain an exclusion mask (b).

and <http://www.fmrib.ox.ac.uk/fsl/fdt/index.html>). Here, we demonstrate the usefulness of DTI tractography to reconstruct pulvinar tracts in humans.

2. METHODS

2.1. Subjects

Six normal subjects (3 females, 3 males), who had no history of neurological and/or ophthalmologic disorders were recruited (age range: 24–36 years). The study was approved by the Montreal Neurological Institute & Hospital (MNI) Research Ethics Committee.

2.2. Data acquisition

A 1.5 Tesla Siemens Sonata scanner at the Brain Imaging Center of the Montreal Neurological Institute (MNI) (Montreal, Canada) was used to obtain T_1 -weighted anatomical MRI images and diffusion-weighted images. Diffusion-weighted images were acquired by using echo-planar imaging (EPI) with a standard head coil (repetition time: 9300 milliseconds, echo time: 94 milliseconds, flip angle: 90° , slice thickness = 2.2 mm, number of slices: 60, in-plane resolution: $2.1875 \text{ mm} \times 2.1875 \text{ mm}$, acquisition time approximately: 9:30 minutes). Diffusion weighting was performed along 60 independent directions, with a b -value of 1000 s/mm^2 . A T_1 -weighted reference anatomical image was also obtained.

2.3. Diffusion-weighted images preprocessing

Diffusion-weighted raw data were first corrected for eddy current distortions and motion artifacts [18]. We then skull-stripped the T_1 -images and fit diffusion tensors at each voxel independently to the data and coregistered diffusion-weighted images to the anatomical image using a

6-parameter transform. Diffusion modeling and probabilistic tractography were carried out using the FMRIB Diffusion Toolbox (FDT, version 1.0), which allows for an estimation of the most probable location of a pathway from a seed point using Bayesian techniques (Oxford Centre for Functional MRI of the Brain (FMRIB), FMRIB Software Library (FSL), version 5.00, UK; <http://www.fmrib.ox.ac.uk/fsl>). Fiber tracking was initiated from all voxels within the seed masks to generate 5000 streamline samples, with a steplength of 0.5 mm and a curvature threshold of 0.2. We used the FSL tools to transform anatomical images to standard space using the MNI coordinates with a 12-parameter transformation (MNI 152 brain, [19]). We first thresholded raw tracts at least at 20 samples (out of the 5000 generated from each seed voxel). We chose to use a threshold of 20 samples to remove only those voxels with very low connectivity probability. This threshold has been used previously and shown very stable results (for further details see also [20]). The results were then binarised, and summed across subject. Results are displayed as a population map, showing only reconstructed tracts that were present in at least 50% of subjects.

2.4. Pulvinar seed masks

A digital atlas of the basal ganglia and thalamus was used [21] to create a seed mask of the left and right pulvinar on each subject's T_1 -weighted image (see Figure 1(a)). This atlas was developed from a set of high-resolution histology sliced coronally. The reconstructed data set has an in-plane voxel-to-voxel spacing of 0.034 mm while the original slice-to-slice thickness is 0.7 mm and was reconstructed using optimized nonlinear slice-by-slice morphological and intensity correction techniques.

The final atlas exists in multiple representations: the original reconstructed histological volume, a voxel-label-atlas where each structure is assigned a unique label to properly identify it, and a 3D geometric atlas. The atlas was warped onto a high-resolution, high signal-to-noise ratio template known as the colin27-MRI-average [22] using a pseudo-MRI derived from the voxel-label-atlas. The atlas-to-template nonlinear transformation was estimated using the ANIMAL algorithm [23]. The ANIMAL algorithm matches a source volume to a target volume by estimating a deformation field of local translations defined on a set of equally spaced nodes which maximizes the similarity between the source and target volumes. The accuracy of this warp and the anatomical definitions on the colin27 template was compared against manual segmentations [24]. The pulvinar of each subject (target volume) was defined as a volume of interest on the atlas (source volume). A high-resolution nonlinear transformation was estimated from the atlas to fit each subject using the parameters identified in Table 1. The transformation is estimated in a hierarchical fashion where large deformations are estimated first and used as the input for the estimation of smaller, more refined transformations. All transformations are estimated on unblurred data (as an effective blurring is done in the subsampling methods used within ANIMAL). The stiffness, weight, and similarity parameters used were those identified in an optimization by

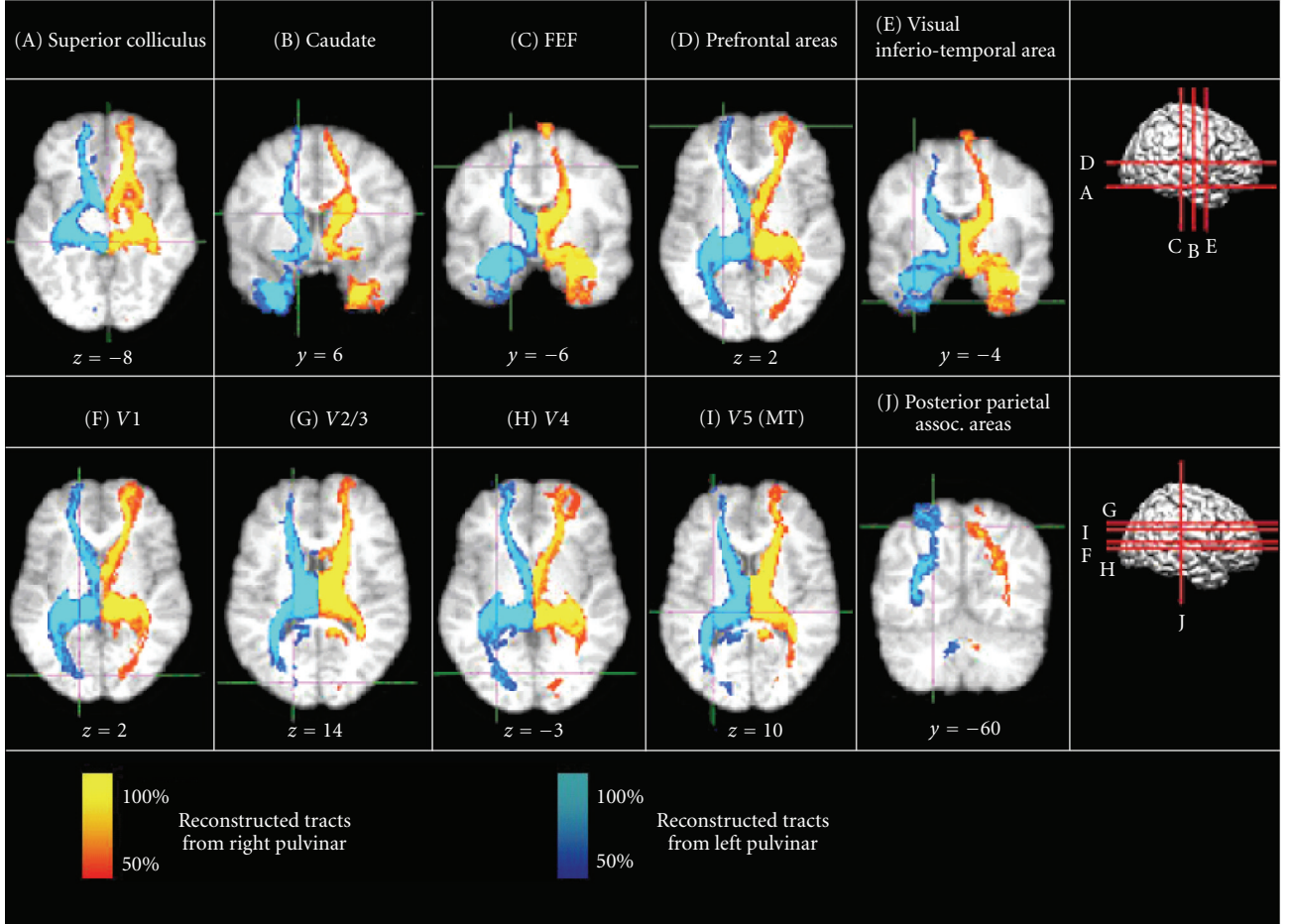


FIGURE 2: Population probability maps of reconstructed pulvinal tracts based on tractography in six healthy subjects. Fiber tracking was initiated from a seed mask in the right pulvinal demonstrated in red hues and from a seed mask in the left pulvinal demonstrated in blue hues. Intensity of the color scales represents the proportion of the population showing a tract at any given voxel. Tracts were registered to MNI standard stereotaxic space, thresholded at 20 samples, and binarised and summed across subjects. For individual subject tracts (see Figure 3). Images demonstrate ipsilateral connections to/from the superior colliculus (A; $x = \pm 4$, $y = -34$, $z = -8$), the caudate (B; $x = \pm 12$, $y = 6$, $z = 16$), the frontal eye fields (C; $x = \pm 18$, $y = -6$, $z = 50$), prefrontal areas (D; $x = \pm 20$, $y = 62$, $z = 2$), visual inferiotemporal area (E; $x = \pm 32$, $y = -4$, $z = -42$), V1 (F; $x = \pm 16$, $y = -86$, $z = 2$), V2/3 (G; $x = \pm 16$, $y = -88$, $z = 14$; $x = \pm 22$, $y = -80$, $z = 22$), V4 (H; $x = \pm 26$, $y = -75$, $z = -3$), V5 (MT) (I; $x = \pm 32$, $y = -74$, $z = 10$), and posterior parietal association areas (J; $x = \pm 20$, $y = -60$, $z = 54$). Note the high consistency of pulvinal tracts across subjects.

TABLE 1: Atlas-to-subject warping parameters used to estimate a high-resolution nonlinear transformation using the ANIMAL algorithm.

Step	Step size (mm)	Sub-lattice diameter (mm)	Sublattice	Iterations
1	4	8	8	15
2	2	6	8	15
3	1	6	6	15

Robbins et al. [25]. The final transformation is defined on a grid where local translations are grid-defined with a 1 mm isotropic spacing and then applied to the mask of the pulvinal for the DTI tractography of each subject.

2.5. Exclusion mask

We then created a single sagittal slice along the midline on the T_1 -image of each subject to restrict analyses to connections of one hemisphere. Fiber tracking was initiated from all voxels within the seed masks (see Figure 1).

3. RESULTS

A seed mask of the right and left pulvinal was created on each subject's T_1 -weighted anatomical image (see Section 2.4). Tracts were reconstructed from all voxels within the pulvinal and analysis was restricted to the ipsilateral hemisphere (see Section 2.5).

Reconstructed pulvinal tracts are displayed as a population map in Figure 2. Only tracts that were present in at least 50% of the subjects are shown. Examples of individual

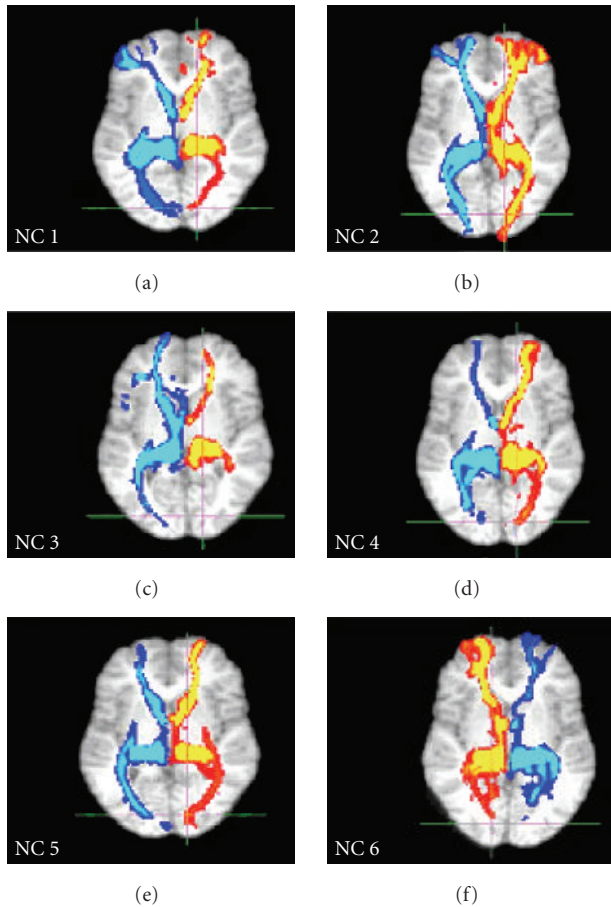


FIGURE 3: Examples of individual pulvinal in six control subjects (NC1-6). Tracts (slice level V1: $x = 16$, $y = -86$, $z = 2$) have been thresholded at 20 samples. Red hues demonstrate reconstructed tracts from the right pulvinal, and blue hues demonstrate reconstructed tracts from the left pulvinal. The intensity of color scales indicates the number of samples that passed through that voxel from red/blue (low probability of connection) to yellow/light blue (high probability of connection).

pulvinal tracts are demonstrated in Figure 3. Reconstructed tracts of the right and left pulvinal projected ipsilaterally to the superior colliculus (A; $x = \pm 4$, $y = -34$, $z = -8$), the caudate (B; $x = \pm 12$, $y = 6$, $z = 16$), the frontal eye fields (C; $x = \pm 18$, $y = -6$, $z = 50$), prefrontal areas (D; $x = \pm 20$, $y = 62$, $z = 2$), visual inferotemporal area (E; $x = \pm 32$, $y = -4$, $z = -42$), V1 (F; $x = \pm 16$, $y = -86$, $z = 2$), V2/3 (G; $x = \pm 16$, $y = -88$, $z = 14$; $x = \pm 22$, $y = -80$, $z = 22$), V4 (H; $x = \pm 26$, $y = -75$, $z = -3$), V5 (MT) (I; $x = \pm 32$, $y = -74$, $z = 10$), and posterior parietal association areas (J; $x = \pm 20$, $y = -60$, $z = 54$). Please note the high consistency of pulvinal tracts across subjects.

4. DISCUSSION

Our DTI tractography study in humans reveals connections between the pulvinal and various cortical and subcortical areas. In accordance with previous primate studies, connections to the superior colliculus and caudate were observed

[1–3, 26–29]. Our reconstructed pulvinal tracts also projected ipsilaterally to prefrontal, inferior temporal, and parietal association areas, as previously shown in nonhuman tracer studies [27, 30–32]. Furthermore, we were able to confirm the existence of connections between the human pulvinal and visual cortical areas V1, V2, V4, and V5 (MT) in keeping with studies in nonhuman primates [2, 8, 33]. Finally, we found that connections between the pulvinal and the frontal eye fields that were previously shown to exist in monkeys [34–36] are also present in humans.

Taken together, our study demonstrates that extensive cortical and subcortical connections from/to the pulvinal also exist in humans. Although DTI tractography is not able to distinguish between feedforward and feedbackward projections, our reconstructed tracts suggest that the pulvinal likely plays an important role in human visual information processing and visual spatial attention as it does in nonhuman primates and cats [4, 6, 12]. Our results also demonstrate that DTI tractography is a useful new imaging technique to investigate human anatomical pathways.

ACKNOWLEDGMENTS

The authors thank the subjects for their participation. This study was supported by a training grant from REPRIC to S. E. Leh, a doctoral scholarship from CRIR and FRSQ to S. E. Leh, and an NSERC research grant to A. Ptito (RGPIN 37354-02).

REFERENCES

- [1] R. E. Weller, G. E. Steele, and J. H. Kaas, "Pulvinal and other subcortical connections of dorsolateral visual cortex in monkeys," *Journal of Comparative Neurology*, vol. 450, no. 3, pp. 215–240, 2002.
- [2] S. Shipp, "Corticopulvinal connections of areas V5, V4, and V3 in the macaque monkey: a dual model of retinal and cortical topographies," *Journal of Comparative Neurology*, vol. 439, no. 4, pp. 469–490, 2001.
- [3] L. M. Chalupa, H. Ansel, and D. B. Lindsley, "Visual input to the pulvinal via lateral geniculate, superior colliculus and visual cortex in the cat," *Experimental Neurology*, vol. 36, no. 3, pp. 449–462, 1972.
- [4] C. Casanova, R. D. Freeman, and J. P. Nordmann, "Monocular and binocular response properties of cells in the striate-recipient zone of the cat's lateral posterior-pulvinal complex," *Journal of Neurophysiology*, vol. 62, no. 2, pp. 544–557, 1989.
- [5] C. Casanova, J. P. Nordmann, and S. Molotchnikoff, "Pulvinal-lateral posterior nucleus complex of mammals and the visual function," *Journal de Physiologie*, vol. 85, no. 1, pp. 44–57, 1991.
- [6] C. Casanova, L. Merabet, A. Desautels, and K. Minville, "Higher-order motion processing in the pulvinal," *Progress in Brain Research*, vol. 134, pp. 71–82, 2001.
- [7] S. Shipp, "The brain circuitry of attention," *Trends in Cognitive Sciences*, vol. 8, no. 5, pp. 223–230, 2004.
- [8] S. Kastner and M. A. Pinsk, "Visual attention as a multilevel selection process," *Cognitive, Affective, & Behavioral Neuroscience*, vol. 4, no. 4, pp. 483–500, 2004.

- [9] M. Palestini, "The integrative sensorimotor function of the LP-pulvinar complex," *Archives Italiennes de Biologie*, vol. 120, no. 1–3, pp. 346–360, 1982.
- [10] L. Merabet, A. Desautels, K. Minville, and C. Casanova, "Motion integration in a thalamic visual nucleus," *Nature*, vol. 396, no. 6708, pp. 265–268, 1998.
- [11] D. Dumbrava, J. Faubert, and C. Casanova, "Global motion integration in the cat's lateral posterior-pulvinar complex," *European Journal of Neuroscience*, vol. 13, no. 12, pp. 2218–2226, 2001.
- [12] M. Y. Villeneuve, R. Kupers, A. Gjedde, M. Ptito, and C. Casanova, "Pattern-motion selectivity in the human pulvinar," *NeuroImage*, vol. 28, no. 2, pp. 474–480, 2005.
- [13] K. L. Grieve, C. Acuña, and J. Cudeiro, "The primate pulvinar nuclei: vision and action," *Trends in Neurosciences*, vol. 23, no. 1, pp. 35–39, 2000.
- [14] P. J. Basser, J. Mattiello, and D. LeBihan, "Estimation of the effective self-diffusion tensor from the NMR spin echo," *Journal of Magnetic Resonance. Series B*, vol. 103, no. 3, pp. 247–254, 1994.
- [15] T. E. J. Behrens, M. W. Woolrich, M. Jenkinson, et al., "Characterization and propagation of uncertainty in diffusion-weighted MR imaging," *Magnetic Resonance in Medicine*, vol. 50, no. 5, pp. 1077–1088, 2003.
- [16] T. E. J. Behrens, H. Johansen-Berg, M. W. Woolrich, et al., "Non-invasive mapping of connections between human thalamus and cortex using diffusion imaging," *Nature Neuroscience*, vol. 6, no. 7, pp. 750–757, 2003.
- [17] T. E. J. Behrens, H. Johansen-Berg, S. Jbabdi, M. F. S. Rushworth, and M. W. Woolrich, "Probabilistic diffusion tractography with multiple fibre orientations: what can we gain?" *NeuroImage*, vol. 34, no. 1, pp. 144–155, 2007.
- [18] M. Jenkinson, P. Bannister, M. Brady, and S. Smith, "Improved optimization for the robust and accurate linear registration and motion correction of brain images," *NeuroImage*, vol. 17, no. 2, pp. 825–841, 2002.
- [19] A. C. Evans, D. L. Collins, S. R. Mills, E. D. Brown, R. L. Kelly, and T. M. Peters, "3D statistical neuroanatomical models from 305 MRI volumes," in *Proceedings of IEEE Nuclear Science Symposium and Medical Imaging Conference*, vol. 3, pp. 1813–1817, San Francisco, Calif, USA, October–November 1994.
- [20] S. E. Leh, H. Johansen-Berg, and A. Ptito, "Unconscious vision: new insights into the neuronal correlate of blindsight using diffusion tractography," *Brain*, vol. 129, no. 7, pp. 1822–1832, 2006.
- [21] M. M. Chakravarty, A. F. Sadikot, J. Germann, G. Bertrand, and D. L. Collins, "Anatomical and electrophysiological validation of an atlas for neurosurgical planning," in *Proceedings of the 8th International Conference on Medical Image Computing and Computer-Assisted Intervention Part II (MICCAI '05)*, vol. 3750, pp. 394–401, 2005.
- [22] C. J. Holmes, R. Hoge, L. Collins, R. Woods, A. W. Toga, and A. C. Evans, "Enhancement of MR images using registration for signal averaging," *Journal of Computer Assisted Tomography*, vol. 22, no. 2, pp. 324–333, 1998.
- [23] D. L. Collins and A. C. Evans, "Animal: validation and application of nonlinear registration-based segmentation," *International Journal of Pattern Recognition and Artificial Intelligence*, vol. 11, no. 8, pp. 1271–1294, 1997.
- [24] M. M. Chakravarty, G. Bertrand, C. P. Hodge, A. F. Sadikot, and D. L. Collins, "The creation of a brain atlas for image guided neurosurgery using serial histological data," *NeuroImage*, vol. 30, no. 2, pp. 359–376, 2006.
- [25] S. Robbins, A. C. Evans, D. L. Collins, and S. Whitesides, "Tuning and comparing spatial normalization methods," *Medical Image Analysis*, vol. 8, no. 3, pp. 311–323, 2004.
- [26] L. A. Benevento and G. P. Standage, "The organization of projections of the retinorecipient and nonretinorecipient nuclei of the pretectal complex and layers of the superior colliculus to the lateral pulvinar and medial pulvinar in the macaque monkey," *Journal of Comparative Neurology*, vol. 217, no. 3, pp. 307–336, 1983.
- [27] E. H. Yeterian and D. N. Pandya, "Corticothalamic connections of the posterior parietal cortex in the rhesus monkey," *Journal of Comparative Neurology*, vol. 237, no. 3, pp. 408–426, 1985.
- [28] D. L. Robinson and J. W. McClurkin, "The visual superior colliculus and pulvinar," *Reviews of Oculomotor Research*, vol. 3, pp. 337–360, 1989.
- [29] J. J. Hutsler and L. M. Chalupa, "Substance P immunoreactivity identifies a projection from the cat's superior colliculus to the principal tectorecipient zone of the lateral posterior nucleus," *Journal of Comparative Neurology*, vol. 312, no. 3, pp. 379–390, 1991.
- [30] G. E. Steele and R. E. Weller, "Subcortical connections of subdivisions of inferior temporal cortex in squirrel monkeys," *Visual Neuroscience*, vol. 10, no. 3, pp. 563–583, 1993.
- [31] M. J. Webster, J. Bachevalier, and L. G. Ungerleider, "Subcortical connections of inferior temporal areas TE and TEO in macaque monkeys," *Journal of Comparative Neurology*, vol. 335, no. 1, pp. 73–91, 1993.
- [32] L. M. Romanski, M. Giguere, J. F. Bates, and P. S. Goldman-Rakic, "Topographic organization of medial pulvinar connections with the prefrontal cortex in the rhesus monkey," *Journal of Comparative Neurology*, vol. 379, no. 3, pp. 313–332, 1997.
- [33] M. M. Adams, P. R. Hof, R. Gattass, M. J. Webster, and L. G. Ungerleider, "Visual cortical projections and chemoarchitecture of macaque monkey pulvinar," *Journal of Comparative Neurology*, vol. 419, no. 3, pp. 377–393, 2000.
- [34] J. Q. Trojanowski and S. Jacobson, "Medial pulvinar afferents to frontal eye fields in rhesus monkey demonstrated by horseradish peroxidase," *Brain Research*, vol. 80, no. 3, pp. 395–411, 1974.
- [35] J. Bos and L. A. Benevento, "Projections of the medial pulvinar to orbital cortex and frontal eye fields in the rhesus monkey (*Macaca mulatta*)," *Experimental Neurology*, vol. 49, no. 2, pp. 487–496, 1975.
- [36] M. F. Huerta, L. A. Krubitzer, and J. H. Kaas, "Frontal eye field as defined by intracortical microstimulation in squirrel monkeys, owl monkeys, and macaque monkeys: I. Subcortical connections," *Journal of Comparative Neurology*, vol. 253, no. 4, pp. 415–439, 1986.

Research Article

Exploring the Anatomical Basis of Effective Connectivity Models with DTI-Based Fiber Tractography

Hubert M. J. Fonteijn,^{1,2} David G. Norris,² and Frans A. J. Verstraten¹

¹ Helmholtz Institute, Universiteit Utrecht, Heidelberglaan 2, 3584 CS Utrecht, The Netherlands

² F.C. Donders Centre for Cognitive Neuroimaging, Radboud University Nijmegen, P.O. Box 9102, 6500 HC Nijmegen, The Netherlands

Correspondence should be addressed to Hubert M. J. Fonteijn, h.fonteijn@cs.ucl.ac.uk

Received 31 August 2007; Revised 26 November 2007; Accepted 17 December 2007

Recommended by Habib Benali

Diffusion tensor imaging (DTI) is considered to be a promising tool for revealing the anatomical basis of functional networks. In this study, we investigate the potential of DTI to provide the anatomical basis of paths that are used in studies of effective connectivity, using structural equation modeling. We have taken regions of interest from eight previously published studies, and examined the connectivity as defined by DTI-based fiber tractography between these regions. The resulting fiber tracts were then compared with the paths proposed in the original studies. For a substantial number of connections, we found fiber tracts that corresponded to the proposed paths. More importantly, we have also identified a number of cases in which tractography suggested direct connections which were not included in the original analyses. We therefore conclude that DTI-based fiber tractography can be a valuable tool to study the anatomical basis of functional networks.

Copyright © 2008 Hubert M. J. Fonteijn et al. This is an open access article distributed under the Creative Commons Attribution License, which permits unrestricted use, distribution, and reproduction in any medium, provided the original work is properly cited.

1. INTRODUCTION

In functional neuroimaging, and particularly in PET and fMRI, study design and analysis have been dominated by the concept of functional *segregation*, which emphasizes the specialization of a brain structure for a specific part of a cognitive function. This has resulted in a large number of studies in which differences in cognitive states are linked to the differential activation of separate brain areas [1]. The concept of functional *integration*, on the other hand, has long been recognized as an equally important principle of brain organization. Functional integration refers to the interaction between brain areas and has been studied with two categories of analyses: functional connectivity analyses and effective connectivity analyses. In functional connectivity analyses [2–4], the covariance structure of a measure of brain activity is studied, from which differences in cognitive states are linked to differences in correlations between regions. These analysis methods are thus limited in their capacity to make inferences about the directionality of these correlations, which makes it difficult to address, for instance, the functional hierarchy of the brain structures under investigation. In effective

connectivity analyses, on the other hand, models are defined a priori, comprising the brain structures of interest and assumptions about the afferent/efferent connections between them [5, 6]. These models are then fitted to the activity of these brain areas to obtain the strength of these connections, which enables inferences on changes in connection strengths in relationship to cognitive states.

Effective connectivity has been defined as the influence one neural system or region exerts over another [7]. There are two ways by which this influence can be mediated: via a direct path between two regions, or via an indirect path in which a third region is involved. The analysis methods that have been applied to functional neuroimaging data, structural equation modeling (SEM) and dynamic causal modeling (DCM), differentiate between these two possibilities, provided that the underlying model (regions and their paths) is completely specified. If two regions are connected via a third region and this third region has furthermore no other influence on the rest of the network, one can choose to incorporate only an indirect path between the two regions and to refrain from explicitly modeling the third region and its direct paths. This is usually done to

keep the model computationally tractable. We are working here, however, on the premise that most of the specified paths should reflect veridical direct paths, because we believe that too many “indirect” paths, involving these “third party” regions, which are not explicitly taken into account in the model, will seriously decrease the biological validity of the model.

SEM has also extensively been applied in the social sciences, where these paths represent abstract causal connections between variables. When this method is applied to functional neuroimaging however, these paths should ultimately correspond to the white matter connectivity of the brain regions under investigation. This hence yields an extra source of model validation. Furthermore, McIntosh and Gonzalez-Lima [8] have studied the effect of erroneous model specification on the estimation of the path coefficients and have found that it could seriously impinge on the estimation of these coefficients. Therefore, it would be highly valuable to incorporate all available knowledge regarding anatomical connections into effective connectivity models. It should be noted that we do not imply that each existing anatomical connection should result in an effective connection in each and every cognitive task. However, it is the role of the model estimation to indicate which anatomical connections have become effective for which task manipulation. Therefore, leaving an anatomical connection, which is known to exist, out of a model specification can only be justified when one has strong beliefs about the functioning of this path in the present context, possibly combined with a requirement for a decrease in model complexity.

Unfortunately, our knowledge about human anatomical connectivity is relatively sparse, because a number of techniques that are used in other species (active tracers) are highly invasive. Therefore, only two classical anatomical methods can be used: *dissection studies*, which only provide information on a relatively coarse scale, and *passive tracer studies*, which are not very well suited to investigate long-range connectivity. Most effective connectivity studies thus can only validate their connections with information from nonhuman primates, which in turn raises problems with the homology of brain structures between different species.

In the last decade, a technique known as diffusion tensor imaging (DTI) [9, 10] has emerged as a good candidate to resolve this situation. In DTI, the sensitivity of the (diffusion-weighted) MR signal to the self-diffusion of water on a microscopic scale is employed to characterize the anisotropic structure of white matter *in vivo*. It is assumed that the direction in which diffusion is largest is collinear to the direction of the axonal bundle in the voxel, because diffusion is assumed to be hindered in directions perpendicular to this direction. With this information, fiber tracking [11, 12] can be performed in which the main diffusion directions of voxels are followed throughout white matter. This method already has provided useful insights in, for instance, the anatomy of the thalamus and the striatum [13, 14].

So far, researchers have acknowledged a number of limitations to this technique. First, DTI provides no information about the afferent or efferent character of the axons, because the diffusion of water does not differentiate between these

two situations. Second, the tensor model can only provide one main direction per voxel, which considerably increases the likelihood of erroneous tracking results through a region of crossing fibers. Finally, in cerebral gray matter there is generally no dominant fiber direction, making it difficult to track fibers to their cortical origin.

The aim of the current study is to investigate to what extent DTI-based tractography can provide support for the anatomical basis of the networks, proposed in effective connectivity studies. Furthermore, we have investigated whether DTI-based tractography is able to reveal any connections that go beyond the ones proposed in the original analysis. To address these questions, we have chosen eight effective connectivity studies all using structural equation modeling. SEM was introduced at an early stage of the development of PET and fMRI, with the consequence that a body of SEM studies is to be found in the literature. DCM, on the other hand, has only relatively recently been introduced, but is gaining a rapid popularity. It should be noted that any conclusions we are able to draw in this study within the context of SEM models can be readily generalized to DCM studies as there is no difference in the role of the underlying anatomical model in both frameworks.

We have chosen networks spanning a number of different cognitive domains, including learning [15, 16], cognitive control [17, 18], working memory [19], visual and auditory perception [20], major depression [21], and the thalamocortical network involved in general-anaesthetic-induced unconsciousness [22]. We performed a standard DTI experiment on 6 subjects and used the coordinates of the network nodes as seed regions for a fiber tracking analysis. In this analysis, we have established whether DTI-based fiber tractography provides evidence about the direct nature of every possible connection, whether or not it was proposed in the original studies.

2. MATERIALS AND METHODS

2.1. Subjects

We studied 6 healthy subjects (2 females, age range 25–32 years) after informed consent was given according to institutional guidelines of the local ethics committee (CMO protocol region Arnhem-Nijmegen, The Netherlands).

2.2. Imaging

DTI was performed using a twice refocused pulsed gradient spin echo EPI sequence [23] at 1.5 T (Sonata system, Siemens, Erlangen, Germany) with a standard head coil. Axial slices were obtained using the following imaging parameters: repetition time = 9900 milliseconds, echo time = 88 milliseconds, flip angle = 90°, 128 × 128 matrix, 320 mm × 320 mm field of view, and slice thickness = 2.5 mm with no gap (2.5 × 2.5 × 2.5 mm isotropic voxels). Diffusion weighting was obtained along sixty noncollinear directions [24] using a *b*-value of 700 s/mm². Five reference images with no diffusion weighting were also obtained. This resulted in a scanning time of approximately 10 minutes per subject.

2.3. Analyses

For each subject the five reference images with no diffusion weighting were averaged and normalized to the MNI T2 template in SPM2 (Statistical Parametric Mapping, <http://www.fil.ion.ucl.ac.uk/spm>). The matrix of normalization parameters was inverted to obtain the transformation matrix from standard space to world space. We have done this to avoid the extensive resampling and reorientation of the data that is involved in the normalization of DTI data [25, 26], because we hypothesize that this would lead to a degradation of the finer details in the fiber tracts. Only linear terms were used in the normalization to ensure that the transformation matrices could be inverted. No motion correction was applied. Diffusion tensors and fractional anisotropy (FA) maps were calculated using the diffusion toolbox [27] in SPM2. The FA maps were used for displaying the anatomical location of the ROI coordinates. These anatomical locations were then used as seed regions for fiber tracking. Fiber tracking was performed in the DTI-Studio package [28] using the FACT algorithm [29]. Tracking was terminated when the angle of two consecutive eigenvectors was larger than 85° , or when a voxel was reached with an FA value smaller than 0.20.

In most of the original studies [15–19, 22], the ROIs that were used for effective connectivity analysis were all spheres of 8 mm radius. However, in two studies [20, 21] only the peak voxels of a partial least-squares analysis [30] were used. Because these voxels represented larger clusters of voxels, we have used ROIs with roughly the same size (spheres of 8 mm radius) as a starting point for all networks. We have chosen not to transform the whole original ROI into subject space, as this might lead to extensive seeding of the white matter adjacent to the seed coordinate, and thus to many false positives. Instead, we have drawn ROIs on the individual subject's FA maps, taking care that the borders of the ROI were at the border of gray and white matters (as visible on the FA map) and that the ROI would approximately be of the same size as the original ROI. All possible combinations of regions were tracked, including the connections that were not proposed in the original effective connectivity studies.

3. RESULTS

The results for all networks under investigation are visualized in Figures 1–8, in which the thickness of the connecting lines indicates the number of subjects in which a particular connection was found. In the appendix, we have also listed these results in Table 1. Our results support the proposed paths to a large extent. The most striking class of paths which are not supported by our findings contains frontal interhemispheric paths. This can however convincingly be explained by methodological shortcomings in regions with crossing fibers in the frontal parts of the brain. We will discuss these issues further in Section 4. In half of the studies, we have also found connections indicating paths that were not included in the original studies. In the following, we will describe these findings for each study separately.

The nomenclature of the original studies is maintained throughout this whole article. This not only leads to the situation that this nomenclature is inconsistent between studies, but may also give the incorrect impression that similar connections are under investigation in different networks. It is therefore important to note that the regions of interest normally are spheres of approximately 8 mm in diameter, and thus two regions with the label “prefrontal cortex” can be quite widely separated.

Büchel et al.

The network of this study can be separated into a dorsal stream (V1, DE, PP, and LP) and a ventral stream (V1, ITp, and ITa) of visual areas. The paths within these streams are supported in the majority of subjects by our DTI results. However, the crucial path under investigation is the path between the two streams (PP-ITp), which is hypothesized to mediate the learning effect under investigation. Interestingly, we have found no evidence for this path, but we have found support for a path (DE-ITa), which was not included in the proposed network and which could be a potential candidate to mediate this effect. Whereas we do not wish to suggest that the original path (PP-ITp) should be dismissed, it would be interesting to investigate whether a part of the learning related effects, reported in the original study, is mediated by the new path we have reported.

Fletcher et al.

In this network, a series of regions (OCC, PAR, and PFC) is proposed in both hemispheres with symmetrical paths within the hemispheres and extensive interhemispheric connections. The paths between occipital and parietal cortices are supported by our findings as are the interhemispheric connections between these regions. Furthermore, we have found evidence for paths that were not included in the original model, namely, interhemispheric connections between occipital and parietal cortices. This is quite remarkable, because interhemispheric connections between nonhomologous regions are rarely found in this kind of analyses.

Also of interest are the cases in which the proposed paths are not supported by our results. The interhemispheric connections we did not find (LPFC-RPFC, LPFC-RPAR, and RPFC-LPAR) fall into the aforementioned problematic class of frontal interhemispheric connections. The most interesting negative result is the lack of connections between right parietal and right prefrontal cortices, in contrast to the presence of these connections in the left hemisphere. In this case, methodological shortcomings are not likely to affect the results, as this would indicate that these shortcomings would exist for the right hemisphere but not for the left hemisphere. The same argument makes the consideration of connections via an extra region, which has not been included in the network, also unattractive. Therefore, we tentatively interpret these findings as a support for an asymmetry in connectivity between these areas in parietal and prefrontal cortices.

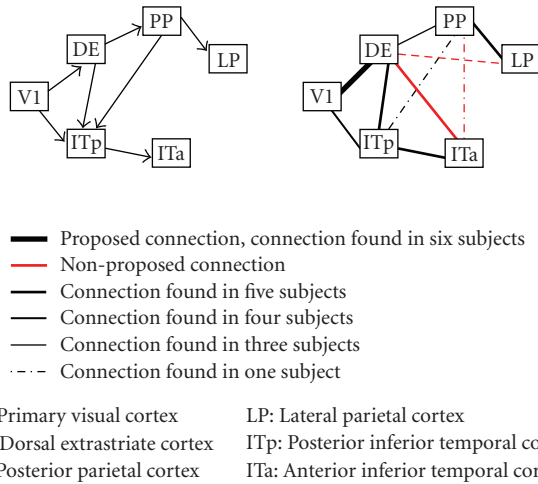


FIGURE 1: The proposed network of Büchel et al. is shown on the left. The connections found in our analysis are shown on the right. The legend indicates the meaning of the color scale and the thickness of the lines. This legend is valid for all the following figures.

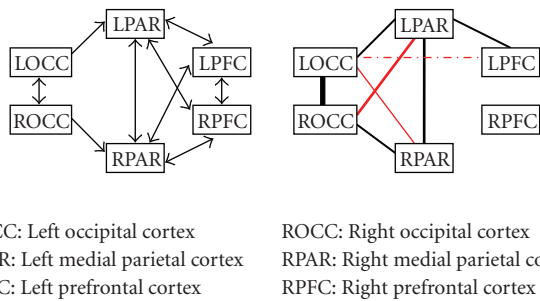


FIGURE 2: The network and results for Fletcher et al.

Koechlin et al.

This network contains a set of motor and prefrontal regions in both hemispheres which are symmetrically connected within the hemispheres. Furthermore, homologous areas are connected with each other. This last set of paths falls again in the class of frontal interhemispheric connections and thus it is not surprising that we have found no support for these paths. We have found connections supporting all intrahemispheric paths in most subjects. Interestingly, Koechlin et al. have proposed an alternative network in their study, which contained also paths directly from premotor cortex to rostral prefrontal cortex. This extra network did not result in significant changes in the original paths, which is in agreement with the lack of support for these paths in our results.

Kondo et al.

Kondo et al. have proposed four network nodes (PFC, ACC, SPL, and IFC). However, two of these nodes (SPL and IFC) can be further split up in four anatomically distinct regions (SPL1, SPL2, IFC1, and IFC2). We have thus decided to treat

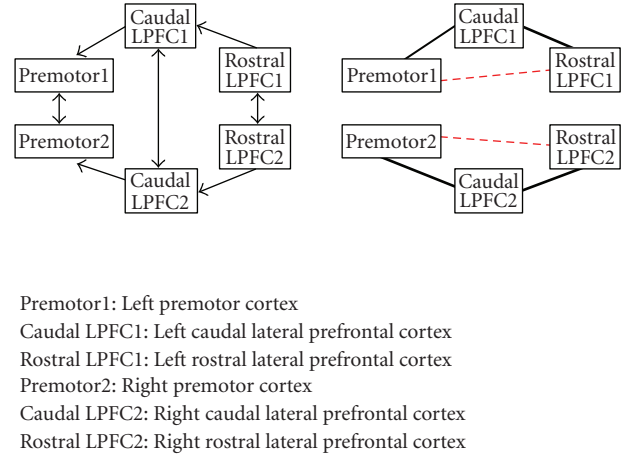


FIGURE 3: The network and results for Koechlin et al.

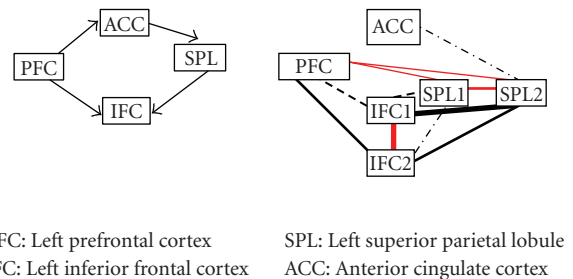
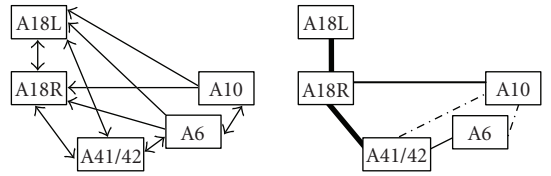


FIGURE 4: The network and results for Kondo et al.

each of these regions as a separate node and have studied the connections between these nodes. Our results show that the regions which constitute each original node (e.g., IFC1 and IFC2) are connected with each other, but they show differential connectivity patterns with the rest of the network, which suggest that they also have a different role within this network. The lack of support for paths from and to the ACC was surprising, especially given the fact that the ACC is known to connect extensively with the prefrontal cortex in the macaque [31].

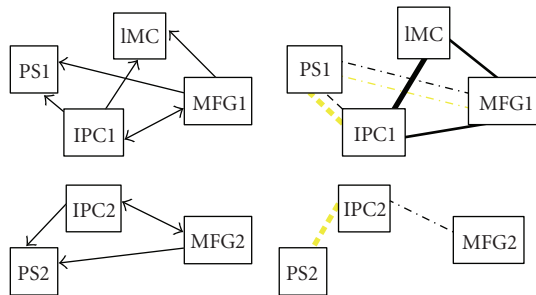
McIntosh et al.

In this network, a set of regions is proposed ranging from occipital, temporal, premotor, and prefrontal regions. Moreover, these regions were proposed to be highly interconnected. Given our results in the other studies, it was not surprising that there was hardly any support for the (nonhomologous) interhemispheric connections originating in frontal and prefrontal cortices. Support was found for paths between occipital cortex and frontal and superior temporal cortices. However, there are also two intrahemispheric paths for which no support was given (A6-A18R, A10-A6). Furthermore, there was no evidence found for paths which were not included in the original analysis. Therefore, within the context of this network, DTI did not deliver any extra information.



A18L: Left Brodmann area 18 (occipital cortex)
 A18R: Right Brodmann area 18
 A41/42: Right Brodmann area 41/42 (superior temporal cortex)
 A6: Right Brodmann area 6 (premotor cortex)
 A10: Right Brodmann area 10 (prefrontal cortex)

FIGURE 5: The network and results for McIntosh et al.



--- Connection found after reanalysis with low FA
 - - - Connection found in two subjects

PS1: Left prestriate cortex PS2: Right prestriate cortex
 IPC1: Left parietal cortex IPC2: Right parietal cortex
 MFG1: Left prefrontal cortex MFG2: Right prefrontal cortex
 IMC: Left motor cortex

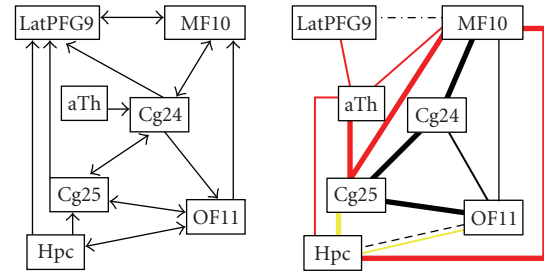
FIGURE 6: The network and results for Rowe et al.

Rowe et al.

Rowe et al. have proposed a network with bilateral parietal, prefrontal, and prestriate areas and a motor area in the left hemisphere only. We have found only scarce support for the paths to and from prestriate area, even after lowering the FA threshold. In the left hemisphere, we have found consistent evidence for all other proposed paths. However, as in the network of Fletcher et al., we have found support for parietal-frontal connections in the left but not in the right hemisphere. Based on the same arguments as in the network of Rowe et al., we again interpret this as an evidence for an asymmetry in these connections. This is even more remarkable, because the locations of parietal and especially prefrontal areas in both studies are quite widely separated.

Seminowicz et al.

The network of Seminowicz et al. consists predominantly of prefrontal subcortical areas in the right hemisphere, with the lateral prefrontal cortex as the only region in the left hemisphere. This might directly explain why we have found only scarce evidence for paths from this region to the rest of



Hpc: Hippocampus
 Cg25: Subgenual cingulate BA 25
 aTh: Anterior thalamus
 LatPFG9: Lateral prefrontal cortex BA 9
 OF11: Orbital frontal cortex BA 11
 Cg24: Rostral anterior cingulate BA 24a
 MF10: Medial frontal cortex BA 10

FIGURE 7: The network and results for Seminowicz et al. BA = Brodmann area.

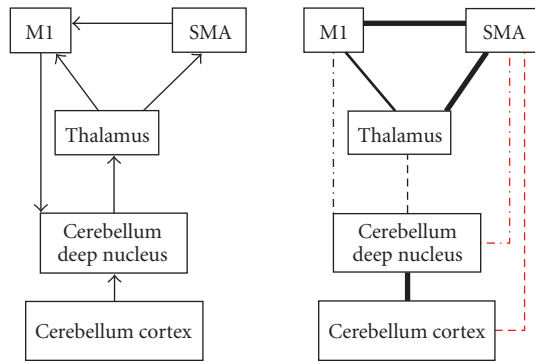
the network, because of the aforementioned methodological problems with frontal interhemispheric connections.

In contrast to the study of Kondo et al., we have found connections supporting the proposed paths from the anterior cingulate cortex. Furthermore, we have found many connections from the thalamus to the rest of the network which do not conform to proposed paths. This is however not surprising, as it is well known that the different nuclei in the thalamus extensively connect to different parts of the cortex [13]. The “extra” connections are thus most probably the result of the fact that the seed region in this case was too large to specifically select the nucleus of the thalamus involved in this network. Further evidence for paths that were not proposed in the original network was found for connections from medial prefrontal cortex to the hippocampus and the subgenual cingulate cortex.

The hippocampus is a region of low FA and thus in an initial analysis showed only very limited connectivity with the rest of the network. We have therefore repeated the analysis with a lowered FA threshold (0.15) which yielded support for the proposed paths from the hippocampus.

White et al.

White et al. have proposed a model with the left motor cortex and supplementary motor area, the thalamus, and two areas from the right cerebellum. We have found support for the intrahemispheric paths but not for the interhemispheric ones. This last finding contradicts findings from the macaque literature in which there are connections found between the primary motor cortex and the contralateral cerebellum deep nucleus [32]. Moreover, there is evidence that the pons, which is a region through which these fibers have to pass, contains crossing fibers [33]. We, therefore, conclude that it is valid to include these connections in an effective connectivity analysis.



M1: Motor cortex
SMA: Supplementary motor area

FIGURE 8: The network and results for White et al.

4. DISCUSSION

In this study, we have for the first time used DTI-based fiber tractography to investigate the anatomical basis of effective connectivity models. The aim of this study was twofold. First, we wanted to establish that DTI-based tractography is able to resolve the connectivity between ROIs of the size typically used in effective connectivity studies. We hypothesized that the majority of the proposed paths were indeed valid, and compared the results of our DTI-based analysis with these paths. We have found positive evidence for a substantial number of paths. The negative findings will be discussed below. However, we believe that the greatest potential advantage of using DTI-based tractography in the context of effective connectivity models lies in establishing paths that are not suggested by the available knowledge (e.g., macaque tracer literature). Our second aim was therefore to investigate the evidence for connections which were not proposed in the original studies. We have found evidence for such connections in half of the models. In the following, we will discuss these findings in the context of current methodological limitations and we will evaluate their implications for the proposed models.

When there was no evidence found for a proposed path, there are two explanations possible:

- (i) there is no direct anatomical connection; in this case, the proposed path can only be supported by an indirect connection with a third region;
- (ii) there is a direct connection, but it has not been found due to methodological limitations (false negative).

The second explanation is especially relevant to a class of frontal interhemispheric connections. As mentioned in the introduction, DTI-based tractography has profound difficulties when tracking through voxels with multiple fiber populations. The frontal interhemispheric connections pass through the corona radiata, which is well known to contain such voxels [34]. Therefore, any negative findings about this class of connections have to be interpreted as being inconclusive.

There is another set of negative findings which merits further discussion: in both networks of Fletcher et al. and of Rowe et al., we have found evidence for a connection between parietal and prefrontal cortices in the left hemisphere but not in the right hemisphere. Here, an explanation in terms of methodological limitations seems unattractive, because this would suggest that these limitations occur in the right hemisphere but not in the left hemisphere. Therefore, we tentatively conclude that these connections are indeed absent in the right hemisphere and that this is an evidence for an asymmetry in parietal-frontal connectivity. We should point out, however, that this asymmetry seems counterintuitive at first, since the right hemisphere is hypothesized to be dominant for visuospatial processing and one would expect that these connections would be especially strong for this hemisphere. However, as we are dealing with relatively small ROIs within the frontal and parietal lobes, this does not rule out the possibility of there being any connections between these lobes in the right hemisphere.

There are a number of paths for which no evidence was found and which cannot be interpreted directly in terms of methodological limitations. As in many neuroimaging studies, these negative findings are difficult to classify and it would certainly be imprudent to conclude that these paths do not exist. Moreover, it is also possible that a path is mediated by connections from and to a third region, which was not included in the network. This situation can be relatively harmless if the function of the missing region is known to be restricted to “message passing”. However, we hypothesize that, if there is a substantial number of such “indirect” connections present in a network, the inclusion of these other regions, which mediate these connections, becomes necessary to ensure the biological validity of the network.

Given the methodological issues discussed above, it is clear that the potential contribution of DTI to connectivity studies lies not in disproving the existence of postulated connections, but in the unique potential for detecting hitherto unconsidered direct anatomical connections. This is because DTI may be prone to type II errors, but it is far less likely to consistently produce type I errors when connections are averaged across subjects. It is hence highly significant that we have also found evidence for a number of paths which have not been taken into account in the original studies. Incorporating these paths in a new analysis of these models can potentially have a significant impact on the interpretation of these models, since they point to improvements in the anatomical validity of the models, which in turn leads to more veridical path coefficients.

At the current state of technology in effective connectivity, one has considerable freedom to choose the connections in a model and to evaluate different models with different connectivity profiles against each other [35]. This model selection procedure can be augmented significantly with DTI-based tractography, because models in which the connections to a large extent overlap with the connections found in a DTI analysis should in turn be more likely. One could potentially formalize this in a Bayesian framework by designing priors on the connections and by subsequently making the priors on the “known” connections high and

TABLE 1: Tractography results for all the proposed networks. The number indicates the number of subjects in which this path was found. Results in black indicate proposed paths, while results in red indicate paths that were not proposed in the original networks.

Büchel et al.		Fletcher et al.		McIntosh et al.		Rowe et al.	
V1-DE	6	LOCC-ROCC	6	A18L-A18R	6	IPC1-MFG1	4
V1-ITp	4	LOCC-LPAR	4	A10-A18L	0	IPC1-IMC	5
DE-ITp	5	ROCC-RPAR	4	A10-A18R	4	MFG1-IMC	4
DE-PP	3	LPAR-RPAR	5	A6-A41/42	3	MFG1-PS1	1
PP-ITp	1	LPAR-LPFC	4	A41/42-A18L	0	IPC1-PS1	2
PP-LP	5	LPAR-RPFC	0	A41/42-A18R	6	MFG2-PS2	0
ITp-ITa	5	RPAR-RPFC	0	A6-A18L	0	IPC2-PS2	0
V1-PP	0	RPAR-LPFC	0	A6-A18R	0	MFG2-IPC2	1
V1-LP	0	LPFC-RPFC	0	A10-A6	1	PS1-IMC	0
V1-ITa	0	LOCC-RPAR	3	A41/42-A10	1	all other possible connections	0
DE-LP	2	ROCC-LPAR	4				
DE-ITa	5	LOCC-LPFC	1				
ITp-LP	0	LOCC-RPFC	0				
ITa-PP	1	ROCC-RPFC	0				
ITa-LP	0	ROCC-LPFC	0				
				Seminowicz et al.			
				LatPFG9-MF10			1
				OF11-MF10			3
				OF11-Hpc			2
				OF11-Cg25			5
				aTh-Cg24			0
				Cg24-LatPFG9			0
				Cg24-MF10			5
				Cg24-Cg25			6
				OF11-Cg24			4
				Cg25-LatPFG9			0
				Hpc-LatPFG9			0
				Hpc-Cg25			1
				aTh-LatPFG9			4
				aTh-MF10			4
				aTh-Cg25			5
				aTh-Hpc			4
				aTh-OF11			0
				LatPFG9-OF11			0
				MF10-Cg25			5
				MF10-Hpc			6
				Cg24a-Hpc			0
				White et al.			
				Cerebellum Cortex-Cerebellum Deep Nucleus			6
				Cerebellum Deep Nucleus-Thalamus			2
				Cerebellum Deep Nucleus-M1			1
				Thalamus-M1			5
				Thalamus-SMA			6
				SMA-M1			6
				Cerebellum Cortex-Thalamus			0
				Cerebellum Cortex-M1			0
				Cerebellum Cortex-SMA			1
				Cerebellum Deep Nucleus-SMA			2

sharp and the priors on the “unknown” connections relatively noninformative.

We have observed a large intersubject variability in our findings. If this would be a veridical variability, it would be a surprising and new finding, since the intersubject variability of anatomical connections is generally considered to be low and is furthermore difficult to assess with either DTI or tracer methods. In DTI, the normalization of findings still makes it difficult to compare findings across subjects, whereas tracer studies are normally performed in very few animals because of ethical considerations, which makes any discussion about differences between animals extremely difficult. Although we have not normalized the fiber tracks to a template, we do believe that normalization problems still play an important role in our studies because they might cause the erroneous placement of seed regions in some subjects, which in turn would lead to misleading tractography results and the above-mentioned intersubject variability. The smoothing strategy, employed in functional studies to reduce the effect of anatomical differences between subjects, cannot be applied in our framework because the directional information, used in the tracking procedure, would be smeared out over other voxels and potentially other tracks, with unpredictable implications for the veridicality of the tracks found. Currently, there is no convincing way of solving this problem, as the basic anatomical landmarks vary substantially over subjects.

Recently, advances have been made towards the estimation of multiple fiber directions within one voxel and also in probabilistic tractography. We will now discuss each of these developments and their potential use for our framework.

The estimation of multiple fiber compartments per voxel, in general, brings this technique closer to producing veridical anatomical connections, and a number of techniques have been proposed to achieve this [33, 36–39]. There is, however, one problem which cannot be solved by this technique alone, and that is the kissing/crossing fiber problem: when a fiber has to track through a voxel with multiple compartments, it is uncertain which compartment has to be used to determine the direction in which the track is to be continued. In a number of studies, the direction that is most collinear with the incoming fiber was chosen, but this does not necessarily have to be the true direction. Whereas the single tensor model is probably too conservative in the connections it yields, multiple compartment models might thus yield a number of false positives.

In probabilistic fiber tracking, a measure of uncertainty of the local fiber direction is estimated per voxel [40–44]. Fiber tracking is now done in a Monte Carlo type experiment: the tracking is performed multiple times, each time with a different orientation drawn from the local fiber direction distributions. Subsequently, the number of times a target voxel was hit by this procedure is calculated, which then is converted to an informal measure of “probability of connection”. While this procedure by itself seems valid, in practice this leads to widespread patterns of connectivity and it is uncertain at which level of “probability” the map should be thresholded. Moreover, the probability of connection tends to decrease with increasing distance. In a SEM

network, both relatively local and long connections can be included, which makes the comparison of these connections difficult. Thus while both techniques (multiple direction estimation and probabilistic fiber tracking) can potentially alleviate some of the problems, we have encountered (e.g., interhemispheric connections), unresolved issues remain.

In conclusion, we have shown that DTI-based tractography can be used to explore the anatomical connections between regions, used in effective connectivity studies, notwithstanding the current limitations of this method. We have observed evidence for the proposed paths in a large number of cases and, more importantly, we have shown in several cases direct connections that were not included in the original models. We therefore conclude that DTI-based tractography is a valuable tool for exploring the anatomical basis of functional networks.

APPENDIX

See Table 1.

ACKNOWLEDGMENTS

The authors wish to thank Meike Grol for useful discussions. This work was supported by the Netherlands Organisation for Scientific Research (NWO-Pionier program).

REFERENCES

- [1] K. J. Friston, A. P. Holmes, K. J. Worsley, J.-P. Poline, C. D. Frith, and R. S. J. Frackowiak, “Statistical parametric maps in functional imaging: a general linear approach,” *Human Brain Mapping*, vol. 2, no. 4, pp. 189–210, 1995.
- [2] B. Biswal, F. Z. Yetkin, V. M. Haughton, and J. S. Hyde, “Functional connectivity in the motor cortex of resting human brain using echo-planar MRI,” *Magnetic Resonance in Medicine*, vol. 34, no. 4, pp. 537–541, 1995.
- [3] K. J. Friston, C. D. Frith, P. F. Liddle, and R. S. J. Frackowiak, “Functional connectivity: the principal-component analysis of large (PET) data sets,” *Journal of Cerebral Blood Flow & Metabolism*, vol. 13, no. 1, pp. 5–14, 1993.
- [4] M. D. Greicius, B. Krasnow, A. L. Reiss, and V. Menon, “Functional connectivity in the resting brain: a network analysis of the default mode hypothesis,” *Proceedings of the National Academy of Sciences of the United States of America*, vol. 100, no. 1, pp. 253–258, 2003.
- [5] K. J. Friston, L. Harrison, and W. Penny, “Dynamic causal modelling,” *NeuroImage*, vol. 19, no. 4, pp. 1273–1302, 2003.
- [6] A. R. McIntosh, C. L. Grady, L. G. Ungerleider, J. V. Haxby, S. I. Rapoport, and B. Horwitz, “Network analysis of cortical visual pathways mapped with PET,” *Journal of Neuroscience*, vol. 14, no. 2, pp. 655–666, 1994.
- [7] K. J. Friston, “Functional and effective connectivity in neuroimaging: a synthesis,” *Human Brain Mapping*, vol. 2, no. 1-2, pp. 56–78, 1994.
- [8] A. R. McIntosh and F. Gonzalez-Lima, “Structural equation modeling and its application to network analysis in functional brain imaging,” *Human Brain Mapping*, vol. 2, no. 1-2, pp. 2–22, 1994.
- [9] P. J. Basser, J. Mattiello, and D. LeBihan, “MR diffusion tensor spectroscopy and imaging,” *Biophysical Journal*, vol. 66, no. 1, pp. 259–267, 1994.

- [10] P. J. Basser and C. Pierpaoli, "Microstructural and physiological features of tissues elucidated by quantitative-diffusion-tensor MRI," *Journal of Magnetic Resonance, Series B*, vol. 111, no. 3, pp. 209–219, 1996.
- [11] T. E. Conturo, N. F. Lori, T. S. Cull, et al., "Tracking neuronal fiber pathways in the living human brain," *Proceedings of the National Academy of Sciences of the United States of America*, vol. 96, no. 18, pp. 10422–10427, 1999.
- [12] S. Mori and P. C. M. van Zijl, "Fiber tracking: principles and strategies—a technical review," *NMR in Biomedicine*, vol. 15, no. 7–8, pp. 468–480, 2002.
- [13] T. E. J. Behrens, H. Johansen-Berg, M. W. Woolrich, et al., "Non-invasive mapping of connections between human thalamus and cortex using diffusion imaging," *Nature Neuroscience*, vol. 6, no. 7, pp. 750–757, 2003.
- [14] S. Lehericy, M. Ducros, A. Krainik, et al., "3-D diffusion tensor axonal tracking shows distinct SMA and pre-SMA projections to the human striatum," *Cerebral Cortex*, vol. 14, no. 12, pp. 1302–1309, 2004.
- [15] C. Büchel, J. T. Coull, and K. J. Friston, "The predictive value of changes in effective connectivity for human learning," *Science*, vol. 283, no. 5407, pp. 1538–1541, 1999.
- [16] P. Fletcher, C. Büchel, O. Josephs, K. Friston, and R. Dolan, "Learning-related neuronal responses in prefrontal cortex studied with functional neuroimaging," *Cerebral Cortex*, vol. 9, no. 2, pp. 168–178, 1999.
- [17] E. Koechlin, C. Ody, and F. Kouneiher, "The architecture of cognitive control in the human prefrontal cortex," *Science*, vol. 302, no. 5648, pp. 1181–1185, 2003.
- [18] J. B. Rowe, K. E. Stephan, K. Friston, R. S. J. Frackowiak, and R. E. Passingham, "The prefrontal cortex shows context-specific changes in effective connectivity to motor or visual cortex during the selection of action or colour," *Cerebral Cortex*, vol. 15, no. 1, pp. 85–95, 2005.
- [19] H. Kondo, M. Morishita, N. Osaka, M. Osaka, H. Fukuyama, and H. Shibasaki, "Functional roles of the cingulo-frontal network in performance on working memory," *NeuroImage*, vol. 21, no. 1, pp. 2–14, 2004.
- [20] A. R. McIntosh, R. E. Cabeza, and N. J. Lobaugh, "Analysis of neural interactions explains the activation of occipital cortex by an auditory stimulus," *Journal of Neurophysiology*, vol. 80, no. 5, pp. 2790–2796, 1998.
- [21] D. A. Seminowicz, H. S. Mayberg, A. R. McIntosh, et al., "Limbic-frontal circuitry in major depression: a path modeling metanalysis," *NeuroImage*, vol. 22, no. 1, pp. 409–418, 2004.
- [22] N. S. White and M. T. Alkire, "Impaired thalamocortical connectivity in humans during general-anesthetic-induced unconsciousness," *NeuroImage*, vol. 19, no. 2, pp. 402–411, 2003.
- [23] T. G. Reese, O. Heid, R. M. Weisskoff, and V. J. Wedeen, "Reduction of eddy-current-induced distortion in diffusion MRI using a twice-refocused spin echo," *Magnetic Resonance in Medicine*, vol. 49, no. 1, pp. 177–182, 2003.
- [24] D. K. Jones, M. A. Horsfield, and A. Simmons, "Optimal strategies for measuring diffusion in anisotropic systems by magnetic resonance imaging," *Magnetic Resonance in Medicine*, vol. 42, no. 3, pp. 515–525, 1999.
- [25] D. C. Alexander, C. Pierpaoli, P. J. Basser, and J. C. Gee, "Spatial transformations of diffusion tensor magnetic resonance images," *IEEE Transactions on Medical Imaging*, vol. 20, no. 11, pp. 1131–1139, 2001.
- [26] H.-J. Park, M. Kubicki, M. E. Shenton, et al., "Spatial normalization of diffusion tensor MRI using multiple channels," *NeuroImage*, vol. 20, no. 4, pp. 1995–2009, 2003.
- [27] V. Glausche, "Diffusion Toolbox," 2007.
- [28] H. Jiang and S. Mori, "DTI-Studio," 2007.
- [29] S. Mori, B. J. Crain, V. P. Chacko, and P. C. M. van Zijl, "Three-dimensional tracking of axonal projections in the brain by magnetic resonance imaging," *Annals of Neurology*, vol. 45, no. 2, pp. 265–269, 1999.
- [30] A. R. McIntosh, F. L. Bookstein, J. V. Haxby, and C. L. Grady, "Spatial pattern analysis of functional brain images using partial least squares," *NeuroImage*, vol. 3, no. 3, pp. 143–157, 1996.
- [31] B. A. Vogt and D. N. Pandya, "Cingulate cortex of the rhesus monkey: II. Corical afferents," *Journal of Comparative Neurology*, vol. 262, no. 2, pp. 271–289, 1987.
- [32] P. J. Orioli and P. L. Strick, "Cerebellar connections with the motor cortex and the arcuate premotor area: an analysis employing retrograde transneuronal transport of WGA-HRP," *Journal of Comparative Neurology*, vol. 288, no. 4, pp. 612–626, 1989.
- [33] K. M. Jansons and D. C. Alexander, "Persistent angular structure: new insights from diffusion magnetic resonance imaging data," *Inverse Problems*, vol. 19, no. 5, pp. 1031–1046, 2003.
- [34] M. R. Wiegell, H. B. W. Larsson, and V. J. Wedeen, "Fiber crossing in human brain depicted with diffusion tensor MR imaging," *Radiology*, vol. 217, no. 3, pp. 897–903, 2000.
- [35] W. D. Penny, K. E. Stephan, A. Mechelli, and K. J. Friston, "Comparing dynamic causal models," *NeuroImage*, vol. 22, no. 3, pp. 1157–1172, 2004.
- [36] T. E. J. Behrens, H. J. Berg, S. Jbabdi, M. F. S. Rushworth, and M. W. Woolrich, "Probabilistic diffusion tractography with multiple fibre orientations: what can we gain?" *NeuroImage*, vol. 34, no. 1, pp. 144–155, 2007.
- [37] T. Hosey, G. Williams, and R. Ansorge, "Inference of multiple fiber orientations in high angular resolution diffusion imaging," *Magnetic Resonance in Medicine*, vol. 54, no. 6, pp. 1480–1489, 2005.
- [38] J.-D. Tournier, F. Calamante, D. G. Gadian, and A. Connelly, "Direct estimation of the fiber orientation density function from diffusion-weighted MRI data using spherical deconvolution," *NeuroImage*, vol. 23, no. 3, pp. 1176–1185, 2004.
- [39] D. S. Tuch, "Q-ball imaging," *Magnetic Resonance in Medicine*, vol. 52, no. 6, pp. 1358–1372, 2004.
- [40] T. E. J. Behrens, M. W. Woolrich, M. Jenkinson, et al., "Characterization and propagation of uncertainty in diffusion-weighted MR imaging," *Magnetic Resonance in Medicine*, vol. 50, no. 5, pp. 1077–1088, 2003.
- [41] O. Friman, G. Farneback, and C.-F. Westin, "A Bayesian approach for stochastic white matter tractography," *IEEE Transactions on Medical Imaging*, vol. 25, no. 8, pp. 965–978, 2006.
- [42] M. A. Koch, D. G. Norris, and M. Hund-Georgiadis, "An investigation of functional and anatomical connectivity using magnetic resonance imaging," *NeuroImage*, vol. 16, no. 1, pp. 241–250, 2002.
- [43] M. Lazar and A. L. Alexander, "Bootstrap white matter tractography (BOOT-TRAC)," *NeuroImage*, vol. 24, no. 2, pp. 524–532, 2005.
- [44] G. J. M. Parker, H. A. Haroon, and C. A. M. Wheeler-Kingshott, "A framework for a streamline-based probabilistic index of connectivity (PICo) using a structural interpretation of MRI diffusion measurements," *Journal of Magnetic Resonance Imaging*, vol. 18, no. 2, pp. 242–254, 2003.

Research Article

Accurate Anisotropic Fast Marching for Diffusion-Based Geodesic Tractography

S. Jbabdi,^{1,2,3} P. Bellec,^{1,2,4} R. Toro,⁵ J. Daunizeau,^{1,2,6} M. Péligrini-Issac,^{1,2} and H. Benali^{1,2,7}

¹Laboratoire d'Imagerie Fonctionnelle, INSERM, U678, 75013 Paris, France

²Faculté de Médecine Pitié Salpêtrière, Université Pierre et Marie Curie, UMR 678 CNRS, 75013 Paris, France

³Oxford Centre for Functional Magnetic Resonance Imaging of the Brain (FMRIB), Oxford OX3 9DU, UK

⁴McConnell Bain Imaging Center, Montreal Neurological Institute, McGill University, Montréal, Canada H3A 2T5

⁵Brain & Body Centre, The University of Nottingham, Nottingham NG7 2RD, UK

⁶Functional Imaging Laboratory, University College London, London WC1E 6BT, UK

⁷Unité d'Imagerie Fonctionnelle, Université de Montréal, Montréal, Canada H3C 3J7

Correspondence should be addressed to S. Jbabdi, saad@fmrib.ox.ac.uk

Received 1 May 2007; Accepted 21 September 2007

Recommended by Oury Monchi

Using geodesics for inferring white matter fibre tracts from diffusion-weighted MR data is an attractive method for at least two reasons: (i) the method optimises a global criterion, and hence is less sensitive to local perturbations such as noise or partial volume effects, and (ii) the method is fast, allowing to infer on a large number of connexions in a reasonable computational time. Here, we propose an improved fast marching algorithm to infer on geodesic paths. Specifically, this procedure is designed to achieve accurate front propagation in an anisotropic elliptic medium, such as DTI data. We evaluate the numerical performance of this approach on simulated datasets, as well as its robustness to local perturbation induced by fiber crossing. On real data, we demonstrate the feasibility of extracting geodesics to connect an extended set of brain regions.

Copyright © 2008 S. Jbabdi et al. This is an open access article distributed under the Creative Commons Attribution License, which permits unrestricted use, distribution, and reproduction in any medium, provided the original work is properly cited.

1. INTRODUCTION

For decades, dissection, lesion studies, or axonal transport of tracers have been the only available techniques for studying the brain's anatomical connections. It is not surprising that due to the invasiveness of these methods, most of the data concerning the large-scale, white matter tracts of the brain were collected on animals, for example, cats [1] or monkeys [2], while structural data for the human brain were largely missing [3]. Diffusion weighted MR imaging now offers a propitious and unique framework to explore noninvasively the organisation of white matter in the living human brain [4, 5]. Despite the poor spatial resolution of this technique, already diffusion data are beginning to inform us about human brain large-scale connections [6–8] and how they relate to the functional role of cortical and subcortical networks [9, 10].

Inferring on white matter architecture from diffusion data relies on the properties of water diffusion in the tissues. Water molecules diffuse more easily along the fibre

tracts than across them, and this anisotropy is captured by the diffusion-weighted MR signal. Inferring on connexions given this local feature is challenging, since the observations (diffusion properties) are indirectly related to the actual structure (axonal orientations, size, and packing). The tractography algorithms use the information of directionality contained in diffusion data to infer connectivity between brain regions. Usually, information about the orientation of white matter fibres is estimated locally, via models (e.g., diffusion tensor imaging (DTI) [11], mixture models [12], or partial volume models [13, 14]) or in a model-free manner (e.g., Q-ball imaging [15]). Fibre tracking consists then in inferring connexions between distant brain regions, given this local orientation. This can be done either in a deterministic way, by trusting the local orientation information and following these directions until reaching a target region (i.e., streamline tractography [16–19]), or in a probabilistic way, by building distributions of connexions, using local probabilistic models for fibre orientation distributions [13, 14, 20].

In both cases, when tracking a fibre between two regions of the brain, these algorithms start in one seed region, and try to find the tracts, or distribution of tracts, that will end up in the target region. In cases where the local orientation information present in the diffusion data is consistent with the presence of this pathway, then these tractography algorithms manage in general to recover the connexion between the seed and the target. However, it often happens that in some parts of the trajectory, the local diffusion information no longer supports the presence of the pathway. This can either be due to a high level of noise compared to the actual signal, or to the presence of a high number of crossing fibres heterogeneous in their orientations. This issue is crucial in streamlining algorithms, and is also met in probabilistic algorithms when a single orientation per voxel is modelled [21]. The problem with those algorithms is that when tracking from a seed, the algorithm has no information about the region it will end up in.

A possible solution to the problem of local perturbations in the diffusion data may be provided by global tractography, that is, optimising a global criterion while seeking for connexions. A global tractography algorithm can potentially overcome errors in estimating local structure, because its goal is to connect two given regions. In other words, if we tell the algorithm which connexion we are looking at, that is, which pair of regions is to be connected, it is better at finding it. Geodesic tractography (GT), first proposed by Parker et al. [22], falls into this category. GT is based on the hypothesis that brain fibers can be interpreted as minimal distance paths (geodesics) for a metric derived from the water diffusion profile. This distance criterion is global by definition.

The basic idea for constructing a geodesic in a metric space is to build a distance field from a seed region, the very same region one would use as a seed for streamline tractography. This is done by solving the so-called Eikonal equation, a partial differential equation (PDE) that describes the time of arrival at each point of the space, as a function of the local speed. In a constant speed field, this PDE can be easily integrated, and the geodesics are simply straight lines. When the speed varies across the space, the geodesics can curve, preferring high local speed locations to decrease the arrival time. Finally, if the speed depends on the direction of travel (e.g., along versus across a fibre tract), then the PDE is said to be anisotropic.

Solving the Eikonal equation in a heterogeneous and highly anisotropic medium, as is the human brain, is a technically challenging problem [23]. This is especially true if one uses single-pass algorithms, which is particularly important when dealing with data containing hundreds of thousands of voxels. There have been a few attempts at solving this problem in the context of diffusion-based tractography [22, 24–27].

We describe a method for constructing geodesics in an anisotropic medium, and apply it to the problem of DTI-based tractography. This method relies on works in optimal path planning [28] and, more recently, vessel extraction in 3D angiography images [29]. It has been shown to be very accurate in anisotropic media [29], and requires less computation than the exact method proposed in Sethian and

Vladimirsky [30] in a general framework for anisotropic optimal path planning. The main contribution of this work is to show how this method applies to the case of an elliptic medium, where the algorithm performs extremely well both in terms of accuracy and efficiency, as shown in the simulations. We also show the feasibility of applying such method to the extraction of structural connectivity in an extended brain network using diffusion data from a healthy subject.

2. METHODS

In this section, we will give some theoretical background on geodesics and the Eikonal equation, and describe a single-pass algorithm for building geodesics.

2.1. Geodesics and the Eikonal equation

A geodesic is a pathway minimising an integral of the form

$$J(\gamma) = \int F(s, \gamma, \gamma') ds, \quad (1)$$

where $F(s, \gamma, \gamma') = \sqrt{\gamma'(s)^T \mathbf{M}(\gamma(s)) \gamma'(s)}$ describes an infinitesimal distance along a pathway γ , relative to a metric tensor \mathbf{M} .

Now, let $u(\mathbf{x})$ be the arrival time function starting from a location \mathbf{x}_0 , that is, $u(\mathbf{x})$ is equal to the minimum value of the integral $J(\gamma)$ along a geodesic connecting \mathbf{x}_0 to \mathbf{x} . Then, the arrival time function and the geodesics satisfy these two fundamental equations:

$$\nabla u^T \mathbf{M}^{-1} \nabla u = 1, \quad (2a)$$

$$\gamma' \propto \mathbf{M}^{-1} \nabla u, \quad (2b)$$

where ∇u is the spatial gradient of u . Equation (2a) is the anisotropic version of the so-called Eikonal equation. In the isotropic case, this equation is usually written $|\nabla u| = 1/v$, where v is the local speed. Hence, this equation tells us two things: (i) it is a generalisation of the speed equation, stating that the time of arrival is inversely proportional to the speed, and (ii) changing the local metric tensor can be seen as changing the local speed. Equation (2b) shows that the tangent of the geodesic lines is parallel to the gradient of the time of arrival function with respect to the inverse metric. This is very important because it gives us a convenient way to reconstruct geodesics from any point in space, given the solution to the Eikonal equation. Figure 1 shows example geodesics in an isotropic space composed of two subsets with different local speeds.

Proof of equation (2). Recall that the function $u(\mathbf{x})$ is the minimum value of J along the geodesic from point \mathbf{x}_0 to an arbitrary point \mathbf{x} :

$$u(\mathbf{x}) = \min_{\gamma} \int_{\mathbf{x}_0}^{\mathbf{x}} F(s, \gamma, \gamma') ds. \quad (3)$$

A general variation of (3) is given (see, e.g., [31]) as

$$\delta u = \frac{\partial F}{\partial \gamma'} \delta \gamma + \int_{\mathbf{x}_0}^{\mathbf{x}} \left(\frac{\partial F}{\partial \gamma} - \frac{d}{ds} \frac{\partial F}{\partial \gamma'} \right) ds. \quad (4)$$

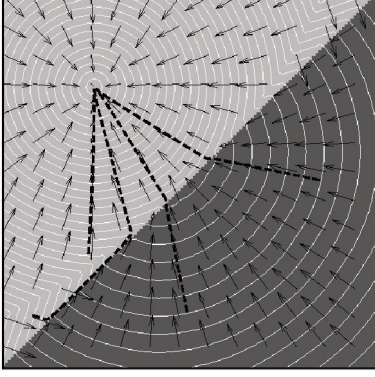


FIGURE 1: Example geodesics in a double isotropic space. Black arrows show the local orientations of the geodesics. The speed in the dark grey region is twice as high as that in the light grey one. Notice that in each separate space, the geodesics are straight lines. Also, notice how one of the geodesics (bold dashed lines) travels backward to the high speed part before getting back to the low speed one.

Since we have integrated along a geodesic, the second term on the right-hand side of (4) equals zero (Euler condition). We obtain

$$\nabla u = \frac{\partial u}{\partial \gamma} = \frac{\partial F}{\partial \gamma'} = \frac{\mathbf{M}\gamma'}{(\gamma'^T \mathbf{M}\gamma')^{1/2}}. \quad (5)$$

Equation (2b) directly follows. Finally, and using the symmetry of the metric tensor \mathbf{M} , we get the Eikonal equation:

$$\nabla u^T \mathbf{M}^{-1} \nabla u = \frac{\gamma'^T \mathbf{M}^T \mathbf{M}^{-1} \mathbf{M} \gamma'}{\gamma'^T \mathbf{M} \gamma'} = 1. \quad (6) \quad \square$$

Equations (2a) and (2b) summarise the two steps for building geodesics: (i) solve the Eikonal equation for u , given a metric tensor \mathbf{M} and a starting point \mathbf{x}_0 ; (ii) construct geodesics between any given point and the starting point \mathbf{x}_0 by following the gradient of u with respect to the inverse metric \mathbf{M}^{-1} .

2.2. Fast-marching algorithm

A few algorithms have been proposed in the literature for computing the function u on a discrete grid. The most popular are Tsitsiklis's method [28] and Sethian's method [32], which are based on the construction of the time of arrival function $u(\mathbf{x})$ using front propagation. These methods are also referred to as fast marching methods because they construct the function u in a single-pass through the grid nodes. Tsitsiklis's method relies on (1) while Sethian's method uses the Eikonal equation (2a). Both methods are suitable in the case of isotropic media, that is, where the metric \mathbf{M} is proportional to the identity matrix, but they fail in anisotropic media [23]. An exact scheme to deal with anisotropy has been proposed by Sethian and Vladimirsky [30], but while remaining a single-pass algorithm, it still requires a computational effort that is growing with the

amount of anisotropy. A variant of the initial fast-marching algorithm of Tsitsiklis [28] has been proposed to deal with anisotropic media [29], which is more computationally efficient than the exact scheme of Sethian [30]. Yet, it relies on a generic optimisation procedure that was undocumented for the special case of the elliptical media we face with DTI tractography. We extended this method by deriving a solution to the optimisation procedure in this case.

The general idea of the fast-marching algorithm was borrowed from the graph theory. It is a direct extension of Dijkstra's algorithm for finding minimal paths in a graph [33]. The algorithm relies on a very simple observation: suppose that the time of arrival is known inside a close set of grid nodes (a set we will refer to as the *known* set). Then, the first nodes that will be encountered by the propagating front are the nodes on the *edge* of the *known* set (this narrow band of grid nodes will be called the *trial* set). Secondly, the first node that will be encountered by the propagating front is the closest one to *known* (in terms of geodesic distance), and crucially, there will be no other way to make this distance smaller after propagating the front further. This means that the arrival time at this voxel will not change, and can be *frozen*. In other words, the value of the time of arrival u can be calculated, starting from \mathbf{x}_0 , in a single-pass through the voxels, only by considering, at each iteration, the neighbouring voxels of the propagating front. The other voxels (the *far* set) are not examined. Figure 2(a) schematises this front propagation scheme. The fast-marching algorithm is summarised in the appendices.

The crucial step in this front propagation is the computation of the distance between the front and the neighbouring voxels in the *trial* set. In our case, this distance is anisotropic, and we cannot use the standard methods, because they rely on the assumption that the gradients of u are parallel to its geodesic lines (see [23] for further details). To account for the anisotropy, we consider a set of simplexes (triangles) that cover the whole neighbourhood around a voxel of the narrow band [29], and minimise the distance function between the simplexes and that voxel (see Figures 2(b) and 2(c)). The introduction of these simplexes allows to describe the trajectories on a continuous rather than a discrete grid. The definition of a simplex neighbouring a point \mathbf{x} is simply a set of three points $(\mathbf{x}_1, \mathbf{x}_2, \mathbf{x}_3)$ that are 26 neighbours of \mathbf{x} , defining a triangle that we denote $\overline{\mathbf{x}_1 \mathbf{x}_2 \mathbf{x}_3}$. There are 48 such triangles around \mathbf{x} for the 26 connexities (Figure 2(c)). The procedure for computing the anisotropic distance between the propagating front and the voxels in the *trial* set is given in the appendices.

During the updating procedure, the time of arrival at a voxel \mathbf{x}_m of the *trial* set is calculated from its neighbours on a simplex using an approximation (strictly speaking, two approximations!). Normally, if the geodesic passing by \mathbf{x}_m comes from simplex $\overline{\mathbf{x}_1 \mathbf{x}_2 \mathbf{x}_3}$, then the time of arrival is given by

$$u(\mathbf{x}_m) = \min_{\mathbf{g} \in \overline{\mathbf{x}_1 \mathbf{x}_2 \mathbf{x}_3}} \left\{ u(\mathbf{g}) + \int_{\mathbf{g}}^{\mathbf{x}_m} F(s, \gamma, \gamma') ds \right\}. \quad (7)$$

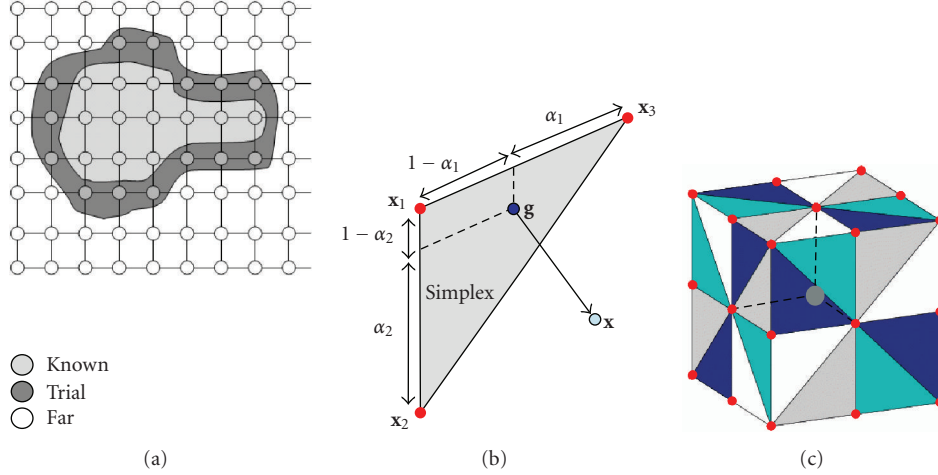


FIGURE 2: (a) Grid representation of the different sets involved during the fast-marching algorithm. (b) Position of the optimal point on a simplex such as to minimise the geodesic distance to \mathbf{x} . (c) Geometry of the 48 simplexes surrounding a voxel (central grey dot). The little red dots represent the centres of the 26 neighbouring voxels.

We use a parametric approximation to this formula, given by the minimisation of the following function:

$$f(\alpha) = \underbrace{\sum_{i=1}^3 \alpha_i u(\mathbf{x}_i)}_{(I)} + \underbrace{\left\| \mathbf{x} - \sum_{i=1}^3 \alpha_i \mathbf{x}_i \right\|_{\mathbf{M}}}_{(II)}, \quad (8)$$

where $\|\cdot\|_{\mathbf{M}}$ is the quadratic norm with respect to the metric \mathbf{M} and $\alpha = (\alpha_1, \alpha_2, \alpha_3)$. Equation (8) follows the approximations of Tsitsiklis [28]. Term (I) approximates the distance from the starting point \mathbf{x}_0 to the simplex centre of mass \mathbf{g} as a weighted sum of the distances to the nodes of the simplex. Term (II) approximates the remaining distance by considering the local metric as being constant, equal to its value at \mathbf{x}_m .

Minimising f in the simplex can be written as a constrained optimisation problem that can be solved explicitly, since f and the simplex are convex. The analytical solution is detailed in the appendices.

2.3. How to choose the metric?

In the GT framework, we make the hypothesis that white matter fibres are geodesics with respect to a metric tensor. But so far, we have not specified which metric tensor we mean. In DTI, the inverse tensor ($\mathbf{M} = \mathbf{D}^{-1}$) seems to be the natural choice. Intuitively, water molecules diffusion is faster along the tract than across them. When inverting the diffusion tensor, the highest eigenvalues become the lowest, and the shortest distance is parallel to the fibres. One can also notice that the inverse tensor defines a metric in a Riemannian space that induces a Laplace-Beltrami operator (generalisation of the Laplace operator) which is encountered in the diffusion equation [25, 34].

However, the inverse tensor is not suitable in all circumstances. Consider the situation described in Figure 3 where a circular tract of radius r connects points A and B, with diffu-

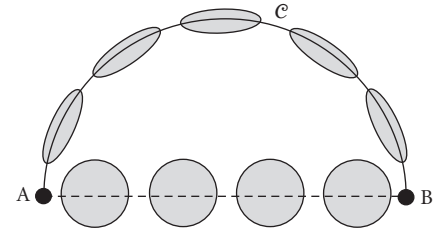


FIGURE 3: Comparison between a straight line and a geodesic.

sion tensors tangent to the tract having the same shape. Suppose the rest of the space is isotropic, with the same mean diffusion as along the tract. If one considers the inverse tensor metric $\mathbf{M} = \mathbf{D}^{-1}$, the distance between A and B through the circular path is

$$\int_c \sqrt{d\mathbf{x}^T \mathbf{D}^{-1} d\mathbf{x}} = \frac{\pi r}{\sqrt{\lambda_1}}, \quad (9)$$

where λ_1 is the largest eigenvalue of the tensors along the circular pathway. On the other hand, the straight line distance between A and B is equal to $2\sqrt{3}r/\sqrt{\text{trace}(\mathbf{D})}$. Hence, a necessary condition for the circular tract to be a geodesic is that its length is smaller than a straight line, that is,

$$\frac{\pi r}{\sqrt{\lambda_1}} \leq \frac{2\sqrt{3}r}{\sqrt{\text{trace}(\mathbf{D})}}, \quad (10)$$

which leads to $\lambda_1 \geq \pi^2 \text{trace}(\mathbf{D})/12$, that is, a condition on the tensor shape to be peaky enough. Of course, one can imagine that even if this condition is satisfied, a geodesic path might certainly lie somewhere in between a straight line and the circular line, as shown in Figure 4. Which metric to choose is hence still debatable. Nonetheless, in our simulations and real data applications, we will use the inverse diffusion tensor as a metric for defining geodesics.

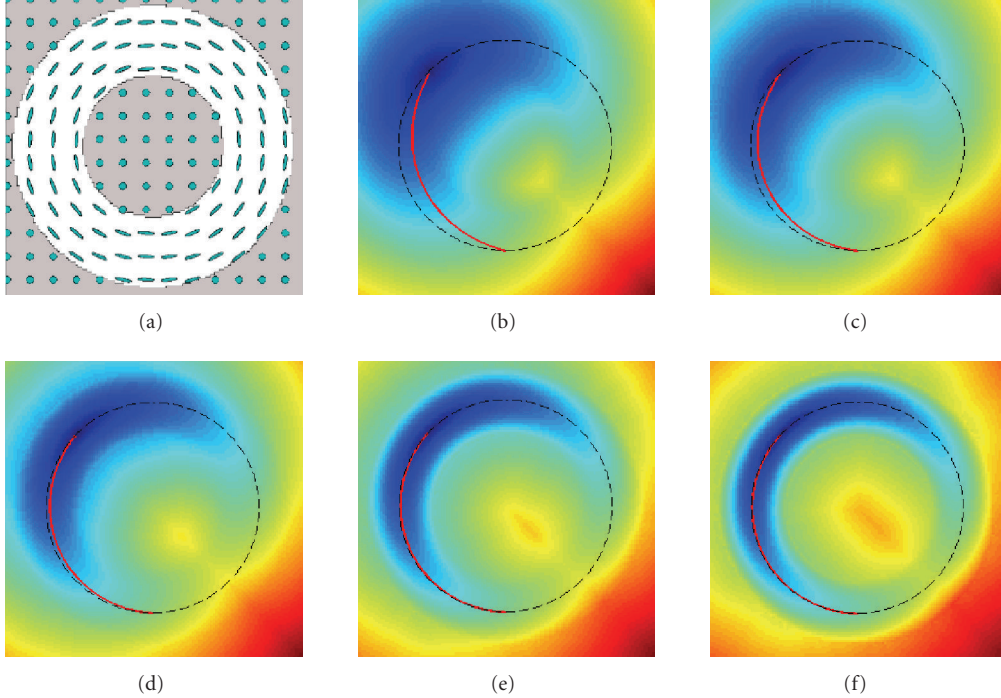


FIGURE 4: (a) Simulated circular tensor field. (b)–(f) Increasing the anisotropy of the circular tensor makes the geodesic path (red line) closer to a circle.

3. APPLICATIONS

3.1. Simulations

We have evaluated the GT method on simulated data. The purpose of these simulations is twofold. First, they show how the anisotropic fast-marching algorithm performs on elliptic media, in both homogeneous field (where the analytical solution is available) and a heterogeneous field. Second, they allow to compare GT with streamlining in cases where the data present local perturbations (crossing fibres).

In a homogeneous medium, where the data support the same diffusion tensor \mathbf{D} in every voxel, the analytic solution to the Eikonal equation is given by

$$u(\mathbf{x}) = \sqrt{(\mathbf{x} - \mathbf{x}_0)^T \mathbf{D}^{-1} (\mathbf{x} - \mathbf{x}_0)}. \quad (11)$$

It is easy to check that in this case, $u(\mathbf{x}_0) = 0$ and $\nabla u^T \mathbf{D} \nabla u = 1$. We generated a tensor where the two smaller eigenvalues are equal, and gradually increased the anisotropy. Figure 5 shows the level curves of the analytic versus the numerical solution to the Eikonal equation. The two solutions are very close even for a large anisotropy, corresponding to a ratio of 50 between the largest and the lowest tensor eigenvalues. Table 1 summarises the mean and standard deviations of the relative error for different values of the anisotropy, which is expressed both in terms of the ratio between the largest and the lowest tensor eigenvalue, or in terms of the more widely used fractional anisotropy (FA, see, e.g., [35]).

In a heterogeneous medium, such an analytical solution does not exist. However, we can verify that the Eikonal equation is satisfied, that is, $\nabla u^T \mathbf{D} \nabla u$ is equal to one. We used the

TABLE 1: Summary of the simulation results with an increasing ratio between the largest and the lowest tensor eigenvalue (the corresponding FA value is shown on the second row). Top: mean and standard deviations of the relative error between numerical and analytic solutions for the Eikonal equation in a homogeneous medium. Bottom: mean and standard deviations of the value of $\nabla u^T \mathbf{D} \nabla u$ in a circular tensor field.

ratio	1	2	5	10	50
FA	0	0.17	0.59	0.79	0.96
mean (%)	0.79	0.93	1.25	1.54	2.16
SD (%)	0.62	0.86	1.53	2.16	3.71
ratio	5	10	20	50	100
FA	0.59	0.79	0.90	0.96	0.98
mean	0.995	0.993	0.989	0.997	1.059
SD	0.068	0.086	0.112	0.213	0.634

same circular tensor field as shown in Figure 4. In Table 1, we show the mean and standard deviations of $\nabla u^T \mathbf{D} \nabla u$ for different anisotropies. Notice that these are close to one, but with a higher deviation from one with increasing anisotropy.

Finally, we show results of GT in the case of local perturbations. We generated a tensor field simulating a crossing fibre situation. The zone where the two fibres cross has a diffusion tensor that is the average of the two crossing fibres' tensors. We increased the crossing fibre area and compared the behaviour of GT to streamlining tractography (Figure 6). As expected, because the streamlining simply follows the direction of highest diffusion given by the tensor, the fibre

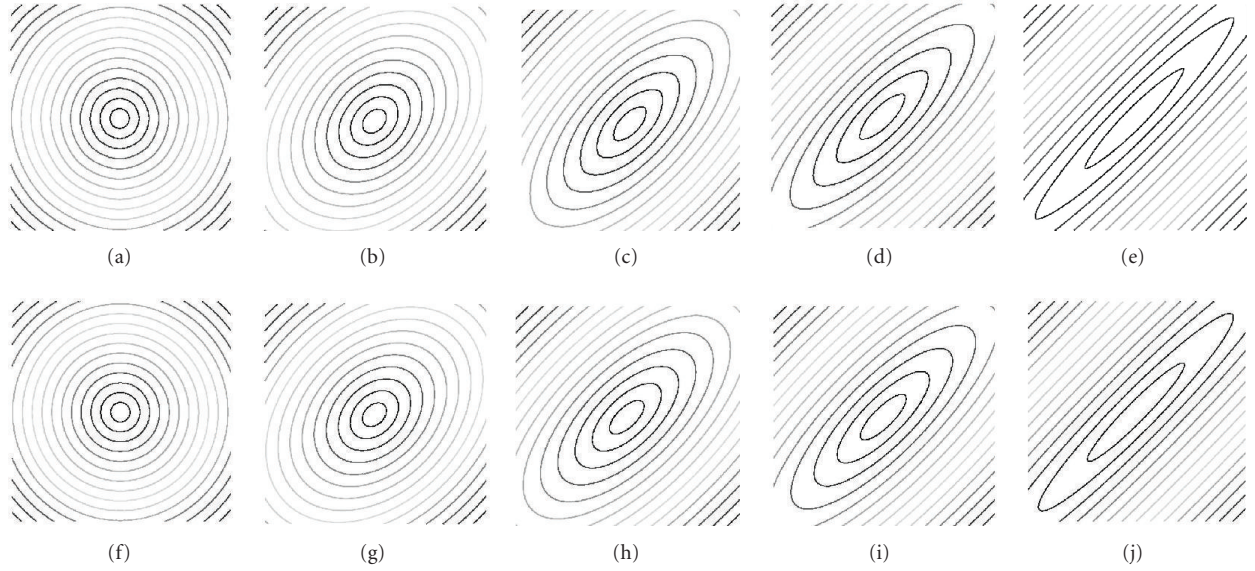


FIGURE 5: Contour plots of the numerical solution (top) and the analytic solution (bottom) to the Eikonal equation in a homogeneous medium. Anisotropy levels are increasing from left (isotropic) to right (ratio of 50 between the extreme tensor eigenvalues).

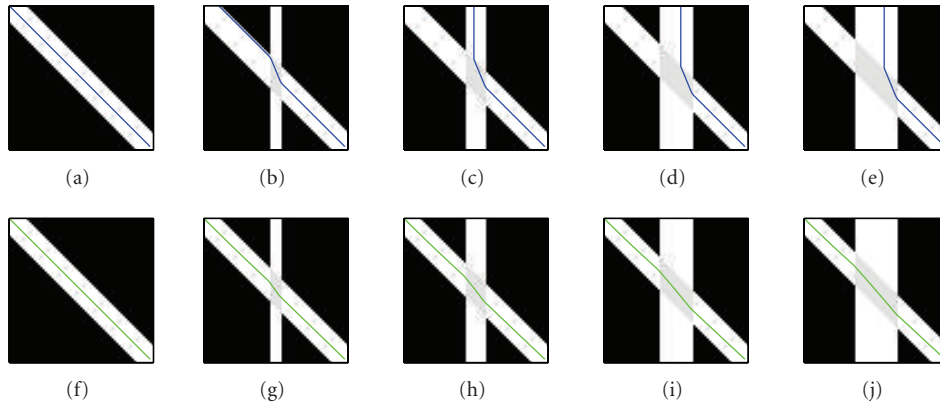


FIGURE 6: Comparison between streamline (top) and geodesic (bottom) tractography in the presence of a crossing fibre bundle, the width of which increases from zero (left) to twice the width of the principal bundle (right). Note how streamlining gets deviated from the straight line because of partial volume effect.

trajectory was deviated. In the case of GT, there was little, if any, deviation from the straight line.

3.2. Real data

Acquisition

Data from a single healthy subject were acquired at *Service de Neuroradiologie (CHNO des Quinze-Vingts, Paris)*. Six gradient weighted and one T_2 -weighted images were acquired on a 1.5 Tesla MR Scanner (GE Signa) using the following scan parameters: 128×128 image matrix, 2.03 mm in-plane pixel size; 3.5 mm slice thickness; $b = 1000$; (TR; TE) = (5000; 91.8) milliseconds; Number of averages = 8. Thirty-six contiguous slices covering the whole brain were acquired. The total scanning time was approximately 14 minutes.

Regions of interest

Five hundred and sixty-seven ($N = 567$) regions covering the whole cortex were manually selected in the DTI space. Each region was represented by a single voxel. The anatomical localization of these regions is shown in Figure 7. We performed a front propagation from each region, which provided the distance functions $(u_i)_{i=1}^N$. Then back propagation allowed us to construct the $N(N-1)/2 = 160,461$ geodesics connecting the whole set of voxel pairs. We computed a heuristic connectivity index consisting of the mean diffusivity along each geodesic, multiplied by the mean FA along the pathways.

In order to better visualize this anatomical connectivity index in a matrix form, the set of brain regions were grouped with respect to their localization. The regions were divided into five groups, including the frontal lobe

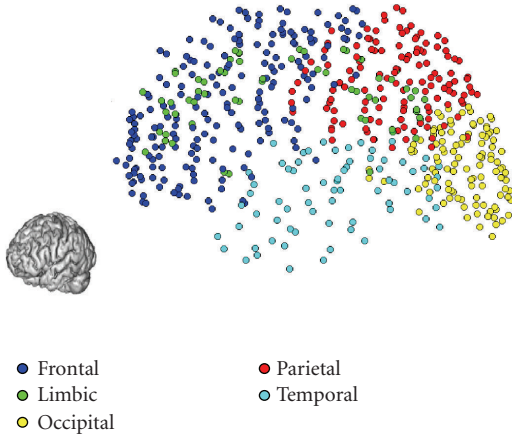


FIGURE 7: Localisation of the regions of interest on the cortex. 3D fronto-sagittal view.

(left: 99 voxels, right: 101 voxels), the limbic cortex (left: 31, right: 30), the occipital lobe (left: 56; right: 54), the parietal lobe (left: 64; right: 62), and the temporal lobe (left: 34; right: 36). This classification was based on an automatic labelling of the voxels locations given by the Talairach Daemon (<http://ric.uthscsa.edu/projects/tdc>), after registering the DTI data into the MNI standard space, and subsequent correction from MNI to Talairach space (see, e.g., [36]). Figure 8 shows the distribution of the connectivity index, in the matrix form, between any two regions, arranged by group and by hemisphere.

The matrix shown in Figure 8 reveals an organization of the connectivity index that follows the anatomical organization of the brain regions regarding their locations. Since the connectivity index encompasses the anisotropy factor, its value highly depends on which regions we are connecting, which means which global pathways the geodesics are close to.

First, the diagonal blocks of the matrix show clearly a lower level of connectivity than the extradiagonal blocks. This seems to indicate that the connectivity index penalises short fibers, and inversely favors long fibers, especially inter-hemispheric fibers. Secondly, the blocks that show the highest connectivity index are the blocks that connect the right and left occipital lobes.

This result is not surprising since the fiber tracts that connect right and left occipital lobes follow a trajectory through the splenium of the corpus callosum (forceps major), which is a highly anisotropic area.

Geodesics

We further investigated which of the constructed geodesics may represent actual fiber trajectories. To approach this question, we thresholded the connectivity matrix in order to emphasize the geodesics with the largest connectivity indices. Specifically, we considered the 10% geodesics with the highest connectivity indices for each interhemispheric block connecting symmetrical groups, taken independently. Figure 9

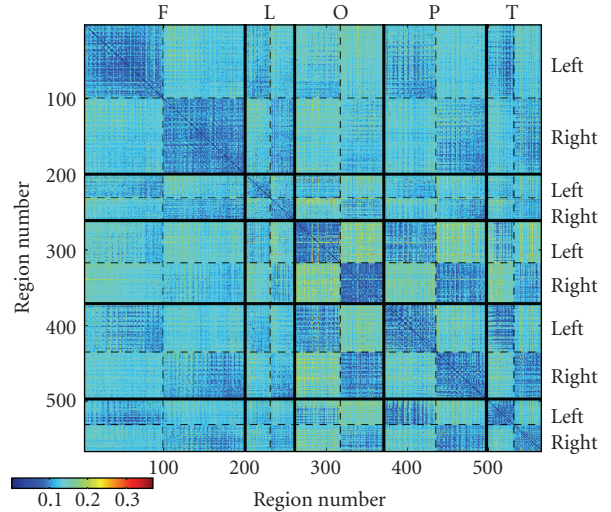


FIGURE 8: Anatomical connectivity matrix rearranged into anatomical groups: F (frontal lobe), L (limbic), O (Occipital), P (parietal), T (temporal). In each group, the left and right hemispheres are also separated.

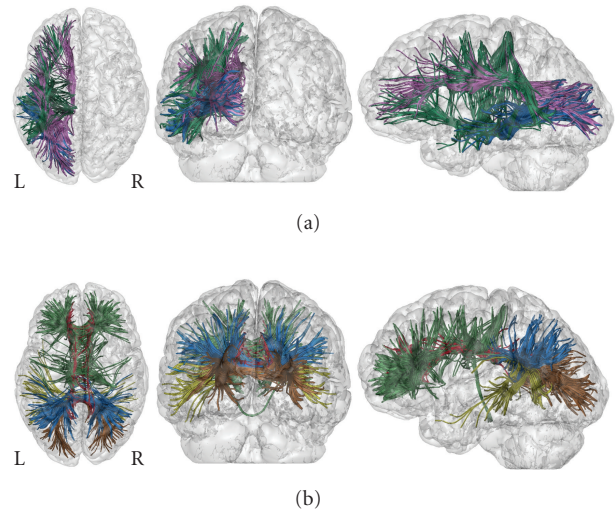


FIGURE 9: (a) 10% most probable intrahemispheric geodesics shown in the left hemisphere. Blue paths connect the occipital lobe to the temporal lobe. Purple paths connect the frontal to the occipital lobe. Green paths connect the frontal lobe to the temporal lobe. (b) 10% most probable interhemispheric geodesics connecting symmetrical regions. Green: frontal lobe, red: limbic lobe, brown: occipital lobe, blue: parietal lobe, yellow: temporal lobe.

represents each group of geodesics in different colors. The most probable geodesics paths follow the principal long association fasciculi. The frontal lobe is connected to the occipital lobe via the fronto-occipital fasciculus. The temporal lobe is connected to the occipital via the inferior longitudinal fasciculus, and to the frontal lobe via the uncinate fasciculus. All major long association tracts are represented by these geodesics.

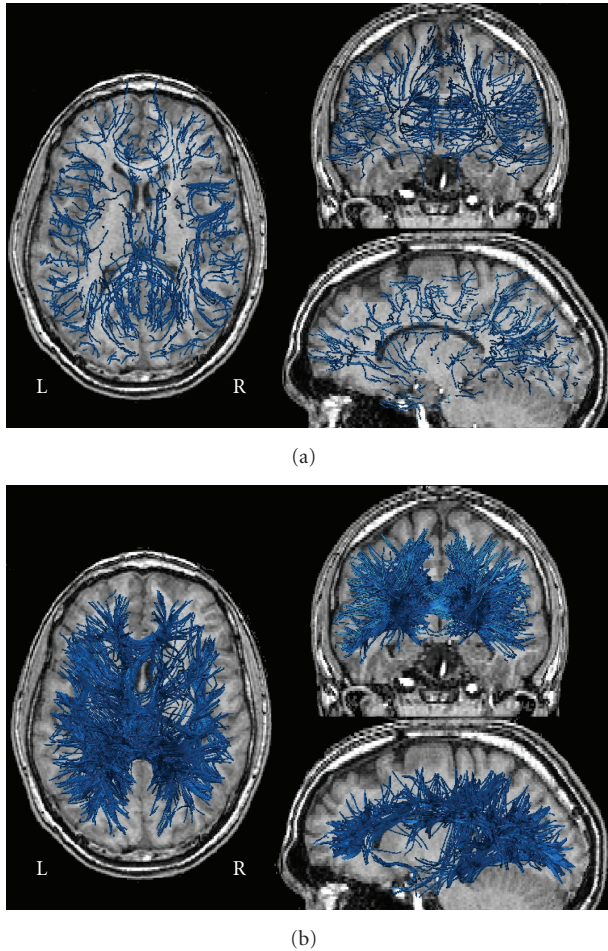


FIGURE 10: (a) Results of the streamline tractography algorithm applied to the set of brain voxels. Four streams per voxel are computed. The stopping criteria are 60° for the maximal angle step, and 0.1 for the minimal anisotropy value. (b) Geodesics computed by the GT method. For each brain voxel of the set, four geodesics with the highest probability index are shown.

Geodesics versus streamlining

Finally, in order to compare the results of our method to a conventional fiber tracking method, we performed a streamline tractography from the N seed voxels, with four tracts per voxel. As a stopping criterion, we chose a maximum step angle of 60° , and an anisotropy threshold of 0.1 [19]. To compare the results to GT, we selected the four geodesics, having the highest probability index, for each voxel in the set of seed voxels. This way, we have the same number of tracts using both methods ($4 \times N$ tracts). Figure 10 shows the results of these two procedures. The streamline method produces many incomplete tracts, especially association tracts, while the proposed GT method succeeded in reconstructing the major association and commissural tracts, including the uncinate, the inferior fronto-temporal, and the callosal fibers. Note that the fronto-occipital tract is not present at this level of threshold (we only considered four geodesics per voxel).

4. DISCUSSION

Global optimisation is a valuable strategy in the context of path planning. When one has the information of where to start and where to go, this information is used to overcome local poor optimality. In the context of white matter diffusion-based tractography, where we often have strong hypotheses about the localisation of the regions in the brain, global optimisation can overcome some serious weaknesses of the process. Mainly, uncertainty about local fibre orientation, reflecting partial volume effects caused by crossing fibres, or local low signal to noise, can be handled efficiently using GT.

We have presented here a method to perform such global-based path planning in an anisotropic medium. The method is very robust to high anisotropy, and provides an extremely accurate numerical solution to the Eikonal equation.

On real-data experiments, the reconstructed geodesics that have a high connectivity index correspond to known fiber tract fasciculi connecting the cortex. These fasciculi can all be retrieved by other tractography methods that use DTI data, providing priors on their location using one or more regions of interest [37, 38], especially intermediate regions located in white matter. GT automatically depicted these fasciculi with no prior.

However, the U-shaped fibers, that is, the short association tracts, are not favored by our connectivity index. This can be easily seen by looking at the diagonal blocks of the matrix in Figure 8. The long association tracts, as well as the commissural fibers, are more present with a higher connectivity index.

GT also allows one to construct interhemispheric tracts between each pair of regions located in different hemispheres. These tracts include homotopic and heterotopic connexions, that is, tracts connecting, respectively, symmetrical and asymmetrical regions lying in different hemispheres. It is worth noting that standard tractography methods usually fail to recover most callosal connexions, apart from the medial ones. This is a good illustration of the problem of crossing fibres, as those connexions cross the superior longitudinal fasciculus. However, recent probabilistic tractography with more complex local models has successfully traced those types of connexions [14, 20, 21].

There is an intuitive relationship between geodesic, for the inverse tensor metric, and probabilistic tractographies. Probabilistic tractography consists of constructing a distribution of connexions, by sampling tracts using local orientation distributions. In the basic case where this local probability model for fibre orientations is defined using the tensor model (i.e., a Gaussian local model with a covariance matrix proportional to the diffusion tensor \mathbf{D}), the probability of a tract following an orientation given by $d\mathbf{x}$ at a location \mathbf{x} writes

$$p(\mathbf{x} + d\mathbf{x} | \mathbf{x}) = \mathcal{N}(\mathbf{x}, \mathbf{D}), \quad (12)$$

then, for some pathway γ connecting \mathbf{x}_0 to \mathbf{x}_1 , and for some discretisation of this pathway, the probability of moving along γ is the product of the infinitesimal step probabilities:

$$\begin{aligned}
p(\mathbf{x}_0 \rightarrow \mathbf{x}_1) &= \prod_{k=1}^n p(\mathbf{x}_0 + k d\mathbf{x} \mid \mathbf{x}_0 + (k-1)d\mathbf{x}) \\
&\propto \prod_{k=1}^n \exp \left\{ -\frac{1}{2} d\mathbf{x}^T \mathbf{D}^{-1} d\mathbf{x} \right\} \\
&= \exp \left\{ -\frac{1}{2} \sum_{k=1}^n d\mathbf{x}^T \mathbf{D}^{-1} d\mathbf{x} \right\} \quad (13) \\
&\rightarrow \exp \left\{ -\frac{1}{2} \int_{\gamma} d\mathbf{x}^T \mathbf{D}^{-1} d\mathbf{x} \right\} \\
&\leq \exp \left\{ -\frac{1}{2} \left(\int_{\gamma} \sqrt{d\mathbf{x}^T \mathbf{D}^{-1} d\mathbf{x}} \right)^2 \right\}.
\end{aligned}$$

Maximising this probability could then be related to minimising the geodesic distance, relative to the inverse tensor metric. While the probabilistic method gives a distribution of connexions, GT gives the mode of this distribution, that is, the path with highest probability. Note also that the probabilistic model given by (12) can be improved to fit the data more accurately (e.g., multiple tensors, etc.), which can be seen as a change in the metric tensor in GT.

Using GT, it is possible to study the organisation of large brain networks in terms of their anatomical connexions. Such networks have been studied in terms of structural invariants in a graph theoretical framework by several authors [39–41]. These works have been conducted for studying the structural organisation of the cat or primate brain, as well as for the human functional brain organisation, but have never been applied to large human anatomical networks, because no method has been proposed to construct such networks. GT could provide this structural information, via a graph that has been thresholded or not, since the connectivity index in itself contains information about the connectional structure.

There are two major issues when using geodesics for the tractography. First, choosing a metric for which geodesics represent fibre pathway trajectories is not straightforward. The correct metric might show more anisotropy than the diffusion tensor, as discussed earlier. Also, the choice of the metric might depend on the white matter fibres under investigation. The second issue is that, for any pair of regions in the brain, there exists a geodesic between those regions. However, this is not true for white matter fibres. One then has to decide when a geodesic is a fibre trajectory, for example, by defining indices and performing statistical thresholding under some null hypothesis. This problem of thresholding tractography results is not specific to GT, but is met by any other tractography method. It is though a bigger problem in the case of GT because every pair of regions is potentially connected. Another problem with GT is that, in the presence of two separate connexions between two regions, we are only able to detect one of them (the shortest one in terms of geodesic distance).

One way to validate GT results would be by comparison with another measure of connectivity. For example, measures of functional connectivity using functional magnetic resonance imaging (fMRI) by means of correlations [42] or partial correlations [43] are thought to be closely linked to the anatomical structure sustaining the brain regions, seen as graph nodes. The GT technique provides a unique tool for performing a comparison between anatomical and functional connectivity, since it can apply to large networks, and provide a measure of anatomical connectivity between each pair of nodes of the brain network. It can readily be used to compare the architectures of brain networks that have been studied in humans from the functional perspective (e.g., Salvador et al. [44] used partial correlations of fMRI data on a set of 100 regions), or using voxel-based morphometry to correlate cortical thickness between different cortical areas (e.g., He et al. [45] used this technique to study 100 cortical areas in humans). Such investigations have considerable possible applications, both cognitive and clinical. On the one hand, this method could serve as a basis for comparing anatomical and functional connectivities, as said earlier, and could help to understand how the brain works as an evolving network. On the other hand, the structure of restricted networks has already helped to distinguish between healthy subjects and patients, for example, Alzheimer disease in the case of functional connectivity [46], and Schizophrenia in the case of white matter morphology [47]. The GT method could serve for the characterisation of the structural organisation of those brain networks in terms of their connectional fingerprints.

APPENDICES

A. ALGORITHMS

Algorithm 1. Fast marching algorithm

Definitions 1. Let *Known* be the set of points whose u -value has been computed and will not change. Let *Trial* be the set of voxels that are being examined (26-neighbourhood of *Known*), and let *Far* be the set of voxels that have not been examined yet. Finally, if S is a set of voxels, let $\#S$ denote the number of voxels that belong to S .

- (i) Initialization:
 - (a) move \mathbf{x}_0 to *Known* and set $u(\mathbf{x}_0) = 0$,
 - (b) move to *Far* every \mathbf{x} such that $\mathbf{x} \neq \mathbf{x}_0$ and set $u(\mathbf{x}) = \infty$,
 - (c) update u in the neighbourhood of \mathbf{x}_0 using Algorithm 2,
- (ii) While $\#Trial \neq 0$:
 - (a) search for the voxel \mathbf{x}_m in *Trial* with the smallest value of u ,
 - (b) move \mathbf{x}_m to *Known*,
 - (c) update u in the neighbourhood of \mathbf{x}_m using Algorithm 2.

Algorithm 2. Updating procedure for the distance function u at voxel \mathbf{x}_m :

- (i) for all \mathbf{x} in the 26-neighborhood of \mathbf{x}_m and $\mathbf{x} \notin \text{Known}$,
- (a) if $\mathbf{x} \in \text{Far}$, move \mathbf{x} to *Trial*,
- (b) for all $\overline{\mathbf{x}_1 \mathbf{x}_2 \mathbf{x}_3}$ surrounding \mathbf{x} ,
- (1) compute $u^*(\mathbf{x}) = \min_{0 \leq \alpha_i \leq 1; \sum \alpha_i = 1} f(\alpha)$,
- (2) $u(\mathbf{x}) := \min \{u^*(\mathbf{x}), u(\mathbf{x})\}$.

B. EXPLICIT SOLUTION FOR THE UPDATING PROCEDURE

Here we provide an explicit solution for the minimisation problem formulated in (8). Recall that the problem was to find the minimum, inside a simplex, for the following expression:

$$\min_{\alpha} f(\alpha) = \sum_{i=1}^3 \alpha_i u(\mathbf{x}_i) + \left\| \mathbf{x} - \sum_{i=1}^3 \alpha_i \mathbf{x}_i \right\|_{\mathbf{M}}$$

$$\alpha \in \Delta = \{(\alpha_1, \alpha_2, \alpha_3) \in [0, 1]^3 / \alpha_1 + \alpha_2 + \alpha_3 = 1\}.$$
 (B.1)

In order to simplify the notations, and considering that $\alpha_3 = 1 - \alpha_1 - \alpha_2$, we will use the following:

$$k_{1:2} = u(\mathbf{x}_{1:2}) - u(\mathbf{x}_3), \quad k_3 = u(\mathbf{x}_3),$$

$$\mathbf{y}_{1:2} = \mathbf{x}_3 - \mathbf{x}_{1:2}, \quad \mathbf{y}_3 = \mathbf{x}_3 - \mathbf{x},$$
 (B.2)
$$r_{ij} = \mathbf{y}_i^T \mathbf{M} \mathbf{y}_j.$$

The function u depends simply on α_1 and α_2 :

$$f(\alpha) = \varphi(\alpha_1, \alpha_2) = \alpha_1 k_1 + \alpha_2 k_2 + k_3 + \|\alpha_1 \mathbf{y}_1 + \alpha_2 \mathbf{y}_2 + \mathbf{y}_3\|_{\mathbf{M}}.$$
 (B.3)

φ is differentiable and convex, it is then minimal when $\Delta\varphi = 0$. When constraining the minimum to lie inside the simplex Δ , the solution is either that for which the gradient is zero, if it lies inside Δ , or it is on the edges of Δ if the gradient is zero outside the simplex. In the latter case, the minimisation problem is 1D, and the solution simplifies greatly.

First, let us write the unconstrained solution: $\nabla\varphi = 0$ implies

$$\underbrace{(k_1 r_{12} - k_2 r_{11})}_{A_1} \cdot \alpha_1 + \underbrace{(k_1 r_{22} - k_2 r_{12})}_{A_2} \cdot \alpha_2 + \underbrace{(k_1 r_{23} - k_1 r_{13})}_B = 0.$$
 (B.4)

This equation means that the minimum of φ lies on the straight line defined by the equation $A_1 x + A_2 y + B = 0$. This simplifies the problem, as the problem is again 1D if we replace $\varphi(\alpha_1, \alpha_2)$ by the function $\tilde{f}(\alpha)$ which expression depends on the values of A_j and B .

(i) If $A_1 = A_2 = 0$,

$$\alpha_1 = \frac{r_{12} r_{23} - r_{13} r_{22}}{r_{11} r_{22} - r_{12}^2},$$

$$\alpha_2 = \frac{r_{13} r_{12} - r_{23} r_{11}}{r_{11} r_{22} - r_{12}^2}.$$
 (B.5)

(ii) If $A_j \neq 0$,

$$\alpha_i = \operatorname{argmin}_{\alpha} \left\{ \alpha \left(k_i - \frac{A_i}{A_j} k_j \right) - k_j \frac{B}{A_j} + u_3 + \left\| \alpha \mathbf{x}_i - \frac{A_i}{A_j} \mathbf{x}_j - \frac{B}{A_j} \mathbf{x}_j + \mathbf{x}_3 \right\|_{\mathbf{M}} \right\}$$
 (B.6)
$$\alpha_j = -\frac{A_i}{A_j} \alpha_i - \frac{B}{A_j}.$$

In the last case, the problem reduces to minimising a 1D function of the form $\tilde{f}(\alpha) = \alpha k + u + \|\alpha \mathbf{z}_1 + \mathbf{z}_2\|_{\mathbf{M}}$, in which case the solution writes

$$\alpha = -\frac{(r_{12} + k\sqrt{|R|/(r_{11} - k^2)})}{r_{11}},$$
 (B.7)

where $r_{ij} = \mathbf{z}_i^T \mathbf{M} \mathbf{z}_j$ and $|R| = r_{11} r_{22} - r_{12}^2$.

Finally, if the solution given by the above lies outside the simplex (i.e., $|\alpha_i| > 0$), then we minimise φ on the edges of the simplex, which is again a 1D problem. This is equivalent to setting one of the $\{\alpha_i\}_{i=1}^3$ to zero, and keeping the results which minimises φ :

(i) $\alpha_1 = 0$:

$$\alpha_2 = \operatorname{argmin}_{\alpha} \{ \alpha k_2 + k_3 + \|\alpha \mathbf{y}_2 + \mathbf{y}_3\|_{\mathbf{M}} \},$$
 (B.8)

(ii) $\alpha_2 = 0$:

$$\alpha_1 = \operatorname{argmin}_{\alpha} \{ \alpha k_1 + k_3 + \|\alpha \mathbf{y}_1 + \mathbf{y}_3\|_{\mathbf{M}} \},$$
 (B.9)

(iii) $\alpha_1 + \alpha_2 = 1$:

$$\alpha_1 = \operatorname{argmin}_{\alpha} \{ \alpha(k_1 - k_2) + k_2 + k_3 + \|\alpha(\mathbf{y}_1 - \mathbf{y}_2) + \mathbf{y}_2 + \mathbf{y}_3\|_{\mathbf{M}} \}$$
 (B.10)
$$\alpha_2 = 1 - \alpha_1.$$

ACKNOWLEDGMENTS

The authors would like to acknowledge funding from the *Association pour la Recherche contre le Cancer* and the Dr. Hadwen Trust For Humane Research (SJ). They are extremely grateful to Dr. Thien Huong N'Guyen, *Service de Neuroradiologie (CHNO des Quinze-Vingts, Paris)*, for kindly providing the diffusion data.

REFERENCES

- [1] J. W. Scannell, G. A. P. C. Burns, C. C. Hilgetag, M. A. O'Neil, and M. P. Young, "The connectonal organization of the cortico-thalamic system of the cat," *Cerebral Cortex*, vol. 9, no. 3, pp. 277–299, 1999.
- [2] D. J. Felleman and D. C. van Essen, "Distributed hierarchical processing in the primate cerebral cortex," *Cerebral Cortex*, vol. 1, no. 1, pp. 1–47, 1991.
- [3] F. Crick and E. Jones, "Backwardness of human neuroanatomy," *Nature*, vol. 361, no. 6408, pp. 109–110, 1993.

- [4] M. Catani, R. J. Howard, S. Pajevic, and D. K. Jones, "Virtual in vivo interactive dissection of white matter fasciculi in the human brain," *NeuroImage*, vol. 17, no. 1, pp. 77–94, 2002.
- [5] S. Wakana, H. Jiang, L. M. Nagae-Poetscher, P. C. M. van Zijl, and S. Mori, "Fiber tract-based atlas of human white matter anatomy," *Radiology*, vol. 230, no. 1, pp. 77–87, 2004.
- [6] T. E. J. Behrens, H. Johansen-Berg, M. W. Woolrich, et al., "Non-invasive mapping of connections between human thalamus and cortex using diffusion imaging," *Nature Neuroscience*, vol. 6, no. 7, pp. 750–757, 2003.
- [7] P. L. Croxson, H. Johansen-Berg, T. E. J. Behrens, et al., "Quantitative investigation of connections of the prefrontal cortex in the human and macaque using probabilistic diffusion tractography," *Journal of Neuroscience*, vol. 25, no. 39, pp. 8854–8866, 2005.
- [8] M. F. S. Rushworth, T. E. J. Behrens, and H. Johansen-Berg, "Connection patterns distinguish 3 regions of human parietal cortex," *Cerebral Cortex*, vol. 16, no. 10, pp. 1418–1430, 2006.
- [9] H. Johansen-Berg, T. E. J. Behrens, M. D. Robson, et al., "Changes in connectivity profiles define functionally distinct regions in human medial frontal cortex," *Proceedings of the National Academy of Sciences of the United States of America*, vol. 101, no. 36, pp. 13335–13340, 2004.
- [10] H. W. Powell, G. J. Parker, D. C. Alexander, et al., "Hemispheric asymmetries in language-related pathways: a combined functional MRI and tractography study," *NeuroImage*, vol. 32, no. 1, pp. 388–399, 2006.
- [11] P. J. Basser, J. Mattiello, and D. LeBihan, "Estimation of the effective self-diffusion tensor from the NMR spin echo," *Journal of Magnetic Resonance*, vol. 103, no. 3, pp. 247–254, 1994.
- [12] K. M. Jansons and D. C. Alexander, "Persistent angular structure: new insights from diffusion magnetic resonance imaging data," *Inverse Problems*, vol. 19, no. 5, pp. 1031–1046, 2003.
- [13] T. E. J. Behrens, M. W. Woolrich, M. Jenkinson, et al., "Characterization and propagation of uncertainty in diffusion-weighted MR imaging," *Magnetic Resonance in Medicine*, vol. 50, no. 5, pp. 1077–1088, 2003.
- [14] T. Hosey, G. Williams, and R. Ansoorge, "Inference of multiple fiber orientations in high angular resolution diffusion imaging," *Magnetic Resonance in Medicine*, vol. 54, no. 6, pp. 1480–1489, 2005.
- [15] D. S. Tuch, T. G. Reese, M. R. Wiegell, N. Makris, J. W. Belliveau, and V. J. Wedeen, "High angular resolution diffusion imaging reveals intravoxel white matter fiber heterogeneity," *Magnetic Resonance in Medicine*, vol. 48, no. 4, pp. 577–582, 2002.
- [16] M. Mori, B. J. Crain, V. P. Chacko, and P. C. M. van Zijl, "Three-dimensional tracking of axonal projections in the brain by magnetic resonance imaging," *Annals of Neurology*, vol. 45, no. 2, pp. 265–269, 1999.
- [17] D. K. Jones, A. Simmons, S. C. R. Williams, and M. A. Horsfield, "Non-invasive assessment of axonal fiber connectivity in the human brain via diffusion tensor MRI," *Magnetic Resonance in Medicine*, vol. 42, no. 1, pp. 37–41, 1999.
- [18] T. E. Conturo, N. F. Lori, T. S. Cull, et al., "Tracking neuronal fiber pathways in the living human brain," *Proceedings of the National Academy of Sciences of the United States of America*, vol. 96, no. 18, pp. 10422–10427, 1999.
- [19] P. J. Basser, S. Pajevic, C. Pierpaoli, J. Duda, and A. Aldroubi, "In vivo fiber tractography using DT-MRI data," *Magnetic Resonance in Medicine*, vol. 44, no. 4, pp. 625–632, 2000.
- [20] G. J. M. Parker and D. C. Alexander, "Probabilistic anatomical connectivity derived from the microscopic persistent angular structure of cerebral tissue," *Philosophical Transactions of the Royal Society of London, Series B, Biological Sciences*, vol. 360, no. 1457, pp. 893–902, 2005.
- [21] T. E. J. Behrens, H. J. Berg, S. Jbabdi, M. F. S. Rushworth, and M. W. Woolrich, "Probabilistic diffusion tractography with multiple fibre orientations: what can we gain?" *NeuroImage*, vol. 34, no. 1, pp. 144–155, 2007.
- [22] G. J. M. Parker, C. A. M. Wheeler-Kingshott, and G. J. Barker, "Estimating distributed anatomical connectivity using fast marching methods and diffusion tensor imaging," *IEEE Transactions on Medical Imaging*, vol. 21, no. 5, pp. 505–512, 2002.
- [23] D. L. Chopp, "Replacing iterative algorithms with single-pass algorithms," *Proceedings of the National Academy of Sciences of the United States of America*, vol. 98, no. 20, pp. 10992–10993, 2001.
- [24] S. Jbabdi, P. Bellec, G. Marrelec, V. Perlbarg, and H. Benali, "A level set method for building anatomical connectivity paths between brain areas using DTI," in *Proceedings of the 2nd IEEE International Symposium on Biomedical Imaging: Macro to Nano (ISBI '04)*, vol. 1, pp. 1024–1027, Arlington, Va, USA, April 2004.
- [25] C. Lenglet, R. Deriche, and O. Faugeras, "Inferring white matter geometry from diffusion tensor MRI: application to connectivity," in *Proceedings of the 8th European Conference on Computer Vision (ECCV '04)*, T. Pajdla and J. Matas, Eds., vol. 3024 of *Lecture Notes in Computer Science*, pp. 127–140, Prague, Czech Republic, April 2004.
- [26] M. Jackowski, C. Y. Kao, M. Qiu, R. T. Constable, and L. H. Staib, "White matter tractography by anisotropic wavefront evolution and diffusion tensor imaging," *Medical Image Analysis*, vol. 9, no. 5, pp. 427–440, 2005.
- [27] P. Staempfli, T. Jaermann, G. R. Crelier, S. Kollias, A. Valavanis, and P. Boesiger, "Resolving fiber crossing using advanced fast marching tractography based on diffusion tensor imaging," *NeuroImage*, vol. 30, no. 1, pp. 110–120, 2006.
- [28] J. N. Tsitsiklis, "Efficient algorithms for globally optimal trajectories," *IEEE Transactions on Automatic Control*, vol. 40, no. 9, pp. 1528–1538, 1995.
- [29] L. Qingfen, *Enhancement, extraction, and visualization of 3D volume data*, Ph.D. thesis, Linköping University, Linköping, Sweden, 2003.
- [30] J. A. Sethian and A. Vladimirov, "Ordered upwind methods for static Hamilton-Jacobi equations," *Proceedings of the National Academy of Sciences of the United States of America*, vol. 98, no. 20, pp. 11069–11074, 2001.
- [31] V. I. Smirnov, *A Course on Higher Mathematics*, vol. 4, Pergamon Press, New York, NY, USA, 1964.
- [32] J. A. Sethian, *Level Set Methods and Fast Marching Methods*, Cambridge University Press, Cambridge, Mass, USA, 2002.
- [33] E. W. Dijkstra, "A note on two problems in connexion with graphs," *Numerische Mathematik*, vol. 1, no. 1, pp. 269–271, 1959.
- [34] L. O'Donnell, S. Haker, and C.-F. Westin, "New approaches to estimation of white matter connectivity in diffusion tensor MRI: elliptic PDEs and geodesics in a tensor-warped space," in *Proceedings of the 5th International Conference on Medical Image Computing and Computer-Assisted Intervention (MICCAI '02)*, T. Dohi and R. Kikinis, Eds., pp. 459–466, Tokyo, Japan, September 2002.
- [35] C.-F. Westin, S. E. Maier, H. Mamata, A. Nabavi, F. A. Jolesz, and R. Kikinis, "Processing and visualization for diffusion tensor MRI," *Medical Image Analysis*, vol. 6, no. 2, pp. 93–108, 2002.

- [36] M. Brett, I. S. Johnsrude, and A. M. Owen, "The problem of functional localization in the human brain," *Nature Reviews Neuroscience*, vol. 3, no. 3, pp. 243–249, 2002.
- [37] S. Mori, K. Frederiksen, P. C. M. van Zijl, et al., "Brain white matter anatomy of tumor patients evaluated with diffusion tensor imaging," *Annals of Neurology*, vol. 51, no. 3, pp. 377–380, 2002.
- [38] S. Mori, S. Wakana, L. M. Nagae-Poetscher, and P. C. M. van Zijl, *MRI Atlas of Human White Matter*, Elsevier Science, Amsterdam, The Netherlands, 2005.
- [39] G. Tononi, A. R. McIntosh, D. P. Russell, and G. M. Edelman, "Functional clustering: identifying strongly interactive brain regions in neuroimaging data," *NeuroImage*, vol. 7, no. 2, pp. 133–149, 1998.
- [40] O. Sporns, G. Tononi, and G. M. Edelman, "Theoretical neuroanatomy and the connectivity of the cerebral cortex," *Behavioural Brain Research*, vol. 135, no. 1-2, pp. 69–74, 2002.
- [41] O. Sporns, D. R. Chialvo, M. Kaiser, and C. C. Hilgetag, "Organization, development and function of complex brain networks," *Trends in Cognitive Sciences*, vol. 8, no. 9, pp. 418–425, 2004.
- [42] M. McIntosh and F. Gonzalez-Lima, "Structural equation modelling and its application to network analysis of functional brain imaging," *Human Brain Mapping*, vol. 2, no. 1-2, pp. 2–22, 1994.
- [43] G. Marrelec, J. Daunizeau, M. Péligrini-Issac, J. Doyon, and H. Benali, "Conditional correlation as a first step toward common framework for functional brain interactivity modeling in functional MRI and MEG/EEG," *IEEE Transactions on Signal Processing*, vol. 53, no. 9, pp. 3503–3516, 2005.
- [44] R. Salvador, J. Suckling, M. R. Coleman, J. D. Pickard, D. Menon, and E. Bullmore, "Neurophysiological architecture of functional magnetic resonance images of human brain," *Cerebral Cortex*, vol. 15, no. 9, pp. 1332–2342, 2005.
- [45] Y. He, Z. J. Chen, and A. C. Evans, "Small-world anatomical networks in the human brain revealed by cortical thickness from MRI," *Cerebral Cortex*, vol. 17, no. 10, pp. 2407–2419, 2007.
- [46] M. D. Greicius, G. Srivastava, A. L. Reiss, and V. Menon, "Default-mode network activity distinguishes Alzheimer's disease from healthy aging: evidence from functional MRI," *Proceedings of the National Academy of Sciences of the United States of America*, vol. 101, no. 13, pp. 4637–4642, 2004.
- [47] R. A. A. Kanaan, J.-S. Kim, W. E. Kaufmann, G. D. Pearson, G. J. Barker, and P. K. McGuire, "Diffusion tensor imaging in schizophrenia," *Biological Psychiatry*, vol. 58, no. 12, pp. 921–929, 2005.

Research Article

Connectivity-Based Parcellation of the Cortical Mantle Using q -Ball Diffusion Imaging

Muriel Perrin,^{1,2,3} Yann Cointepas,^{1,2} Arnaud Cachia,^{2,4} Cyril Poupon,^{1,2} Bertrand Thirion,⁵ Denis Rivière,^{1,2} Pascal Cathier,^{1,2} Vincent El Kouby,^{1,2} André Constantinesco,⁶ Denis Le Bihan,^{1,2} and Jean-François Mangin^{1,2,4}

¹NeuroSpin Institut d'Imagerie BioMédicale, Commissariat l'Energie Atomique (CEA), Gif-sur-Yvette 91191, France

²Institut Fédératif de Recherche 49, Gif-sur-Yvette 91191, France

³GE Healthcare, 11 avenue Morane Saulnier, Vélizy 78457, France

⁴Inserm U.797, CEA-INSERM Research Unit "Neuroimaging & Psychiatry", Service Hospitalier Frédéric Joliot, Orsay, Orsay Cedex 91401, France

⁵Parietal Project, INRIA Futurs, NeuroSpin, Gif-sur-Yvette 91191, France

⁶Service de Biophysique et Médecine Nucléaire, Hôpital de Hautepierre, 1 ave Molière, Strasbourg 6708, France

Correspondence should be addressed to Muriel Perrin, muriel.perrin@ge.com

Received 1 September 2007; Revised 30 November 2007; Accepted 16 December 2007

Recommended by Habib Benali

This paper exploits the idea that each individual brain region has a specific connection profile to create parcellations of the cortical mantle using MR diffusion imaging. The parcellation is performed in two steps. First, the cortical mantle is split at a macroscopic level into 36 large gyri using a sulcus recognition system. Then, for each voxel of the cortex, a connection profile is computed using a probabilistic tractography framework. The tractography is performed from q -ball fields using regularized particle trajectories. Fiber ODF are inferred from the q -balls using a sharpening process focusing the weight around the q -ball local maxima. A sophisticated mask of propagation computed from a T1-weighted image perfectly aligned with the diffusion data prevents the particles from crossing the cortical folds. During propagation, the particles father child particles in order to improve the sampling of the long fascicles. For each voxel, intersection of the particle trajectories with the gyri lead to a connectivity profile made up of only 36 connection strengths. These profiles are clustered on a gyrus by gyrus basis using a K -means approach including spatial regularization. The reproducibility of the results is studied for three subjects using spatial normalization.

Copyright © 2008 Muriel Perrin et al. This is an open access article distributed under the Creative Commons Attribution License, which permits unrestricted use, distribution, and reproduction in any medium, provided the original work is properly cited.

1. INTRODUCTION

Diffusion magnetic resonance imaging is a probe allowing noninvasive studies of the microscopic structure of brain tissues. For instance, inside white matter, preferential orientations of fiber bundle axonal membranes induce anisotropy of the local Brownian motion of water molecules. The fiber orientation can be inferred from this anisotropy. Hence, one of the most attractive applications of diffusion imaging is the tractography of white matter fiber bundles and the inference of brain connectivity.

Tractography has been developed first from diffusion tensor imaging (DTI) [1], a technique indicating for each voxel the direction of the highest amplitude of the diffusion process. Assuming that this direction corresponds to the

main fiber orientation inside the voxel, some of the tracts can be reconstructed step by step [2–4]. Unfortunately this simplistic approach can not resolve fiber crossings, which are numerous in the brain. The problem is partially overcome with either preprocessing of tensor field [3, 5–9] or more sophisticated methods of tractography involving either regularization of the bundle trajectories [10, 11] or probabilistic strategies based on Monte Carlo sampling and models of uncertainty about fiber orientations [12–14]. The fiber orientation distribution function (ODF) inferred in each voxel from DTI, however, is not sufficient to map successfully the large-scale connectivity of the cortex because of the amount of crossings involved [15].

The emergence of high angular resolution diffusion imaging (HARDI) provides the opportunity to better model

water mobility in fiber crossing. Hence, more reliable mapping of the corticocortical pathways can be achieved, which is exploited in this paper. There is no consensus yet on the best way to interpret HARDI data for tractography [16–23]. The main issue is the choice of the method used to build fiber ODFs. In this paper, we explore the potential of q -ball imaging, a method pushing further than DTI the idea that the fiber directions can be inferred from the local maxima of the amplitude of water molecule radial displacements [24, 25].

The network of anatomical connections linking the neuronal elements of the human brain is still largely unknown [26, 27]. Therefore, compiling the connection matrix or the “connectome” of the human brain represents an indispensable foundation for basic and applied neurobiological research [27]. One of the challenges faced by this research program is that the structural elements of the human brain, in terms of interesting nodes for the connection matrix, are difficult to define. Attempting to assemble the human connectome at the level of single neurons is unrealistic and will remain infeasible at least in the near future. Nevertheless, a higher scale of representation is more attractive: there is an overwhelming evidence that human cognitive functions depend on the activity of large populations of neurons in distributed network. Unfortunately, brain areas and neuronal populations are difficult to delineate.

No single universally accepted parcellation scheme currently exists for the human brain. In the cerebral cortex, neurons are arranged in an unknown number of anatomically distinct regions and areas, perhaps on the order of 100 or more [28]. The most standard parcellation, which has been proposed by Brodmann one hundred years ago from cytoarchitectonic criterions, cannot be mapped in vivo. Anyway, while cyto- and myeloarchitectonics are powerful methods to highlight anatomical segregation, animal studies have shown that further parcellations of architectonically homogeneous areas can be obtained using connectivity [29]. Therefore, the most promising avenue for parcellating the brain and compiling the brain connectome originates from the notion that individual brain regions maintain individual connection profiles [27]. What defines a segregated brain region is that all its structural elements share highly similar long-range connectivity patterns, and that these patterns are dissimilar between regions. These connectivity patterns determine the region functional properties [30], and also allow their anatomical delineation and mapping.

Tractography has been used previously to distinguish thalamic areas using a lobar parcellation of the cerebral cortex as input [31]. For this application, each thalamus voxel was attached to the lobe with the strongest connection. The idea that the whole patterns of connectivity can be used to identify areal boundaries has been demonstrated in the human medial frontal cortex [32]. First, connection strengths from voxels within the medial frontal cortex to all other voxels in the rest of the brain were obtained. Connection profiles were then used to calculate a cross-correlation matrix, which was examined for the existence of distinct clusters of voxels with shared connection patterns. The resulting clusters matched an independent clustering of the same region obtained from functional imaging. The robustness of the ap-

proach has been studied further in [33]. Another successful local parcellation related to Broca’s area has been recently achieved by another group in [34].

In this paper, we extend further the idea of parcellating the cerebral cortex using connectivity profiles. The main difference with the works mentioned above is that we address the parcellation of the complete cortical mantle. Following the approach of Oxford group [31–33], our purpose would involve the difficult clustering of a huge cross-correlation matrix. To overcome this problem, our parcellation framework relies on an initial macroscopic parcellation of the cortex into 36 large gyri performed with a pipeline of processing [35] provided in brainVISA framework (<http://brainvisa.info>). This initial parcellation is used to reduce each voxel connectivity profile to a short vector of 36 values, namely the strength of connection to each of the gyri. A second use of the gyral parcellation is to split the initial global clustering problem into 36 smaller problems: the gyri are clustered one by one. The justification leading to the use of a gyral parcellation to reduce the complexity of the problem lies in the strong link between this large scale division of the cortex and its functional and architectonic organizations [36, 37]. An additional argument stems from the hypothesis that the fiber bundle organization is deeply related to the folding patterns of the cerebral cortex [38].

In the following, we provide first a brief overview of our data, of the preprocessing steps and, of our choice for the fiber ODF. While this part of the paper is not detailed, it should be noted that we deal with especially high-quality datasets based on 200 directions of diffusion and a b value of 3000 s/mm² increasing the contrast between crossing bundles. Moreover, a dedicated MR sequence and several steps of distortion correction are used to achieve a perfect alignment between the diffusion data and the high-resolution T1-weighted image used to compute the gyral parcellations. All this care is mandatory to address the mapping of the corticocortical interareal pathways. This dataset is provided to the community [39].

The next part describes the different steps of our parcellation method. We first describe our “probabilistic” tractography framework dedicated to q -ball fields and based on regularized particle trajectories. Our method includes several original refinements compared to its first introduction [40]: (1) an algorithm initially dedicated to the detection of the cortical sulci [41] is used to build a mask preventing the particles from spuriously crossing the cortical folds; (2) a local sharpening of the q -ball ODF is performed to concentrate the Monte Carlo sampling around the most probable fiber directions; (3) a processus creating children fibers during the tracking has been designed in order to improve the sampling of long bundles. The behavior of these refinements is illustrated using virtual phantoms of crossing computed via simulation of the random walks of the water molecules in a restricted geometric environment.

Then, we describe the method dedicated to the clustering of the voxels of the cortical mantle from the connectivity profile provided by the probabilistic tractography. We first rapidly recall the basic ideas underlying the computation of our gyral parcellation [35]. Then we describe the clustering

algorithm, which is based on a K -means framework including a Markov random field regularization procedure. Finally, the method is tested with three brains through the clustering of 14 different gyri. We compare the connectivity matrices obtained for the 14 gyri and study the reproducibility of the clustering using a spatial normalization method.

2. METHOD

2.1. Fiber orientation distribution function

2.1.1. Data acquisition

Diffusion-weighted and T_1 -weighted images were acquired in three healthy subjects on a GE Healthcare Signa 1.5 Tesla Excite II scanner provided with a 40 mT/m whole body gradient coil, eight receiver channel acquisition system, and an eight channel head surface coil.

T_1 -weighted anatomical images were acquired using fast gradient echo with inversion recovery sequence (echo time 2 milliseconds, repetition time 9.9 milliseconds, inversion preparation time 600 milliseconds, flip angle 10° , bandwidth 12.5 kHz, FOV 24 cm, and repetition time 2 leading to a 15 minutes and 52 seconds scan time). Voxel size is $0.9375 \times 0.9375 \text{ mm}^2$ with a slice thickness of 1.2 mm. We used 2 repetitions in order to get a very good contrast to noise ratio simplifying grey/white classification.

Diffusion weighted data were acquired with HARDI scheme. The sequence is a dual spin echo (echo time is 93.2 milliseconds, volume repetition time is 19000 milliseconds, flip angle is 90° , bandwidth is 200 kHz, FOV is 24 cm). Voxel size is $1.98 \times 1.98 \text{ mm}^2$ with a slice thickness of 2 mm. The diffusion weighting was isotropically distributed along 200 directions using a b value of 3000 s/mm^2 . Along the acquisition, 25 additional volumes without diffusion sensitization were acquired and finally averaged to obtain a T_2 -weighted image perfectly aligned with the diffusion-weighted dataset. The scan time for this diffusion protocol was 72 minutes and 50 seconds. A phase map for diffusion data was acquired using a 2D double gradient echo sequence (echo time 4.5 milliseconds, slice repetition time 441 milliseconds, flip angle 60° , bandwidth 15 kHz, FOV 24 cm, and the same slice location as for diffusion protocol leading to a 3 minutes and 25 seconds scan time).

2.1.2. Diffusion data preprocessing

The use of a twice refocusing diffusion module compensates for the echoplanar distortions, due to eddy currents, at the first order. However, two other kinds of geometric distortions had to be corrected, related to the nonlinearities of the gradients and to the local static field inhomogeneities induced by tissue/air interfaces. The first kind of distortions was overcome during reconstruction using GE warping procedures. The second kind related to susceptibility was corrected using the phase map [42, 43]. This method corrects intensity variation and voxel shifts caused by the local field inhomogeneities. After these procedures, T_1 and diffusion-weighted datasets could be aligned perfectly using a rigid transformation. This transformation was computed by maximizing the

mutual information between the T_1 -weighted image and the average T_2 -weighted image (cf. Figure 1).

2.1.3. From q -ball to fiber ODF

In order to develop a probabilistic tractography algorithm, HARDI datasets have to be converted into a fiber ODF in each voxel. Numerous ideas have been proposed for this purpose. The first class of approaches is based on models of the signal observed with one single bundle. The model is used to solve in each voxel a local inverse problem according to different alternative frameworks [16–21, 23, 44–46]. The HARDI signal is then explained as a mixture of models. These approaches convert HARDI data into a fiber ODF focusing on a small set of putative crossing fiber directions. Hence, the local distribution around each of these directions is an estimate of the uncertainty associated with the fiber orientation. It is beyond the scope of this paper to provide a comparison of all the existing approaches.

A second strategy consists in using iconic representations of the diffusion process to build the fiber ODF. This point of view does not rely on model fitting or deconvolution procedures. This is supposed to alleviate the risk of misinterpreting the MR data either because of some weaknesses of the model or because of some failure of the method used to perform the local inverse problem. Diffusion spectrum imaging (DSI), which provides for each voxel a 3D image of the water displacement probability distribution, is at the origin of this research direction [47]. DSI is based on sampling the 3D Fourier space of the water displacement distribution, which requires large pulsed field gradients. The radial projection of the diffusion function, called the diffusion ODF, is supposed to convey most of the information about the diffusion process required to guess fiber orientations [48]. It has been shown recently that the diffusion ODF can be approximated from HARDI acquisitions using a spherical tomographic inversion called the Funk-Radon transform, also known as the spherical Radon transform [24, 25]. In this paper, we use the ODF resulting from this numerical transform, which is called q -ball. The most recent refinement leading to a robust analytical reconstruction was not used here [22]. There is no consensus yet on the comparison between the diffusion ODF and the q -ball approximation for the accuracy of the fiber direction estimation [49, 50].

The exact link between q -ball and fiber ODF is still unclear, but simple hypotheses lead to convert the q -ball into interesting candidates for the fiber ODF. Assuming that at high b value most of the diffusion weight which stems from intra-axonal water leads to considering the amplitude of the radial displacement of water molecules a good marker of putative fiber directions. The simplest use of this idea consists in associating the q -ball local maxima with the fiber orientations, obtaining a small set of directions playing the same role as the sets provided by the model-based methods mentioned above. This approach assumes the equivalence between the local maxima of the q -ball and the local maxima of the fiber ODF, which can be discussed [24]. It is known to often fail when two fiber bundles cross with an angle of less than 45 degrees.

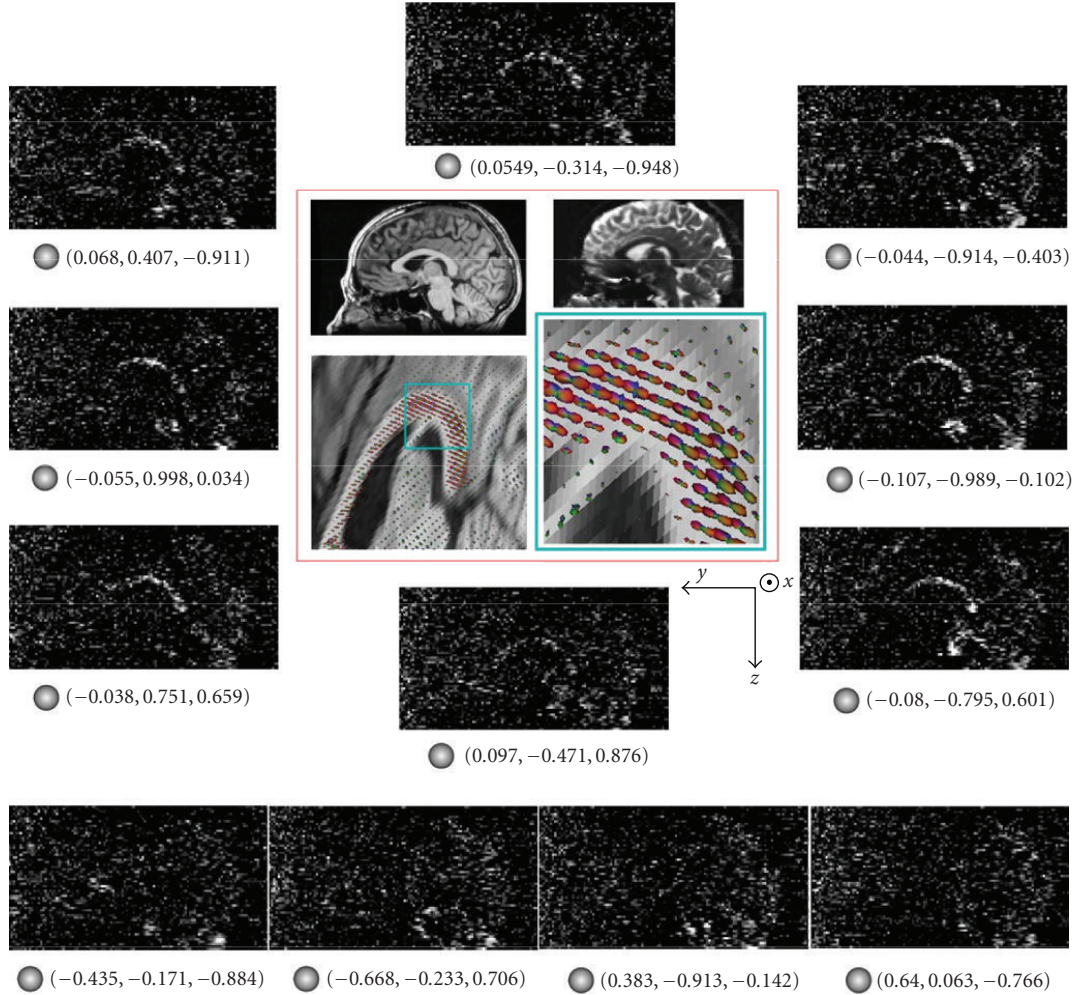


FIGURE 1: An illustration of the links between high b value diffusion-weighted data, Funk-Radon transform, diffusion ODF, and fiber ODF: the slice cuts the corpus callosum, whose fibers approximately follow the X direction. The figure proposes the aligned T1- and T2-weighted slices and a number of diffusion-weighted slices. When the diffusion gradient is not orthogonal to the fibers (unit vector under corresponding slice), most of the MR signal is destroyed by water diffusion: the corpus callosum is black (row of slices at the bottom). When the diffusion gradient is orthogonal to the fibers, water diffusion is restricted by the axonal membranes: some noisy signal survives in the corpus callosum. Hence, the sum of the raw signal along the equator around the X axis leads to a peak of the q -ball indicating the fiber direction. In this figure, the q -balls are scaled according to their anisotropy.

Pushing further the hypothesis of a strong equivalence between both ODFs, one can consider that the shape of the q -ball around a local maximum provides a good estimation of the uncertainty related to the orientation of the underlying fibers. This is the strategy chosen in this paper to sample the fiber directions during the probabilistic tractography. We will not address here the validity of this hypothesis, which requires a crucial research program based on physical phantoms of fiber crossing [51–53] and a better understanding of the physics of diffusion in biological tissues (choice of the b value, membrane permeability, number of compartments, etc.). This program, however, needs time to deliver some answers, which should not stop the development of tractography algorithms. These algorithms, indeed, have the possibility to use contextual knowledge, namely the neighborhood of a voxel, in order to tackle locally the inverse problem.

Therefore, they can overcome some of the weaknesses of the current fiber ODFs and provide meaningful neuroscience results.

In the following, q -ball data are visualized according to the following rules. Each q -ball is represented by a spherical mesh. Each node of the mesh is moved outward according to the amplitude ψ of the water molecule displacement (more precisely the result of the radial summation of the diffusion function). In order to maximize the information provided by this deformation process, this move is computed as $(\psi - \min_S(\psi)) / (\max_S(\psi) - \min_S(\psi))$, where S is the sampled sphere of the current voxel. To improve visualization further, each node is given a color related to its orientation relative to the image axis: red for x axis (left-right), green for y axis (frontal-occipital), and blue for z axis (top-down), interpolated in between. Finally, the resulting mesh is sometimes

scaled according to the q -ball anisotropy in order to highlight the regions with the largest influence on tractography (cf. Figure 1).

2.2. Probabilistic regularized tractography in q -ball fields

The probabilistic tractography framework used in this paper is an extension of a method described before [40]. This method has been designed in order to remain as simple as possible. It should be considered as a first attempt to explore the potential of the new generation of high-quality data recently provided by our MR physicists. Hence, this method aims at paving the way for more sophisticated developments [15]. The initial algorithm was based on regularized particle trajectories used to perform the Monte Carlo sampling of the white matter geometry. Validation has been provided using a crossing phantom made up of sheets of parallel haemodialysis fibers and through the successful tracking of the primary auditory tract in the human brain [40]. This last achievement was especially impressive because of the problematic crossing of this tract with a thick orthogonal pathway. However, the shortness of this tract and the simple geometry of the phantom were too favorable configurations to consider these first experiments as warrant of success with long cortico-cortical pathways. Therefore, in the following, after describing briefly the initial method (1, 2), three important refinements are proposed (3, 4, 5).

2.2.1. Particles with inertia

Each origin voxel is spatially sampled in order to define the starting points of n particles. These particles move inside a continuous q -ball field defined by linear interpolation. The particles are given an initial speed in the direction corresponding to the maximum of the local q -ball. This q -ball is sampled in the $400 = 2 \times 200$ directions of acquisitions.

Then, each particle moves with constant speed according to a simplistic sampling scheme: let us note $p(i)$ the location of the particle at time i , and $\vec{v}(i)$ the direction of the particle speed at time i :

$$p(i + \delta t) = p(i) + \vec{v}(i) * \delta t. \quad (1)$$

The behavior of the particle speed direction can be understood from a simple mechanical analogy: at each step of the trajectory sampling, the new speed $\vec{v}(i + \delta t)$ results from a tradeoff between inertia ($\vec{v}(i)$) and a force stemming from the local q -ball (\vec{v}_q) (see Figure 2):

$$\vec{v}(i + \delta t) = \alpha \vec{v}_q + (1 - \alpha) \vec{v}(i), \quad (2)$$

where α is a parameter ranging between 0 and 1 that will be described latter. The orientation \vec{v}_q of the force acting on the particle is chosen randomly inside a half cone defined from the inertia direction $\vec{v}(i)$. The probability distribution $F_q(\vec{v}(i))$ driving this drawing corresponds to the restriction

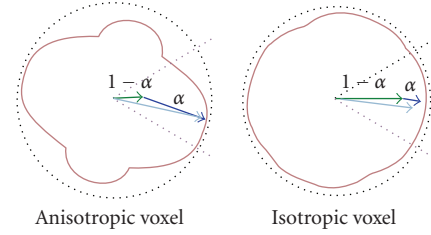


FIGURE 2: The normalized standard deviation of the q -ball provides a measure of anisotropy α that is used to weight the influence of the q -ball on the particle trajectories: particle inertia increases for low anisotropy q -balls.

of the q -ball to this half cone. This distribution, called further the restricted fiber ODF, is build after renormalizing the q -ball values within the half cone. The renormalization and the drawing are performed among the sampled directions of the q -ball belonging to the half cone. Therefore, the maximum of the q -ball inside the half cone has the highest probability to influence the particles.

The weight α is the standard deviation of the q -ball normalized by its maximum in the field, computed after removing the 5% highest values to prevent the influence of spurious extreme values resulting for instance from motion artifacts. Hence, this weight depends on the location in the q -ball field. In fact, α is a measure of anisotropy [54]. A slice of α can be visualized in Figure 7(b) For isotropic voxels, α parameter is small and the algorithm favors inertia direction; while for anisotropic voxels, α parameter is large and the algorithm favors q -ball distribution (see Figure 2). Hence, the particles have a tendency to proceed further in the initial direction in voxels where the diffusion peaks are not reliable.

The particle trajectory regularization depends on three parameters:

- (i) the half-cone angle is used to discard the diffusion peaks leading to high curvature of the trajectory;
- (ii) the q -ball standard deviation (α parameter) tunes the weight of the inertia;
- (iii) the constant sampling δt provides another level of tuning: increasing the trajectory sampling decreases curvature regularization.

In this paper, the influence of these ad hoc parameters is not explored. In the following, we use a half-cone angle of 30 degree and a constant sampling equal to half the minimal voxel size, namely 1 mm.

2.2.2. Validation on a fiber crossing phantom

The lack of knowledge about the white matter organization of the human brain is a huge handicap for the community developing fiber tracking algorithms. Considering the complexity of the MR diffusion signal, it is rather difficult to validate such algorithms using only simulated data. Therefore, the development of phantoms with known geometry is in our opinion crucial for a better understanding of the algorithm behaviors [51].

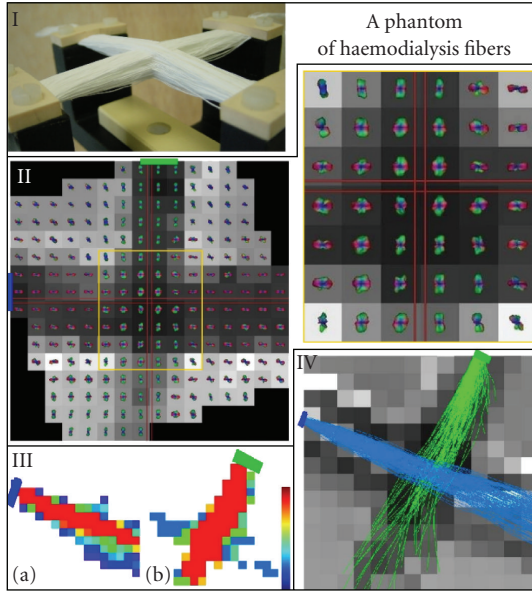


FIGURE 3: I: a phantom of fiber crossing. II: a slice of the 512 directions q -ball acquisition with a zoom on the crossing area. q -balls are superimposed on a T2-weighted MR image whose intensity is related to water amount. q -balls and MR data have been slightly rotated in order to simplify the reading of the q -ball 3D color code. Green and blue rectangles denote the regions of interest at the origin of fiber tracking. III: slices of the number of particles crossing each voxel at the end of the fiber sampling (left: blue bundle, right: green bundle). IV: trajectories selected by a threshold on the particle density map for each bundle. A T2-weighted slice of the phantom crossing the bundles is used as a background and hides some trajectories.

For this purpose, we have designed a phantom corresponding to two intersecting fiber bundles. It consists of sheets of parallel haemodialysis fibers (Gambro, Polyflux 210 H) with an inner diameter of 200 micrometers and an outer diameter of 250 micrometers. Sheets of two different orientations intersecting at 90 degrees were stacked on each other in an interleaved fashion [51]. Crossing thickness is above 2 cm. Fibers are suspended and hold by two arms as seen in Figure 3. Fibers are permeable to water. They are dived in pure water mixed with gadolinium.

We performed DW-MRI acquisitions on a 1.5 Tesla Signa Excite II MRI system (GE Healthcare, Milwaukee) with maximal gradient intensity of 40 mT m^{-1} . Acquisitions were performed with spin-echo EPI sequence and Stejskal and Tanner diffusion gradient [55]: b value is 700 s/mm^{-2} , equivalent to 2000 s/mm^{-2} for diffusion in brain white matter, 512 orientations of the diffusion gradient (HARDI), matrix 64×64 , in-plane voxel resolution $3.75 \times 3.75 \text{ mm}$, slice thickness 2.0 mm, TE 66.6 milliseconds, TR 3000 milliseconds, 1 shot, field of view 24 cm. Spatial distortions of the diffusion-weighted images induced by eddy currents were corrected before estimating the q -ball field. This correction relies on a slice-by-slice affine geometric model and maximization of mutual information with the diffusion free T2-weighted image [56].

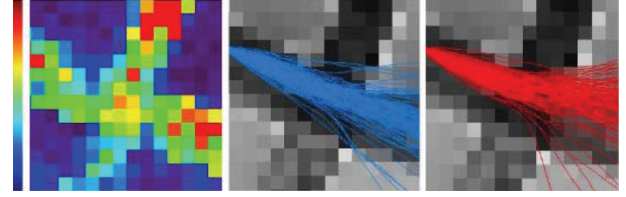


FIGURE 4: (a) A slice of the normalized standard deviation of the q -ball (α). (b) Particle trajectories in the initial q -ball field (T2-weighted image behind). (c) Particle trajectories in the field where the q -balls of the crossing area have been rotated around the z -axis (20 degrees). A lot of trajectories are bended which shows that the algorithm is not overregularized.

A slice of the q -ball field is shown in Figure 3. Unfortunately, because of a difficult positioning of the phantom due to the shape of its container, the two crossing bundles are not parallel to the slice axes. To clarify the visualization of the q -ball data based on color encoding, a rotation around the z -axis has been applied to the data before visualization. Then the orientation of each bundle corresponds to a pure color in the q -ball meshes (green and red). A zoom on the crossing area highlights the additional information provided by the q -ball compared to a tensor model. The diffusion peaks, however, would provide a better angular discrimination with higher b value (q').

For each bundle, the tracking algorithm is fed with a ROI made up of 3 voxels, using 3×130 particles. The particles propagate throughout a mask defined from the T2-weighted image. This mask corresponds to the part of the field of view including the artificial fibers. It was defined from a high threshold on intensity (the voxels including fibers contain less water, which leads to less signal), followed by a morphological closing in order to fill up spurious holes. A slice of the two resulting particle density maps is shown in Figure 3. A threshold of 5 particles is applied to these maps in order to create a mask used to select reliable trajectories. The remaining trajectories do not include any spurious fork in the crossing area.

A second experiment was performed to check that the successful result was not only due to the fact that the phantom bundles have a straight geometry. With such a geometry, indeed, curvature regularization is sufficient for the particles to pass through the crossing area without trouble. For this second experiment, a 20 degree rotation around the z -axis was applied to the q -balls of the crossing area corresponding to the zoom of Figure 3. Then the tracking algorithm was triggered with the same set of particles as for the first experiment using first the initial q -ball field and second the modified field. However, the particles could propagate throughout the whole field (no mask) and no filtering of the trajectories was applied using the particle density map. The results shown in Figure 4 prove that the curvature regularization does not prevent the particle to follow the rotated fiber direction indicated by the q -balls of the crossing area. This observation means that the q -balls of the crossing area are anisotropic enough to oppose the particle inertia.

2.2.3. The mask of propagation

The particles propagate throughout a mask and trajectories stop only when they leave this mask. Thanks to the perfect alignment between the high resolution T1-weighted image and the diffusion dataset, a first refinement of our initial method could be designed: a mask preventing the particle from crossing the cortical folds. This can be achieved using a pipeline of processing dedicated to T1-weighted images and proposed by BrainVISA. A mask of the brain is first defined through bias correction, histogram analysis, and mathematical morphology [57, 58]. Then an homotopic chain of processing is providing a hole-proof skeleton of the cerebrospinal fluid that can be viewed as a negative mold of the brain filling up the folds [41]. A dilation is applied to this skeleton through the addition of its 26-connected neighbors in order to create a wall that particles cannot cross whatever their trajectory. The dilated skeleton is finally removed from the brain mask in order to yield the mask of propagation. A slice of this mask is proposed in Figure 7(a). Because of the 1 mm resolution of T1-weighted images and the minimal 2 mm thickness of the cortex on both sides of the folds, this dilated skeleton does not include any white matter voxel. In fact the mask is made up of the white matter and of a thin layer of cortical grey matter.

2.2.4. Sampling of long fascicles

Let us consider a long fascicle of 5 cm. Let us consider also a particle traveling step by step along this fascicle with 1 mm jumps. Let us assume that the q -balls located along this fascicle always present a very strong peak in the direction of the fascicle. This means that at each step, the sampling of the restricted fiber ODF $F_q(\vec{v}(i))$ providing the next direction to follow has a very high chance to select the actual fascicle direction. However, for the particle to reach the end of the fascicle, this event has to occur 50 times in a row, which is almost impossible except with q -ball close to Dirac distributions. Therefore, even with a very large number of particles, our probabilistic tractography is highly biased toward short range connections. Two refinements of our sampling strategy have been introduced to improve the situation:

- (i) a processus creating child particles while sampling long fascicles supported by high probabilities when drawing from the restricted fiber ODFs;
- (ii) a sharpening of the restricted fiber ODFs: the drawing weight is concentrated around the maximum of the q -ball in the underlying half cone.

The creation of child particles follows an intuitive heuristics, tuned by a threshold on the probability drawn from the restricted fiber ODFs. At each step, the threshold is defined as a percentage of the maximum of $F_q(\vec{v}(i))$. A mother particle fathers a child at each jump as long as the series of probabilities drawn since the beginning of its trajectory remains above the threshold. The mother particle becomes sterile after the first drawing under the threshold. The children are not fertile. Their initial speed is the same as the mother's one. The process is illustrated in Figure 5 using artificial q -ball

fields computed from a random walk simulator briefly described in the appendix [59]. From these simulated crossing bundles, we perform tracking from a ROI located at the left extremity of one of the bundles using different thresholds. For each experiment, a density map is computed: each voxel reports the number of times it has been intersected by a trajectory. Without child birth, the density drops down rapidly with the distance from the initial ROI: most of the particles rapidly quit the bundle. With the child creation process, it is possible to find a threshold compensating the particle lost.

2.2.5. Sharpening the q -ball

Working with q -ball fields raises the issue of the optimal b value for q -ball acquisitions. Increasing the b value, indeed, sharpens the Bessel kernel and increases the ability to resolve distinct diffusion peaks but at the cost of a lower signal-to-noise ratio. The 3000 s/mm² b value used in this paper leads to a very low signal-to-noise with our scanner, that is fortunately compensated by the 200 directions of diffusion sensitization. The resulting q -balls are not focused enough around the putative fiber direction to be used safely as fiber ODF. Therefore, we propose to sharpen the q -ball restriction in inertia half cones in order to build the restricted fiber ODF. For this purpose, $F_q(\vec{v}(i))$ is defined further as

$$F_q(\vec{v}(i))(d) = \frac{1}{N} \exp\left(\frac{1}{S} \frac{\psi(d) - \psi_{\min}}{\psi_{\max} - \psi_{\min}}\right), \quad (3)$$

where S is the sharpening parameter, ψ_{\max} and ψ_{\min} are the extrema of the q -balls in the inertia half cone, and N is a normalizing factor. As S tends to 0, the restricted ODF gets closer to a Dirac function putting most of the sampling weight around the local maximum of the q -ball supposed to indicate the most reliable trajectories. An illustration of the effect of sharpening applied to the q -balls is proposed in Figure 6 thanks to the diffusion simulator described in Appendix. Simulated data with a weighting in diffusion of $b = 700$ s/mm², can be compared to simulated data with higher b value. Decreasing the sharpening parameter, as well as increasing the b value, tends to refine the q -balls to their maxima. It should be noted that our naive sharpening approach will have to be improved, because it is not robust to large differences in the amplitudes of the peaks of the q -ball ODF. A very attractive candidate based on spherical deconvolution has been recently proposed by Descoteaux et al. [23].

Figure 7 shows also the global sharpening of the q -ball on our human diffusion data. It should be noted that our sharpening approach preserves the shape of the q -ball around a local maximum. For instance, a fan of fibers should lead to a crest of high probability, therefore preserving more of the information provided by the fiber ODF than the simple selection of the local maximum. The tuning of the sharpening parameter mixed up with the child creation process is illustrated with simulated data (cf. Figure 8).

In conclusion, this set of refinements improve the behavior of our framework relative to long fibers. In the following, the child creation threshold and the sharpening parameters have been set following our experiment with simulated

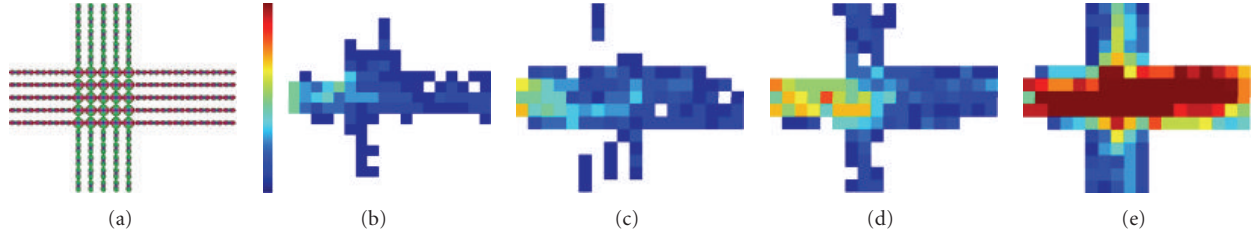


FIGURE 5: Tuning the child particle creation process. Tracking is performed from a ROI of 5×3 voxels located at the left extremity of one of the bundles of the simulated crossing with 4 particles per voxel and different tunings. For each experiment, a density map is computed: each voxel reports the number of times it has been intersected by a trajectory. For one slice of the phantom: (a) q -ball, (b) no child particles. For other experiments, each initial particle fathers a child particle at each step as long as the restricted ODF probability remains above a percentage of the local maximum. (c) Birth threshold of 97%, (d) birth threshold of 95%, (e) birth threshold of 90%.

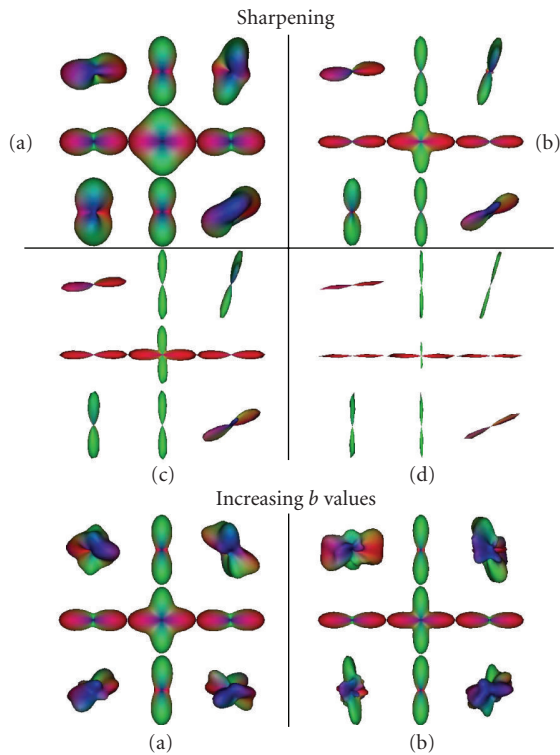


FIGURE 6: Influence of the sharpening parameter on q -balls. Simulated crossing (90 degrees). *Top*: (a) native meshes, $b = 700 \text{ s/mm}^{-2}$. (b) Sharpened meshes with $S = 0.2$. (c) Sharpened meshes with $S = 0.1$. (d) Sharpened meshes with $S = 0.002$. *Bottom*: simulated data with high b values. (a) Native meshes $b = 2000 \text{ s/mm}^{-2}$. (b) Native meshes, $b = 4000 \text{ s/mm}^{-2}$.

phantoms. We are well aware, however, that more careful studies have to be carried on for a better tuning of these parameters in noisy situations. Nevertheless, it should be noted that the most noisy q -balls occur inside grey-matter, where anisotropy is low. Therefore, they should not be able to stand strongly against the particle inertia. It should be noted that the q -ball field visualizations provided in this paper do not always scale the q -ball according to anisotropy (cf. Figure 1). Hence, the grey matter q -balls visibility is sometimes higher than their influence on the tracking process.

2.3. Connectivity-based parcellation

The tractography method introduced above is used to compute the connectivity profiles of all the voxels of the cortical mantle. Similarities between these profiles are used to parcellate the cortex into areas with stable profiles. The parcellation is computed in two steps. The cortex is first parcellated into large gyri, then each gyrus is parcellated into smaller entities according to the profiles of connectivity to the gyral parcellation.

Projecting a parcellation from one anatomical structure toward another using tractography-based connectivity is bound to become a very powerful tool for neuroscience. Its potential has been shown for instance to project a cortical lobar parcellation toward the thalamus [31] or toward the corpus callosum [60]. A very attractive extension of the same idea will consist in projecting areas mapped with functional imaging. Another variant of the idea described in this paper is the “feedback” projection: our clustering aims at parcellating further the initial parcels.

For the two pioneer applications mentioned above, the projection is performed from the parcel with the maximum connectivity strength. In this paper, this “maximum connectivity-strength-” type of projection is used to initialize a non supervised clustering algorithm with a more ambitious objective: the clustering is performed according to similarities between vectors made up of the connectivity-strength with each of the parcels. This objective is mandatory to address the cortex parcellation, because what defines a cortical area is not one but a set of connections [27].

2.3.1. Gyral parcellation

The gyral parcellation used by our method has been computed from the T1-weighted image, using pipelines of processing embedded in BrainVISA framework. The cortical folds are first extracted one by one [61], then a pattern-recognition system made up of 500 multilayer perceptrons gathers the elementary folds to identify the main sulci [62]. For the three brains of this paper, a human expert checked the result of this recognition and performed some manual corrections. Finally, a last pipeline of processing uses the sulci to perform an automatic parcellation of the cortical surface into gyri [35]. This parcellation of the cortical surface

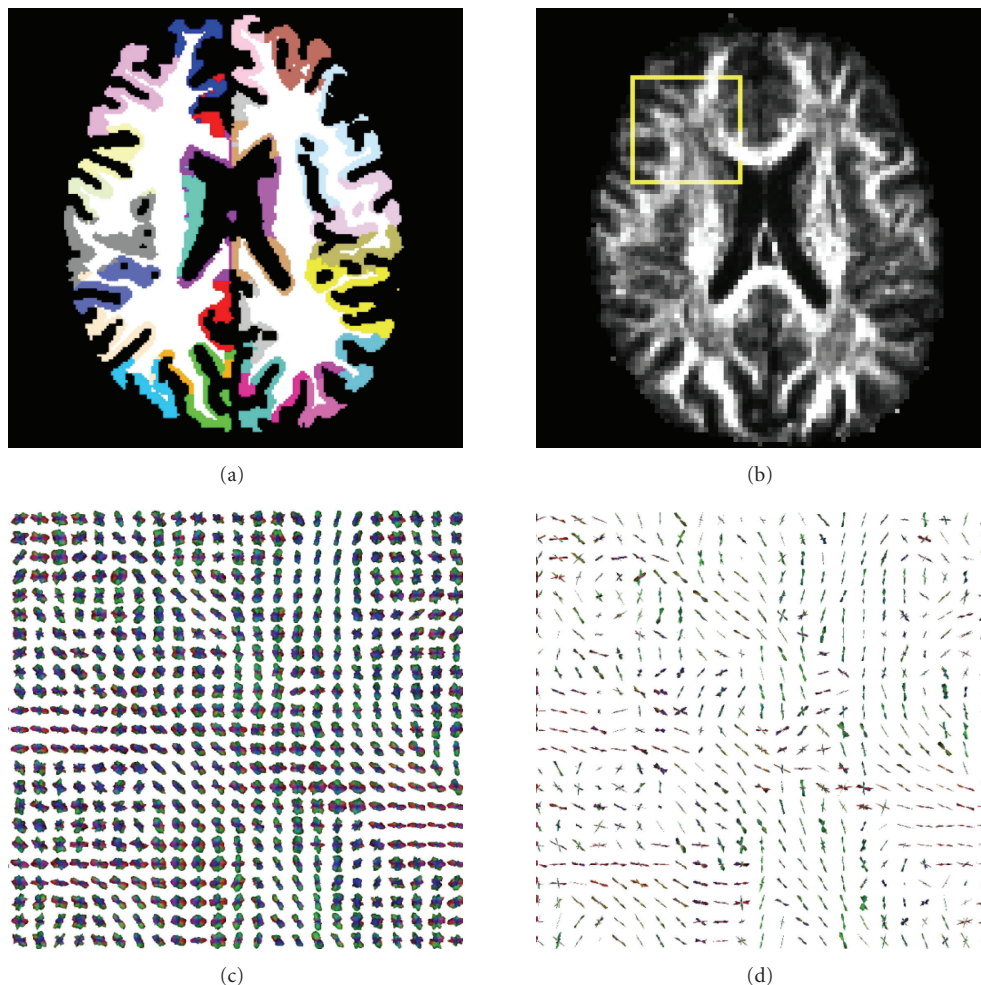


FIGURE 7: Propagation mask and tuning of inertia. (a) A slice of the propagation mask superimposed with the gyral parcellation. (b) Alpha map: alpha is a measure of anisotropy increasing the influence of the q -ball versus the particle inertia. (c) Zoom on the q -ball of the yellow area. (d) Zoom on the q -ball of the yellow area with a global sharpening focusing the distribution weight around the q -ball maximum $S = 0.1$ (it should be noted that during the tracking, the sharpening is performed locally inside a half cone of directions defined by the particle inertia).

projected to the whole cortical mantle using standard techniques of mathematical morphology. A set of views describing the gyral parcellations obtained for the three brains is presented in Figure 9. The result is relatively stable across subjects and hemispheres, although the large variability of the folding patterns and some weaknesses of our system lead to some differences. The color code labelling the 36 gyri is used further in the rest of the paper to describe the projected parcellations.

2.3.2. Connectivity profiles

The parameters of the tractography are the following: the threshold controlling the child creation is 5% and the sharpening parameter is 0.1. For practical reasons, only four mother particles are triggered from each voxel of the cortical mantle defined at the resolution of the T1-weighted image. For a given voxel, the four mother particles father an average of 80 children, and a maximum of 250 children. The

number of voxels making up a gyrus is variable: 25000 voxels for a typical superior parietal gyrus and 45000 for a typical superior frontal gyrus. For practical reasons, the tractography was performed for only 14 of the gyri, covering the external part of frontal and parietal lobes in each hemisphere. The whole computation took four days on a network of 14 computers. For each voxel, we count the number of particles reaching each of the 36 gyri, including mothers and children, in order to build the connectivity profiles. The number corresponding to the gyrus including the voxel is set to zero to discard suspicious particles propagating mainly throughout grey matter.

Considering a gyrus of n voxels, the whole information is gathered into a $p \times n$ connectivity matrix C . The columns of the matrix are normalized for the number of particles in order to get comparable profiles. Hence, a connectivity profile looks like a probability distribution. It is fairly impossible to visualize globally the matrix obtained for one gyrus. We observed that a lot of voxels are connected to more than

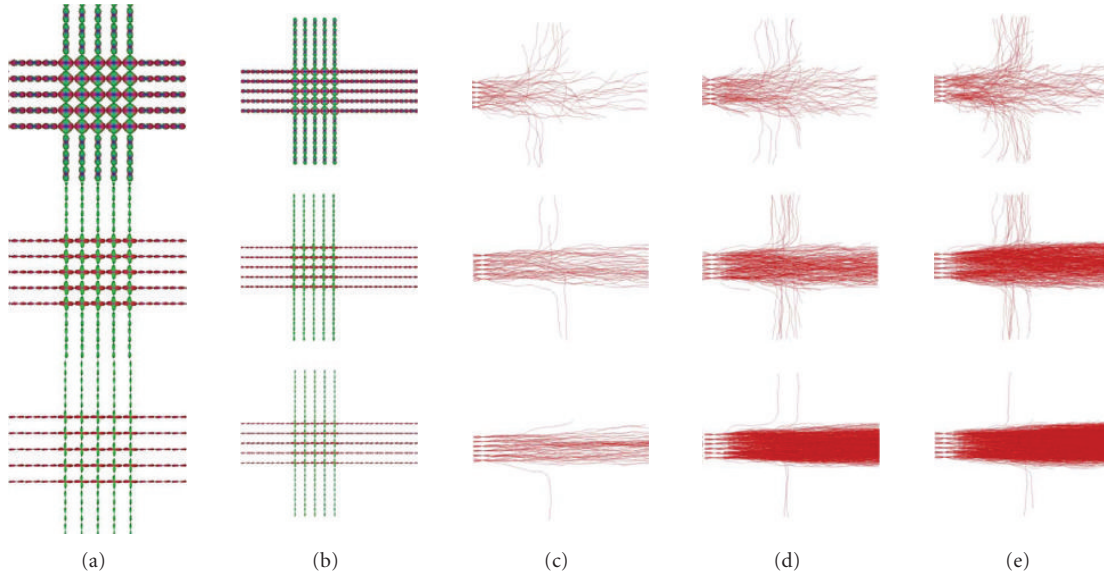


FIGURE 8: Influence of sharpening parameter on q -ball meshes and tracking. Top: no sharpening. Middle: $S = 0.2$. Bottom: $S = 0.1$. (a) q -ball zoom on crossing, (b) slice of q -ball simulated data, (c) no child fibers, (d) threshold birth of 3%, (e) threshold birth of 5%.

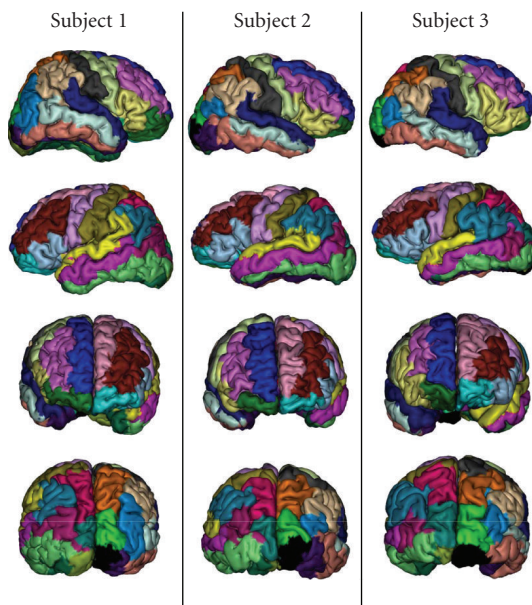


FIGURE 9: External views of the gyral parcellation of the two hemispheres of the three subjects. The color code is used in most of the following figures about connectivity-based parcellation.

one gyrus, which justifies the idea of basing the clustering on the connectivity profiles. To provide a global overview of the tractography, each matrix was averaged to a mean column vector. Gathering the resulting vectors leads to the connectivity matrix of the gyri. The matrices obtained for the three subjects are proposed in Figure 10. They present a lot of similarities across subjects and hemispheres.

A careful observation leads to discovering a specificity of this matrix: the symmetric connectivity strengths estimated

for a pair of gyri, when they are computed, are not necessarily identical. In fact, this is not necessarily a failure of the system. Indeed, these two strengths should be identical only if the connections between both gyri are symmetrical.

2.3.3. Clustering

The unsupervised clustering approach used to gather voxels with similar profiles is based on the classical K -means algorithm associated with a spatial regularization provided by a Markov random field model [63]. In order to stabilize the K -means approach, which is known for its high dependence on initialization, we use the maximum connectivity strength idea mentioned above [31, 60]. Hence, the gyrus is first split in potentially 35 areas, each voxel being associated with the gyrus corresponding to the highest value in its profile. Usually, the actual number of areas is much lower, which can be understood considering the average profile of each gyrus (see Figure 10). The resulting parcellation is especially noisy, which can be visualized in the example provided in Figure 11(b). This observation calls for several possible explanations.

- (1) The poor sampling of white matter performed during the tractography (only four mother particles) could lead to a weak estimation of the maximum strength.
- (2) Many voxels turn out to have several important connections of equivalent strength; hence, in a group of nearby voxels with similar profiles, the winner gyrus could switch randomly between the competing gyri.
- (3) The initial tracking directions provided by the q -balls of cortical grey matter could often be spurious, either because of noise or because of some microstructures of the cortical layers corresponding to tangential myelinated fibers.

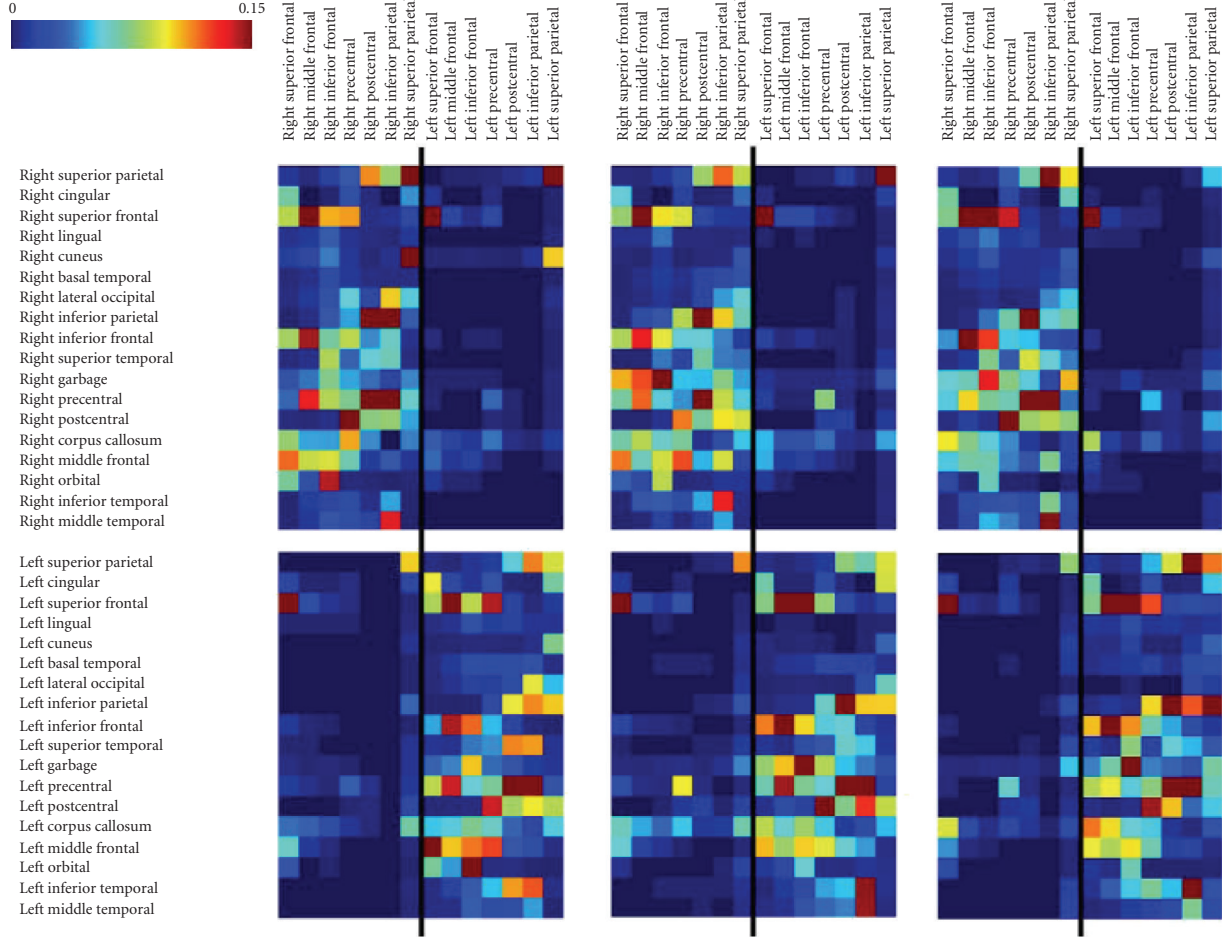


FIGURE 10: Global connectivity matrix of the gyri implied in the tractography (subjects 1, 2, and 3).

These difficulties would benefit a lot from the addition of contextual knowledge in the clustering process, which is done further using a simple model of spatial regularization stemming from the domain of Markov random fields. Furthermore, the second difficulty could be largely overcome by the use of the complete connectivity profiles during the clustering, which is done further by the K -means algorithm. The K largest areas of the maximum connectivity parcelation are used to compute the K initial centroids of the K -means.

Let us note $Y = (y_1, \dots, y_n)$ the observable set corresponding to the data: the normalized connectivity profiles of the n voxels of the gyrus. Let us note $X = (x_1, \dots, x_n)$ the unobservable (hidden) set corresponding to the cluster assignments of the voxels. Each hidden variable x_i denotes the cluster label of the point i and takes values from the set of cluster indices $(1, \dots, K)$. Finally, let $M = (\mu_1, \dots, \mu_K)$ denote the cluster centroids. When considering the conditional probability $p(\cdot | x = h)$, the probability of generating a profile from the h th cluster, we restrict our attention to probability densities from the exponential family, where the expectation parameter corresponding to the h th cluster is μ_h . Using this assumption and the bijection between regular exponential distributions and regular Bregman divergences [64], the

conditional density for observed data, which corresponds to data attachment, can be represented as

$$p(y_s | x_s) \propto \exp(-D(y_s, \mu_s)). \quad (4)$$

In the following, D is the Euclidean distance, but it would be of interest to compare with results obtained using KL-divergence.

The Markovian prior probability of our clustering method is the standard Potts model, which penalizes the number of adjacencies between clusters. This is minimizing the area of each cluster interface hence leading to spatially smooth clusters. This probability is a Gibbs distribution based on potentials acting on the set of cliques of order 2 called C_2 :

$$U_2(x_r, x_s) = -\beta \quad \text{if } x_r = x_s, \\ U_2(x_r, x_s) = +\beta \quad \text{if } x_r \neq x_s. \quad (5)$$

In the following β is fixed to 0.05.

The a posteriori energy whose minimum is the target of the clustering is finally

$$U(x | y) = \sum_{s \in [1, n]} D(y_s, \mu_s) + \sum_{(r, s) \in [1, n]} U_2(x_r, x_s). \quad (6)$$

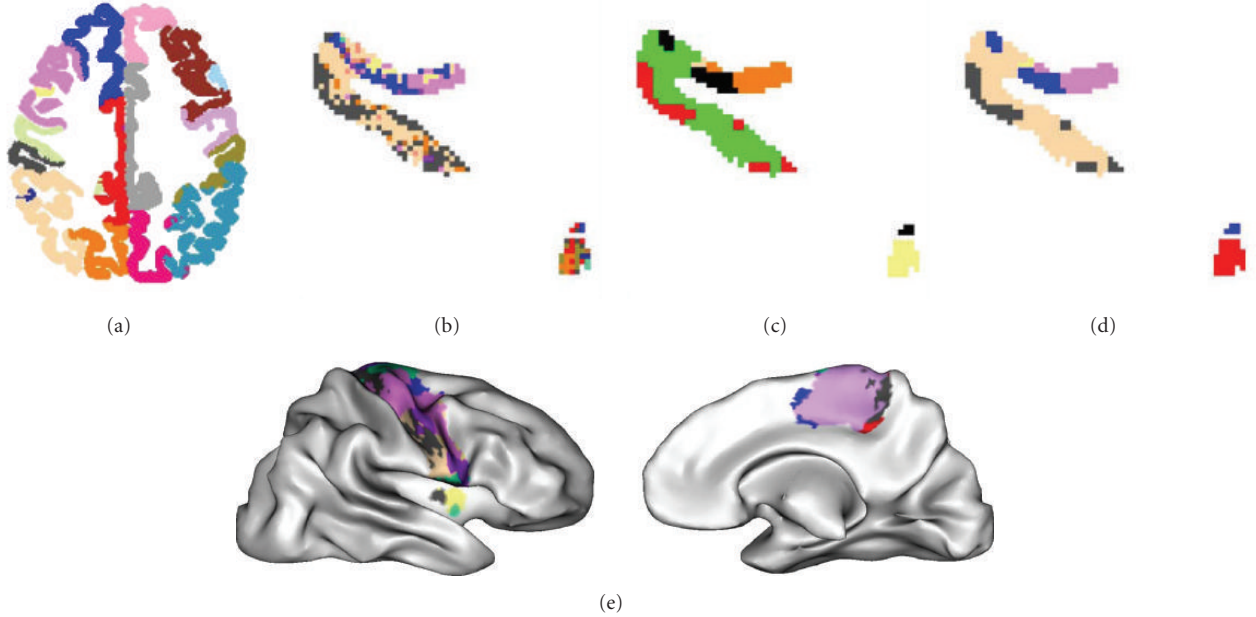


FIGURE 11: Slice results in a precentral right gyrus. (a) Slice location. Precentral gyrus is in light green color, (b) max of connectivity results for the same slice, (c) clustering results for the same slice, (d) clustering result for the same slice with the labelization of the most connected gyrus. Light pink: inferior parietal gyrus, yellow: inferior frontal right gyrus, blue: superior frontal right gyrus, purple: medial frontal, gray: postcentral right gyrus. (e) 3D projection of the clustering with labeling of the most connected gyrus.

This energy is minimized alternating the standard ICM algorithm and the centroid update. The initial centroids are the average profiles of the K largest areas of the max-connectivity parcellation.

- (i) Initialize the k clusters centroids $M = (\mu_1, \dots, \mu_K)$.
- (ii) Repeat until convergence.
 - (a) Given centroids $M = (\mu_1, \dots, \mu_K)$, reassign cluster labels to minimize U using ICM.
 - (b) Given cluster labels, recalculate centroids M .

Voxels with no starting particles or whose particles end their trajectory in the starting gyrus have no data attachment and do not contribute to centroid computation. For the sake of simplicity, for all the results presented in this paper, each gyrus has been split using a K -means with ten clusters. The spatial regularization term sometimes reduces the final number of clusters. The fact that a frequent profile including more than one strong connection may be split into two clusters during initialization and merged back during the K -means can also reduce the final number of clusters. But we have no reason to expect that our procedure systematically performs a successful split and merge, which will be discussed further later on. Exploring techniques to adapt the number of initial clusters to each of the gyri is difficult and beyond the scope of the paper. Number ten was chosen because it was larger than the number of significant parcels obtained by the max-connectivity clustering for most of the gyri. An additional motivation was the fact that standard architectonic parcellations do not split the gyri of our macroscopic parcellation into more than ten areas. The denoising

of the max-connectivity parcellation obtained by our non-supervised regularized clustering is illustrated in Figure 11.

3. RESULTS

3.1. Color coding the parcellation

In the following, we illustrate the method developed in this paper through a study of the reproducibility of the parcellation across three subjects. The seven gyri parcellated in each hemisphere are the three elongated gyri of the external part of the frontal lobe, called superior, medial, and inferior (F3, F2, and F1 in monkey literature), the precentral (motor) and postcentral (somesthetic) gyri, the superior and inferior parts of the external parietal lobes. The results of such a 3D parcellation are especially difficult to visualize or compare. To simplify the comparison across subjects, we have decided to label each cluster with the color of the most connected gyrus, using the color code introduced in Figure 9. This color code has some limitations: some cluster boundaries are hidden, either because the stereotype profile of two neighboring clusters share the same maximum, or because two neighboring clusters belong to two different gyri.

3.2. 3D projections

The second choice has been to develop a method to present the results in 3D. For this purpose, a spherical mesh representing the grey/white interface is computed using BrainVISA [41]. This mesh is slightly inflated in order to preserve only the largest folds corresponding to the main boundaries

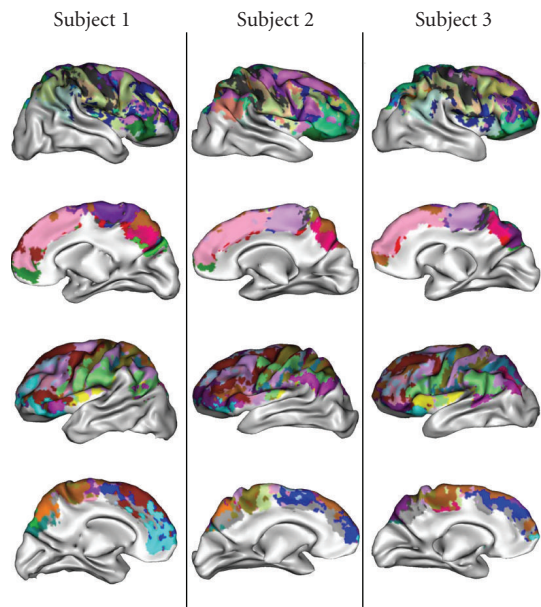


FIGURE 12: Projection of the parcellation with cluster colors corresponding to the most connected gyrus.

between the macroscopic gyri. Then the node of the mesh is colored with the label of the closest parcellation voxel. This projection provides an interesting glimpse of the global parcellation but hides a lot of information when several clusters compete to color a mesh node. This method has been applied to the three subjects to build the Figure 12. The similarities observed across subjects are relatively encouraging, but some severe differences are observed for some clusters. We will see further that these differences result from weaknesses of our color coding, when a stereotype profile includes two equivalent strong connections.

3.3. Spatial normalization

While the method described in this paper aims at developing structural representations of the cortex supposed to overcome some weaknesses of the standard spatial normalization framework, we have tried to support the comparison of subjects using brain alignment. Affine transformation aligning the T1-weighted image of each of the subjects toward a corresponding template was computed using SPM2 [65]. These transformations were applied to the parcellations of the cortical mantles using a nearest neighbor interpolator. Finally, for each pair of subjects and for the triplet of subjects, the intersections of the parcellations were computed. The result of such an intersection includes only voxels with the same colors in the compared parcellations. Each of these intersections are projected on one of the compared brains in Figure 13. This figure highlights a lot of similarities when comparing 2 subjects, and a sharp decline with three subjects (cf. Figure 13). This decline is partly due to nonperfect spatial normalization, but also largely to the color-code problem already mentioned above.

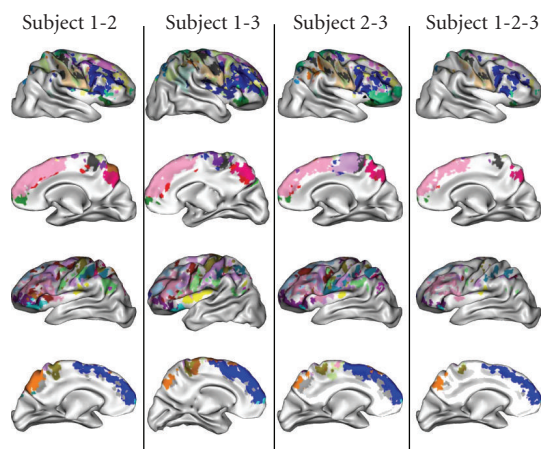


FIGURE 13: Intersection of the color-coded parcellations after affine spatial normalization.

To help the decoding of the anatomical information embedded in our color code, we collected the list of connections surviving after the intersection of the three subjects.

Frontal projections

Frontal superior gyri project in inferior frontal, in precentral, in orbital frontal, and in cingular gyri of the same hemisphere and in frontal superior gyrus of the other hemisphere via corpus callosum. Furthermore, right superior frontal gyrus projects in right middle frontal gyrus. Medial frontal gyri project in inferior and superior frontal gyri and in precentral gyrus of the same hemisphere. Inferior frontal gyri project toward superior frontal and orbital frontal gyri of the same hemisphere. Right inferior frontal gyrus has additional connections in right lingual and right superior temporal gyrus. Left inferior frontal gyrus project in precentral left gyrus.

Precentral projections

Precentral gyri project in superior and medial frontal and in postcentral gyri. Right precentral gyrus has additional connections in right inferior frontal, right inferior parietal, and right precentral gyri. Left precentral gyrus projects in left inferior temporal gyrus and in right precentral gyrus via the corpus callosum.

Postcentral projections

Postcentral gyrus projects toward inferior parietal, superior temporal, and precentral gyri of the same hemisphere. Right postcentral gyrus projects in right inferior frontal, left postcentral gyrus projects in left superior parietal gyrus.

Parietal projections

Right superior parietal gyrus projects in occipital lateral and precentral gyri of the same hemisphere and in left superior parietal gyrus via corpus callosum. Left superior parietal

gyrus connects cingular, postcentral and inferior parietal of the same hemisphere and right superior parietal via corpus callosum. Right and left inferior parietal gyri have main connections in superior parietal and precentral gyri of the same hemisphere. Furthermore, right superior parietal gyrus has connections in occipital lateral and middle temporal gyri of the right hemisphere; left inferior parietal gyrus has also connections in left inferior and superior temporal gyri.

3.4. Matching clusters across subjects

We mentioned already that the simple-color coding proposed above to compare the parcellations has some flaws with profiles including several strong connections. We will now illustrate this aspect with two examples. Let us first consider the top of the right precentral gyrus in the internal face presented in the second row of Figure 12. We observe a large dark violet cluster for subject 1. For the two other subjects, however, we observe a large light violet cluster, surrounded by a few dark violet points. To understand this configuration, we computed the matrix of profiles of the right precentral gyrus for each of the subjects (cf. Figure 14). Since this gyrus is made up of more than 30000 voxels, the snapshots expose only a few profiles picked up randomly. The profiles are ranked according to the result of the clustering. The ten clusters of subject 1 are underlined. The five dark and light violet clusters mentioned above are highlighted in the profile matrices. It can be observed that the profiles of these five clusters are very similar, presenting several strong connections with the same gyri. The most connected gyrus, however, is not the same for each of the subjects. This observation can be confirmed quantitatively by comparing the average profiles across subject using the dual KL divergence, a measure of distance between probability distributions. The charts provide the distances of the violet clusters of subjects 2 and 3 to each cluster of subject 1. The dark violet cluster of subject 1 turns out to be each time the closest one, which shows that the five clusters should be matched as corresponding to the same anatomical entity. The main connections of this entity are the gyrus located above corpus callosum, the left postcentral gyrus and the left superior frontal gyrus.

4. DISCUSSION AND CONCLUSION

The method exposed in this paper is still largely exploratory, relying on several parameters whose influence should be studied. However, the new opportunities for neuroscience provided by the connectivity-based parcellation paradigm are very attractive [31, 32, 34, 60] and we need to push the exploration as far as possible before tuning the method. It is too early to decide if the connectivity matrices and the parcellations inferred from our framework are meaningful, but their level of reproducibility across subjects is impressive. It should be noted that according to anatomical knowledge, architectonic areas can double or triple in size from one subject to another [28]. Therefore, there is no simple way to quantify

the reproducibility of our parcellations. The mandatory approach will be a correlation of such connectivity-based parcellations with mappings obtained from functional imaging or postmortem anatomical studies [27, 32].

In our opinion, despite our care to improve the sampling of long bundles, an important weakness of our framework is the bias of our probabilistic tractography for the short tracts, which could explain the small amount of inter-hemispheric connections. This bias stems from the way we introduced the trajectory regularization in our framework, requiring the particles to follow the fascicles from the beginning to the end. Some local regularization could be designed to overcome the problem, extending the method initially introduced by Behrens et al. [12], or using the spin glass framework introduced by our group [10, 15]. Another solution could be provided by the normalization of the connectivity strength relative to the path length [34] or using more sophisticated models of the length dependence [66].

An alternative to the probabilistic framework for the computation of the connectivity profiles lies in the methods based on front propagation assimilating the tracts to geodesics [67–69]. While these methods seem prohibitively expensive for the computation of the one million connectivity profiles used in this paper, they do not suffer from the sampling weaknesses of our particle-based approach. Furthermore, the sampling used in this paper for cortical mantle is unrealistic relative to the spatial resolution of the diffusion data. Therefore, dealing with a more reasonable sampling of the cortex is one of the key future refinements of our method. Considering that the current spatial resolution of diffusion data cannot give access to the myeloarchitecture of the cortical layers, an attractive solution would be to address the parcellation of a spherical model of the cortical surface [28], following the approach proposed in [70] to align connectivity matrices. The surface-based approach would largely reduce the number of connectivity profiles to be clustered. Surface-based analysis would overcome the piling up of different clusters orthogonally to the cortical surface. A surface-based 2D model for Markovian regularization would be more reliable than our 3D approach depending on the sampling of the cortical mantle in the direction orthogonal to the surface. The initial starting speed could be defined by the surface normal, and the visualization of the parcellation would be straightforward. Finally, this approach would fit the current knowledge of the columnar organization of the cortex: the large scale connectivity is shared by small groups of neurons organized orthogonally to the cortical surface [27, 71].

Our framework for clustering requires an input parcellation whose influence on the result can be discussed a lot. However, whatever the weaknesses of the input parcellation, we would like to advocate that basing the clustering on similarities between profiles of connectivity with a parcellation rather than the whole brain, like in the work of the Oxford group mentioned in the introduction, can lead to two very different almost orthogonal results [32]. This is illustrated by Figure 15, which depicts a synthetic system of three areas linked by a retinotopic-like network of connections. A clustering based on the profiles of connectivity with the whole brain will gather voxels with similar retinotopic coordinates.

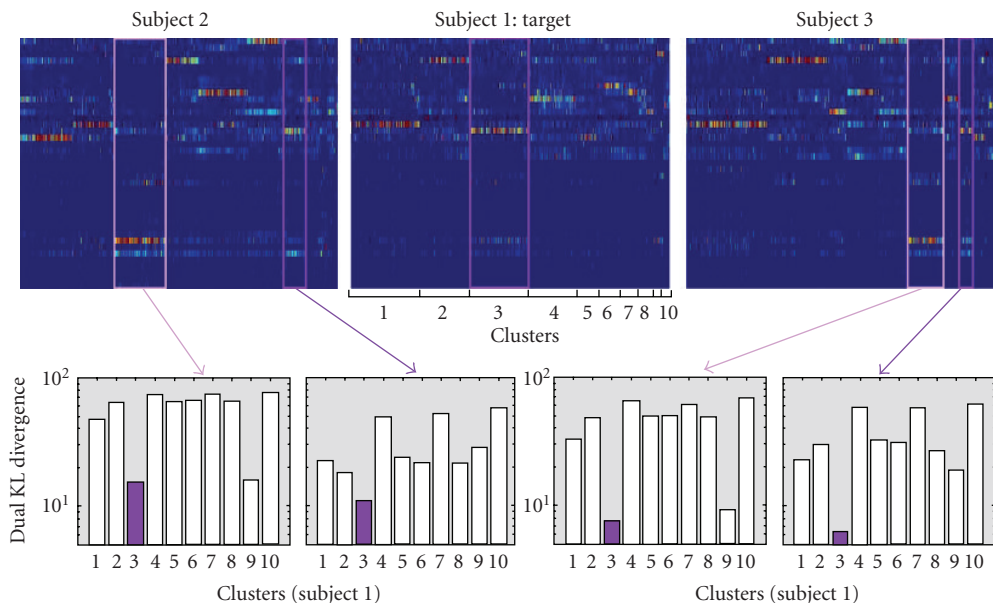


FIGURE 14: Matching clusters of the precentral gyrus across subjects using distance between mean connectivity profiles provided by dual KL divergence (see text).

In return, if the three retinotopic areas belong to different parcels of the initial large scale parcellation, a clustering based on the profiles of connectivity with this parcellation will split the system into the three areas (areas blue, yellow, and red). This example illustrates the richness of the world of possibilities offered by the connectivity-based parcellation paradigm.

Following the previous discussion, the dependence of the output parcellation on the input parcellation, provided that this one can be defined in a reproducible way across subjects, is a richness rather than a problem. It should be noted also that the idea of performing a feedback projection from one parcellation to itself can be iterated. This could be interesting to perform some hierarchical parcellation. Adding a merging step between each iteration, in order to gather neighboring clusters with similar profiles, could help to reduce the influence of the initial parcellation. For instance, it could be used to overcome some inadequations of the macroscopic parcellation relatively to the actual architecture. It could also correct some failures of the process defining the gyri occurring for subjects with unusual cortical folding patterns. Finally, this iterative process would turn into a split and merge principle famous in the field of computer vision.

The split and merge approach may be the perfect tool to improve the robustness of the parcellation framework. But the real challenge for the future will be to design a split and merge process acting on a group of brains, defining the clusters across subjects or matching the individual clusters according to their similarities, as performed above using the dual KL divergence. Group analysis, indeed, seems to be the only way to discard the various bias and artifacts disturbing the tractography and the clustering of the profiles. In our opinion, the usual spatial normalization paradigm will not

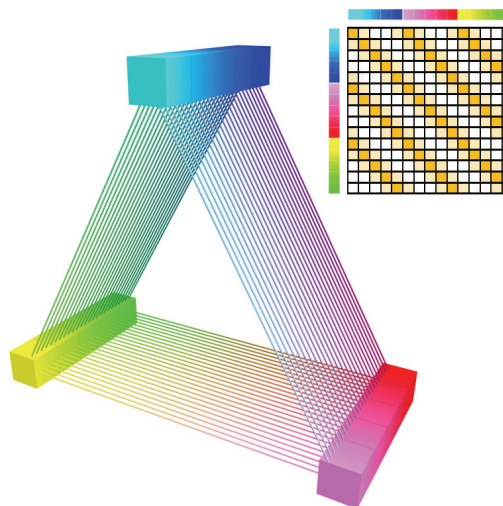


FIGURE 15: A synthetic retinotopic-like network of three areas and its connectivity matrix. A clustering based on the profiles of connectivity with the whole brain will gather voxels with similar retinotopic coordinates (light colors with light colors, dark colors with dark colors). In return, if the three retinotopic areas belong to different parcels of a large scale parcellation, a clustering based on the profiles of connectivity with this parcellation will split the system into the three areas.

be sufficient to perform this kind of group analysis: dealing with brain architecture requires a group analysis performed at a structural level [72]. For this purpose, the ideal units relatively to the human brain connectome [27] could correspond to the connectivity-based clusters described in this paper.

APPENDIX

SIMULATED RANDOM WALK

We have developed a simulation environment limited to tissue made up of tubular fibers and water molecules moving inside and outside fibers [59]. Water molecules follow a Brownian motion and when a particle meets a fiber membrane, it reflects elastically against its surface. This numerical phantom is built from 82 layers of 82 parallel fibers forming two bundles crossing at 90 degrees (diameter $5\ \mu\text{m}$, interspace $2\ \mu\text{m}$). The distance between two consecutive random displacements is set to $1\ \mu\text{m}$ with a duration of 82.5 microseconds. Particles are submitted to a Stejskal-Tanner diffusion sensitizations ($\delta = 17.2$ milliseconds, $\Delta = 26.4$ milliseconds) with a gradient magnitude of 40 mT/m and a b value of $700\ \text{s}/\text{mm}^{-2}$. With this simulator we get q -ball with single fiber population along x - and y -axes and crossing q -ball with both fiber population ($3 \times 3 \times 3$ dimension data). We duplicate these data in order to build a $18 \times 15 \times 5$ dataset with a resolution of $1 \times 1 \times 1\ \text{mm}^3$.

ACKNOWLEDGMENTS

The data used in this paper are part of the NMR database, which is the property of CEA Neurospin and can be provided on demand to cyril.poupon@cea.fr. Data were acquired with NMR pulse sequences, reconstructed with NMR reconstructor package and postprocessed with AIMS/Anatomist/BrainVISA software, freely available at <http://brainvisa.info>.

REFERENCES

- [1] P. J. Basser, J. Mattiello, and D. Le Bihan, "Estimation of the effective self-diffusion tensor from the NMR spin echo," *Journal of Magnetic Resonance, Series B*, vol. 103, no. 3, pp. 247–254, 1994.
- [2] S. Mori, B. J. Crain, V. P. Chacko, and P. C. M. Van Zijl, "Three-dimensional tracking of axonal projections in the brain by magnetic resonance imaging," *Annals of Neurology*, vol. 45, no. 2, pp. 265–269, 1999.
- [3] P. J. Basser, S. Pajevic, C. Pierpaoli, J. Duda, and A. Aldroubi, "In vivo fiber tractography using DT-MRI data," *Magnetic Resonance in Medicine*, vol. 44, no. 4, pp. 625–632, 2000.
- [4] T. E. Conturo, N. F. Lori, T. S. Cull, et al., "Tracking neuronal fiber pathways in the living human brain," *Proceedings of the National Academy of Sciences of the United States of America*, vol. 96, no. 18, pp. 10422–10427, 1999.
- [5] O. Coulon, D. C. Alexander, and S. Arridge, "Diffusion tensor magnetic resonance image regularization," *Medical Image Analysis*, vol. 8, no. 1, pp. 47–67, 2004.
- [6] C.-F. Westin, S. E. Maier, H. Mamata, A. Nabavi, F. A. Jolesz, and R. Kikinis, "Processing and visualization for diffusion tensor MRI," *Medical Image Analysis*, vol. 6, no. 2, pp. 93–108, 2002.
- [7] D. Tschumperlé and R. Deriche, "Orthonormal vector sets regularization with PDE's and applications," *International Journal of Computer Vision*, vol. 50, no. 3, pp. 237–252, 2002.
- [8] P. Filiard, X. Pennec, V. Arsigny, and N. Ayache, "Clinical DT-MRI estimation, smoothing, and fiber tracking with log-euclidean metrics," *IEEE Transactions on Medical Imaging*, vol. 26, no. 11, pp. 1472–1482, 2007.
- [9] Z. Wang, B. C. Vemuri, Y. Chen, and T. Mareci, "Simultaneous smoothing and estimation of the tensor field from diffusion tensor MRI," in *Proceedings of the IEEE Computer Society Conference on Computer Vision and Pattern Recognition (CVPR '03)*, vol. 1, pp. 461–466, Madison, Wis, USA, June 2003.
- [10] C. Poupon, C. A. Clark, V. Frouin, et al., "Regularization of diffusion-based direction maps for the tracking of brain white matter fascicles," *NeuroImage*, vol. 12, no. 2, pp. 184–195, 2000.
- [11] M. Lazar, D. M. Weinstein, J. S. Tsuruda, et al., "White matter tractography using diffusion tensor deflection," *Human Brain Mapping*, vol. 18, no. 4, pp. 306–321, 2003.
- [12] T. E. J. Behrens, M. W. Woolrich, M. Jenkinson, et al., "Characterization and propagation of uncertainty in diffusion-weighted MR imaging," *Magnetic Resonance in Medicine*, vol. 50, no. 5, pp. 1077–1088, 2003.
- [13] G. J. M. Parker and D. C. Alexander, "Probabilistic anatomical connectivity derived from the microscopic persistent angular structure of cerebral tissue," *Philosophical Transactions of the Royal Society B*, vol. 360, no. 1457, pp. 893–902, 2005.
- [14] A. Ramirez-Manzanares and M. Rivera, "Basis tensor decomposition for restoring intra-voxel structure and stochastic walks for inferring brain connectivity in DT-MRI," *International Journal of Computer Vision*, vol. 69, no. 1, pp. 77–92, 2006.
- [15] J.-F. Mangin, C. Poupon, Y. Cointepas, et al., "A framework based on spin glass models for the inference of anatomical connectivity from diffusion-weighted MR data—a technical review," *NMR in Biomedicine*, vol. 15, no. 7-8, pp. 481–492, 2002.
- [16] J.-D. Tournier, F. Calamante, D. G. Gadian, and A. Connelly, "Direct estimation of the fiber orientation density function from diffusion-weighted MRI data using spherical deconvolution," *NeuroImage*, vol. 23, no. 3, pp. 1176–1185, 2004.
- [17] J.-D. Tournier, F. Calamante, and A. Connelly, "Robust determination of the fibre orientation distribution in diffusion MRI: non-negativity constrained super-resolved spherical deconvolution," *NeuroImage*, vol. 35, no. 4, pp. 1459–1472, 2007.
- [18] F. Dell'Acqua, G. Rizzo, P. Scifo, R. A. Clarke, G. Scotti, and F. Fazio, "A model-based deconvolution approach to solve fiber crossing in diffusion-weighted MR imaging," *IEEE Transactions on Biomedical Engineering*, vol. 54, no. 3, pp. 462–472, 2007.
- [19] E. Kaden, T. R. Knösche, and A. Anwender, "Parametric spherical deconvolution: inferring anatomical connectivity using diffusion MR imaging," *NeuroImage*, vol. 37, no. 2, pp. 474–488, 2007.
- [20] B. Jian, B. C. Vemuri, E. Özarslan, P. R. Carney, and T. H. Mareci, "A novel tensor distribution model for the diffusion-weighted MR signal," *NeuroImage*, vol. 37, no. 1, pp. 164–176, 2007.
- [21] T. E. J. Behrens, H. J. Berg, S. Jbabdi, M. F. S. Rushworth, and M. W. Woolrich, "Probabilistic diffusion tractography with multiple fibre orientations: what can we gain?" *NeuroImage*, vol. 34, no. 1, pp. 144–155, 2007.
- [22] M. Descoteaux, E. Angelino, S. Fitzgibbons, and R. Deriche, "Regularized, fast, and robust analytical q -ball imaging," *Magnetic Resonance in Medicine*, vol. 58, no. 3, pp. 497–510, 2007.
- [23] M. Descoteaux, R. Deriche, and A. Anwender, "Deterministic and probabilistic q -ball tractography: from diffusion to sharp fiber distributions," Research Report 6273, INRIA, Sophia Antipolis, France, 2007.

- [24] D. S. Tuch, T. G. Reese, M. R. Wiegell, and V. J. Wedeen, "Diffusion MRI of complex neural architecture," *Neuron*, vol. 40, no. 5, pp. 885–895, 2003.
- [25] D. S. Tuch, "Q-ball imaging," *Magnetic Resonance in Medicine*, vol. 52, no. 6, pp. 1358–1372, 2004.
- [26] F. Crick and E. Jones, "Backwardness of human neuronatomy," *Nature*, vol. 361, pp. 109–110, 1993.
- [27] O. Sporns, G. Tononi, and R. Kötter, "The human connectome: a structural description of the human brain," *PLoS Computational Biology*, vol. 1, no. 4, p. e42, 2005.
- [28] D. C. Van Essen, H. A. Drury, S. Joshi, and M. I. Miller, "Functional and structural mapping of human cerebral cortex: solutions are in the surfaces," *Proceedings of the National Academy of Sciences of the United States of America*, vol. 95, no. 3, pp. 788–795, 1998.
- [29] D. J. Felleman and D. C. Van Essen, "Distributed hierarchical processing in the primate cerebral cortex," *Cerebral Cortex*, vol. 1, no. 1, pp. 1–47, 1991.
- [30] R. E. Passingham, K. E. Stephan, and R. Kötter, "The anatomical basis of functional localization in the cortex," *Nature Reviews Neuroscience*, vol. 3, no. 8, pp. 606–616, 2002.
- [31] T. E. J. Behrens, H. Johansen-Berg, M. W. Woolrich, et al., "Non-invasive mapping of connections between human thalamus and cortex using diffusion imaging," *Nature Neuroscience*, vol. 6, no. 7, pp. 750–757, 2003.
- [32] H. Johansen-Berg, T. E. J. Behrens, M. D. Robson, et al., "Changes in connectivity profiles define functionally distinct regions in human medial frontal cortex," *Proceedings of the National Academy of Sciences of the United States of America*, vol. 101, no. 36, pp. 13335–13340, 2004.
- [33] J. C. Klein, T. E. J. Behrens, M. D. Robson, C. E. Mackay, D. J. Higham, and H. Johansen-Berg, "Connectivity-based parcellation of human cortex using diffusion MRI: establishing reproducibility, validity and observer independence in BA 44/45 and SMA/pre-SMA," *NeuroImage*, vol. 34, no. 1, pp. 204–211, 2007.
- [34] A. Anwender, M. Tittgemeyer, D. Y. von Cramon, A. D. Friederici, and T. R. Knösche, "Connectivity-based parcellation of Broca's area," *Cerebral Cortex*, vol. 17, no. 4, pp. 816–825, 2007.
- [35] A. Cachia, J.-F. Mangin, D. Rivière, et al., "A generic framework for the parcellation of the cortical surface into gyri using geodesic Voronoi diagrams," *Medical Image Analysis*, vol. 7, no. 4, pp. 403–416, 2003.
- [36] W. Welker, "Why does cerebral cortex fissure and fold?" in *Cerebral Cortex*, vol. 8B, pp. 3–136, Plenum Press, New York, NY, USA, 1988.
- [37] B. Fischl, N. Rajendran, E. Busa, et al., "Cortical folding patterns and predicting cytoarchitecture," to appear in *Cerebral Cortex*.
- [38] D. C. Van Essen, "A tension-based theory of morphogenesis and compact wiring in the central nervous system," *Nature*, vol. 385, no. 6614, pp. 313–318, 1997.
- [39] C. Poupon, F. Poupon, L. Allirol, et al., "NMR: a free database dedicated to the anatomo-functional study of the human brain connectivity," in *Proceedings of the 12th Annual Meeting of the Organization for Human Brain Mapping (HBM '06)*, Florence, Italy, June 2006.
- [40] M. Perrin, C. Poupon, Y. Cointepas, et al., "Fiber tracking in q-ball fields using regularized particle trajectories," in *Proceedings of the 19th International Conference on Information Processing in Medical Imaging (IPMI '05)*, pp. 52–63, Glenwood Springs, Colo, USA, July 2005.
- [41] J.-F. Mangin, V. Frouin, I. Bloch, J. Régis, and J. López-Krahe, "From 3D magnetic resonance images to structural representations of the cortex topography using topology preserving deformations," *Journal of Mathematical Imaging and Vision*, vol. 5, no. 4, pp. 297–318, 1995.
- [42] P. Jezzard and R. S. Balaban, "Correction for geometric distortion in echo planar images from B0 field variations," *Magnetic Resonance in Medicine*, vol. 34, no. 1, pp. 65–73, 1995.
- [43] G. Dennis, C. Ghiglia, and M. D. Pritt, *Two-Dimensional Phase Unwrapping: Theory, Algorithms, and Software*, Wiley Interscience, New York, NY, USA, 1998.
- [44] K. M. Jansons and D. C. Alexander, "Persistent angular structure: new insights from diffusion magnetic resonance imaging data," *Inverse Problems*, vol. 19, no. 5, pp. 1031–1046, 2003.
- [45] D. S. Tuch, T. G. Reese, M. R. Wiegell, N. Makris, J. W. Belliveau, and V. J. Wedeen, "High angular resolution diffusion imaging reveals intravoxel white matter fiber heterogeneity," *Magnetic Resonance in Medicine*, vol. 48, no. 4, pp. 577–582, 2002.
- [46] G. J. M. Parker and D. C. Alexander, "Probabilistic Monte Carlo based mapping of cerebral connections utilising whole-brain crossing fibre information," in *Proceedings of the 18th International Conference on Information Processing in Medical Imaging (IPMI '03)*, vol. 18, pp. 684–695, Ambleside, UK, July 2003.
- [47] V. J. Wedeen, T. G. Reese, D. S. Tuch, et al., "Mapping fiber orientation spectra in cerebral white matter with fourier-transform diffusion," in *Proceedings of the 8th Annual Meeting of the International Society for Magnetic Resonance in Medicine (ISMRM '00)*, p. 82, Denver, Colo, USA, April 2000.
- [48] P. Hagmann, M. Kuran, X. Gigandet, et al., "Mapping human whole-brain structural networks with diffusion MRI," *PLoS ONE*, vol. 2, no. 3, p. e597, 2007.
- [49] K.-H. Cho, C.-H. Yeh, Y.-P. Chao, J.-H. Chen, and C.-P. Lin, "Accuracy assessment of q-ball imaging with phantom models," in *Proceedings of the 14th Annual Meeting of the International Society for Magnetic Resonance in Medicine (ISMRM '06)*, p. 642, Seattle, Wash, USA, May 2006.
- [50] Y.-C. Li, K.-H. Cho, K.-H. Chou, and C.-P. Lin, "Optimal imaging parameters for minimum angular discrimination in diffusion spectrum imaging," in *Proceedings of the 14th Annual Meeting of the International Society for Magnetic Resonance in Medicine (ISMRM '06)*, p. 644, Seattle, Wash, USA, May 2006.
- [51] C.-P. Lin, V. J. Wedeen, J.-H. Chen, C. Yao, and W.-Y. I. Tseng, "Validation of diffusion spectrum magnetic resonance imaging with manganese-enhanced rat optic tracts and ex vivo phantoms," *NeuroImage*, vol. 19, no. 3, pp. 482–495, 2003.
- [52] M. Perrin, C. Poupon, B. Rieul, et al., "Validation of q-ball imaging with a diffusion fibre-crossing phantom on a clinical scanner," *Philosophical Transactions of the Royal Society B*, vol. 360, no. 1457, pp. 881–891, 2005.
- [53] J. S. W. Campbell, K. Siddiqi, V. V. Rymar, A. F. Sadikot, and G. B. Pike, "Flow-based fiber tracking with diffusion tensor and q-ball data: validation and comparison to principal diffusion direction techniques," *NeuroImage*, vol. 27, no. 4, pp. 725–736, 2005.
- [54] L. A. Frank, "Anisotropy in high angular resolution diffusion-weighted MRI," *Magnetic Resonance in Medicine*, vol. 45, no. 6, pp. 935–939, 2001.
- [55] E. O. Stejskal and J. E. Tanner, "Spin diffusion measurements: spin echoes in the presence of a time-dependent field gradient," *Journal of Chemical Physics*, vol. 42, no. 1, pp. 288–292, 1965.

- [56] J.-F. Mangin, C. Poupon, C. A. Clark, D. Le Bihan, and I. Bloch, "Distortion correction and robust tensor estimation for MR diffusion imaging," *Medical Image Analysis*, vol. 6, no. 3, pp. 191–198, 2002.
- [57] J.-F. Mangin, "Entropy minimization for automatic correction of intensity nonuniformity," in *IEEE Workshop on Mathematical Methods in Biomedical Image Analysis (MMBIA '00)*, pp. 162–169, IEEE Press, Hilton Head Island, SC, USA, June 2000.
- [58] J.-F. Mangin, O. Coulon, and V. Frouin, "Robust brain segmentation using histogram scale-space analysis and mathematical morphology," in *Proceedings of the 1st International Conference on Medical Image Computing and Computer-Assisted Intervention (MICCAI '98)*, vol. 1496 of *Lecture Notes in Computer Science*, pp. 1230–1241, Springer, Cambridge, Mass, USA, October 1998.
- [59] M. Perrin, C. Poupon, D. Rivière, A. Constantinesco, D. Le Bihan, and J.-F. Mangin, "Q-ball imaging simulation with a numerical diffusion fiber crossing phantom," in *Proceedings of the 12th Annual Meeting of the Organization for Human Brain Mapping (HBM '06)*, Florence, Italy, June 2006.
- [60] H. Huang, J. Zhang, H. Jiang, et al., "DTI tractography based parcellation of white matter: application to the mid-sagittal morphology of corpus callosum," *NeuroImage*, vol. 26, no. 1, pp. 195–205, 2005.
- [61] J.-F. Mangin, D. Rivière, A. Cachia, et al., "Object-based morphometry of the cerebral cortex," *IEEE Transactions on Medical Imaging*, vol. 23, no. 8, pp. 968–982, 2004.
- [62] D. Rivière, J.-F. Mangin, D. Papadopoulos-Orfanos, J.-M. Martinez, V. Frouin, and J. Régis, "Automatic recognition of cortical sulci of the human brain using a congregation of neural networks," *Medical Image Analysis*, vol. 6, no. 2, pp. 77–92, 2002.
- [63] S. Basu, *Semi-supervised clustering: probabilistic models, algorithms and experiments*, Ph.D. thesis, University of Texas, Austin, Tex, USA, 2005.
- [64] A. Banerjee, S. Merugu, I. S. Dhillon, and J. Ghosh, "Clustering with Bregman divergences," in *Proceedings of the 4th SIAM International Conference on Data Mining (SDM '04)*, pp. 234–245, Lake Buena Vista, Fla, USA, April 2004.
- [65] K. Friston, J. Ashburner, J.-B. Poline, C. D. Frith, J. D. Heather, and R. S. J. Frackowiak, "Spatial realignment and normalisation of images," *Human Brain Mapping*, vol. 3, no. 3, pp. 165–189, 1995.
- [66] D. M. Morris, K. V. Embleton, and G. J. M. Parker, "Definition of connection significance using probabilistic tractography," in *Proceedings of the Annual Meeting of the International Society for Magnetic Resonance in Medicine (ISMRM '06)*, p. 434, Seattle, Wash, USA, May 2006.
- [67] G. J. M. Parker, C. A. M. Wheeler-Kingshott, and G. J. Barker, "Estimating distributed anatomical connectivity using fast marching methods and diffusion tensor imaging," *IEEE Transactions on Medical Imaging*, vol. 21, no. 5, pp. 505–512, 2002.
- [68] C. Lenglet, R. Deriche, and O. Faugeras, "Inferring white matter geometry from diffusion tensor MRI: application to connectivity mapping," in *Proceedings of the 8th European Conference on Computer Vision (ECCV '04)*, Prague, Czech Republic, May 2004.
- [69] S. Jbabdi, P. Bellec, G. Marrelec, V. Perlbarg, and H. Benali, "A level set method for building anatomical connectivity paths between brain areas using DTI," in *Proceedings of the IEEE International Symposium on Biomedical Imaging: Macro to Nano (ISBI '04)*, vol. 1, pp. 1024–1027, Arlington, Va, USA, April 2004.
- [70] P. Cathier and J.-F. Mangin, "Registration of cortical connectivity matrices," in *Proceedings of the IEEE Computer Society Workshop on Mathematical Methods in Biomedical Image Analysis (MMBIA '06)*, p. 66, New York, NY, USA, June 2006.
- [71] V. B. Mountcastle, "The columnar organization of the neocortex," *Brain*, vol. 120, no. 4, pp. 701–722, 1997.
- [72] J.-F. Mangin, D. Rivière, O. Coulon, et al., "Coordinate-based versus structural approaches to brain image analysis," *Artificial Intelligence in Medicine*, vol. 30, no. 2, pp. 177–197, 2004.

Research Article

Diffusion Maps Clustering for Magnetic Resonance Q-Ball Imaging Segmentation

Demian Wassermann,^{1,2} Maxime Descoteaux,¹ and Rachid Deriche¹

¹ *Odyssee Project Team INRIA/ENPC/ENS INRIA, Sophia-Antipolis, 2004 Route des Lucioles, 06902 Sophia Antipolis, France*

² *Computer Science Department, FCEyN, UBA, Pabellón 1, Ciudad Universitaria, C1428EGA Buenos Aires, Argentina*

Correspondence should be addressed to Demian Wassermann, demian.wassermann@sophia.inria.fr

Received 2 July 2007; Accepted 28 August 2007

Recommended by Habib Benali

White matter fiber clustering aims to get insight about anatomical structures in order to generate atlases, perform clear visualizations, and compute statistics across subjects, all important and current neuroimaging problems. In this work, we present a diffusion maps clustering method applied to diffusion MRI in order to segment complex white matter fiber bundles. It is well known that diffusion tensor imaging (DTI) is restricted in complex fiber regions with crossings and this is why recent high-angular resolution diffusion imaging (HARDI) such as Q-Ball imaging (QBI) has been introduced to overcome these limitations. QBI reconstructs the diffusion orientation distribution function (ODF), a spherical function that has its maxima agreeing with the underlying fiber populations. In this paper, we use a spherical harmonic ODF representation as input to the diffusion maps clustering method. We first show the advantage of using diffusion maps clustering over classical methods such as N-Cuts and Laplacian eigenmaps. In particular, our ODF diffusion maps requires a smaller number of hypothesis from the input data, reduces the number of artifacts in the segmentation, and automatically exhibits the number of clusters segmenting the Q-Ball image by using an adaptive scale-space parameter. We also show that our ODF diffusion maps clustering can reproduce published results using the diffusion tensor (DT) clustering with N-Cuts on simple synthetic images without crossings. On more complex data with crossings, we show that our ODF-based method succeeds to separate fiber bundles and crossing regions whereas the DT-based methods generate artifacts and exhibit wrong number of clusters. Finally, we show results on a real-brain dataset where we segment well-known fiber bundles.

Copyright © 2008 Demian Wassermann et al. This is an open access article distributed under the Creative Commons Attribution License, which permits unrestricted use, distribution, and reproduction in any medium, provided the original work is properly cited.

1. INTRODUCTION

Recent work shows that diffusion magnetic resonance imaging (dMRI) can help recovering complex white matter fiber bundles. However this is still an open problem due to the structural complexity of the fiber bundles, which can have crossing configurations. Diffusion tensor imaging (DTI) [1] is restricted in these conditions due to the hypothesis that the diffusion within a voxel follows a Gaussian distribution, a model that cannot model intravoxel crossings. Q-ball imaging (QBI) [2], a recent high-angular resolution diffusion imaging (HARDI) technique, overcomes this limitation by reconstructing a diffusion orientation distribution function (ODF), a spherical function that has its maxima agreeing with the underlying fiber populations. The ODF reconstruction from QBI is attractive because it is model-free and has been recently shown possible with a regularized and analytical solution [3], which produces a robust and very fast

ODF reconstruction. In fact, the ODF estimation is, in practice, as fast as a standard least-square diffusion tensor (DT) estimation.

Efficient segmentation of fiber tracts in dMRI images is an important problem in neuroimaging problem because it has many potential applications. For example, it could potentially provide important information on diseases that affect fiber tracts. Alteration of the fiber tracts may provide new biomarkers in white matter pathologies and segmentation of these tracts can also improve our understanding of the functional role these tracts have and the cognitive consequences of their disruption.

The goal of this work is to provide a segmentation method that can separate the main white matter fiber bundles in the brain. We propose a new method that can segment fiber bundles and deal with fiber crossings while also requiring a minimum number of hypothesis from the data and a small number of algorithmic parameters. Spectral

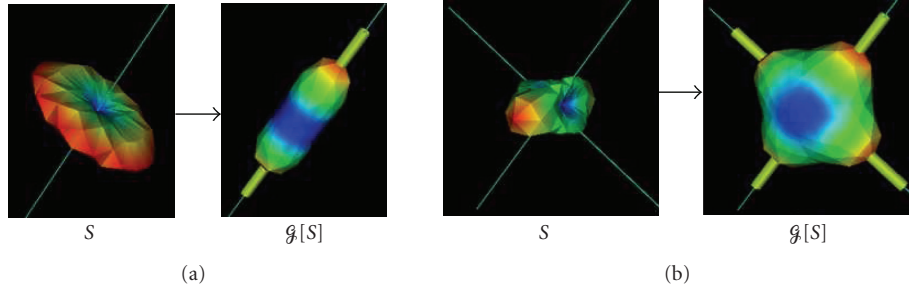


FIGURE 1: Funk-Radon transform \mathcal{G} illustrated for the input diffusion attenuation signal S ($b = 1000 \text{ s/mm}^2$) with 1 fiber (left) and two orthogonal fibers (right). The thin lines are the true underlying fiber directions and the thicker tubes are the detected maxima. One must imagine these functions as living on the surface of the sphere. Here, for visualization purposes, the radius of the respective spheres are scaled by the corresponding value on the surface. Blue-to-red colors represent low-to-high spherical values.

embedding and clustering methods have recently proved to be effective in image segmentation [4, 5]. However, classical approaches require restrictive hypotheses that are difficult to meet in real applications. For instance, N-Cuts [4] and Laplacian eigenmaps [6] require data within each cluster to be uniformly sampled, which produces artifacts when this hypothesis is not met. Moreover, classical approaches for image segmentation also assume that the scale within each cluster is the same using a single-scale parameter for the whole dataset. In order to overcome these limitations, we propose to use diffusion maps [7] as spectral embedding method. This method loses the dependence on the sampling of the elements to cluster. Moreover, we propose to use an adaptive scale-space parameter in order to deal with space-scale differences across different clusters. Finally, we propose two approaches to automatically determine the number of clusters by analyzing the spectra of the image embedding.

Another contribution of this paper is to show that the Q-ball ODF clustering using diffusion maps can reproduce the DT clustering using N-Cuts on simple synthetic images without crossings. On more complex data with crossings, we show that our method succeeds to separate fiber bundles and crossing regions on synthetic data, where the DT-based methods generate artifacts and exhibit wrong number of clusters. Finally, we successfully segment the fiber bundles in a real-human brain dataset in different regions with fibers crossing.

2. METHODS

The main goal of this work is to produce a segmentation algorithm able to segment white matter fiber bundles from dMRI data. In order to represent intravoxel crossings with the ODF, we need at least 15 real coefficients when a spherical harmonic basis is used [3, 8, 9]. This leads to 3D images with a high dimensional element at each voxel. This high dimensionality makes previous diffusion imaging segmentation approaches based on level set methods such as [10–12] computationally expensive. Moreover, these methods require an initialization step. In order to perform the segmentation in an initialization-free manner and with a lower-dimensionality image, we use spectral clustering methods [4, 5] which perform dimensionality reduction before performing the seg-

mentation and do not need initialization. The segmentation is then performed on the statistics within each cluster and the fiber crossings can be identified.

In this section, we present the three main parts of our algorithm. First, the estimation of the Q-ball diffusion ODF and its compact representation using spherical harmonics. Second, the metric used to measure distances between Q-ball ODFs. Last, the diffusion maps spectral clustering technique used to segment the ODF image into the background and the Different fiber bundles.

2.1. ODF estimation from QBI

QBI [2] reconstructs the diffusion ODF directly from the HARDI measurements on a single sphere by the Funk-Radon transform (FRT). In practice, the FRT value at a given spherical point is the great circle integral of the signal on the sphere defined by the plane through the origin with normal vector. The FRT is qualitatively illustrated in Figure 1. The ODF is intuitive because it has its maximum(a) aligned with the underlying population of fiber(s). However, computing statistics on a large number of discrete ODF values on the sphere is computationally heavy and infeasible to integrate into a segmentation algorithm of the whole brain. A more compact representation of the ODF is thus needed. In [3, 8, 9, 13] a simple analytic spherical harmonic (SH) reconstruction of the ODF is proposed. For completeness of the article, we now review and develop the main parts of our regularized analytical ODF reconstruction solution. The idea is to first estimate HARDI signal on the sphere with a regularized spherical harmonics approximation and then do a simple linear transformation of the harmonics to obtain the desired regularized ODF.

Spherical harmonic (SH) estimation of the HARDI signal

The SH, normally indicated by Y_ℓ^m (ℓ denotes the order and m the phase factor), are a basis for complex functions on the unit sphere. Explicitly, they are given as follows:

$$Y_\ell^m(\theta, \phi) = \sqrt{\frac{2\ell + 1}{4\pi} \frac{(\ell - m)!}{(\ell + m)!}} P_\ell^m(\cos \theta) e^{im\phi}, \quad (1)$$

where (θ, ϕ) obey physics convention ($\theta \in [0, \pi]$, $\phi \in [0, 2\pi]$) and P_ℓ^m is an associated Legendre polynomial. For $k = 0, 2, 4, \dots, \ell$ and $m = -k, \dots, 0, \dots, k$, we define the new index $j := j(k, m) = (k^2 + k + 2)/2 + m$ and define our modified basis \mathbf{Y} with elements Y_j such that

$$Y_j = \begin{cases} \sqrt{2} \cdot \text{Re}(Y_k^m) & \text{if } -k \leq m < 0, \\ Y_k^0 & \text{if } m = 0, \\ \sqrt{2} \cdot \text{Im}(Y_k^m) & \text{if } 0 < m \leq k, \end{cases} \quad (2)$$

where $\text{Re}(Y_\ell^m)$ and $\text{Im}(Y_\ell^m)$ represent the real and imaginary parts of Y_ℓ^m , respectively. The basis is designed to be symmetric, real, and orthonormal. Symmetry is ensured by choosing only even order SH and the ratios in front of each term also ensure that the modified basis is real and orthonormal with respect to the inner product $\langle f, g \rangle = \int_\Omega f^* g d\Omega$, where Ω denotes integration over the unit sphere and f^* is the complex conjugate of f for f and g complex functions on the sphere. We thus approximate the signal at each of the N gradient directions i as

$$S(\theta_i, \phi_i) = \sum_{j=1}^R c_j Y_j(\theta_i, \phi_i), \quad (3)$$

where $R = (\ell + 1)(\ell + 2)/2$ is the number of terms in the modified SH basis \mathbf{Y} of order ℓ . Letting \mathbf{S} be the $N \times 1$ vector representing the input signal for every encoding gradient direction, \mathbf{C} the $R \times 1$ vector of SH coefficients c_j , and \mathbf{B} is the $N \times R$ matrix constructed with the discrete modified SH basis

$$\mathbf{B} = \begin{pmatrix} Y_1(\theta_1, \phi_1) & Y_2(\theta_1, \phi_1) & \cdots & Y_R(\theta_1, \phi_1) \\ \vdots & \vdots & \ddots & \vdots \\ Y_1(\theta_N, \phi_N) & Y_2(\theta_N, \phi_N) & \cdots & Y_R(\theta_N, \phi_N) \end{pmatrix}. \quad (4)$$

We can write the set of equations as an overdetermined linear system $\mathbf{S} = \mathbf{B}\mathbf{C}$. We want to solve for the SH series coefficients c_j , where $c_j = \int_\Omega S(\theta, \phi) Y_j(\theta, \phi) d\Omega$. At this point, instead of simply evaluating the integrals directly as done in [14] or performing a straightforward least-squared minimization as in [15, 16], we add local regularization directly into our fitting procedure. This is to be able to use a high-order estimation without overmodeling the small perturbations due to noise in the input diffusion MRI signal. We thus define a measure, E , of the deviation from smoothness of a function f defined on the unit sphere as $E(f) = \int_\Omega (\Delta_b f)^2 d\Omega$, where Δ_b is the Laplace-Beltrami operator. Using the orthonormality of the modified SH basis, where we have $\int_\Omega Y_i(\theta, \phi) Y_j(\theta, \phi) d\Omega = \delta_{ij}$, the above functional E can be rewritten straightforwardly [3, 13] as

$$\begin{aligned} E(f) &= \int_\Omega \Delta_b \left(\sum_p c_p Y_p \right) \Delta_b \left(\sum_q c_q Y_q \right) d\Omega \\ &= \sum_{j=1}^R c_j^2 \ell(j)^2 (\ell(j) + 1)^2 = \mathbf{C}^T \mathbf{L} \mathbf{C}, \end{aligned} \quad (5)$$

where \mathbf{L} is simply the $R \times R$ matrix with entries $\ell(j)^2 (\ell(j) + 1)^2$ along the diagonal ($\ell(j)$ is the order associated with the j th coefficient, that is, for $j = 1, 2, 3, 4, 5, 6, 7, \dots$ $\ell(j) = 0, 2, 2, 2, 2, 4, \dots$). We thus obtain a closed-form expression for the regularization term. Therefore, the quantity we wish to minimize can be expressed in matrix form as

$$M(\mathbf{C}) = (\mathbf{S} - \mathbf{B}\mathbf{C})^T (\mathbf{S} - \mathbf{B}\mathbf{C}) + \lambda \mathbf{C}^T \mathbf{L} \mathbf{C}, \quad (6)$$

where λ is the weight on the regularization term. The coefficient vector minimizing this expression can then be determined just as in the standard least-squares fit ($\lambda = 0$) from which we obtain the generalized expression for the desired spherical harmonic series coefficient vector

$$\mathbf{C} = (\mathbf{B}^T \mathbf{B} + \lambda \mathbf{L})^{-1} \mathbf{B}^T \mathbf{S}. \quad (7)$$

From this SH coefficient vector we can recover the signal on the Q-ball for any (θ, ϕ) as $S(\theta, \phi) = \sum_{j=1}^R c_j Y_j(\theta, \phi)$. Intuitively, this approach penalizes an approximation function for having higher-order terms in its modified SH series. This eliminates most of the higher-order terms due to noise while leaving those that are necessary to describe the underlying function. However, obtaining this balance depends on choosing a good value for the parameter λ . We use the *L-curve* numerical method [17] and experimental simulations to determine a good smoothing parameter [3, 13, 18]. Here, $\lambda = 0.006$ is used as in [3, 13, 18].

Analytical ODF estimation

The true diffusion orientation distribution function (ODF) in a unit direction \mathbf{u} , $\Psi(\mathbf{u})$, is given by the radial projection of the probability distribution function (PDF) of the diffusing water molecule. Tuch [2] showed that this diffusion ODF could be estimated directly from the raw HARDI signal \mathbf{S} on a single sphere of Q-space by the Funk-Radon transform (FRT) (Figure 1). In [3, 13], we showed how this FRT can be evaluated analytically with an elegant corollary to the Funk-Hecke theorem [19]. The final ODF reconstruction on the sphere then becomes a simple linear transformation of the SH coefficients c_j describing the input HARDI signal \mathbf{S} ,

$$\Psi(\theta, \phi) = \sum_{j=1}^R \underbrace{2\pi P_{\ell(j)}(0)}_{f_j} c_j Y_j(\theta, \phi), \quad (8)$$

where f_j are the SH coefficients describing the ODF Ψ and $P_{\ell(j)}(0) = (-1)^{\ell/2} (1 \cdot 3 \cdot 5 \cdots (\ell(j) - 1) / 2 \cdot 4 \cdot 6 \cdots \ell(j))$ because $\ell(j)$ is always even in our modified SH basis. We see that the SHs are eigenfunctions of the Funk-Radon transform with eigenvalues depending only on the order ℓ of the SH series.

Hence, by using an SH estimation of the HARDI signal, we have showed that the QBI can be solved analytically. This was also showed in [8, 9]. An important contribution in favor of our approach is that this solution can be obtained while imposing a well-defined regularization criterion. The

accuracy of the modified SH series approximation with the Laplace-Beltrami smoothing was established in [18] and our regularized ODF solution was also shown to have better fiber detection properties and shown to be more robust to noise than similar solutions [8, 9].

2.2. Distances between ODFs

Once the ODF are computed, we want to capture similarities and dissimilarities between two ODFs, that is, two spherical functions $\Psi, \Psi' \in \mathcal{S}^2$ that can be represented by real-SH vectors of length R , $f = \{f_1, \dots, f_R\}$ and $f' = \{f'_1, \dots, f'_R\} \in \mathbb{R}^R$, as shown in (8) in the previous section. Since the ODFs come from real physical diffusion measurements they are bounded and form an open subset of the space of real-valued \mathcal{L}^2 spherical functions with an inner product $\langle \cdot, \cdot \rangle$ defined as

$$\begin{aligned} \langle \Psi, \Psi' \rangle &= \int_{\Omega} \Psi(\theta, \phi) \cdot \Psi'(\theta, \phi) d\Omega \\ &= \int_{\Omega} \left(\sum_{i=1}^R f_i Y_i(\theta, \phi) \sum_{j=1}^R f'_j Y_j(\theta, \phi) \right) d\Omega. \end{aligned} \quad (9)$$

Again, because of the orthonormality of the spherical harmonic basis, the cross-terms cancel and the expression is simply

$$\langle \Psi, \Psi' \rangle = \sum_{j=1}^R f_j \cdot f'_j. \quad (10)$$

Therefore, the induced \mathcal{L}^2 norm $\|\Psi\| = \sqrt{\langle \Psi, \Psi \rangle}$ giving us the distance metric between two ODFs is

$$\|\Psi - \Psi'\| = \sqrt{\sum_{j=1}^R (f_j - f'_j)^2}. \quad (11)$$

The Euclidean distance was also used successfully for ODF segmentation in [12] and for DTI segmentation in [11] even though more appropriate metrics exist such as the J-divergence [11, 20] and Riemannian geodesic distances [11]. Similarly, one can think of choosing another metric to compare ODFs. For instance, since the ODF can be viewed as a probability distribution function (PDF) of fiber orientations, one can use the Kullback-Leibler distance between two PDFs, as done in [2]. However, in that case the problem quickly blows up computationally because one needs to use all N discrete HARDI data on the sphere instead of the R SH coefficients ($R \ll N$).

2.3. Diffusion maps-based clustering

We now want to segment white matter fiber bundles in a Q-ball image. One of the open questions in Q-ball image analysis and clustering is that which metric should be used to compare Q-ball ODFs. Here, we describe a clustering algorithm that infers an embedding and a metric to compare ODF images. We derive an affinity measure incorporating the Euclidean distance and the spatial location distance between

ODFs. This affinity measure then used in a spectral embedding framework. As mentioned in [7], the Euclidean distance within this embedding actually represents an *intrinsic metric of the data*, which can be used to perform statistics in the embedded space and can thus be used to segment Q-ball ODF images into white matter fiber bundles.

Spectral embedding and clustering

In recent years, spectral manifold learning and clustering techniques [4, 6, 21–23] have become one of the most popular modern clustering family of methods. They are simple to implement, they can be solved efficiently by standard linear algebra software, and they very often outperform traditional manifold learning and clustering algorithms such as the classical principal component analysis (PCA) [24] and k -means [25] algorithms. Moreover, due to the dimensionality reduction properties, they are especially well suited to work with high-dimensional data. These techniques have been recently used to cluster various types of images [4, 5] and white matter fiber tracts [26]. In our case, we perform the spectral clustering for two different types of elements: the DT and the ODF. In the DT case, the element is represented by a 6-dimensional vector corresponding to the upper (or lower) triangular part of the DT 3×3 symmetric matrix. In the ODF case, the element is represented by the 15-dimensional vector corresponding to the 4th-order spherical harmonic ODF estimation.

Spectral clustering reduces the clustering problem to a graph partitioning problem. Each element to be clustered is represented as a node in a graph and the edges joining the vertex are a measure of affinity between the elements. This affinity measure lies between 0 and 1, 0 being the less affine case. A spectral decomposition of this graph is taken by calculating the eigenvalue decomposition (EVD) of the graph Laplacian [27]. Then a low-dimensional Euclidean manifold embedding is inferred from this decomposition. Finally, the clustering is performed in the inferred Euclidean manifold.

All the above techniques rely on three hypotheses.

- (1) Preservation of the distance relationship: after a distance is defined between elements, the learned manifold should preserve the distance relation.
- (2) Uniform sampling of the elements: the density of the extracted elements changes if and only if these elements belong to anatomically different bundles.
- (3) Convexity of the elements: if two elements are in the dataset, almost all of the intermediate tracts obtained by the interpolation that can be inferred from the metric used to build the affinity matrix are in the dataset.

It is not easy to guarantee that the data to be embedded and clustered will adhere to these hypotheses. Donoho and Grimes, in [13], analyze when a spectral embedding algorithm is able to recover the true parameterization of a set of images. As medical images represent the discretization of a continuous space, hypotheses 1 and 3 are plausible. However, there is no indication that within a fiber bundle the distribution of the elements (DT or ODF) are uniformly sampled. Moreover, in [29] it is shown that different sampling

frequencies within one cluster leads the N-Cuts and Laplacian eigenmaps methods to subdivide the cluster in several parts. In order to overcome this limitation and to be resilient to sampling frequency differences within a cluster, we use the diffusion maps [7] spectral embedding technique. We now describe the three steps involved in the diffusion maps algorithm in turn.

Step 1 (Computing the affinity matrix). Letting X represent the set of all ODF elements to cluster, the main idea is to look for a representation between the elements of X that is more representative than \mathbb{R}^R (recall that ODFs are $\in \mathbb{R}^R$) and reduces the dimensionality of the problem. With keeping this in mind, a fairly good way of representing any set of elements with an affinity function $a : X \times X \rightarrow \mathbb{R}_{>0}$, is a weighted graph, $G(X, E, w(\cdot))$, where the weight of the edge between two vertices represents the affinity of the elements connected by this edge. More formally, for an edge,¹ $e = (f_i, f_j) \in E$, the weight of the edge is $w(e) = a(f_i, f_j)$. Hence, each element of the adjacency matrix of G or conversely the affinity matrix of $(X, a(\cdot))$ is

$$A_{ij} = a(f_i, f_j). \quad (12)$$

Taking this in account, the weighted graph $G(X, E, w(\cdot))$ can be also noted as $G(X, A)$.

Usually, a distance function $d(\cdot)$ instead of an affinity function is given. The distances can be easily converted into affinities by applying a kernel to the distance function

$$a(f_i, f_j) = e^{-d(f_i, f_j)^2 / \sigma_{ij}^2}, \quad (13)$$

where σ is an adaptive scale-space parameter that may depend on the elements f_i and f_j . In this work, the adaptive scale-space parameter is taken following [30]. A “neighbor-number” k is given as parameter to the algorithm and then $\sigma_{ij}^2 = d(f_i, f_{i_k})d(f_j, f_{j_k})$, where f_{i_k} is the k th closest neighbor according to the distance function $d(\cdot, \cdot)$ of element f_i . This choice of a scaling parameter for each point allows self-tuning of the point-to-point distances according to the local statistics of the neighborhoods surrounding points i and j .

As in image segmentation, the spatial position of each element is important, the spatial dependency should be incorporated into the affinity matrix. Following [5, 31], we use Markovian relaxation to incorporate this information. In order to represent the affinity of all the elements that can be reached within one spatial step, the affinity matrix is modified in the following way:

$$A_1 = \begin{cases} A_{ij} & \text{if } \|\text{coords}(f_i) - \text{coords}(f_j)\|_2 \leq 1, \\ 0 & \text{in any other case,} \end{cases} \quad (14)$$

¹ In this section, for simplicity, the subindexed variables f_i, f_j represent different elements to be clustered and not spherical harmonic coefficients as in Section 2.2. f_i is the full ODF element $\in \mathbb{R}^R$ at position i .

where $\text{coords}(f)$ are spatial coordinates of element f in the image

$$P_1 = \frac{1}{\max_i D(A_1)_{ii}} \begin{cases} \max_i D(A_1)_{ii} \\ -D(A_1)_{ii} \\ A_1 \end{cases} \quad \begin{cases} \text{if } i = j, \\ \text{in any other case,} \end{cases} \quad (15)$$

where $D(A_1)$ is a diagonal matrix with $D(A_1)_{ii} = \sum_j A_{1ij}$, usually called the row-sum or degree matrix of A_1 .

Then, obtaining the affinities of elements that can be reached within s spatial steps is enough to elevate P_1 to the power of s , $P_s = (P_1)^s$ as stated in [31]. Moreover, s can be chosen to be the smallest positive integer which results in nonzero elements in the whole matrix in order to represent the weakest connected induced graph. The diagonal adjustment forces the inherent random walk to a uniform steady state, hence every part of the Markov field will be explored at the same speed. For the sake of clarity, P_s will be referred to as affinity matrix A in the rest of the paper.

Step 2 (Performing the embedding). The algorithm must embed the elements of X into an n -dimensional Euclidean space $\mathbf{y}(X)$. This is done by applying eigenvalue decomposition to the Laplacian of the affinity matrix. This embedding must be compliant with hypothesis 1. As in [6, 7, 27], this is done by performing the spectral decomposition of the graph Laplacian of the graph induced by A ,

$$\Delta = D(A) - A \in \mathbb{R}^{|X| \times |X|}, \quad (16)$$

where $|X|$ is number of elements to be clustered.

In order to overcome the necessity of hypothesis 2, we prenormalize the affinity matrix as done in [7]. This is done by normalizing the weight of each edge of the graph, A_{ij} , by the probability density of both elements relating through the edge,

$$(A_p)_{ij} = \frac{A_{ij}}{p(i)p(j)}, \quad (17)$$

where $p(\cdot)$, the probability density function of the elements in X , is not known but can be approximated up to a multiplication factor by

$$p(i) = \sum_k A_{ik} = \sum_k A_{ki}. \quad (18)$$

Due to the necessity of having a uniform behavior of the clustering algorithm without minding the scale of the affinity measure taken, a doubly stochastic matrix normalization is performed:

$$A_{ds} = D(A_p)^{-1/2} A_p D(A_p)^{-1/2} \in \mathbb{R}^{|X| \times |X|}. \quad (19)$$

As A_{ds} is a double stochastic symmetric matrix, the eigenvalue decomposition of (16) can be calculated by taking the singular value decomposition (SVD)

$$VSV^T = A_{ds} \in \mathbb{R}^{|X| \times |X|}. \quad (20)$$

Finally, the Euclidean coordinates \mathbf{y}_i of an element $f_i \in X$ in the n -dimensional embedding manifold are

$$\mathbf{y}(f_i) = \mathbf{y}_i = \frac{1}{\mathbf{v}_i^0} (\lambda_1 \mathbf{v}_i^1, \dots, \lambda_n \mathbf{v}_i^n)^T, \quad f_i \in X, \quad (21)$$

where

$$V = (\mathbf{v}^0 \dots \mathbf{v}^{|X|-1}) \in \mathbb{R}^{|X| \times |X|} \quad (22)$$

is the eigenvector column matrix and the corresponding eigenvalues are, $1 = \lambda_0 \geq \lambda_1 \geq \dots \geq \lambda_{|X|-1} \geq 0$. The first eigenvector \mathbf{v}_0 is not taken into account as a component in the embedding because it is constant and hence meaningless as shown in [6, 7, 27].

Step 3 (Clustering). Once the embedding has been performed, several techniques have been proposed for the clustering step [4, 6, 32].

The first step in this process is to determine the number of clusters, this can be done in two ways. The first, as in [33], is choosing the number of clusters according to the ‘‘elbow.’’ This is present in the eigenvalue plot. For instance, if the slope of the eigenvalue plot changes noticeably at eigenvector λ_i , the number of clusters should be $i + 1$. The second way is reordering the affinity matrix rows and columns following the second eigenvector as proved in [34], which shows the block structure of the matrix as squared blocks along the matrix diagonal. Then, the number of clusters is the number of blocks. Their commended number of dimensions for the embedding is the same as the number of clusters. Finally, the clustering is performed by running a k -means clustering algorithm on the space spanned by $\mathcal{Y}(X)$. A formal justification for this approach can be found in [6, 32].

2.4. Q-ball data generation and acquisitions

Synthetic data

We generate synthetic HARDI data using the multitensor model which is simple and leads to an analytical expression of the ODF [2, 18]. For a given b -factor and noise level, we generate the diffusion-weighted signal

$$S(\mathbf{u}_i) = \sum_{k=1}^n \frac{1}{n} \exp(-b \mathbf{u}_i^T \mathbf{D}_k(\theta) \mathbf{u}_i) + \text{noise}, \quad (23)$$

where \mathbf{u}_i is the i th gradient direction on the sphere, n is the number of fibers, and $1/n$ is the volume fraction of each fiber. In practice, we use $N = 81$ from a 3rd-order tessellation of the icosahedron, $b = 3000 \text{ s/mm}^2$, and $n = 1$ or 2 . $\mathbf{D}_k(\theta)$ is the diffusion tensor with standard eigenvalues $[3, 3, 1.7] \times 10^{-2} \text{ mm}^2/\text{s}$ oriented in direction θ , which agree with reported physiological values [35]. Finally, we add complex Gaussian noise with standard deviation of $1/35$, producing a signal with signal-to-noise ratio of 35.

We generate three synthetic data example, two simple examples: one with a ring of sinusoidal-shaped fibers, one with fibers with different sizes and scales, and the other with complex crossing areas simulating the ‘‘U’’-fibers (corticocortical

fibers) that can occur in the brain. These synthetic datasets help understand the behavior of the different spectral clustering methods when confronted with simple and complex fiber geometries.

Human brain data

Diffusion-weighted data and high-resolution T1-weighted images were acquired on a whole-body 3 Tesla Magnetom Trio scanner (Siemens, Erlangen) equipped with an 8-channel head array coil [36]. The spin-echo echo-planar-imaging sequence, TE = 100 ms, TR = 12 s, 128×128 image matrix, FOV = $220 \times 220 \text{ mm}^2$, consists of 60 diffusion encoding gradients [37] with a b -value of 1000 s/mm^2 . Seven images without any diffusion weightings are placed at the beginning of the sequence and after each block of 10 diffusion-weighted images as anatomical reference for offline motion correction. The measurement of 72 slices with 1.7 mm^2 thickness (no gap) covered the whole brain. Random variations in the data were reduced by averaging 3 acquisitions, resulting in an acquisition time of about 45 minutes. No cardiac gating was employed to limit the acquisition time. The issue of cardiac gating is discussed in [38]. Additionally, fat saturation was employed and we used 6/8 partial Fourier imaging, a Hanning window filtering, and parallel acquisition (generalized autocalibrating partially parallel acquisitions, reduction factor = 2) in the axial plane.

The brain is peeled from the T1-anatomy, which was aligned with the Talairach stereotactical coordinate system [39]. The 21 images without diffusion weightings distributed within the whole sequence were used to estimate motion correction parameters using rigid-body transformations [40], implemented in [41]. The motion correction for the 180 diffusion-weighted images was combined with a global registration to the T1 anatomy computed with the same method. The gradient direction for each volume was corrected using the rotation parameters. The registered images were interpolated to the new reference frame with an isotropic voxel resolution of 1.72 mm^2 and the 3 corresponding acquisitions and gradient directions were averaged.

Distance functions between elements to cluster

In order to implement the diffusion maps spectral clustering method a distance function for each data type is chosen. This distance function is used to calculate the affinity matrix as expressed by (13). In the DT case, following [42], we use the Riemannian tensor distance. In the ODF case we use the distance shown in (11).

3. RESULTS

3.1. Synthetic data experiments

Diffusion maps versus N-cuts

The first experiment shows the difference in performance between the diffusion maps and N-Cuts approach. The N-Cut algorithm does not perform the sampling-based normalization described by (17) and is thus sensitive to sampling

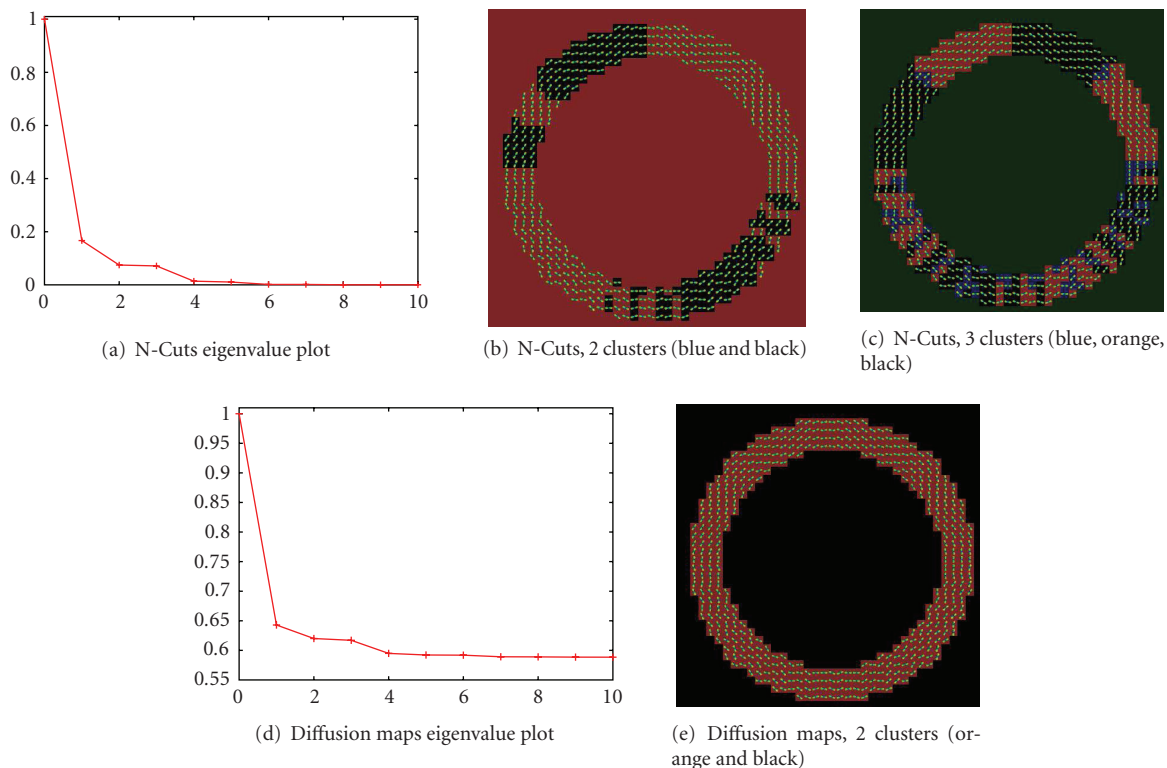


FIGURE 2: N-Cuts generates overclustering due to sampling frequency variation in ODF images. In both eigenvalue plots Figures 2(a) and 2(d), the slope between the line joining λ_0 and λ_1 and the line joining λ_1 and λ_2 changes drastically, expressing an elbow in λ_1 , which indicates two clusters. The clustering results with Figures 2, 2(b), 3, 2(c), clusters are shown. Diffusion maps correctly finds two clusters, the object and the background, Figure 2(e). In the labeling, the ODFs are overlaid on the labels.

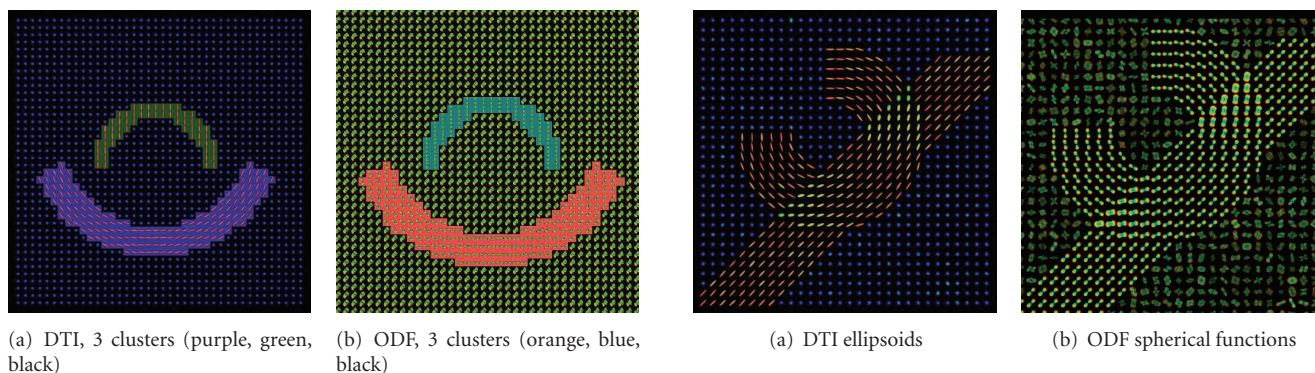


FIGURE 3: Synthetic image without fiber crossings. The results for the DT and ODF images are equivalent. The colors behind the DTs and ODFs indicate the clusters.

FIGURE 4: Synthetic DT and ODF images. The expected number is four, one for each fiber, one for the crossing between the two fibers and one for the background.

frequency differences within the clusters. In order to show this sampling hypothesis problem, we used a ring fiber bundle with different sampling frequencies. Within the ring, the fibers have a sinusoidal shape and the frequency of the modulating sine function is 4 times bigger in the lower half of the ring. More formally, the fibers follow the angular function $o(\theta) = \theta + (1/8)\pi\sin(\mu\cdot\theta)$, $0 \leq \theta < 2\pi$, where $\mu = 8$ for the upper half of the ring and $\mu = 32$ for the lower half. Two clusters are expected, the ring and the background. The results of

both clustering techniques are shown in Figure 2, where the background has been masked out. Figure 2(a) shows the plot of the first 10 eigenvalues for the N-Cuts method, shown in Figures 2(b) and 2(c), and the slope between the line joining λ_0 and λ_1 and the line joining λ_1 and λ_2 changes drastically. This elbow at λ_1 indicates that there are 2 clusters. Figure 2(d) shows the plot of the first 10 eigenvalues for the diffusion maps method whose clustering results are shown in Figure 2(e). The N-Cuts exhibits frequency-dependent

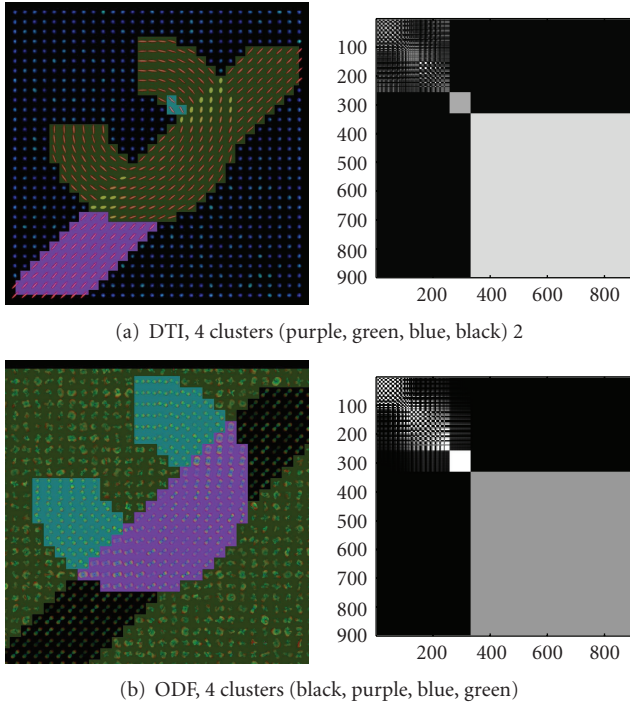


FIGURE 5: Clustering results in ODF and DT images, only ODF show the correct clustering. In both cases the clustering result and the reordered affinity matrix are shown.

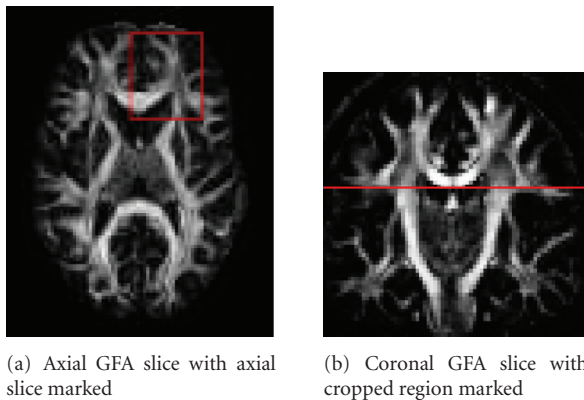


FIGURE 6: Generalized fractional anisotropy axial, Figure 6(a), and coronal, Figure 6(b) slices in the real dataset.

clustering artifacts while the diffusion maps method clearly shows two clusters. In the diffusion maps, the clustering has correctly segmented the background and the ring.

ODF versus DT images

In Figure 3, a single fiber scenario with no fiber crossing is shown. The DT-based and ODF-based image clustering produce the same results. Hence, ODF clustering reproduces DT-based results on a simple fiber population example.

Finally, Figure 4 shows a fiber crossing scenario with two overlapping fiber bundles that have different geometries.

Segmentation was performed over the DT and the ODF image shown in Figure 5. Note that the cluster number is correctly estimated only in the ODF image. Moreover, the ODF N-Cuts segmentation exhibits artifacts not present in the ODF diffusion maps segmentation. The ODF diffusion maps effectively identify the two different fiber bundles as well as the fiber crossing areas.

3.2. Real data

The real-data experiment presented in this section shows the segmentation and labeling of a cropped axial and coronal slice. The cropped slices were chosen by an expert in regions of known fiber crossings where the DT model is normally limited. The ROIs show intersection of several fiber bundles. Hence, our segmentation algorithm is confronted with elements that have different orientation and different diffusion characteristics.

In order to show that ODF data segments the white matter fiber bundles better than the DT data in real cases, we analyze the evolution of the affinity matrix as the scale-space parameter changes in the axial cropped slice shown in Figure 6. Affinity matrices were computed with varying scale-space parameter between $1/5$, $1/10$, $1/20$, and $1/40$ of the quantity of elements ($|X|$) to cluster, respectively. In order to show the block structure of the affinity matrices, they were reordered using the second (Fiedler) biggest eigenvector [34]. It can be seen in Figure 7 that as the scale diminishes, the DT data shows a high correlation between all the elements of the slice. This makes clustering very difficult because the blocks are small and highly correlated. On the other hand, the ODF data shows a very clear block structure across all scales. This block structure shows a high correlation of the elements within each block and a low interblock correlation, giving a much better input to the clustering algorithm than the DT data.

In Figure 6, the location of the cropped axial slice is shown in the axial slice, Figure 6(a), and coronal slice, Figure 6(b). As it can be seen in the segmented and labeled axial slice, Figure 8, the segmentation also allows to identify and label some of the main white matter structures, Corpus Callosum (CC), Anterior Corona Radiata (ACR), Forceps Major (fmajor) and Forceps Minor (fminor).

In Figure 9, the location of the cropped coronal slice is shown in the axial slice, Figure 9(a), and coronal slice, Figure 9(b). As it can be seen in the segmented and labeled coronal slice, Figure 9(c), the segmentation allows to identify and label main white matter structures: Corpus Callosum (CC), Cingulum (CG), Corona Radiata (CR), Superior Longitudinal Fasciculus (SLF). Note that the segmentation is resilient to crossing areas such as seen at the interface between CR and CC.

4. DISCUSSION

We have presented an algorithm to perform Q-ball imaging segmentation of white matter fiber bundles. The proposed method combines state-of-the-art HARDI reconstruction and state-of-the-art spectral clustering techniques. Our

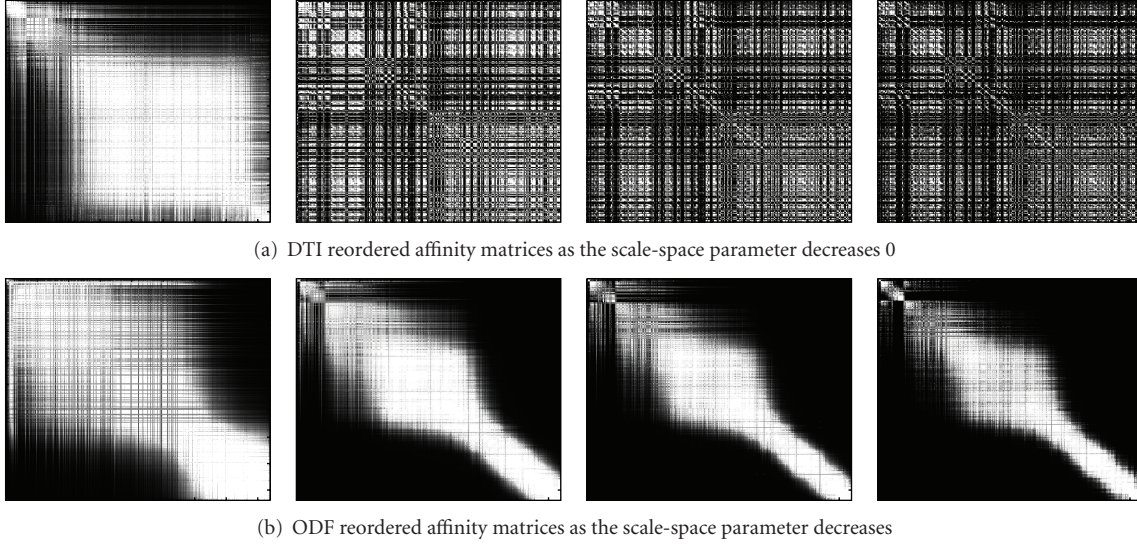


FIGURE 7: Plots of DTI and ODF affinity matrices of an axial cropped slice shown in Figure 6. The matrices are reordered according to the second (Fiedler) eigenvector. The plots of DTI affinity matrices are shown in decreasing order of σ , which takes the values 1/5, 1/10, 1/20, and 1/40 of the quantity of elements to cluster. In the DTI case, the decreasing on the scale parameter σ leads to a matrix with highly correlated elements that is very difficult to cluster. In the ODF case, the block structure is clear and is better suited to apply a clustering algorithm.

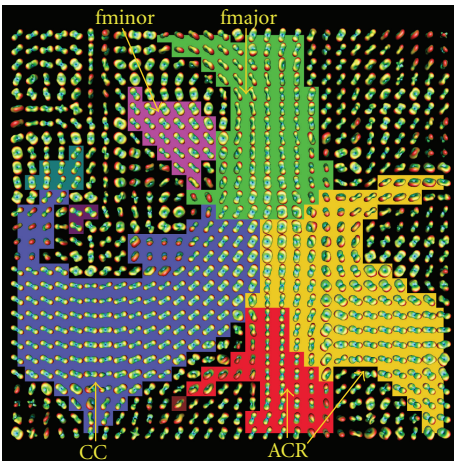


FIGURE 8: Our proposed algorithm is able to identify important white matter fiber bundles on an axial slice of a real dataset. The cropped axial slice shown in Figure 6(a) has been segmented. In the labeled ODF visualization, each color represents one of the clusters found. The white matter labels are CC: Corpus Callosum, ACR: Anterior Corona Radiata, fmajor: Forceps Major and fminor: Forceps Minor.

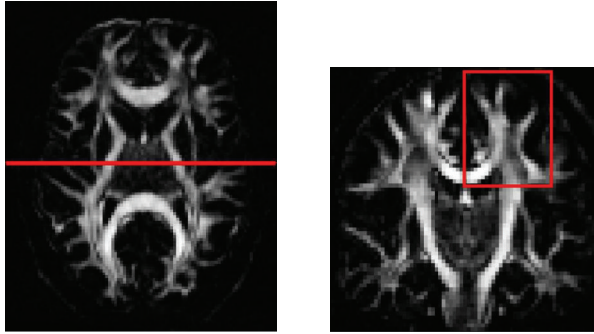
algorithm is initialization-free and has only two parameters. A scale-space parameter and the number of regions (clusters) are to be found. Regarding this number of clusters parameter, we have proposed to estimate it automatically. We have introduced a spectral embedding technique that does not require uniform sampling of the elements. To do so, the affinity measure used incorporates an Euclidean distance measure between the spherical harmonic coefficients describing the Q-ball ODFs and also incorporates the spatial location distance between ODFs. The affinity measure and the metric

induced in the embedded space is then used to cluster Q-ball ODF images into multilabel segmentation representing the fiber bundles. Spectral embedding has already been applied to dMRI (e.g., [5]). However, to our knowledge, this is the first work using the diffusion maps that avoids the high dependence on element sampling. It is also the first work attempting Q-ball ODFs.

We have illustrated that the ODFs are the desirable elements to use for clustering in the white matter because the classical DT model is limited in regions of fiber crossings. The ODF is even more attractive because of the recent analytical spherical harmonic solution to the ODF reconstruction [3, 8, 9, 13]. The analytical solution is in fact as fast as a standard DT least-square estimation. In this work, we believe that we have used the state-of-the-art ODF reconstruction method [13], which is regularized, robust and very simple to implement.

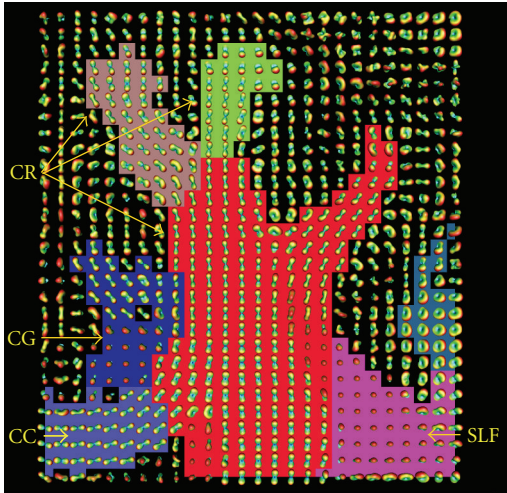
The spectral embedding performed by the diffusion maps technique is at the heart of our segmentation algorithm. Whereas other spectral embedding techniques have a tendency to produce artifacts in the presence of different sampling characteristics within a cluster, the technique used in this work greatly reduces this tendency by performing the simple linear algebra calculation shown in (17).

Spectral embedding techniques produce a representation of the embedded data based on element-to-element affinities. This leads to the fundamental issue: how to choose the affinity measure? It is a challenge to find a measure that incorporates similarities between elements as well as the spatial location difference between elements. For similarities between elements, we chose the Euclidean distance between spherical harmonic coefficients describing the ODFs. This approach is simple and very efficient because it allows to process the ODFs directly on the SH coefficients. The Euclidean distance



(a) Axial GFA slice with coronal slice marked

(b) Coronal GFA slice with cropped region marked



(c) Labeled ODF visualization of the cropped region

FIGURE 9: Our proposed algorithm is able to identify important white matter fiber bundles on a coronal slice of a real dataset. Generalized fractional anisotropy axial, Figure 9(a), and coronal, Figure 9(b) slices are shown. Labeled ODF visualization, Figure 9(c), each color represents one of the 7 clusters found. The white matter labels are CC: Corpus Callosum, CG: Cingulum, CR: Corona Radiata, SLF: Superior Longitudinal Fasciculus.

has also been used successfully in a level set segmentation framework [12] and it would be interesting to compare our spectral clustering approach against it. For spatial location difference, we chose Markovian relaxation in order to be consistent with the graph theoretical representation of the diffusion maps technique. Although this way of representing the distance involves an artificial elimination of all the non-neighboring relations of the ODF elements in the affinity matrix and an adjustment of the diagonal elements, we believe that the resulting affinity relations represent the affinity better. The affinity of two neighboring elements at the beginning of the Markovian relaxation algorithm is represented by a function of the Euclidean distance between them. This affinity can be interpreted as the probability that a random walker has of going from the first element to the second. The affinity of two elements at the end of the relaxation is the probability of a random walker starting from one element and reaching the second in a certain number of steps.

The final step of our algorithm is k -means clustering. We believe that there is room for improvement in this last part of the algorithm. In the first place, the k -means algorithm needs an explicit number of clusters to find. This can be heuristically determined by analyzing the eigenvalue plot or the reordered affinity matrix structure, as shown in this work. However, an automatic method that could find the number of clusters would considerably improve the algorithm. In the second place, the k -means algorithm and its variants, for instance, k -medians, k -medioids, search for isotropic clusters in the embedding space [25]. These methods are able to perform clustering on convex structures. This could also improve the last clustering phase of our algorithm.

Finally, in order to analyze the importance of the difference between our diffusion maps algorithm and the widely used N-Cuts, we used synthetic simulations. In these simulations, we generated a synthetic image with a single cluster within which the sampling of the elements changed. We showed that when this sampling changes, the N-cuts algorithm produces artifacts while our diffusion maps method does not. As uniform sampling within a cluster is a difficult property to guarantee in the white matter fiber bundles, our diffusion maps method is better suited for this task. We thus believe that diffusion maps are the right clustering method to be used on dMRI processing problems.

5. CONCLUSIONS

In this work, we have presented two contributions. First, we have shown that in order to perform spectral clustering on complex dMRI with crossing fiber bundles, an HARDI technique such as Q-ball imaging is better than the classical DTI technique. This is because the ODF reconstructed from QBI is able to recover multiple crossing fiber populations. Second, a diffusion maps-based technique for image segmentation was introduced to reduce artifacts arising from the widely used N-Cuts image segmentation. We have illustrated the advantages of the ODF diffusion maps segmentation algorithm, and showed on a real dataset that our algorithm is able to identify important and complex white matter fiber bundles.

Finally, the diffusion maps technique has been shown to be more robust to sampling frequency variations within each object to be segmented. In order to cluster the elements, we have used an adaptive scale-space parameter and we have used Markovian relaxation in order to incorporate spatial dependencies. Overall, the approach is theoretically sound with the graph-based representation which lies at the heart of spectral clustering methods.

Therefore, we have an algorithm to perform fiber bundle clustering for a single brain. It is now important to study the behavior over several subjects in order to assess the reproducibility of the algorithm. In time, this will enable to perform multisubject statistics within bundles in the embedded space. This will help characterize the white matter fiber bundles of several subjects and study if the alteration of these segmented tracts can provide new biomarkers for white matter diseases.

ACKNOWLEDGMENTS

The authors would like to thank the Max Planck Institute for Human Cognitive and Brain Sciences (Leipzig, Germany) and, in particular, to Timm Wetzel for providing the diffusion-weighted MR datasets and Alexandre Gramfort and Marc Niethammer for useful comments. Part of this work was supported by PAI Procope and the Diffusion MRI ARC. Demian Wassermann would like to acknowledge CONICET (Argentina).

REFERENCES

- [1] D. C. Alexander, G. J. Barker, and S. R. Arridge, "Detection and modeling of non-Gaussian apparent diffusion coefficient profiles in human brain data," *Magnetic Resonance in Medicine*, vol. 48, no. 2, pp. 331–340, 2002.
- [2] A. W. Anderson, "Measurement of fiber orientation distributions using high-angular resolution diffusion imaging," *Magnetic Resonance in Medicine*, vol. 54, no. 5, pp. 1194–1206, 2005.
- [3] G. Andrews, R. Askey, and R. Roy, *Special Functions*, Cambridge University Press, Cambridge, UK, 1999.
- [4] A. Anwander, M. Tittgemeyer, D. Y. Von Cramon, A. D. Friederici, and T. R. Knosche, "Connectivity-based parcellation of Broca's area," *Cerebral Cortex*, vol. 17, no. 4, pp. 816–825, 2007.
- [5] P. J. Basser and D. K. Jones, "Diffusion-tensor MRI: Theory, experimental design and data analysis—a technical review," *NMR in Biomedicine*, vol. 15, no. 7-8, pp. 456–467, 2002.
- [6] M. Belkin and P. Niyogi, "Laplacian eigenmaps for dimensionality reduction and data representation," *Neural Computation*, vol. 15, no. 6, pp. 1373–1396, 2003.
- [7] F. Chung, "Spectral graph theory," CBMS-AMS, 1997.
- [8] R. R. Coifman, S. Lafon, A. B. Lee, M. Maggioni, B. Nadler, F. Warner, et al., "Geometric diffusions as a tool for harmonic analysis and structure definition of data: diffusion maps," in *Proceedings of the National Academy of Sciences of the United States of America*, vol. 102, no. 21, pp. 7426–7431, May 2005.
- [9] M. Descoteaux, E. Angelino, S. Fitzgibbons, and R. Deriche, "Apparent diffusion coefficients from high-angular resolution diffusion imaging: estimation and applications," *Magnetic Resonance in Medicine*, vol. 56, no. 2, pp. 395–410, 2006.
- [10] M. Descoteaux, E. Angelino, S. Fitzgibbons, and R. Deriche, "Regularized, fast, and robust analytical Q-ball imaging," *Magnetic Resonance in Medicine*, vol. 58, no. 3, pp. 497–510, 2007.
- [11] M. Descoteaux, E. Angelina, S. Fitzgibbons, and R. Deriche, "A fast and robust ODF estimation algorithm in Q-ball imaging," in *Proceedings of the 3rd IEEE International Symposium on Biomedical Imaging: From Nano to Macro*, vol. 2006, pp. 81–84, Arlington, Va, USA, April 2006.
- [12] M. Descoteaux and R. Deriche, "Segmentation of q-ball images using statistical surface evolution," in *Medical Image Computing and Computer-Assisted Intervention (MICCAI '07)*, Springer, Brisbane, Australia, 2007.
- [13] D. L. Donoho and C. Grimes, "Image manifolds which are isometric to Euclidean space," *Journal of Mathematical Imaging and Vision*, vol. 23, no. 1, pp. 5–24, 2005.
- [14] M. Fiedler, "A property of eigenvectors of nonnegative symmetric matrices and its application to graph theory," *Czechoslovak Mathematical Journal*, vol. 25, pp. 619–633, 1975.
- [15] L. R. Frank, "Characterization of anisotropy in high-angular resolution diffusion-weighted MRI," *Magnetic Resonance in Medicine*, vol. 47, no. 6, pp. 1083–1099, 2002.
- [16] FSL, *Fmrib Software Library*, University of Oxford, 2006.
- [17] P. Hansen, "The l-curve and its use in the numerical treatment of inverse problems," in *Computational Inverse Problems in Electrocardiology*, pp. 119–142, 2001.
- [18] C. Hess, P. Mukherjee, E. Han, D. Xu, and D. Vigneron, "Q-ball reconstruction of multimodal fiber orientations using the spherical harmonic basis," *Magnetic Resonance in Medicine*, vol. 56, pp. 104–117, 2006.
- [19] A. K. Jain, M. N. Murty, and P. J. Flynn, "Data clustering: A review," *ACM Computing Surveys*, vol. 31, no. 3, pp. 316–323, 1999.
- [20] M. Jenkinson, P. Bannister, M. Brady, and S. Smith, "Improved optimization for the robust and accurate linear registration and motion correction of brain images," *NeuroImage*, vol. 17, no. 2, pp. 825–841, 2002.
- [21] I. Jolliffe, *Principal Component Analysis*, Springer Series in Statistics, Berlin, Germany, 1986.
- [22] L. Jonasson, P. Hagmann, C. Pollo, X. Bresson, C. Richero Wilson, R. Meuli, et al., "A level set method for segmentation of the thalamus and its nuclei in DT-MRI," *Signal Processing*, vol. 87, no. 2, pp. 309–321, 2007, Special Issue of Signal Processing on Diffusion Tensor Imaging.
- [23] D. K. Jones, M. A. Horsfield, and A. Simmons, "Optimal strategies for measuring diffusion in anisotropic systems by magnetic resonance imaging," *Magnetic Resonance in Medicine*, vol. 42, no. 3, pp. 515–525, 1999.
- [24] D. K. Jones, S. C. R. Williams, D. Gasston, M. A. Horsfield, A. Simmons, and R. Howard, "Isotropic resolution diffusion tensor imaging with whole brain acquisition in a clinically acceptable time," *Human Brain Mapping*, vol. 15, no. 4, pp. 216–230, 2002.
- [25] S. Lafon, *Diffusion Maps and Geometric Harmonics*, Ph.D. thesis, Yale University, New Haven, Conn, USA, 2004.
- [26] S. Lafon and A. B. Lee, "Diffusion maps and coarse-graining: a unified framework for dimensionality reduction, graph partitioning, and data set parameterization," *IEEE Transactions on Pattern Analysis and Machine Intelligence*, vol. 28, no. 9, pp. 1393–1403, 2006.
- [27] C. Lenglet, M. Rousson, and R. Deriche, "DTI segmentation by statistical surface evolution," *IEEE Transactions on Medical Imaging*, vol. 25, no. 6, pp. 685–700, 2006.
- [28] C. Lenglet, M. Rousson, R. Deriche, and O. Faugeras, "Statistics on the manifold of multivariate normal distributions: theory and application to diffusion tensor MRI processing," *Journal of Mathematical Imaging and Vision*, vol. 25, no. 3, pp. 423–444, 2006.
- [29] B. Nadler, S. Lafon, R. R. Coifman, and I. G. Kevrekidis, "Diffusion maps, spectral clustering and eigenfunctions of Fokker-Planck operators," in *Advances in Neural Information Processing Systems 18*, Y. Weiss, B. Schölkopf, and J. Platt, Eds., pp. 955–962, MIT Press, Cambridge, MA, USA, 2006.
- [30] L. O'Donnell and C.-F. Westin, "High-dimensional white matter atlas generation and group analysis," in *Medical Image Computing and Computer-Assisted Intervention (MICCAI '06)*, R. Larsen, M. Nielsen, and J. Sporring, Eds., vol. 4191 of *Lecture Notes in Computer Science*, pp. 243–251, Springer, Copenhagen, Denmark, 2006.
- [31] C. Pierpaoli, P. Jezzard, P. J. Basser, A. Barnett, and G. Di Chiro, "Diffusion tensor MR imaging of the human brain," *Radiology*, vol. 201, no. 3, pp. 637–648, 1996.

- [32] S. T. Roweis and L. K. Saul, "Nonlinear dimensionality reduction by locally linear embedding," *Science*, vol. 290, no. 5500, pp. 2323–2326, 2000.
- [33] J. Shi and J. Malik, "Normalized cuts and image segmentation," *IEEE Transactions on Pattern Analysis and Machine Intelligence*, vol. 22, no. 8, pp. 888–905, 2000.
- [34] J. Talairach and P. Tournoux, *Co-Planar Stereotaxic Atlas of the Human Brain: 3-Dimensional Proportional System: An Approach to Cerebral Imaging*, Thieme Medical Publishers, New York, NY, USA, 1988.
- [35] J. B. Tenenbaum, V. De Silva, and J. C. Langford, "A global geometric framework for nonlinear dimensionality reduction," *Science*, vol. 290, no. 5500, pp. 2319–2323, 2000.
- [36] N. Tishby and N. Slonim, "Data clustering by Markovian relaxation and the information bottleneck method," in *Neural Information Processing Systems (NIPS '00)*, Denver, Colo, USA, June 2000.
- [37] J.-D. Tournier, F. Calamante, D. G. Gadian, and A. Connelly, "Direct estimation of the fiber orientation density function from diffusion-weighted MRI data using spherical deconvolution," *NeuroImage*, vol. 23, no. 3, pp. 1176–1185, 2004.
- [38] D. S. Tuch, "Q-ball imaging," *Magnetic Resonance in Medicine*, vol. 52, no. 6, pp. 1358–1372, 2004.
- [39] Z. Wang and B. C. Vemuri, "DTI segmentation using an information theoretic tensor dissimilarity measure," *IEEE Transactions on Medical Imaging*, vol. 24, no. 10, pp. 1267–1277, 2005.
- [40] Y. Weiss, "Segmentation using eigenvectors: a unifying view," in *Proceedings of the IEEE International Conference on Computer Vision (ICCV '99)*, vol. 2, pp. 975–982, Kerkyra, Greece, September 1999.
- [41] L. Zelnik-Manor and P. Perona, "Self-tuning spectral clustering," *Advances in Neural Information Processing Systems*, vol. 17, pp. 1601–1608, 2004.
- [42] U. Ziyen, D. Tuch, and C.-F. Westin, "Segmentation of thalamic nuclei from DTI using spectral clustering," in *Medical Image Computing and Computer-Assisted Intervention (MICCAI '06)*, vol. 4191 LNCS - II of *Lecture Notes in Computer Science*, pp. 807–814, Springer, Copenhagen, Denmark, October 2006.

Research Article

Repetitive Transcranial Magnetic Stimulation of Dorsolateral Prefrontal Cortex Affects Performance of the Wisconsin Card Sorting Task during Provision of Feedback

Ji Hyun Ko,^{1,2} Oury Monchi,³ Alain Ptito,¹ Michael Petrides,¹ and Antonio P. Strafella^{2,4}

¹Montreal Neurological Institute, McGill University, Montréal, PQ, Canada H3A 2B4

²PET Imaging Centre, Centre for Addiction and Mental Health, University of Toronto, Toronto, ON, Canada M5T 1R8

³Functional Neuroimaging Unit, Geriatric's Institute, University of Montréal, Montréal, PQ, Canada H3W 1W5

⁴Toronto Western Research Institute and Hospital, University of Toronto, Toronto, ON, Canada M5T 2S8

Correspondence should be addressed to Antonio P. Strafella, antonio.strafella@uhnres.utoronto.ca

Received 20 October 2007; Accepted 22 December 2007

Recommended by Julien Doyon

Early functional neuroimaging studies of tasks evaluating executive processes, such as the Wisconsin card sorting task (WCST), only assessed trials in blocks that may contain a large amount of different cognitive processes. More recently, we showed using event-related fMRI that the dorsolateral prefrontal cortex (DL-PFC) significantly increased activity during feedback but not matching periods of the WCST, consistent with its proposed role in the monitoring of information in working memory. Repetitive transcranial magnetic stimulation (rTMS) is a method that allows to disrupt processing within a given cortical region and to affect task performance for which this region is significantly solicited. Here we applied rTMS to test the hypothesis that the DL-PFC stimulation influences monitoring of working memory without interfering with other executive functions. We applied rTMS to the right DL-PFC and the vertex (control site) in different time points of the WCST. When rTMS was applied to the DL-PFC specifically during the period when subjects were receiving feedback regarding their previous response, WCST performance deteriorated, while rTMS did not affect performance during matching either when maintaining set or during set-shifting. This selective impairment of the DL-PFC is consistent with its proposed role in monitoring of events in working memory.

Copyright © 2008 Ji Hyun Ko et al. This is an open access article distributed under the Creative Commons Attribution License, which permits unrestricted use, distribution, and reproduction in any medium, provided the original work is properly cited.

1. INTRODUCTION

There is considerable evidence that damage to the prefrontal cortex impairs performance on cognitive set-shifting tasks [1–3]. In one such task, the Wisconsin card sorting task (WCST), the subject has to match, over successive trials, a test card to one of four reference cards based on a matching rule that the subject acquires on the basis of feedback provided after each matching response. Patients with prefrontal lesions are often impaired in shifting the principle of matching when the feedback provided indicates that a cognitive shift in mental set is required. Functional neuroimaging studies support these observations [4–6]. In a recent study, conducted with functional magnetic resonance imaging (fMRI), we demonstrated differential activation of different parts of the prefrontal cortex during the performance of the WCST. In particular, we were able to show that the dorsolateral prefrontal

cortex (DL-PFC) was engaged when feedback was provided [4]. This selective engagement of the mid-DL-PFC during the provision of feedback after each matching response by the subject is consistent with the proposed role of this part of the prefrontal cortex in the monitoring of events in working memory [7–9]. Neuroimaging studies, however, suffer from the limitation that they provide neuronal correlates of cognitive performance and cannot determine a causal relation between observed brain activity and cognitive performance [10, 11]. Thus the specific functional relevance of the DL-PFC in monitoring the feedback provided during the performance of set-shifting tasks remains to be established.

Here we have used repetitive transcranial magnetic stimulation (rTMS) to examine this issue. The application of rTMS to an area of cortex that, at a particular point in time, is actively involved in the processing of task-relevant information should cause performance to decline [12–14]. In other

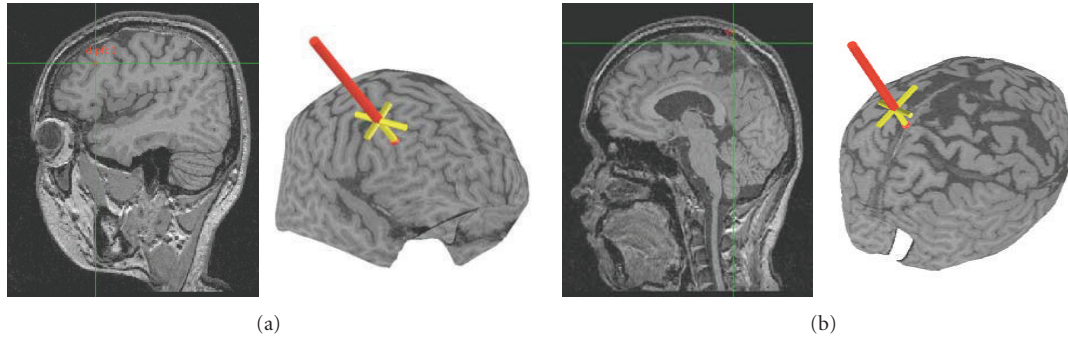


FIGURE 1: TMS coil was located over (a) the right DL-PFC ($X = 45$, $Y = 33$, $Z = 25$) or (b) the vertex (control) ($X = 0$, $Y = -35$, $Z = 80$). The positioning of the TMS coil over these locations, marked on the native MRI, was performed with the aid of a frameless stereotaxic system.

words, rTMS acts as a “virtual lesion” producing a temporary interruption of processing [15]. In the present study, we tested the hypothesis that rTMS of the human DL-PFC influences monitoring of the information held in the working memory without interfering with other executive functions. To test this specific hypothesis, we used a computerized version of the WCST [4] in which different stages of task performance can be isolated. We applied rTMS to the right DL-PFC and over a control site (the vertex) in three different ways: at the beginning of the feedback period, at the beginning of the matching response period, and independently of task timing. Our previous functional neuroimaging study had indicated the involvement of the DL-PFC during the provision of feedback, but not during the matching response. To further strengthen our findings, we also added a control task (Figure 3(b)) that only required matching to a twin card.

2. MATERIALS AND METHODS

Ten healthy subjects (19–33 years) participated in the study after having given written informed consent. All subjects were right-handed according to the Edinburgh handedness inventory [16], they had no previous personal or family history of neurological or psychiatric disorders and were not taking any medication at the time of experiments. The experiments were approved by the Research Ethics Committee of the Montreal Neurological Institute and Hospital. Figure 2 displays an overview and timing of the experimental setup.

2.1. Cognitive task

Subjects were trained for 30 minutes on the WCST before the rTMS sessions. Prior to the training sessions, the subjects were instructed to perform as well as they could. During the WCST, four reference cards and one matching card were presented on a computer screen (Figure 3(a)). On each trial, the subjects had to match a test card to one of the four reference cards according to one of three rules: shape, number, or color. The currently appropriate rule for classification is found by trial and error based on the 3-second positive or negative feedback that is provided immediately after each matching decision. The rule for classification changed randomly after the subject answers correctly on six consecutive

trials. In the control task, the matching card was identical to one of the reference cards so that the subject simply selected the identical card and did not have to find an appropriate rule for classification as in the WCST (Figure 3(b)). Subjects performed the card-sorting tasks in six different rTMS sessions (2×3 design). Five-minute breaks were given in between sessions. Each session lasted six minutes.

2.2. Frameless stereotaxy system

In order to target the DL-PFC and vertex (control site) in all our subjects (Figure 1), we used a procedure that takes advantage of the standardized stereotaxic space of Talairach and Tournoux [17] and frameless stereotaxy [18, 19]. A high-resolution MRI of the subjects’ brain was acquired and transformed into standardized stereotaxic space using the algorithm of Collins et al. [20]. The coordinates selected for the right DL-PFC ($X = 45$, $Y = 33$, $Z = 25$) were based on a previous functional activation study that yielded increased activity during the feedback period [4]. Of note, in this study, we stimulated the DL-PFC located in the right hemisphere because this side appeared to be more consistently and robustly activated [4]. The control stimulation site (i.e., vertex region, $X = 0$, $Y = -35$, $Z = 80$) was also chosen based on its lack of activation during performance of the WCST in these previous studies.

The Talairach coordinates were converted into each subject’s native MRI space using the reverse native-to-talairach transformation [18]. The positioning of the TMS coil over these locations, marked on the native MRI (Figure 1), was performed with the aid of a frameless stereotaxic system (Rogue Research, Montreal, Canada).

2.3. TMS protocol

Repetitive TMS was carried out with the Magstim high-speed magnetic stimulator (Magstim, UK) using a figure-eight coil. The coil was held in a fixed position over the stimulation sites by a mechanical arm. It was positioned so that magnetically induced current under the coil flowed in a posterior-anterior direction. Stimulus intensities, expressed as a percentage of the maximum stimulator output, were set at 110% of the resting motor threshold (RMT). RMT was defined as

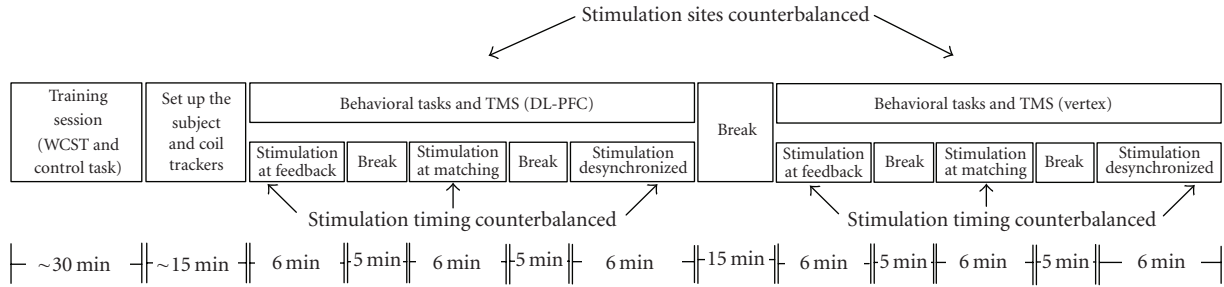


FIGURE 2: Timeline of the experimental setup. All subjects were trained for approximately 30 minutes at the beginning of the experiment. After registering the subjects’ anatomical landmarks to their structural MRIs, the subjects performed 6 minutes of the behavioral tasks while rTMS was administered at DL-PFC or vertex (control) in three different timing conditions. The orders of stimulation sites and timings were counterbalanced. The behavioral tasks consisted of WCST and control task.

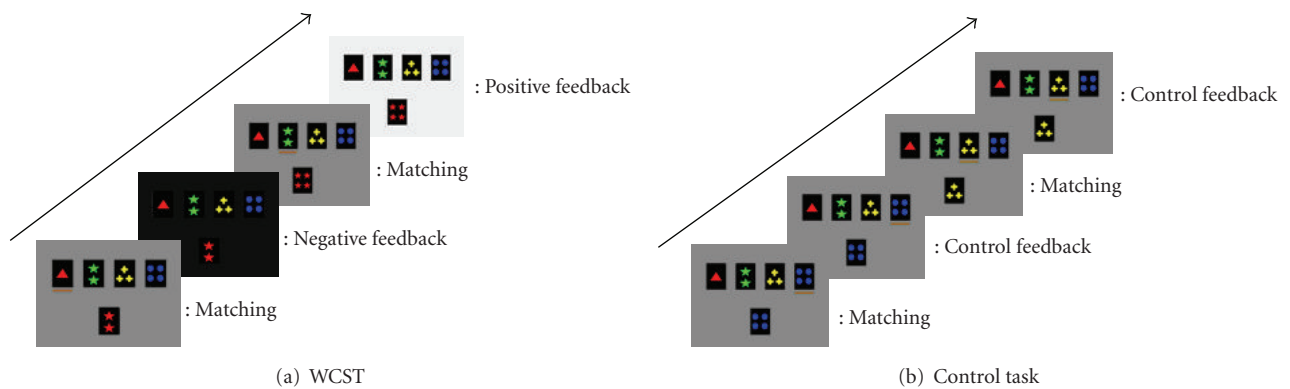


FIGURE 3: Behavioral tasks. (a) WCST: the four cards shown on the top in the computer screen are reference cards, and the card on the bottom is the test card. The subjects could move a yellow bar which was displayed under the reference cards by pressing the left button of a mouse with their index finger. Pressing the right button with the middle finger confirmed the selection of the card followed by negative or positive feedback. The subjects had to find out the rule of classification (color, shape, and number) by trial and error. (b) Control task: the test card was identical to one of the reference cards. The rest was the same as WCST.

the lowest stimulus intensity able to elicit, in the contralateral first dorsal interosseous (FDI) muscle, 5 motor evoked potentials (MEPs) of at least 50 μ V amplitude in a series of 10 stimuli delivered over the right primary motor cortex at intervals longer than 5 seconds. MEPs were recorded from the FDI muscle with Ag\Cl surface electrodes fixed on the skin with a belly-tendon montage. The EMG signal was filtered (10 Hz–1 kHz bandpass), digitized at 2 kHz, and displayed on a computer screen [19].

Three rTMS blocks (6 minutes each) were applied to the right DL-PFC and the vertex during the WCST and control task (Figure 2). Each block was separated by a 5-minute interval. In each block, 5 pulse trains of 250-millisecond duration were delivered at a stimulation frequency of 20 Hz with between-train interval dependent on the subject’s performance time (PT) (i.e., 4 to 6 second). For each block, rTMS was delivered either (*block-1*) at the beginning of each feedback period (number of trials: 72.05 ± 0.75) (Figure 4), (*block-2*) at the beginning of each matching period (number of trials: 74.15 ± 1.19) (Figure 5), or (*block-3*) every 6 second regardless of the moment in the task (i.e., desynchronized condition) (number trials: 75.53 ± 2.14) (Figure 6). This last paradigm was applied in order to investigate whether the

rTMS effect was timing dependent (i.e., block-1 and -2) or not (block-3). Block order was counterbalanced across subjects and performed on the same day (Figure 2). The stimulation parameters followed safety guidelines for rTMS [21].

2.4. Data analysis

PT and error rate were calculated. Each subject’s PT and error rate were averaged within each condition (stimulation site, timing, and task). PT was measured from the presentation of the test card to the subject’s response, that is, the selection of a reference card (Figures 4, 5, and 6).

Repeated-measures ANOVA was used to compare the effect of the two different stimulation sites, the three timings of stimulation, and the two different tasks on PT.

The paired samples *t*-test (two-tailed) was used to compare the mean PT and error rate in the WCST between the DL-PFC and vertex stimulations during the three different rTMS timing conditions (rTMS during feedback, during matching, and desynchronized). The mean PT for the control task was also compared in the same manner. Data are presented as mean \pm SE. All statistical analysis was performed using SPSS 13.0 for Windows (SPSS Inc., USA).

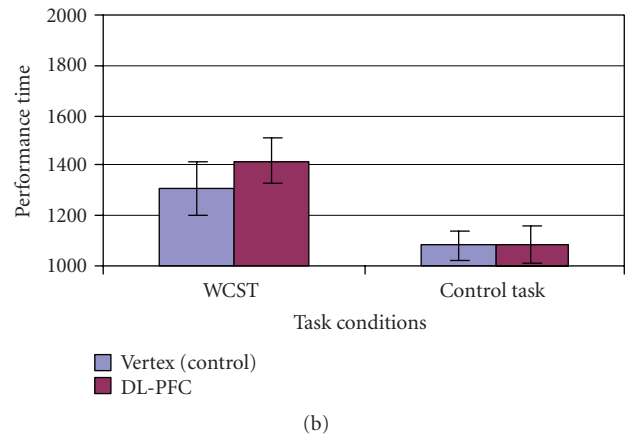
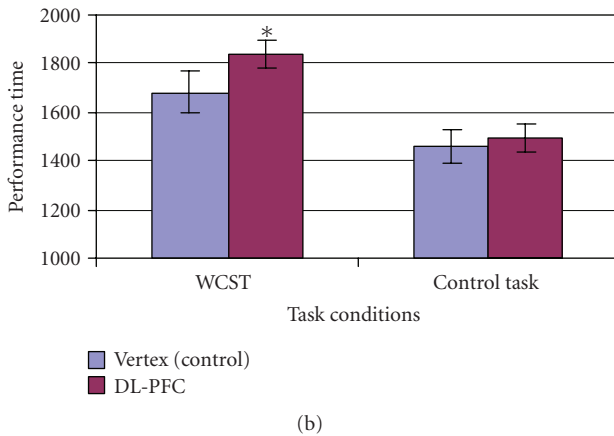
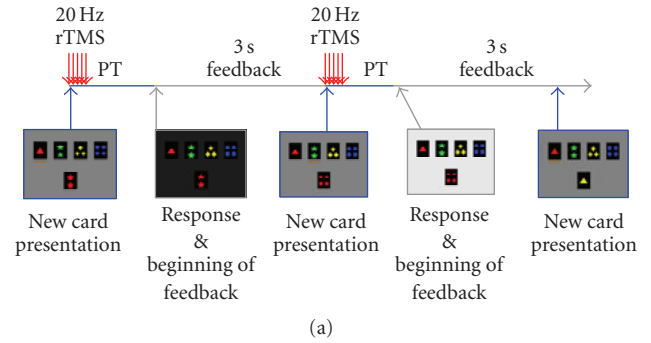
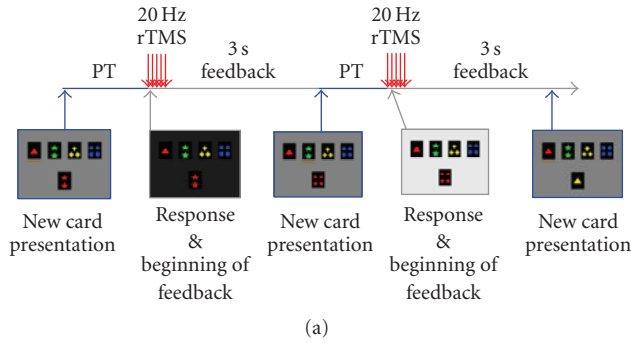


FIGURE 4: (a) rTMS at the beginning of feedback: while the subject performed the WCST or control task, rTMS was applied over the right DL-PFC or vertex at the beginning of receiving feedback. (b) DL-PFC stimulation during the feedback phase of the WCST increased performance time (PT) compared to the vertex stimulation ($*P = .023$; two-tailed). No stimulation effect was observed in the control task.

FIGURE 5: (a) rTMS at the beginning of matching: while the subject performed the WCST or control task, rTMS was applied over the right DL-PFC or vertex at the beginning of matching. (b) DL-PFC stimulation during the matching phase of WCST or control task had no effect on PT compared to the vertex stimulation.

3. RESULTS

TMS intensity was $58.4 \pm 2.8\%$. There was no significant difference between numbers of trials among different blocks. Repeated-measures ANOVA on PT revealed a significant main effect of different tasks (WCST versus control; $F(1,9) = 71.3$; $P < .001$) confirming that the WCST was more demanding than the control task. There was also a significant main effect of stimulation timing on PT (beginning of feedback versus beginning of matching versus desynchronized; $F(2,18) = 23.845$; $P < .001$) indicating that the timing of stimulation, overall, was an important factor influencing task performance more than stimulation site (DL-PFC versus vertex; $F(1,9) = 2.516$; $P = .147$). A significant interaction effect was observed between tasks and stimulation site ($F(1,9) = 7.642$; $P = .022$) indicating that stimulation site affected PT differently depending on which task was used.

To test the effect of different stimulation sites within each task and stimulation timing condition, a paired t -test (two-tailed) was performed. When comparing DL-PFC versus vertex during the WCST, PT increased significantly when rTMS was delivered at the beginning of the feedback period (DL-PFC = 1840.04 ± 87.18 ms, Vertex = 1682.46 ± 61.23 ms;

$t(9) = 2.727$; $P = .023$) (Figure 4). Further analysis revealed that the magnitude of impairment did not correlate with intensity of TMS ($r = -0.063$; $P = .863$). No changes in PT were observed when rTMS was given at the beginning of the matching period (DL-PFC = 1419.19 ± 107.48 ms, Vertex = 1309.87 ± 88.07 ms; $t(9) = 1.382$; $P = .200$) (Figure 5) nor when it was desynchronized with task performance (DL-PFC = 1739.13 ± 148.26 ms, Vertex = 1659.70 ± 98.24 ms; $t(9) = 0.944$; $P = .370$) (Figure 6). When comparing DL-PFC versus vertex during the control task, rTMS did not induce significant changes in PT either during the feedback (DL-PFC = 1491.66 ± 65.47 ms, Vertex = 1459.48 ± 59.60 ms; $t(9) = 0.669$; $P = .521$) (Figure 4), matching (DL-PFC = 1084.92 ± 62.15 ms, Vertex = 1080.26 ± 77.11 ms; $t(9) = 0.074$; $P = .943$) (Figure 5), or desynchronized (DL-PFC = 1517.38 ± 147.72 ms, Vertex = 1490.91 ± 90.36 ms; $t(9) = 0.314$; $P = .760$) conditions (Figure 6).

The repeated-measures ANOVA on error rate did not show any significant main effect of task conditions, stimulation timing, or the sites of stimulation, nor significant interaction effects except when comparing DL-PFC and vertex at the beginning of feedback which came close to significance. More specifically, the results obtained when performing a paired t -test on the error rates between DL-PFC and vertex

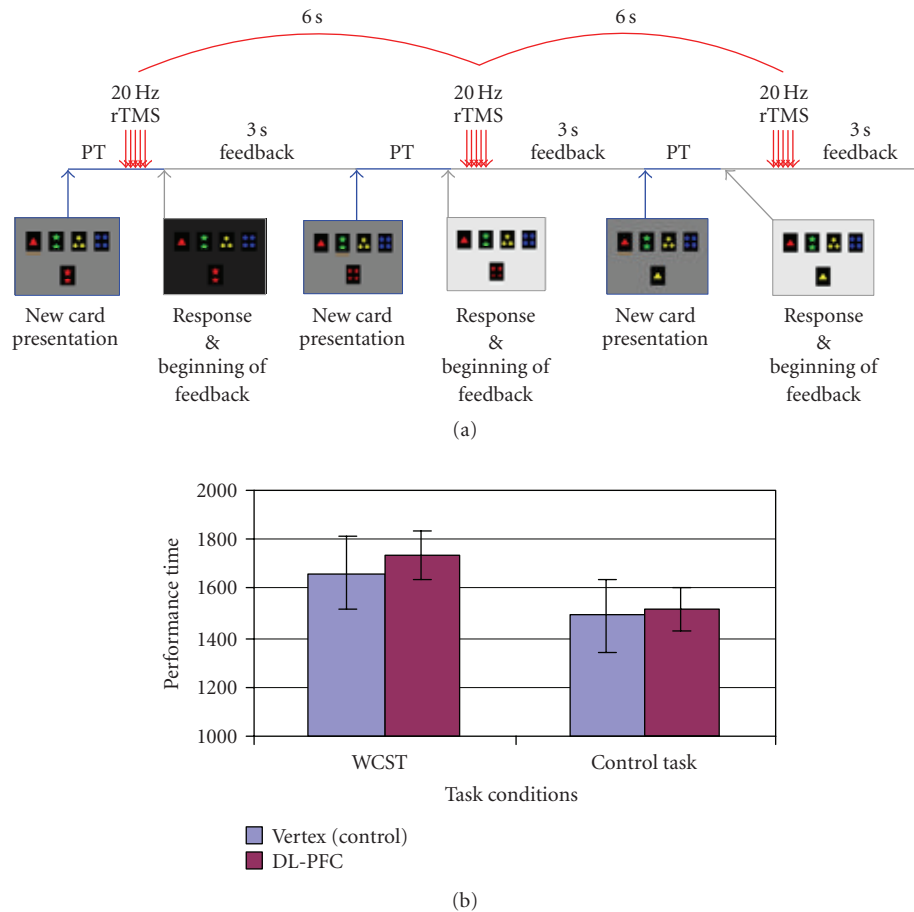


FIGURE 6: (a) Desynchronized rTMS: while the subject performed the WCST or control task, rTMS was applied over the right DL-PFC or vertex at every 6 seconds which was desynchronized with the tasks. (b) Desynchronized DL-PFC stimulation had no effect on PT compared to the vertex stimulation.

stimulation during the WCST were at the beginning of the feedback (DL-PFC = 6.10 ± 1.71 , Vertex = 3.28 ± 1.16 ; $t(9) = 2.120$; $P = .063$); at the beginning of matching (DL-PFC = 4.79 ± 1.04 , Vertex = 4.86 ± 1.27 ; $t(9) = -0.057$; $P = .956$); during the desynchronized condition (DL-PFC = 5.21 ± 0.83 , Vertex = 3.56 ± 0.51 ; $t(9) = 1.941$; $P = .084$).

4. DISCUSSION

The present study demonstrated that when rTMS was applied to the DL-PFC specifically during the period when the subject was receiving feedback regarding his/her matching response, performance of the WCST deteriorated. It appeared that the effect of rTMS was significantly timing dependent. In fact, rTMS-induced interference of DL-PFC affected performance specifically during the receiving of feedback (Figure 4), but not during the matching response (Figure 5) nor when the interference was desynchronized with specific stages of the WCST (Figure 6).

This observation of a selective rTMS-induced impairment in task performance during specific timing of a task has already been reported in the literature in relation to several of the tasks and cortical areas stimulated. For instance,

rTMS of the medial frontal cortex affected task switching and at the time of response set switching when delivered before or at time of response selection [10, 22]. Similarly, rTMS affected DL-PFC depending on whether this area, at a particular point in time, is actively involved in processing task relevant information [11, 23].

The selective rTMS-induced impairment in WCST performance of DL-PFC during the receiving of feedback is in accordance with imaging, lesion, and neurophysiological investigations. In a previous fMRI study, Monchi et al. [4] have shown that DL-PFC is engaged when the subject is receiving feedback during the WCST. That is, the period when monitoring of information held in working memory, as demonstrated by lesion studies in monkeys, is critical [8, 24]. This specific involvement has also been confirmed with neuronal recordings from DL-PFC in monkeys during a WCST analog which have shown the activation of DL-PFC cells during monitoring and use of feedback information. A large population of DL-PFC cells were strongly engaged in assessing behavioral outcome/feedback [25].

Interestingly, while rTMS induced selective impairment in WCST performance, it did not affect error rate very

significantly. This observation is consistent with previous work by Wagner et al. [26] who, stimulating the DL-PFC, observed no significant effect on error making during the WCST. There are two potential alternatives that could explain these findings.

The first explanation is that error making may be influenced by a different prefrontal area. In fact, lesions of DL-PFC in monkeys have shown impairment in monitoring of information but did not compromise maintenance of information and set shifting per se [8, 9, 24], which presumably may influence errors during set-shifting tasks. Set shifting from a previously relevant to a new response mode engages a more ventral area of the PFC (i.e., ventrolateral PFC) [4] and is impaired by lesioning of this area [24, 27]. Another cortical area that may also have a relevant role is the medial PFC which can influence error trials during performance-monitoring processes [25].

A second explanation, considering the fact that rTMS-induced error trials have been reported less frequently in relation to different tasks and cortical area stimulated [10, 22, 23, 28], it may also be that rTMS parameters (e.g., intensity, frequency, and unilateral stimulation) used so far in different studies have not been strong enough to induce a complete “virtual lesion.” Against the latter hypothesis, however, stands the fact that the magnitude of selective impairment in WCST performance observed in this study did not correlate with intensity of TMS which at least excludes a possible relationship between intensity and effect on performance.

While our study provides some insights over the debate regarding the role of DL-PFC during set-shifting tasks, overall it emphasizes the importance of rTMS in delineating the functional relevance of neuronal correlates of performance observed during neuroimaging studies [10, 11]. In other words, our results suggest that just because a cortical area (i.e., DL-PFC) is functionally activated during the course of an executive task [4], it may not necessarily play the same critical and essential role during the whole task, and that rTMS may be a useful tool to complement fMRI in order to infer functionality of a cortical region of the human brain.

To date, the neural mechanisms underlying executive processes are still poorly understood, even less are the mechanisms by which rTMS interferes with cortical information processing and induces such a “temporary lesion.” It is believed that the rTMS-induced “noise” into neural processes may, perhaps, be the consequence of a stimulation-induced synchronization of neuronal firing disrupting active processing in the underlying cortex [15, 29]. A valid alternative, however, may also be represented by a suppression in cortical excitability (lasting up to 1 second) observed following short trains of rTMS at 20 Hz [30] or induced abnormality in the release of prefronto-striatal dopamine [19].

The latter is suggested by the contribution of the striatum and role played by dopamine during the performance of tasks requiring executive processes. Indeed, studies of dopamine depletion in nonhuman primates suggest a possible involvement of striatal dopamine in set-shifting tasks [31, 32] while other neuroimaging studies have proposed that changes in striatal dopamine levels can modulate certain set-shifting

processes [33] and that level of cognitive impairment may be dependent on the level of dopamine depletion [34].

Whatever the rTMS mechanisms may be, the ultimate outcome appears to be a transient interruption of the specific normal cortical processing (i.e., provision of feedback) in a restricted area of the prefrontal cortex (i.e., DL-PFC).

ACKNOWLEDGMENTS

This work was funded by the Canadian Institutes of Health Research and Canadian Foundation Innovation (CFI) to APS, Fonds de la Recherche en Santé du Québec to APS and OM, and Regroupement Provincial en Imagerie Cérébrale to APS and OM.

REFERENCES

- [1] B. Milner, “Effects of brain lesions on card sorting,” *Archives of Neurology*, vol. 9, pp. 90–100, 1963.
- [2] H. E. Nelson, “A modified card sorting test sensitive to frontal lobe defects,” *Cortex*, vol. 12, no. 4, pp. 313–324, 1976.
- [3] D. T. Stuss, B. Levine, M. P. Alexander, et al., “Wisconsin Card Sorting Test performance in patients with focal frontal and posterior brain damage: effects of lesion location and test structure on separable cognitive processes,” *Neuropsychologia*, vol. 38, no. 4, pp. 388–402, 2000.
- [4] O. Monchi, M. Petrides, V. Petre, K. Worsley, and A. Dagher, “Wisconsin Card Sorting revisited: distinct neural circuits participating in different stages of the task identified by event-related functional magnetic resonance imaging,” *The Journal of Neuroscience*, vol. 21, no. 19, pp. 7733–7741, 2001.
- [5] O. Monchi, M. Petrides, A. P. Strafella, K. J. Worsley, and J. Doyon, “Functional role of the basal ganglia in the planning and execution of actions,” *Annals of Neurology*, vol. 59, no. 2, pp. 257–264, 2006.
- [6] A. M. Owen, “Cognitive dysfunction in Parkinson’s disease: the role of frontostriatal circuitry,” *The Neuroscientist*, vol. 10, no. 6, pp. 525–537, 2004.
- [7] M. Petrides, “Functional specialization within the dorsolateral frontal cortex for serial order memory,” *Proceedings of the Royal Society. Series B*, vol. 246, no. 1317, pp. 299–306, 1991.
- [8] M. Petrides, “Frontal lobes and behaviour,” *Current Opinion in Neurobiology*, vol. 4, no. 2, pp. 207–211, 1994.
- [9] M. Petrides, “The role of the mid-dorsolateral prefrontal cortex in working memory,” *Experimental Brain Research*, vol. 133, no. 1, pp. 44–54, 2000.
- [10] M. F. Rushworth, K. A. Hadland, T. Paus, and P. K. Sipila, “Role of the human medial frontal cortex in task switching: a combined fMRI and TMS study,” *Journal of Neurophysiology*, vol. 87, no. 5, pp. 2577–2592, 2002.
- [11] J. A. Johnson, A. P. Strafella, and R. J. Zatorre, “The role of the dorsolateral prefrontal cortex in bimodal divided attention: two transcranial magnetic stimulation studies,” *Journal of Cognitive Neuroscience*, vol. 19, no. 6, pp. 907–920, 2007.
- [12] A. Pascual-Leone, J. Valls-Solé, E. M. Wassermann, and M. Hallett, “Responses to rapid-rate transcranial magnetic stimulation of the human motor cortex,” *Brain*, vol. 117, no. 4, pp. 847–858, 1994.
- [13] H. Enomoto, Y. Ugawa, R. Hanajima, et al., “Decreased sensory cortical excitability after 1 Hz rTMS over the ipsilateral primary motor cortex,” *Clinical Neurophysiology*, vol. 112, no. 11, pp. 2154–2158, 2001.

- [14] Y. Z. Huang, M. J. Edwards, E. Rounis, K. P. Bhatia, and J. C. Rothwell, "Theta burst stimulation of the human motor cortex," *Neuron*, vol. 45, no. 2, pp. 201–206, 2005.
- [15] V. Walsh and A. Cowey, "Transcranial magnetic stimulation and cognitive neuroscience," *Nature Reviews Neuroscience*, vol. 1, no. 1, pp. 73–79, 2000.
- [16] R. C. Oldfield, "The assessment and analysis of handedness: the Edinburgh inventory," *Neuropsychologia*, vol. 9, no. 1, pp. 97–113, 1971.
- [17] J. Talairach and P. Tournoux, *Co-Planar Stereotaxic Atlas of the Human Brain: 3-Dimensional Proportional System: An Approach to Cerebral Imaging*, Thieme Medical Publishers, New York, NY, USA, 1988.
- [18] T. Paus, "Imaging the brain before, during, and after transcranial magnetic stimulation," *Neuropsychologia*, vol. 37, no. 2, pp. 219–224, 1998.
- [19] A. P. Strafella, T. Paus, J. Barrett, and A. Dagher, "Repetitive transcranial magnetic stimulation of the human prefrontal cortex induces dopamine release in the caudate nucleus," *The Journal of Neuroscience*, vol. 21, no. 15, pp. RC1571–RC1574, 2001.
- [20] D. L. Collins, P. Neelin, T. M. Peters, and A. C. Evans, "Automatic 3D intersubject registration of MR volumetric data in standardized Talairach space," *Journal of Computer Assisted Tomography*, vol. 18, no. 2, pp. 192–205, 1994.
- [21] E. M. Wassermann, "Risk and safety of repetitive transcranial magnetic stimulation: report and suggested guidelines from the International Workshop on the Safety of Repetitive Transcranial Magnetic Stimulation, June 5–7, 1996," *Electroencephalography and Clinical Neurophysiology*, vol. 108, no. 1, pp. 1–16, 1998.
- [22] S. W. Kennerley, K. Sakai, and M. F. Rushworth, "Organization of action sequences and the role of the pre-SMA," *Journal of Neurophysiology*, vol. 91, no. 2, pp. 978–993, 2004.
- [23] K. A. Hadland, M. F. Rushworth, R. E. Passingham, M. Jahanshahi, and J. C. Rothwell, "Interference with performance of a response selection task that has no working memory component: an rTMS comparison of the dorsolateral prefrontal and medial frontal cortex," *Journal of Cognitive Neuroscience*, vol. 13, no. 8, pp. 1097–1108, 2001.
- [24] M. Petrides, "Lateral prefrontal cortex: architectonic and functional organization," *Philosophical Transactions of the Royal Society of London. Series B*, vol. 360, no. 1456, pp. 781–795, 2005.
- [25] F. A. Mansouri, K. Matsumoto, and K. Tanaka, "Prefrontal cell activities related to monkeys' success and failure in adapting to rule changes in a Wisconsin Card Sorting Test analog," *The Journal of Neuroscience*, vol. 26, no. 10, pp. 2745–2756, 2006.
- [26] M. Wagner, T. A. Rihs, U. P. Mosimann, H. U. Fisch, and T. E. Schlaepfer, "Repetitive transcranial magnetic stimulation of the dorsolateral prefrontal cortex affects divided attention immediately after cessation of stimulation," *Journal of Psychiatric Research*, vol. 40, no. 4, pp. 315–321, 2006.
- [27] S. D. Iversen and M. Mishkin, "Perseverative interference in monkeys following selective lesions of the inferior prefrontal convexity," *Experimental Brain Research*, vol. 11, no. 4, pp. 376–386, 1970.
- [28] V. Walsh and A. Pascual-Leone, *Transcranial Magnetic Stimulation: A Neurochronometrics of Mind*, MIT Press, Cambridge, Mass, USA, 2003.
- [29] A. Pascual-Leone, V. Walsh, and J. Rothwell, "Transcranial magnetic stimulation in cognitive neuroscience—virtual lesion, chronometry, and functional connectivity," *Current Opinion in Neurobiology*, vol. 10, no. 2, pp. 232–237, 2000.
- [30] N. Modugno, Y. Nakamura, C. D. MacKinnon, et al., "Motor cortex excitability following short trains of repetitive magnetic stimuli," *Experimental Brain Research*, vol. 140, no. 4, pp. 453–459, 2001.
- [31] A. C. Roberts, M. A. De Salvia, L. S. Wilkinson, et al., "6-Hydroxydopamine lesions of the prefrontal cortex in monkeys enhance performance on an analog of the Wisconsin Card Sort Test: possible interactions with subcortical dopamine," *The Journal of Neuroscience*, vol. 14, no. 5, pp. 2531–2544, 1994.
- [32] P. Collins, L. S. Wilkinson, B. J. Everitt, T. W. Robbins, and A. C. Roberts, "The effect of dopamine depletion from the caudate nucleus of the common marmoset (*Callithrix jacchus*) on tests of prefrontal cognitive function," *Behavioral Neuroscience*, vol. 114, no. 1, pp. 3–17, 2000.
- [33] O. Monchi, J. H. Ko, and A. P. Strafella, "Striatal dopamine release during performance of executive functions: a [¹¹C] raclopride PET study," *NeuroImage*, vol. 33, no. 3, pp. 907–912, 2006.
- [34] V. L. Cropley, M. Fujita, R. B. Innis, and P. J. Nathan, "Molecular imaging of the dopaminergic system and its association with human cognitive function," *Biological Psychiatry*, vol. 59, no. 10, pp. 898–907, 2006.

Research Article

Dorsolateral Prefrontal Cortex: A Possible Target for Modulating Dyskinesias in Parkinson's Disease by Repetitive Transcranial Magnetic Stimulation

I. Rektorova, S. Sedlackova, S. Telecka, A. Hlubocky, and I. Rektor

First Department of Neurology, Masaryk University, Saint Anne's Hospital, Pekařská 53, 65691 Brno, Czech Republic

Correspondence should be addressed to I. Rektorova, irena.rektorova@fnusa.cz

Received 30 April 2007; Accepted 2 October 2007

Recommended by Antonio P. Strafella

We studied whether five sessions of 10 Hz repetitive transcranial magnetic stimulation (rTMS treatment) applied over the dorsolateral prefrontal cortex (DLPFC) or the primary motor cortex (MC) in advanced Parkinson's disease (PD) patients would have any effect on L-dopa-induced dyskinesias and cortical excitability. We aimed at a randomised, controlled study. Single-pulse transcranial magnetic stimulation (TMS), paired-pulse transcranial magnetic stimulation, and the Unified Parkinson's Disease Rating Scale (UPDRS parts III and IV) were performed prior to, immediately after, and one week after an appropriate rTMS treatment. Stimulation of the left DLPFC induced a significant motor cortex depression and a trend towards the improvement of L-dopa-induced dyskinesias.

Copyright © 2008 I. Rektorova et al. This is an open access article distributed under the Creative Commons Attribution License, which permits unrestricted use, distribution, and reproduction in any medium, provided the original work is properly cited.

1. INTRODUCTION

The neural mechanisms that underlie L-dopa-induced dyskinesias in Parkinson's disease (PD) remain poorly understood [1–4]. Dyskinesias have been associated with pulsatile stimulation of dopamine receptors, downstream changes in genes and proteins, and changes in nondopamine transmitter systems [4–6]. All these changes lead to alterations in the firing patterns within the basal ganglia, causing overactivations of the primary motor cortex and premotor cortical areas [7, 8]. Activation studies in PD patients ($H_2^{15}O$ positron emission tomography (PET) and ^{133}Xe single photon emission computed tomography (SPECT)) are in line with these results, and indicate that L-dopa-induced dyskinesias are associated with inappropriate overactivity of striatofrontal projections both at rest and during volitional actions [2, 9]. Comparison of rest with dyskinesias versus rest without dyskinesias showed a relative activation of the motor cortex, the lateral and mesial premotor areas including the supplementary motor area (SMA), the dorsal prefrontal cortex, and the basal ganglia. The comparison of dyskinetic versus nondyskinetic states during voluntary movement revealed additional activation of the same brain regions [9]. Unfortunately, in the

PET study of Brooks et al. [9] mentioned above, regional cerebral blood flow (rCBF) in PD patients with and without L-dopa induced dyskinesias was not compared to that of healthy subjects, and therefore, it is difficult to speculate whether the relative increases in rCBF observed in patients with dyskinesias were in fact above or still below that of controls in all the reported areas including the DLPFC.

Repetitive transcranial magnetic stimulation (rTMS) can produce changes in excitability of cortical circuits that outlast the period of stimulation, opening the possibility of intervening directly with the mechanisms of cortical plasticity in the human cortex. rTMS is also a suitable tool to investigate plasticity within a distributed functional network since conditioning effects of rTMS are not limited to the stimulated area but give rise to functional changes in interconnected cortical areas. The magnitude and the direction of rTMS-induced plasticity depend on extrinsic factors (i.e., the variables of stimulation such as intensity, frequency, and total number of stimuli) and intrinsic factors (i.e., the functional state of the cortex targeted by rTMS). High frequencies of rTMS applied over the motor cortex lead to facilitatory aftereffects on corticospinal excitability while low-frequency stimulations lead to opposite (i.e., inhibitory) aftereffects (for review, see 10).

The main problem remains, that the basic mechanisms mediating the effects of rTMS are still poorly understood.

Recently, several studies have suggested the therapeutic efficacy of rTMS in PD while other studies have found no clinical improvement of motor performance in PD [11–15]. Using rTMS over the SMA, an Italian group [4] showed that 900 pulses of 1 Hz rTMS with an intensity set at 90% of the resting motor excitability threshold markedly reduced drug-induced dyskinesias in 8 advanced PD patients. In spite of this promising result, a year later the same group [16] discovered that 5 repeated sessions of the 1 Hz rTMS failed to enhance and/or prolong the beneficial effects of the procedure, and thus could not be considered clinically useful. Very similar results were reported by a Toronto group [17] who used the same stimulation parameters but targeted the primary motor cortex contralateral to the side with more severe dyskinesias in 6 PD patients. Although the benefit was evident at day 1 after a two-week course of rTMS, the authors have not managed to obtain more sustained clinical improvement after the treatment.

We recently reported the results of a pilot study that investigated whether 5 repeated sessions of high frequency rTMS at 10 Hz applied over the motor cortex (MC) of the relevant leg or over the left dorsolateral prefrontal cortex (DLPFC) might result in a modification of “off”-related freezing of gait and motor symptoms of PD in 6 advanced PD patients [18]. The selection of MC and DLPFC targets for rTMS was based on dopamine release in the putamen and caudate, respectively [19, 20]. The target selection was further supported by the results of Lomarev et al. [14] who had reported positive cumulative benefit of high-frequency rTMS applied over the same targets for improving gait, as well as reducing upper limb bradykinesia in PD patients. In our study, rTMS was well tolerated. Despite a reported trend towards improvement of the Stroop test interference after rTMS over the left DLPFC, freezing of gait and motor symptoms of PD remained unchanged by rTMS.

Interestingly, patients who had undergone the DLPFC treatment reported a subjective improvement of their dyskinesias. Therefore, in this paper, we present a post hoc analysis of the data from the same group of patients that focuses on cortical excitability and on the possible modification of L-dopa-induced dyskinesias by repeated sessions of rTMS over the DLPFC.

2. PATIENTS AND METHODS

We studied 6 patients (5 men and 1 woman, mean age 67.3 ± 7.7 years) with advanced PD according to the UK Parkinson's Disease brain bank criteria [21, 22], a Hoehn-Yahr stage [23] between 2.5 and 4 while in the “off” state, and without dementia (Mini-Mental State Examination [24] score > 24). A Montgomery-Asberg Depression Rating Scale [25] cut-off score of 14 was used to exclude patients with depression. Patients with a predominant tremor form of PD were also excluded from the study. All patients had dyskinesias, motor fluctuations, and “off”-related freezing of gait. The disease duration was 11.3 ± 3.1 years. The daily L-dopa dose equivalent was 1145.8 ± 413.2 mg; all patients were on

L-dopa \pm entacapone plus a dopamine receptor agonist. The antiparkinsonian medication was stable for at least 4 weeks prior to the study commencement and during the study. All patients signed the informed consent form, which was approved by the Ethics Committee of Saint Anne's Hospital in Brno.

rTMS was applied over the left DLPFC (5 cm anterior to the optimum scalp position for activation of the contralateral first dorsal interosseus muscle [26]) or over the optimal position for the tibialis anterior muscle contralateral to the foot which was most frequently used by the patient to make the first step after freezing of gait (i.e., MC), using the Magstim Super Rapid stimulator and a figure-of-eight coil with a mean diameter of 7 cm. The coil was placed tangentially to the scalp with the handle pointing backwards and laterally at 45° angle away from the midline inducing a posterior-anterior current in the brain. Nowadays, the frameless stereotaxy has been used in order to target the region of brain corresponding to cytoarchitectonic area 9/46 as defined by Petrides and Pandya [27]. Nevertheless, this part of the brain was found to overlap with the region targeted by the standard procedure (Rektorova and Paus, unpublished data), used in most studies.

rTMS was delivered in the “on” state (i.e., when PD medication was working and providing benefit) without dyskinesias according to the individual patients' diaries, at the same time of day. One treatment consisted of 5 sessions over 5 consecutive days. We chose a repeated sessions design, and our patients were stimulated while being in their “on” state since both conditions have been associated with better rTMS outcomes in literature [12, 14]. One session consisted of 1350 pulses delivered at 10 Hz frequency, at an intensity of 90% of the resting motor excitability threshold (for the right first dorsal interosseus muscle when stimulating the left DLPFC, and the appropriate tibialis anterior muscle when stimulating the MC). Each patient completed at least one rTMS treatment. The order of stimulation sites was randomized using closed envelopes. Although we aimed at a crossover design, only two patients completed both treatments (with a one-month interval between them).

In order to ensure the method was safe with regard to cognitive functions, a brief neuropsychological battery of tests was administered prior to, immediately after, and one week after each rTMS treatment. The results have been published elsewhere [18].

Experienced neurologists who were blinded to the stimulation site performed a neurological evaluation prior to, immediately after, and one week after appropriate rTMS treatment. The evaluation was conducted during the patients' relative “off” state (i.e., when PD medication was not improving PD symptoms resulting in a lack of mobility) according to the individual patients' diaries, at the same time of day. It consisted of the UPDRS, part III (motor examination) and part IV (treatment complications) [28]. A more detailed evaluation and analysis of gait and “off”-related freezing of gait has been reported elsewhere [18].

Single-pulse and paired-pulse TMS was performed while the patient was “on” to study the effects of rTMS treatments on cortical excitability. We used the paired-pulse TMS

TABLE 1: Effects of rTMS treatments on motor symptoms of PD and treatment complications as assessed by the UPDRSs III and IV. UPDRS III: Unified Parkinson’s Disease Rating Scale, part III, motor examination; UPDRS IV: Unified Parkinson’s Disease Rating Scale, part IV, treatment complications; Pre-rTMS/MC: prior to the repetitive transcranial magnetic stimulation treatment applied over the motor cortex; Post-rTMS/MC: immediately after the repetitive transcranial magnetic stimulation treatment applied over the motor cortex; Pre-rTMS/PFC: prior to the repetitive transcranial magnetic stimulation treatment applied over the prefrontal cortex; Post-rTMS/PFC: immediately after the repetitive transcranial magnetic stimulation treatment applied over the prefrontal cortex.

	Pre-rTMS/MC scores	Post-rTMS/MC scores	Pre-rTMS/PFC scores	Post-rTMS/PFC scores
UPDRS III “on”	21.25 ± 13.43	21.75 ± 13.67	20.75 ± 12.87	20.00 ± 14.12
UPDRS IV	6.00 ± 1.83	7.00 ± 2.50	6.25 ± 1.71	4.75 ± 0.96

paradigm of Ridding et al. [29] at interstimulus intervals (ISI) of 1, 3, 7, and 15 milliseconds [30]. We evaluated motor evoked potentials (MEPs) elicited by single and paired-pulse TMS pulses over the MC contralateral to either the right first dorsal interosseus muscle (prior to, immediately after, and one week after the rTMS treatment over the left DLPFC) or the appropriate tibialis anterior muscle (prior to, immediately after, and one week after the rTMS treatment over the appropriate MC). The motor cortical sites were chosen to specifically accommodate the primary goal of our freezing of gait protocol design. A circular coil was used. MEP size reflects more globally the corticospinal input-output balance, excitatory inputs from high-threshold glutamatergic pathways to the motor cortex lead to intracortical facilitation, whereas inhibitory inputs from low-threshold GABA-A-mediated pathways lead to intracortical inhibition at short ISI [13].

3. STATISTICAL ANALYSIS

The effects of rTMS treatments on single MEP amplitudes and UPDRS before and after the rTMS treatments were analysed by a two-tailed paired-sample *t* test. A two-factor repeated measures ANOVA, with the factors of “TIME” (3 levels: baseline, immediately after the rTMS treatment, and 1 week after the rTMS treatment) and “ISI” (3 levels: averaged data from the inhibiting ISI (1 and 3 milliseconds), the facilitating ISI (15 milliseconds), and the intermediate ISI (7 milliseconds)) was performed to evaluate the effects of the rTMS treatment applied over the MC and the DLPFC, respectively.

4. RESULTS

4.1. Clinical effects

Despite our aim to perform a randomised crossover design, the study was stopped prematurely as several patients withdrew the consent form before completing both treatments. A subjective lack of treatment effect on freezing of gait (i.e., the primary outcome) was the reason for the study withdrawal. This study presents the results from four patients that completed the rTMS treatment over the MC and four patients that completed the treatment over the DLPFC. Despite the lack of effect of rTMS on freezing of gait and motor symptoms of PD [18], the patients reported a decreased frequency and intensity of dyskinesias after 5 consecutive sessions of rTMS targeted over the left DLPFC. These changes were reflected by the mean UPDRS IV decrease immediately after

5 sessions of the stimulation as compared with the baseline scores (see Table 1). The result did not reach statistical significance ($P = .06$) but could be suggestive of a mild improvement of dyskinesias. No such changes were observed after rTMS of the MC.

4.2. Effects on cortical excitability

There was no cumulative effect of the rTMS treatment over the MC on corticospinal excitability as measured by MEP responses produced by single TMS pulses over the left MC contralateral to the appropriate tibialis anterior muscle (see Table 2). However, we found that 5 consecutive sessions of high frequency rTMS of the left DLPFC produced a significant decrease in the amplitude of MEP responses produced by single TMS pulses over the left MC contralateral to the right first dorsal interosseus muscle (see Table 2).

There were no effects of any rTMS treatments on the time course of intracortical inhibition or intracortical facilitation in the appropriate motor cortex; this was verified with a two-factor repeated measures ANOVA with the factors “TIME” and “ISI”: $F(4,26) = 0.72$, $P = .6$ for rTMS treatment over the DLPFC; $F(4,10) = 2.4$, $P = .1$ for rTMS treatment over the MC.

5. DISCUSSION

The results of our study point to a possible impact of repeated sessions of rTMS applied over the left DLPFC on L-dopa-induced dyskinesias in advanced PD patients. The mean change in the UPDRS IV scores did not reach a statistical significance, but we did not evaluate dyskinesias by more appropriate standardized scales since the assessment of dyskinesias was not the primary outcome of our pilot study. On the other hand, UPDRS IV was used to test dyskinesias in a PET study by Brooks et al. [9]. There are a number of hypothetical mechanisms that might underlie the possible effects of rTMS of the DLPFC on L-dopa-induced dyskinesias in advanced PD.

It appears that changes of the excitability of the primary motor cortex may be more efficiently performed through stimulation of premotor and/or other more anterior brain regions, for review, see [31]. We found that 5 consecutive sessions of high frequency rTMS of the left DLPFC produced a significant decrease in the amplitude of MEP responses produced by single TMS pulses over the left MC for the right first dorsal interosseus muscle (i.e., decrease of the cortico-spinal excitability). These results are in accord with the results of

TABLE 2: Effects of rTMS treatments on the amplitude of MEP responses produced by single TMS pulses. MEP: motor evoked potential; Pre-rTMS/MC: prior to the repetitive transcranial magnetic stimulation treatment applied over the motor cortex; Post-rTMS/MC: immediately after the repetitive transcranial magnetic stimulation treatment applied over the motor cortex; Pre-rTMS/PFC: prior to the repetitive transcranial magnetic stimulation treatment applied over the prefrontal cortex; Post-rTMS/PFC: immediately after the repetitive transcranial magnetic stimulation treatment applied over the prefrontal cortex.

	Pre-rTMS/MC	Post-rTMS/MC	Pre-rTMS/PFC	Post-rTMS/PFC
MEP amplitude μV	1.60 ± 0.79	1.52 ± 0.68	$2.02 \pm 0.10^*$	$1.22 \pm 0.32^*$

* $P = .03$ (paired samples t test).

Rollnick et al. [32] who also demonstrated that stimulation of the DLPFC via subthreshold 5 Hz rTMS induces motor cortex depression in healthy subjects. It was posited by the authors that this finding might be explained by the fact that prefrontal brain areas contribute to motor cortex inhibition through antagonisms between frontal and parietal lobes [32, 33] but the exact mechanisms are not fully understood. Primary motor cortex “overactivity” in rather advanced PD patients was found by means of PET and functional magnetic resonance imaging (fMRI) while studying simple or complex motor hand tasks [34, 35]. It was also observed in SPECT and PET studies of PD patients with L-dopa-induced dyskinesias [2, 9]. Electrophysiological data further support this notion: increased MEP amplitudes at rest were found in PD patients with L-dopa induced dyskinesias [36, 37]. Neuroimaging studies have shown that subthalamic nucleus stimulation acts through the reduction of abnormal overactivity in the motor system at rest [34, 38]. Even though dyskinesias were not systematically monitored in these studies, it has been well known that subthalamic nucleus stimulation surgery is able to reduce L-dopa-induced dyskinesias [39]. Taken together, normalizing (i.e., reducing) the excitability of the primary motor cortex, for example, by rTMS of the DLPFC might be one possible factor in improving L-dopa-induced dyskinesias in advanced PD patients.

rTMS applied over the left DLPFC can induce significant increases of rCBF in the stimulated area [40]. Functional imaging studies (PET and fMRI) report decreases in rCBF and MRI signal in the DLPFC and the rostral SMA in advanced PD patients compared to controls [35, 41–45]. The DLPFC is connected with the rostral SMA [46]. Pallidotomy [44] and subthalamic nucleus stimulation [47] reversed such a hypoactivation. After unilateral pallidotomy, glucose metabolism increased in the DLPFC, in addition to metabolic changes in other cortical and subcortical areas [48]. rCBF increases were reported in the DLPFC and the rostral SMA during apomorphine pumps [49]. Again, pallidotomy, subthalamic nucleus stimulation and continuous apomorphine are able to reverse dyskinesias [39, 49–51]. Therefore, the direct involvement of the DLPFC and the degeneration of mesofrontal dopaminergic afferents might also be hypothesized to play some role in the development of dyskinesias.

Finally, involvement of the dorsolateral “prefrontal” circuit may well be possible. The prefrontal circuit encompasses the dorsal prefrontal cortex, the dorsal caudate nucleus, the dorsal medial globus pallidus, and the ventral anterior nucleus of the thalamus. Strafella et al. have shown that high

frequency rTMS of the DLPFC leads to dopamine release in the ipsilateral caudate nucleus [19, 20]. We used the same parameters as Strafella et al. with regard to frequency and intensity of stimulation. Therefore, subcortical mechanisms cannot be excluded either.

Taken together, we have shown for the first time that repeated sessions of subthreshold 10 Hz rTMS of the DLPFC induced significant reductions of the ipsilateral motor cortex excitability in advanced PD population, and might possibly be suggestive of an improvement of L-dopa-induced dyskinesias. It has to be pointed out that this was a small observational study not specifically designed to assess dyskinesias in PD. DLPFC stimulation was not controlled by the placebo rTMS and therefore a possible placebo effect cannot be excluded either [15]. On the other hand, the DLPFC stimulation was controlled by yet another active stimulation over the MC. Improvement of dyskinesia could not have been expected by patients since changes in the motor complications score were not included in the primary outcomes of our pilot study.

Further research is warranted to explore more precisely whether the unilateral or bilateral stimulation of the DLPFC via repeated sessions of high frequency rTMS induces beneficial effects on L-dopa-induced dyskinesias in advanced PD patients, and whether it could be considered clinically useful.

ACKNOWLEDGMENTS

The authors would like to thank Zdenek Novotny for his assistance with data analysis. This study was supported by Research Project of the Czech Ministry of Education, MSM 0021622404.

REFERENCES

- [1] R. Marconi, D. Lefebvre-Caparros, A.-M. Bonnet, M. Vidailhet, B. Dubois, and Y. Agid, “Levodopa-induced dyskinesias in Parkinson’s disease phenomenology and pathophysiology,” *Movement Disorders*, vol. 9, no. 1, pp. 2–12, 1994.
- [2] O. Rascol, U. Sabatini, C. Brefel, et al., “Cortical motor overactivation in parkinsonian patients with L-dopa-induced peak-dose dyskinesia,” *Brain*, vol. 121, no. 3, pp. 527–533, 1998.
- [3] O. Rascol, D. J. Brooks, A. D. Korczyn, P. P. De Deyn, C. E. Clarke, and A. E. Lang, “A five-year study of the incidence of dyskinesia in patients with early Parkinson’s disease who were treated with ropinirole or levodopa,” *The New England Journal of Medicine*, vol. 342, no. 20, pp. 1484–1491, 2000.
- [4] G. Koch, L. Brusa, C. Caltagirone, et al., “rTMS of supplementary motor area modulates therapy-induced dyskinesias

- in Parkinson disease,” *Neurology*, vol. 65, no. 4, pp. 623–625, 2005.
- [5] P. Piccini, R. A. Weeks, and D. J. Brooks, “Alterations in opioid receptor binding in Parkinson’s disease patients with levodopa-induced dyskinesias,” *Annals of Neurology*, vol. 42, no. 5, pp. 720–726, 1997.
- [6] E. Bezard, J. M. Brotchie, and C. E. Gross, “Pathophysiology of levodopa-induced dyskinesia: potential for new therapies,” *Nature Reviews Neuroscience*, vol. 2, no. 8, pp. 577–588, 2001.
- [7] J. A. Obeso, M. C. Rodriguez-Oroz, M. Rodriguez, M. R. DeLong, and C. W. Olanow, “Pathophysiology of levodopa-induced dyskinesias in Parkinson’s disease: problems with the current model,” *Annals of Neurology*, vol. 47, no. 4, supplement 1, pp. S22–S34, 2000.
- [8] A. M. Lozano, A. E. Lang, R. Levy, W. Hutchison, and J. Dostrovsky, “Neuronal recordings in Parkinson’s disease patients with dyskinesias induced by apomorphine,” *Annals of Neurology*, vol. 47, no. 4, supplement 1, pp. S141–S146, 2000.
- [9] D. J. Brooks, P. Piccini, N. Turjanski, and M. Samuel, “Neuroimaging of dyskinesia,” *Annals of Neurology*, vol. 47, no. 4, supplement 1, pp. S154–S158, 2000.
- [10] H. R. Siebner and J. Rothwell, “Transcranial magnetic stimulation: new insights into representational cortical plasticity,” *Experimental Brain Research*, vol. 148, no. 1, pp. 1–16, 2003.
- [11] A. Pascual-Leone, J. Valls-Solé, J. P. Brasil-Neto, A. Cammarota, J. Grafman, and M. Hallett, “Akinesia in Parkinson’s disease. II. Effects of subthreshold repetitive transcranial motor cortex stimulation,” *Neurology*, vol. 44, no. 5, pp. 892–898, 1994.
- [12] R. Cantello, R. Tarletti, and C. Civardi, “Transcranial magnetic stimulation and Parkinson’s disease,” *Brain Research Reviews*, vol. 38, no. 3, pp. 309–327, 2002.
- [13] J.-P. Lefaucheur, “Motor cortex dysfunction revealed by cortical excitability studies in Parkinson’s disease: influence of antiparkinsonian treatment and cortical stimulation,” *Clinical Neurophysiology*, vol. 116, no. 2, pp. 244–253, 2005.
- [14] M. P. Lomarev, S. Kanchana, W. Bara-Jimenez, M. Iyer, E. M. Wassermann, and M. Hallett, “Placebo-controlled study of rTMS for the treatment of Parkinson’s disease,” *Movement Disorders*, vol. 21, no. 3, pp. 325–331, 2006.
- [15] A. P. Strafella, J. H. Ko, and O. Monchi, “Therapeutic application of transcranial magnetic stimulation in Parkinson’s disease: the contribution of expectation,” *NeuroImage*, vol. 31, no. 4, pp. 1666–1672, 2006.
- [16] L. Brusa, V. Versace, G. Koch, et al., “Low frequency rTMS of the SMA transiently ameliorates peak-dose LID in Parkinson’s disease,” *Clinical Neurophysiology*, vol. 117, no. 9, pp. 1917–1921, 2006.
- [17] A. Wagle-Shukla, M. J. Angel, C. Zadikoff, et al., “Low-frequency repetitive transcranial magnetic stimulation for treatment of levodopa-induced dyskinesias,” *Neurology*, vol. 68, no. 9, pp. 704–705, 2007.
- [18] I. Rektorova, S. Sedlackova, S. Telecka, A. Hlubocky, and I. Rektor, “Repetitive transcranial stimulation for freezing of gait in Parkinson’s disease,” *Movement Disorders*, vol. 22, no. 10, pp. 1518–1519, 2007.
- [19] A. P. Strafella, T. Paus, M. Fraraccio, and A. Dagher, “Striatal dopamine release induced by repetitive transcranial magnetic stimulation of the human motor cortex,” *Brain*, vol. 126, no. 12, pp. 2609–2615, 2003.
- [20] A. P. Strafella, T. Paus, J. Barrett, and A. Dagher, “Repetitive transcranial magnetic stimulation of the human prefrontal cortex induces dopamine release in the caudate nucleus,” *Journal of Neuroscience*, vol. 21, no. 15, p. RC157, 2001.
- [21] W. R. G. Gibb and A. J. Lees, “The relevance of the Lewy body to the pathogenesis of idiopathic Parkinson’s disease,” *Journal of Neurology Neurosurgery and Psychiatry*, vol. 51, no. 6, pp. 745–752, 1988.
- [22] A. J. Hughes, S. E. Daniel, L. Kilford, and A. J. Lees, “Accuracy of clinical diagnosis of idiopathic Parkinson’s disease: a clinicopathological study of 100 cases,” *Journal of Neurology Neurosurgery and Psychiatry*, vol. 55, no. 3, pp. 181–184, 1992.
- [23] M. M. Hoehn and M. D. Yahr, “Parkinsonism: onset, progression and mortality,” *Neurology*, vol. 17, no. 5, pp. 427–442, 1967.
- [24] M. F. Folstein, S. E. Folstein, and P. R. McHugh, ““Mini mental state” a practical method for grading the cognitive state of patients for the clinician,” *Journal of Psychiatric Research*, vol. 12, no. 3, pp. 189–198, 1975.
- [25] S. A. Montgomery and M. A. Asberg, “A new depression scale designed to be sensitive to change,” *The British Journal of Psychiatry*, vol. 134, pp. 382–389, 1979.
- [26] M. S. George, E. M. Wassermann, T. A. Kimbrell, et al., “Mood improvement following daily left prefrontal repetitive transcranial magnetic stimulation in patients with depression: a placebo-controlled crossover trial,” *American Journal of Psychiatry*, vol. 154, no. 12, pp. 1752–1756, 1997.
- [27] M. Petrides and D. N. Pandya, “Dorsolateral prefrontal cortex: comparative cytoarchitectonic analysis in the human and the macaque brain and corticocortical connection patterns,” *European Journal of Neuroscience*, vol. 11, no. 3, pp. 1011–1036, 1999.
- [28] S. Fahn and R. L. Elston, “Unified Parkinson’s disease rating scale,” in *Recent Developments in Parkinson’s Disease*, S. Fahn, C. D. Marsden, M. Goldstein, and D. B. Calne, Eds., vol. 2, pp. 153–163, Macmillan, New York, NY, USA, 1987.
- [29] M. C. Ridding, R. Inzelberg, and J. C. Rothwell, “Changes in excitability of motor cortical circuitry patients with Parkinson’s disease,” *Annals of Neurology*, vol. 37, no. 2, pp. 181–188, 1995.
- [30] M. Bareš, P. Kaňovský, H. Klajblová, and I. Rektor, “Intracortical inhibition and facilitation are impaired in patients with early Parkinson’s disease: a paired TMS study,” *European Journal of Neurology*, vol. 10, no. 4, pp. 385–389, 2003.
- [31] P. B. Fitzgerald, S. Fountain, and Z. J. Daskalakis, “A comprehensive review of the effects of rTMS on motor cortical excitability and inhibition,” *Clinical Neurophysiology*, vol. 117, no. 12, pp. 2584–2596, 2006.
- [32] J. D. Rollnik, M. Schubert, and R. Dengler, “Subthreshold prefrontal repetitive transcranial magnetic stimulation reduces motor cortex excitability,” *Muscle and Nerve*, vol. 23, no. 1, pp. 112–114, 2000.
- [33] K. Sakai, O. Hikosaka, S. Miyauchi, R. Takino, Y. Sasaki, and B. Pütz, “Transition of brain activation from frontal to parietal areas in visuomotor sequence learning,” *Journal of Neuroscience*, vol. 18, no. 5, pp. 1827–1840, 1998.
- [34] B. Haslinger, K. Kalteis, H. Boecker, F. Alesch, and A. O. Ceballos-Baumann, “Frequency-correlated decreases of motor cortex activity associated with subthalamic nucleus stimulation in Parkinson’s disease,” *NeuroImage*, vol. 28, no. 3, pp. 598–606, 2005.
- [35] U. Sabatini, K. Boulanouar, N. Fabre, et al., “Cortical motor reorganization in akinetic patients with Parkinson’s disease. a functional MRI study,” *Brain*, vol. 123, no. 2, pp. 394–403, 2000.
- [36] R. Chen, R. R. Garg, A. M. Lozano, and A. E. Lang, “Effects of internal globus pallidus stimulation on motor cortex excitability,” *Neurology*, vol. 56, no. 6, pp. 716–723, 2001.

- [37] N. Modugno, A. Curra, F. Gilio, C. Lorenzano, S. Bagnato, and A. Berardelli, "Transcranial magnetic stimulation in movement disorders," in *Magnetic Stimulation in Clinical Neurophysiology*, M. Hallett and S. Chokroverty, Eds., pp. 181–191, Elsevier, Philadelphia, Pa, USA, 2nd edition, 2005.
- [38] P. Payoux, P. Remy, P. Damier, et al., "Subthalamic nucleus stimulation reduces abnormal motor cortical overactivity in Parkinson disease," *Archives of Neurology*, vol. 61, no. 8, pp. 1307–1313, 2004.
- [39] C. G. Goetz, W. Poewe, O. Rascol, and C. Sampaio, "Evidence-based medical review update: pharmacological and surgical treatments of Parkinson's disease: 2001 to 2004," *Movement Disorders*, vol. 20, no. 5, pp. 523–539, 2005.
- [40] D. Knoch, V. Treyer, M. Regard, R. M. Müri, A. Buck, and B. Weber, "Lateralized and frequency-dependent effects of prefrontal rTMS on regional cerebral blood flow," *NeuroImage*, vol. 31, no. 2, pp. 641–648, 2006.
- [41] M. Jahanshahi, I. H. Jenkins, R. G. Brown, C. D. Marsden, R. E. Passingham, and D. J. Brooks, "Self-initiated versus externally triggered movements. I. An investigation using measurement of regional cerebral blood flow with PET and movement-related potentials in normal and Parkinson's disease subjects," *Brain*, vol. 118, no. 4, pp. 913–933, 1995.
- [42] E. D. Playford, I. H. Jenkins, R. E. Passingham, J. Nutt, R. S. J. Frackowiak, and D. J. Brooks, "Impaired mesial frontal and putamen activation in Parkinson's disease: a positron emission tomography study," *Annals of Neurology*, vol. 32, no. 2, pp. 151–161, 1992.
- [43] C. Haegelen, M. Verin, B. A. Broche, et al., "Does subthalamic nucleus stimulation affect the frontal limbic areas? A single-photon emission computed tomography study using a manual anatomical segmentation method," *Surgical and Radiologic Anatomy*, vol. 27, no. 5, pp. 389–394, 2005.
- [44] M. Samuel, A. O. Ceballos-Baumann, N. Turjanski, et al., "Pallidotomy in Parkinson's disease increases supplementary motor area and prefrontal activation during performance of volitional movements an $H_2^{15}O$ PET study," *Brain*, vol. 120, no. 8, pp. 1301–1313, 1997.
- [45] S. Thobois, S. Guillouet, and E. Broussolle, "Contributions of PET and SPECT to the understanding of the pathophysiology of Parkinson's disease," *Neurophysiologie Clinique*, vol. 31, no. 5, pp. 321–340, 2001.
- [46] J. F. Bates and P. S. Goldman-Rakic, "Prefrontal connections of medial motor areas in the rhesus monkey," *Journal of Comparative Neurology*, vol. 336, no. 2, pp. 211–228, 1993.
- [47] P. Limousin, J. Greene, P. Pollak, J. Rothwell, A.-L. Benabid, and R. Frackowiak, "Changes in cerebral activity pattern due to subthalamic nucleus or internal pallidum stimulation in Parkinson's disease," *Annals of Neurology*, vol. 42, no. 3, pp. 283–291, 1997.
- [48] D. Eidelberg, J. R. Moeller, T. Ishikawa, et al., "Regional metabolic correlates of surgical outcome following unilateral pallidotomy for Parkinson's disease," *Annals of Neurology*, vol. 39, no. 4, pp. 450–459, 1996.
- [49] I. H. Jenkins, W. Fernandez, E. D. Playford, et al., "Impaired activation of the supplementary motor area in Parkinson's disease is reversed when akinesia is treated with apomorphine," *Annals of Neurology*, vol. 32, no. 6, pp. 749–757, 1992.
- [50] A. M. Lozano, A. E. Lang, N. Galvez-Jimenez, et al., "Effect of GPi pallidotomy on motor function in Parkinson's disease," *The Lancet*, vol. 346, no. 8987, pp. 1383–1387, 1995.
- [51] R. Katzenschlager, A. Hughes, A. Evans, et al., "Continuous subcutaneous apomorphine therapy improves dyskinesias in Parkinson's disease: a prospective study using single-dose challenges," *Movement Disorders*, vol. 20, no. 2, pp. 151–157, 2005.

Research Article

BOLD-Perfusion Coupling during Monocular and Binocular Stimulation

Claudine Gauthier^{1,2} and Richard D. Hoge^{1,2,3}

¹Unité de Neuroimagerie Fonctionnelle, Institut Universitaire de Gériatrie de Montréal, Montreal, QC, Canada H3W 1W5

²Department of Physiology, Faculty of Medicine, University of Montreal, Montreal, QC, Canada H3W 1W5

³Institute of Biomedical Engineering, Faculty of Medicine, University of Montreal, Montreal, QC, Canada H3W 1W5

Correspondence should be addressed to Richard D. Hoge, rhoge@umontreal.ca

Received 17 October 2007; Accepted 29 December 2007

Recommended by Oury Monchi

Previous studies have suggested that during selective activation of a subset of the zones comprising a columnar system in visual cortex, perfusion increases uniformly in all columns of the system, while increases in oxidative metabolism occur predominantly in the activated columns. This could lead to disproportionately large blood oxygenation level-dependent (BOLD) signal increases for a given flow increase during monocular (relative to binocular) stimulation, due to contributions from columns which undergo large increases in perfusion with little or no change in oxidative metabolism. In the present study, we sought to test this hypothesis by measuring BOLD-perfusion coupling ratios in spatially averaged signals over V1 during monocular and binocular visual stimulation. It was found that, although withholding input to one eye resulted in statistically significant decreases in BOLD and perfusion signals in primary visual cortex, the ratio between BOLD and perfusion increases did not change significantly. These results do not support a gross mismatch between spatial patterns of flow and metabolism response during monocular stimulation.

Copyright © 2008 C. Gauthier and R. D. Hoge. This is an open access article distributed under the Creative Commons Attribution License, which permits unrestricted use, distribution, and reproduction in any medium, provided the original work is properly cited.

1. INTRODUCTION

Although blood oxygenation level-dependent (BOLD) functional MRI has assumed a role of great importance in systems neuroscience, our understanding of factors determining the amplitude and spatial extent of the BOLD effect under different conditions remains incomplete. Relevant parameters include baseline values and reactive capacity for cerebral perfusion, oxidative metabolism, and blood volume. An understanding of how these contribute to the BOLD response is important, since in general they may vary due to age or disease, and also depending on the nature of the neural system targeted by an applied stimulus. In particular, the exact nature and extent of the coupling between changes in oxidative metabolism and perfusion increases during neuronal activation is still the subject of debate. While recent studies have focused on quantification of responses during nonspecific activation of diffuse regions of sensory and motor cortex [1–4], this topic has also arisen in the context of highly localized responses in cortical columnar systems [5, 6]. In the present study, we sought to bridge the gap between these two regimes

by looking at the effect of selective activation of only part of a small-scale cortical columnar system on the apparent BOLD response observed at a spatial resolution typical of studies used in human subjects.

Early optical imaging studies [7–9] suggested that although evoked changes in oxidative metabolism exhibit a high degree of spatial specificity, brain perfusion is regulated on a much coarser spatial scale. If this is true, then there might be profound implications for the BOLD MRI signal, especially when measured during manipulations such as monocular stimulation, which preferentially activates the set of ocular dominance columns projecting to the stimulated eye. In particular, one might expect the spatial pattern of perfusion response evoked by stimulation of a single eye to be similar to that seen during binocular stimulation, despite a substantial reduction in the metabolic response (compared to binocular stimulation) in columns projecting to the occluded eye. Since the BOLD signal reflects changes in the level of venous deoxygenated hemoglobin, this gratuitous hyperperfusion in unstimulated ocular dominance columns could be expected to result in a higher BOLD signal at a given level

of perfusion increase (considering spatial averages over multiple columns, which would be applicable at commonly used spatial resolutions in fMRI).

The present study examines joint changes in perfusion and BOLD signals during monocular and binocular stimulation, to test the hypothesis that spatial decoupling of flow and metabolic responses during stimulation of only a partial subset of the columnar regions distributed within primary visual cortex leads to a significant shift in the ratio between spatially averaged BOLD and perfusion signals (measured using arterial spin-labeling). By combining quantitative MRI-based measures of these two physiological quantities, we hope to provide new insight into the spatial precision with which cerebral blood flow is regulated, as well as factors which determine BOLD contrast amplitude in cortical tissues exhibiting columnar organization.

2. METHODS

2.1. Subjects

Eight healthy subjects (five males and three females) 24 ± 2.6 years old, one left eye and hand dominant (male) and seven right eye and hand dominant, participated in the study. The subjects did not suffer from any known visual deficits except myopia (MRI-compatible corrective glasses were fitted in these cases). All gave informed consent and the project was approved by the Comité mixte d'éthique de la recherche du Regroupement Neuroimagerie/Québec. Data from two of the subjects was not analyzed due to the poor quality of the arterial spin-labeling (perfusion) data.

2.2. Visual stimulation

Subjects were fitted with a neoprene rubber mask which allowed occlusion of one eye by a removable patch. The patch was applied and removed as needed between the appropriate scans, by an experimenter, from the back of the scanner bore.

Each scanning session included eight six-minute acquisitions, during which alternating one-minute blocks of baseline (uniform grey screen with central fixation point) and one-minute blocks of visual stimulation (black and white checkerboard reversing contrast at a rate producing four white periods per second within a square) were presented, starting with baseline. During each scanning run, the subject received either binocular (B) or monocular (M) stimulation to their nondominant eye with separate scans conducted in the following order: B-B-M-M-B-B-M-M. Subjects were instructed to direct their gaze at the central fixation point throughout all scans. The nondominant eye was selected for monocular stimulation to maximize the difference in activation between the monocular and binocular trials given that there may presumably be more extensive activation of V1 for the dominant eye [10].

2.3. MRI data acquisition

MRI data acquisition was carried out using a Siemens Trio 3 Tesla MRI system, at software revision VA25A. Im-

ages reflecting relative perfusion were acquired using a PICORE/Q2TIPS arterial spin-labeling (ASL) acquisition [11, 12]. The spatial resolution was $3.4 \text{ mm} \times 3.4 \text{ mm}$ on a 64×64 matrix, with 10 slices of 5 mm thickness. Other sequence parameters included TR/TE/alpha = 2 s/19 ms/90° and TI1/TI2 = 700 ms/1400 ms. A slab thickness of 200 mm was used, with a 10 mm gap between the top of the label slab and the most inferior image slice. The Q2TIPS stop time was 1350 ms. MR signals were received using an eight-channel receive-only head coil, with excitation and labeling performed using the system body coil.

A T1-weighted structural scan was also acquired for later use in spatial normalization. These scans were at 1 mm isotropic resolution, acquired using an MPRAGE sequence with TI/TR/TE/alpha = 900/2300/2.94/9. Voxel size was $1.0 \times 1.0 \times 1.2 \text{ mm}$.

2.4. Analysis

Flow and BOLD images were generated using the “surround subtraction” approach described in Wong et al. [13], reducing artifactual flow signals during periods of BOLD signal transition. The sequence of flow images was generated by computing the difference between each image and the average of the previous and subsequent images. The sequence of BOLD images was computed by adding each image to the average of its two neighbors. For each run, the effect and standard error maps were then generated by fitting a linear signal model to each voxel in the flow and BOLD series. The model consisted of a term representing the three task epochs in the run convolved with a dual gamma function including positive response plus undershoot [14], plus a third-order polynomial. Multiple runs for each subject were then combined using a mixed-effects model, followed by spatial normalization to the MNI 152 brain and combination of normalized maps for different subjects again using a mixed-effects model (as described in Worsley et al. [15]). Individual and multisubject maps were then thresholded at $P = .001$ significance with correction for multiple comparisons using the `stat_threshold` routine of the `fMRIstat` software package [15].

Regions of interest (ROIs) were generated using the NeuroLens software package (www.neurolens.org). Average BOLD statistical maps for each subject were used to make a V1 ROI by thresholding as described above. Voxels exceeding threshold in the BOLD map but located outside the banks of the calcarine sulcus as visualized in the T1-weighted structural scan were manually edited from the ROI, to ensure that the signals extracted were associated with primary visual cortex and therefore contained tissue organized as ocular dominance columns. The effect values were then averaged within the ROI for each functional scan and tabulated as effect size \pm standard error. Values were converted to percent change as needed by dividing the effect size by the constant (DC) term fit during linear modeling and multiplying by 100.

3. RESULTS

Figure 1 shows mixed-effects BOLD and flow maps over all subjects for monocular and binocular stimulation. Occlusion

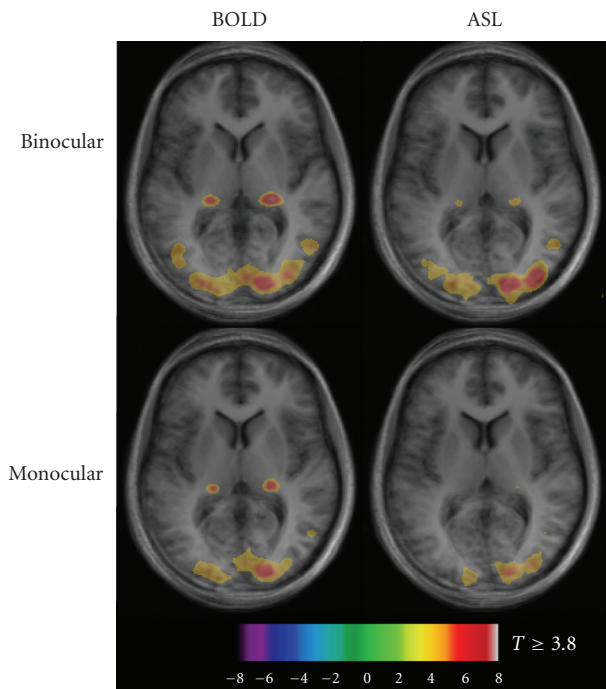


FIGURE 1: Mixed-effects response maps for BOLD and flow changes in response to monocular and binocular visual stimulation ($n = 6$). Spatial extent and intensity are greater for binocular stimulation than for monocular, for both BOLD and flow signals. Thresholded activation maps are overlaid on average T1 maps for the six subjects.

of input to one eye reduced the amount of activation detected in extrastriate areas. However, the significance levels observed within primary visual cortex appeared similar during both monocular and binocular stimulation.

Averaged time course signals for flow and BOLD are shown in Figure 2, revealing the initial BOLD signal overshoot and poststimulus undershoot commonly observed in visual cortex during checkerboard stimulation (seen here during both monocular and binocular stimulation). The flow signal illustrates the lower signal-to-noise ratio generally obtained in arterial spin-labeling measurements.

The bar graphs in Figure 3 show average percent changes in BOLD and flow signals within the V1 ROIs of all subjects. The average percent change in BOLD signal for monocular stimulation was 0.93 ± 0.04 , which was significantly ($P < .05$) less than the percent change of 1.11 ± 0.05 observed during binocular stimulation. The percent flow increase measured during monocular stimulation was 29 ± 2 , also significantly less than the percent change of 37 ± 2 observed during binocular stimulation. Expressed as a percent reduction in the response amplitude, withholding input from one of the two eyes resulted in a $16 \pm 6\%$ decrease in the BOLD response and $19 \pm 9\%$ decrease in the perfusion response.

The percent changes in BOLD signal per percent signal increase in flow (i.e., the quotient $\Delta\%BOLD \div \Delta\%flow$) during monocular and binocular stimulation were found, respectively, to be 0.031 ± 0.004 and 0.030 ± 0.004 (Figure 4). The difference between these ratios was not statistically sig-

nificant, failing to support any difference in flow-metabolism coupling during the two forms of stimulation.

4. DISCUSSION

In this study, we examined the coupling between BOLD and CBF responses in primary visual cortex during monocular and binocular stimulation. We found that the BOLD and CBF responses to monocular visual stimulation were both significantly reduced in V1 relative to the responses observed during binocular stimulation (Figure 3). The ratio of BOLD to CBF effect sizes did not differ significantly between the two stimulation conditions (Figure 4), indicating comparable coupling between flow and oxidative metabolism regardless of the columnar fraction that was activated.

The results obtained in the present study do not support the “strong” form of the theory that tissue perfusion is regulated only on a coarse spatial scale, irrespective of the spatial precision with which metabolism might change. This notion has been described previously as “watering the entire garden for the sake of one thirsty flower” [9]. To borrow the garden analogy, the experiments described here could be described as an attempt to measure the total water intake of the garden, as well as the runoff of unused water, to test this hypothesis. Our results are consistent with recent MRI studies showing that there is in fact sufficient spatial contrast in the perfusion response, as imaged using arterial spin-labeling, to resolve columnar structures in the visual cortex [6]. The study by Duong et al. [6] found that the early negative BOLD response (initial dip) also exhibited a high degree of spatial localization, whereas the late positive BOLD response was more diffuse. It is important to remember that the apparent resolution of each signal is dictated both by the underlying physiological regulatory precision and by the degree to which confounding vascular structures are superimposed on the pattern of parenchymal activation. Based on our results and those from Duong et al., it appears likely that the lack of precision in the late BOLD signal is due primarily to obscuring effects from the macrovascular anatomy, rather than a diffuse parenchymal BOLD effect. It has been suggested by other authors [16] that the increase in the apparent precision of the initial dip arises because BOLD signal increases in large draining veins do not arise until after the initial transit of blood through the local capillary bed postulated to take approximately one second.

Given that functional signals of interest may exhibit bias due to vascular anatomy, designating regions of interest using objective criteria is an important part of quantitative neuroimaging studies. In the present study, the use of phase-encoded retinotopic mapping to identify V1 in a separate mapping experiment would have been the optimal approach, since this procedure yields a set of voxels exhibiting a specific spatial trend in the polar angle or eccentricity of their projection in visual field that is unlikely to appear in a large vein. This would have led to excessively long scan sessions, however. Instead, we used the fact that the optic radiations terminate in the calcarine sulcus, making it very probable that activated regions lying in this anatomical zone are in fact part of primary visual cortex. It is still possible that the

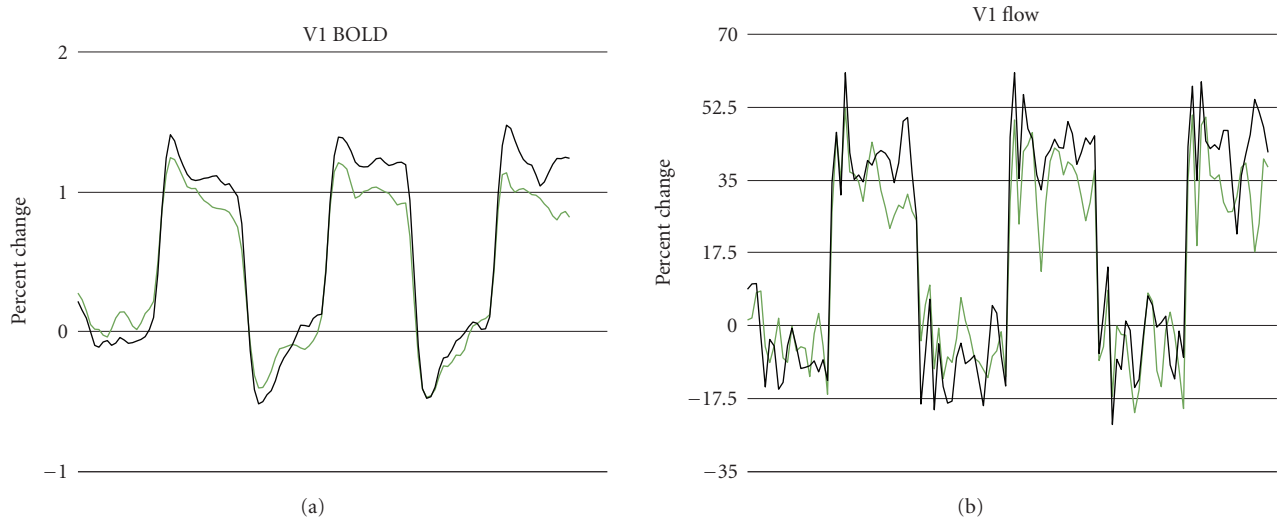


FIGURE 2: BOLD and flow signals (expressed as percent change; black = binocular, green = monocular) in response to monocular and binocular visual stimulation, averaged over all subjects (6 subjects \times 4 averages per subject = 24 averages per signal). Initial overshoot and poststimulus undershoot are observed in BOLD signal for both monocular and binocular stimulation, as is typical for checkerboard stimulation.

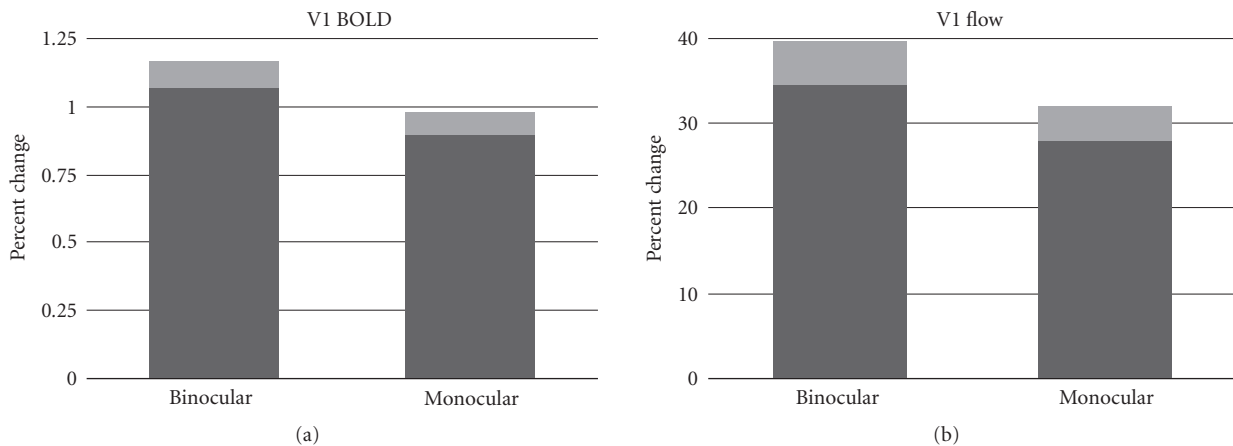


FIGURE 3: Percent change (\pm SE in lighter shade of gray) in BOLD and CBF signals in response to binocular and monocular stimulation. Responses evoked by binocular stimulation are significantly greater than those produced by monocular stimulation.

BOLD activation maps used to create ROIs based on a simple “activation minus baseline” contrast could contain a disproportionate contribution from large draining veins. These veins mix venous outflow from multiple visual areas, including regions which do not exhibit eye-specific columnar segregation, diluting any shift in flow-BOLD coupling present specifically in V1. In a pilot study of six subjects performed at 1.5T using retinotopic mapping to identify V1 (but performed using single-slice ASL at 1.5 T), we obtained a virtually identical result [17]. We therefore do not feel that the results of the present study are substantially impacted by our ROI selection procedure. Moreover, the relatively large voxel size and intense stimulus used in the present study yielded diffuse regions of robust activation that did not appear to be limited to macrovascular responses (as can occur at higher spatial resolutions or with weaker stimuli).

By measuring total flow and BOLD responses in V1 during activation of different columnar fractions, we were able to achieve high signal-to-noise ratios (SNRs) compared to studies that have used extremely high spatial resolution to actually resolve the columns. The purpose of the present study was to provide insight into two questions: the first is whether there is in fact a fundamental difference in the spatial precision with which perfusion and oxidative metabolism is measured; the second was to determine the impact of partial activation of a cortical columnar system on the BOLD signal characteristics observed at a customary fMRI spatial resolution. If there is indeed a profound mismatch in the spatial extent of increases in oxidative metabolism and flow, this should be apparent in the total average signal over V1. That none was found suggests that similar extents are likely to be found at higher spatial resolutions.

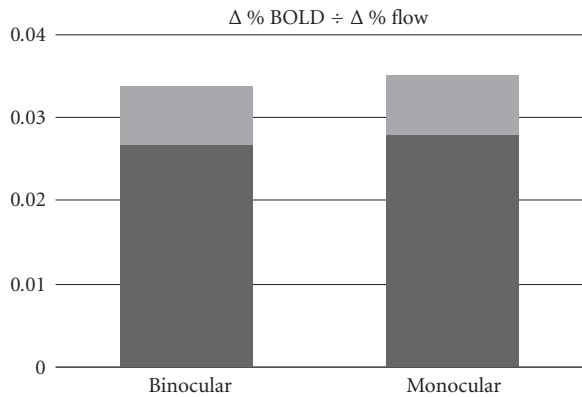


FIGURE 4: Percent change ratios (\pm SE in lighter shade of gray) for BOLD and CBF during binocular and monocular stimulation. There is no significant difference between the ratios for the two forms of stimulation, suggesting a comparable degree of flow-metabolism coupling throughout V1 regardless of the columnar fraction activated.

However, it is notable that while removal of input from one of the two eyes did result in a reduction of both BOLD and flow signals, the response decreased by much less than one half. This is consistent with detailed autoradiographic studies showing that pronounced ocular dominance segregation is mainly limited to cortical layer IV, with layers II and III actually exhibiting *higher* activation during binocular than monocular stimulation [10, 18]. This is consistent with later human neuroimaging studies, in which some regions showed higher apparent activity levels during the appropriate monocular stimulation than during binocular input [16, 19]. The columnar structure associated with ocular dominance is therefore most appropriately viewed as reflecting a moderate bias in overall selectivity, associated primarily with a single cortical sublayer, superimposed on numerous other modulating influences.

In light of the issues discussed above, it is clear that the columnar segregation of brain activation is not “all or nothing” during selective stimulation such as monocular or single-orientation conditions. Much of the early research in this area, performed using optical imaging methods capable of producing compelling maps of the columnar architecture, examined the perfusion of orientation domains (e.g., Malonek and Grinvald [9]) and not ocular dominance columns although a number of authors have imaged ocular dominance using a variety of other methods [5, 6, 10, 19, 20]. It would therefore be informative to replicate the present study using different combinations of oriented stimuli. It is also possible that certain stimuli might achieve a higher degree of selectivity than the ones used in this and prior studies. Perhaps under such conditions a small difference in flow-BOLD coupling might become detectable. Future investigation of this topic might include the use of different stimuli designed to selectively activate pathways involved in stereopsis.

5. CONCLUSION

Our results do not support the theory of spatially decoupled responses in blood flow and oxidative metabolism during activation of a subset of cortical ocular dominance columns. The limited impact of monocular blockade on flow and BOLD response amplitudes is also demonstrated, and should serve as a caution that ocular dominance contrast is likely to be faint in hemodynamic imaging methods.

ACKNOWLEDGMENTS

This study was supported by a grant from the Canadian Institutes of Health Research (MOP 84378). The authors would like to thank Carollyn Hurst and André Cyr for assistance with data acquisition and stimulus presentation.

REFERENCES

- [1] P. A. Chiarelli, D. P. Bulte, D. Gallichan, S. K. Piechnik, R. Wise, and P. Jezzard, “Flow-metabolism coupling in human visual, motor, and supplementary motor areas assessed by magnetic resonance imaging,” *Magnetic Resonance in Medicine*, vol. 57, no. 3, pp. 538–547, 2007.
- [2] O. Leontiev and R. B. Buxton, “Reproducibility of BOLD, perfusion, and CMRO₂ measurements with calibrated-BOLD fMRI,” *NeuroImage*, vol. 35, no. 1, pp. 175–184, 2007.
- [3] P. I. Tuunanen, I. J. Murray, N. R. A. Parry, and R. A. Kauppinen, “Heterogeneous oxygen extraction in the visual cortex during activation in mild hypoxic hypoxia revealed by quantitative functional magnetic resonance imaging,” *Journal of Cerebral Blood Flow and Metabolism*, vol. 26, no. 2, pp. 263–273, 2006.
- [4] K. Uludağ, D. J. Dubowitz, E. J. Yoder, K. Restom, T. T. Liu, and R. B. Buxton, “Coupling of cerebral blood flow and oxygen consumption during physiological activation and deactivation measured with fMRI,” *NeuroImage*, vol. 23, no. 1, pp. 148–155, 2004.
- [5] K. Cheng, R. A. Waggoner, and K. Tanaka, “Human ocular dominance columns as revealed by high-field functional magnetic resonance imaging,” *Neuron*, vol. 32, no. 2, pp. 359–374, 2001.
- [6] T. Q. Duong, D.-S. Kim, K. Uğurbil, and S.-G. Kim, “Localized cerebral blood flow response at submillimeter columnar resolution,” *Proceedings of the National Academy of Sciences of the United States of America*, vol. 98, no. 19, pp. 10904–10909, 2001.
- [7] A. Das and C. D. Gilbert, “Long-range horizontal connections and their role in cortical reorganization revealed by optical recording of cat primary visual cortex,” *Nature*, vol. 375, no. 6534, pp. 780–784, 1995.
- [8] D. Malonek, U. Dirnagl, U. Lindauer, K. Yamada, I. Kanno, and A. Grinvald, “Vascular imprints of neuronal activity: relationships between the dynamics of cortical blood flow, oxygenation, and volume changes following sensory stimulation,” *Proceedings of the National Academy of Sciences of the United States of America*, vol. 94, no. 26, pp. 14826–14831, 1997.
- [9] D. Malonek and A. Grinvald, “Interactions between electrical activity and cortical microcirculation revealed by imaging spectroscopy: implications for functional brain mapping,” *Science*, vol. 272, no. 5261, pp. 551–554, 1996.

- [10] R. B. Tootell, S. L. Hamilton, M. S. Silverman, and E. Switkes, "Functional anatomy of macaque striate cortex. I. Ocular dominance binocular interactions, and baseline conditions," *Journal of Neuroscience*, vol. 8, no. 5, pp. 1500–1530, 1988.
- [11] W.-M. Luh, E. C. Wong, P. A. Bandettini, and J. S. Hyde, "QUIPSS II with thin-slice TI_1 periodic saturation: a method for improving accuracy of quantitative perfusion imaging using pulsed arterial spin labeling," *Magnetic Resonance in Medicine*, vol. 41, no. 6, pp. 1246–1254, 1999.
- [12] E. C. Wong, R. B. Buxton, and L. R. Frank, "Quantitative imaging of perfusion using a single subtraction (QUIPSS and QUIPSS II)," *Magnetic Resonance in Medicine*, vol. 39, no. 5, pp. 702–708, 1998.
- [13] E. C. Wong, R. B. Buxton, and L. R. Frank, "Implementation of quantitative perfusion imaging techniques for functional brain mapping using pulsed arterial spin labeling," *NMR in Biomedicine*, vol. 10, no. 4-5, pp. 237–249, 1997.
- [14] G. H. Glover, "Deconvolution of impulse response in event-related BOLD fMRI," *NeuroImage*, vol. 9, no. 4, pp. 416–429, 1999.
- [15] K. J. Worsley, C. H. Liao, J. Aston, et al., "A general statistical analysis for fMRI data," *NeuroImage*, vol. 15, no. 1, pp. 1–15, 2002.
- [16] R. S. Menon and B. G. Goodyear, "Submillimeter functional localization in human striate cortex using BOLD contrast at 4 Tesla: implications for the vascular point-spread function," *Magnetic Resonance in Medicine*, vol. 41, no. 2, pp. 230–235, 1999.
- [17] R. D. Hoge, J. Atkinson, B. Gill, G. R. Crelier, S. Marrett, and G. B. Pike, "Comparison of bulk CBF/CMRO₂ coupling in human V1 during monocular and binocular stimulation," in *Proceedings of the 5th International Conference on Functional Mapping of the Human Brain*, vol. 9, p. S307, Dusseldorf, Germany, June 1999.
- [18] J. C. Horton and D. R. Hocking, "Monocular core zones and binocular border strips in primate striate cortex revealed by the contrasting effects of enucleation, eyelid suture, and retinal laser lesions on cytochrome oxidase activity," *Journal of Neuroscience*, vol. 18, no. 14, pp. 5433–5455, 1998.
- [19] B. G. Goodyear and R. S. Menon, "Brief visual stimulation allows mapping of ocular dominance in visual cortex using fMRI," *Human Brain Mapping*, vol. 14, no. 4, pp. 210–217, 2001.
- [20] G. G. Blasdel, "Differential imaging of ocular dominance and orientation selectivity in monkey striate cortex," *Journal of Neuroscience*, vol. 12, no. 8, pp. 3115–3138, 1992.

Review Article

Contribution of Exploratory Methods to the Investigation of Extended Large-Scale Brain Networks in Functional MRI: Methodologies, Results, and Challenges

V. Perlberg^{1,2} and G. Marrelec^{1,2}

¹U678, Inserm, Paris 75013, France

²Faculté de Médecine Pitié-Salpêtrière, Université Pierre et Marie Curie, Paris 75013, France

Correspondence should be addressed to G. Marrelec, marrelec@imed.jussieu.fr

Received 31 August 2007; Accepted 7 December 2007

Recommended by Oury Monchi

A large-scale brain network can be defined as a set of segregated and integrated regions, that is, distant regions that share strong anatomical connections and functional interactions. Data-driven investigation of such networks has recently received a great deal of attention in blood-oxygen-level-dependent (BOLD) functional magnetic resonance imaging (fMRI). We here review the rationale for such an investigation, the methods used, the results obtained, and also discuss some issues that have to be faced for an efficient exploration.

Copyright © 2008 V. Perlberg and G. Marrelec. This is an open access article distributed under the Creative Commons Attribution License, which permits unrestricted use, distribution, and reproduction in any medium, provided the original work is properly cited.

1. INTRODUCTION

Blood-oxygen-level-dependent (BOLD) functional magnetic resonance imaging (fMRI) is an imaging technique that makes it possible to dynamically and noninvasively track metabolic and hemodynamic changes in the brain [1, 2]. The early developments of BOLD fMRI data analysis have mostly relied on a method called general linear model (GLM), whose objective is to pinpoint the differential involvement of certain regions during various tasks [3–5]. Voxel clusters that exhibited such a behavior are declared “activated” and gathered into a so-called activation map that provides the output of the GLM approach; each map represents all regions that are significantly correlated with the stimulus time course. GLM-based methods have been extensively used in order to extract regions in a wide variety of conditions (see, e.g., [6] for a review of activation studies related to the premotor cortex).

The GLM, however, does not properly render the brain’s intricate organization, which is believed to be based on two major principles: segregation and integration [7, 8]. According to these two principles, functional tasks are performed by specific collections of brain regions, also called networks, that are anatomically connected and can engage

in complex interactions [9–11]. Even though the BOLD contrast is only remotely related to neuronal activity, it was first hypothesized, and then evidenced, that this imaging modality is able to reflect, at least to some extent, the strong constraints imposed on the brain by segregation and integration. This realization came from the investigation of the (misleadingly called) “rest” condition. First, studies showed that brain regions could still be correlated at rest, hinting for the existence of functional brain networks that could still be present and imaged even when no task was explicitly required from the subject [12, 13]. Network investigation also started with a closer examination of the “baseline,” that is, the signal measured when a subject is in the “rest” condition of a protocol, between two task conditions [14]. This approach was justified from the fact that, from an energetic perspective, the brain uses a significant part of the body’s energy, independently of the presence or absence of a “task” [15, 16]. As methods of increasing complexity were developed and validated, the objective of many methodological developments shifted from GLM-related procedures to methods that were able to extract networks from BOLD fMRI data.

This paper is an attempt to review the latest advances in investigation of extended large-scale networks in fMRI

from a methodological perspective, as well as the networks that have been found using these methods. This new methodology, if confirmed, has very deep implications in terms of methods that should be developed, and we discuss some of the issues that such methods will have to deal with in order to provide reliable and useful results.

2. LARGE-SCALE NETWORKS AS A CONSEQUENCE OF BRAIN ORGANIZATION

An extended large-scale functional brain network may be defined as a (potentially large) number of segregated regions (potentially spread over the whole brain) that interact in order to execute a coherent task. While Bressler and Tognoli [17] mostly consider “high-level brain functions of which cognition is comprised,” it is important to emphasize the fact that about any function that the brain is able to process is likely to have a network representation (see, e.g., Section 4 for a description of some low-level brain functions, such as vision and audition processing).

Large-scale networks share many important features. First, they are widely distributed over the brain. As a consequence of the segregation principle, it is hypothesized that they can be broken down into small brain regions, coined “nodes” by Mesulam [18], “units” by Marrelec et al. [19], and “local cortical area networks” by Bressler and Tognoli [17], each region being characterized by a consistent functional behavior. Such nodes can readily be identified in subcortical structures, which are often gathered into nuclei [20]. As to the cortex, despite cytoarchitectonic features (embodied, e.g., by the work of Brodmann [21] and his eponymous regions) that vary across its surface, its parcellation based on structural criteria alone remains globally a challenge. Nonetheless, local brain areas are also strongly characterized by their function [17]. For instance, primary sensory regions (e.g., visual) have been localized in a quite reproducible manner; within these regions, areas responding more specifically to certain types of inputs have been successfully identified (e.g., vertical versus horizontal lines in the primary visual cortex [22]). Still, even though various levels of specialization can usually be observed, there is a general agreement that most regions cannot be unambiguously associated with one specific function (see, e.g., [23] for Broca’s area) and, in general, a region will exhibit a certain level of “multifunctionality” [17]: its contribution will not be limited to one task but will be allowed to vary within a given range of functions that it is able to implement.

As a consequence of the integration principle, large-scale networks are also characterized by potentially distant regions with strong (anatomical) connections and (functional) interactions. Whether top-down or bottom-up, serial or parallel, connections and interactions are quintessential of networks [18, 24, 25]. Anatomically, interregional connectivity is suspected to be rather sparse [26–30]. Even though most connections originating from one region are thought to re-enter the same region, axons are known to connect regions that are far apart from each other, for example, homologue regions [e.g., [31–33]]. Functionally, these connections have

translations at all levels, from electrophysiology [34–38] to measures of the electromagnetic field [39] and of the BOLD signal [12, 13].

Whether coined “new phrenology” [40] or considered as being “beyond phrenology” [25], such an approach leads to a model of brain functions in which most functional tasks are subserved by functional brain networks, that is, collections of specialized regions that collaborate in order to generate a coherent behavior [11, 36]. In support of this approach, several networks have already been described and documented. Luria [10] refers to three blocks: one that “regulates the energy level and tone of the cortex,” another one that is strongly implicated in information processing, and a last one that is involved in higher, complex tasks, such as “the formation of intentions and programs for behavior.” Mesulam [18] proposed two distinct subdivisions of the brain. First, based on the co-occurrence of functions with similar features, the brain can be divided into five major “subtypes”: primary sensory-motor, unimodal association, heteromodal association, paralimbic, and limbic. There are also at least five large-scale networks, each dealing with a specific cognitive function: spatial awareness, language, explicit memory/emotion, face-object recognition, and working memory-executive function. These networks are not isolated from one another, but interact in very complex fashion, for example, through “transmodal” areas.

3. fMRI INVESTIGATION OF LARGE-SCALE NETWORKS

Relying on the assumption that BOLD fMRI is indeed able to image brain networks (see, e.g., [15] for a review of the neurophysiological substrate of neuroimaging), two categories of methods may be identified for such studies: approaches that make use of prior cognitive information and fully exploratory methods.

3.1. Using neurocognitive information

Correlational methods were historically the first ones to be applied to investigate large-scale networks in fMRI data analysis, in the form of functional connectivity studies and functional connectivity maps [12, 41–47]. Starting from a voxel or region—the so-called “seed” voxel/region—one extracts all voxels whose time courses are significantly correlated with that of the seed. Measures other than temporal correlation have also been used, such as coherence and partial coherence [48, 49]. Selection of the seed region is a key issue in studies of functional connectivity. First, a brain region is selected according to its function (e.g., cortical representation for hand movement, [47]). The corresponding seed is then obtained from either prior anatomical knowledge or functional manipulation. Anatomically, common approaches consist of using coordinates in a standardized space (Talairach or MNI) [44], or having an expert delineate the region on anatomical images [48]. Functionally, the seed can be obtained from an activation map, provided that the region of interest can be characterized by its implication in

a specific task (e.g., the primary motor cortex in a simple movement) [41, 45, 47].

As opposed to effective connectivity—where Gonçlaves and Hall [50] showed that results of SEM analyses may vary depending on the choice of the seed voxel—robustness of functional connectivity maps with regard to the selection of the seed region and its spatial extent have barely been examined yet. Vincent et al. [51] showed that, for the visual or the somatomotor network, the resulting functional connectivity map was robust to the choice of the starting seed region. Many other parameters (e.g., design, size of each region) may have an influence on the outcome of the analysis, potentially leading to different spatial structures or correlation values between structures. Full exploration of a whole network (i.e., with many regions) would imply the recourse to several successive computations of functional connectivity maps, each map being used to select a region significantly correlated as seed voxel for the next step—a procedure that is lengthy, complex, and whose convergence is not assured. Wang and Xia [52] have recently proposed a method to perform this exploration in only one step.

3.2. *Blind exploration*

The goal of fully exploratory methods is to provide data-driven approaches of large-scale network detection in which no prior cognitive information is required for the methods to proceed. A number of such procedures have been proposed, most of them relying more or less closely on either of the two key features of large-scale networks, namely integration and segregation.

The vast majority of approaches proceed as follows. Based on a similarity measure, they gather voxels irrespective of their anatomical proximity (and, hence, of segregation) into separate classes that are strongly similar to each other and dissimilar from one another. For each class, the output is a map representative of the class and an associated time course. All methods have one or several parameters whose tuning affects the number of classes. Since each class tends to gather voxels that are strongly correlated, it is often univocally identified with a large-scale network. Blind approaches include methods based on eigenvalue decomposition, such as principal component analysis (PCA) [53–55], correlation clustering [56], Kendall’s coefficient of concordance [57, 58], K-means [59, 60], fuzzy clustering methods [54, 56], self-organizing map algorithms [61], Kohonen clustering neural network and fuzzy C-means [62], hierarchical clustering [60, 63], integration and information-theoretic quantities [64, 65], and spatial independent component analysis (sICA) [66]. While most methods provide maps that are exclusive (a voxel can only belong to one map), a few (e.g., fuzzy clustering or ICA) provide an index of the plausibility for a voxel to belong to each of the different classes. Most methods also provide local criteria, calling for stepwise analyses, at the exception of PCA and ICA that use global measures and, consequently, are able to perform classification in one step.

Most approaches mentioned in the previous paragraph have only been used a limited number of time in fMRI data analysis so far. This can probably be accounted for by the

complexity of their algorithms, which is commensurate with the difficulty of the task at hand. Outstandingly, sICA has been used quite a lot recently, with results that are rather promising. Regardless of its popularity, though, the network interpretation of the results obtained needs to be proved beyond simple criteria (these include, e.g., that voxels located close to each other or in homologue regions tend to belong to the same class). For instance, for PCA, Friston and Büchel [67] mention that the interpretation of the eigenimages in biological terms might be dubious, since they could be rotated in the data space and still be a solution to the problem (but see [68]). By contrast, components obtained through ICA can be more easily related to known physiological noises or functional processes [66, 69]. The methodological reasons for this success are, however, still not clear, and many explanations are plausible: the relevance of the assumption of spatial independence, the adequacy of the underlying mixing model, the efficiency of the global criterion/one-step discrimination approach, or some interesting feature of the information-theoretic optimization algorithm. In any case, the fact that its application simplifies the results to a maximum and produces a very limited number of widespread networks, making interpretation easier, clearly plays in its favor (compare, e.g., with [70, 71], or [72]). Its sensitivity, which is much higher than that of clustering methods, might also explain its success. Nevertheless, it must still be kept in mind that the assumptions underlying ICA (perfect synchrony within a network and spatial independence between networks) impose an extreme and unrealistic case of integration. While the simplification of several time courses into one is performed only once for ICA, the stepwise procedures implemented by other methods essentially go through the same approximation at each step, leading to an error that is probably far larger.

Unlike the numerous approaches to functional integration, few methods have specifically sought to extract segregated regions. Some methods decrease the complexity of the data by using predefined regions (e.g., according to the Tzourio-Mazoyer et al. [81] template). Approaches using predefined regions do not check that all voxels within a region exhibit homogeneous behaviors; they merely assume that it is the case. Average signals are then extracted from each region, on which any integration-based approach, such as hierarchical clustering [71, 72], can be applied. Intuitively, many clustering methods mentioned previously (e.g., K-means, hierarchical clustering, or information-theoretic measures) could easily be applied for the purpose of detecting segregated regions by incorporating a constraint of contiguity between voxels that could be merged. Among these, only the information-theoretic approach explicitly takes both within- and between-classes measures of similarity into account. Specifically, they optimize a so-called functional clustering index (FCI) that keeps a balance between region homogeneity (strong segregation) and sparseness of inter-regional interactions (low integration) [64, 65]—the latter constraint being hard to justify from a network perspective. As to other clustering methods, as noted by Goutte et al. [60] in accordance to Huygens’ formula, maximizing a measure of the internal coherence of a class (associated with

TABLE 1: Literature summary of the different networks found in network investigation of fMRI data. Methods—HC: hierarchical clustering, SOM: self-organizing map algorithm, ICA: independent component analysis. Networks—M/SM: motor/sensorimotor, V: visual, A: auditory, DM: default mode, dAtt: dorsal attentional, vAtt: ventral attentional, EC: executive control. Networks found are denoted by “X.” (*) In addition to primary cortices (sensorimotor, visual, and auditory), the clusters shown by Cordes et al. [63] were essentially bilateral single regions (thalami, fusiform gyri, and frontal gyri) which were parts of different networks of reference. (†) Except for the sensorimotor system, the networks identified by Peltier et al. [61] were not properly labeled; the spatial organizations of the maps shown seemed similar to the attentional networks. (‡) The results presented by Calhoun et al. [73] were partial, mentioning the extraction of other networks that they did not show neither comment; another study on similar datasets showed that the sensorimotor and the dorsal attentional networks might be detected too [74].

Task	Reference	Method	Network						
			M/SM	V	A	DM	dAtt	vAtt	EC
At rest	[61]	HC	X	X	X		X(*)	X(*)	
	[63]	SOM	X				(†)	(†)	
	[73]	ICA	X	X	X	X			
	[75]	ICA	X	X	X	X	X		X
	[76]	ICA	X	X	X	X	X	X	X
	[77]	ICA	X	X		X	X	X	
Blocked visual	[78]	ICA	X(‡)	X	X		X(‡)		
	[79]	ICA		X		X	X		
Blocked motor	[80]	LSNI	X			X	X		

segregation) is often equivalent to minimizing the same measure of coherence but computed between classes (that could be associated with integration). As such, the behavior of such methods with regard to networks would again lead to questioning.

A tentative approach to consider simultaneously segregation and integration has been conducted by the large scale network identification (LSNI) method by Bellec et al. [80]. LSNI first clusters neighboring voxels into small regions using a region-growing algorithm [82] and then selects regions that exhibit a significant correlation with other distant regions. Such a procedure allows to define brain functional regions and networks in a purely data-driven way. While the sensitivity of the algorithm proposed was rather low, it had the great advantage to explicitly define and address the two principles of functional segregation and integration. So far, this method seems adapted for individual analyses; its extension to group studies seems limited due to the subject-dependent definition of regions.

4. TYPOLOGY OF NETWORKS EXTRACTED WITH fMRI

During the last decade, several brain systems have been studied in fMRI using functional connectivity-related approaches. These studies have revealed integrated systems, including primary systems and associative networks. Exploratory approaches have also allowed to extract several functional networks at once. Even if all brain areas are not included in a network, these networks involve many areas and constitute a possible functional parcellation of the brain.

The motor network was the first network studied through functional connectivity analyses. Biswal et al. [12] reported correlations in low-frequency resting-state fluctuations between left and right motor areas using single-slice fast-sampled acquisitions. This result was later reproduced

with multislice acquisitions where an extended motor network was shown to correlate with a region in the primary motor cortex [44, 47]. Lowe et al. [44] showed that other functional networks could be detected using other seed regions, namely the visual network with a seed around the calcarine fissure and a limbic network with a seed in the amygdala. An auditory and a language systems were later extracted in the same way [41, 43]. Other networks were also studied using the seed-region functional connectivity approach, such as the default-mode network [83–86], the attentional networks [42, 83, 87], and memory networks [46, 88].

More recently, a larger number of functional networks were revealed using exploratory methods based on ICA [76–78]. Even if the number of extracted networks varied, their spatial organizations were reproducible across studies. For instance, all three studies just mentioned found functional networks involving the same systems that were sometimes split into different parts (e.g., left/right, rostral/caudal). Using group ICA studies of resting-state datasets [76–78], which were the most reproducible, we selected seven functional networks: a motor/sensorimotor system, a visual system, an auditory system, a default-mode network, a dorsal attentional network, a ventral attentional network, and an executive control network. Van de ven et al. [75] systematically studied the reproducibility of ICA results on individual datasets and the results using hierarchical clustering [63] and self-organizing map algorithm (SOM) [61] were presented on an individual level. The results from studies that provided a systematic description of all networks found are reported in Table 1. In Figure 1 and Table 2, we also reported results from a study on a population of 20 healthy subjects acquired at rest, where networks were extracted using spatial ICA and a hierarchical clustering approach similar to that of Esposito et al. [79].

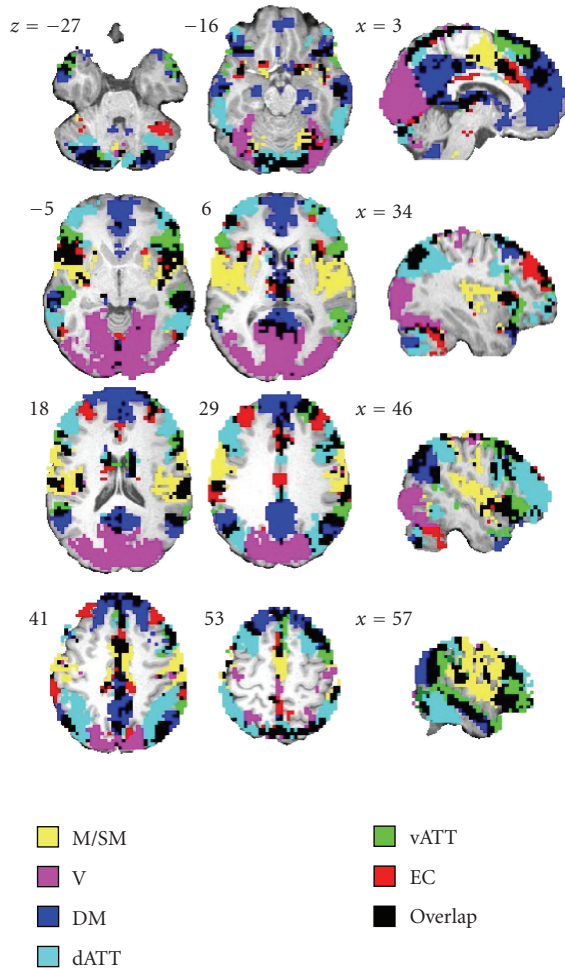


FIGURE 1: Example of extended large-scale networks extracted in fMRI at rest. The six networks were identified using spatial ICA and a hierarchical clustering approach similar to that of [79] on a group of 20 healthy subjects acquired at rest. Networks—M/SM: motor/sensorimotor, V: visual, DM: default mode, dAtt: dorsal attentional, vAtt: ventral attentional, EC: executive control. The auditory network was not found as a separate network but some temporal regions of the primary auditory cortex are overlapped by other networks (in particular the M/SM network and the two attentional networks). The union of all networks does not add up to comprise the entire brain; for instance, some parts of the frontal cortex do not belong to any reported networks. By contrast, some brain regions simultaneously belong to several networks (in black).

The sensorimotor system involves at least the pre- and postcentral gyri (including the primary motor cortex and supplementary motor area). The visual system involves both medial striate and extrastriate regions (calcarine sulcus and lingual gyrus), as well as lateral occipital regions (nonprimary visual regions); these two visual networks (primary and associative) were identified separately by the three group-ICA studies. The auditory system involves principally lateral superior temporal gyri, the Heschl’s gyrus and insular cortex. The so-called default-mode network involves the anterior and posterior cingulate cortices, the medial prefrontal cortex and lateral parietal regions [15, 89–91].

The dorsal attentional network involves lateral prefrontal and dorsal parietal cortex; these regions are involved in visio-spatial control [42, 92, 93]. The ventral attentional network involves inferior occipito-parietal regions and inferior lateral prefrontal regions; these regions are principally involved in new item recognition [42, 94]. Last, the executive control network involves superior and middle prefrontal cortices, ventrolateral prefrontal cortex and anterior cingulate gyrus [95].

Other studies have applied these exploratory approaches to extract integrated functional networks from fMRI datasets acquired during external stimulation [73, 79, 80]. The results of these three studies are also compiled in Table 1. These results showed that the detection of the functional networks not directly related to the stimulation were less sensitive than that without external stimulation.

5. FUTURE ISSUES

Tracking the presence of extended large-scale networks in BOLD fMRI data raises many issues. We have here focused on some aspects related to the neurocognitive aspects of networks, their identifiability by fMRI, and the methodological questions raised by network analyses.

5.1. Neurocognitive aspects

The major issue to be faced is arguably the very definition of an extended large-scale brain network. Indeed, even though the brain is far from being fully connected, any region is eventually connected to any other regions if one takes polysynaptic connections into account. Obviously, stating that the brain can be considered as one network is by no way satisfying, no more than it is to say that each macrocolumn forms a networks by itself. The strongly hierarchical nature of the brain’s anatomical and structural organization induces similar characteristics at all levels. As the brain can be decomposed in networks, each network can in turn be further partitioned into subnetworks, subnetworks into subsubnetworks, and so on. Furthermore, even though there probably is a (potentially loose) relationship between anatomical and functional organizations, it is still unknown how functional integration and segregation are coded in anatomical terms. For the exact same structural organization, it has been shown that networks can be observed to break down as one discriminates different sets of functional tasks or behaviors with increasing precision. For instance, the visual system can be decomposed into a ventral and a dorsal stream [22]. These two subnetworks, albeit interacting, have very distinct functions [42, 92, 96]. Similarly, the motor system can be further separated into a cerebello-cortical and a basal-cortical loop with different patterns of involvement [97, 98]. The difficulty to define a network does not yield for primary networks only. For instance, it has been argued that the fronto-parietal network could be further partitioned into two subnetworks subserving attention and working memory, respectively, [99], while the working memory network itself could be further broken down in two, with one subnetwork mediating attentional selection and another

TABLE 2: Example of extended large-scale networks extracted in fMRI at rest. Peak foci corresponding to the six networks identified using spatial ICA and a hierarchical clustering approach similar to that of [79] on a group of 20 healthy subjects acquired at rest—M/SM: motor/sensorimotor, V: visual, DM: default mode, dAtt: dorsal attentional, vAtt: ventral attentional, EC: executive control.

(a) M/SM network			(d) dATT network		
Names	BA	Talairach coordinates	Names	BA	Talairach coordinates
<i>Frontal</i>			<i>Frontal</i>		
SMA	6	(0, -4, 52) (0, -4, 52)	PreSMA	6/8	(-3, 23, 50) (3, 19, 47)
Primary motor cortex	4	(-45, -12, 56) (45, -14, 56)	Lateral premotor	6/8	(-33, 13, 58) (33, 13, 58)
Rolandic opercule	43	(-46, -15, 15) (46, -19, 15)	Ventral prefrontal	46	(-36, 50, 1) (45, 44, 1)
<i>Cingulate cortex</i>			Ventral prefrontal	44	(-50, 7, 23) (50, 7, 23)
ACC	32	(0, 14, 39) (0, 14, 39)	Dorsal prefrontal	46	(-44, 30, 30) (45, 31, 30)
<i>Parietal</i>			Precentral	9	(-48, 8, 37) (49, 9, 38)
Postcentral	3	(-51, -15, 38) (53, -11, 38)	<i>Cingulate cortex</i>		
SII	40/43	(-55, -30, 22) (55, -30, 22)	PCC	31	(0, -36, 31) (0, -36, 31)
<i>Insula</i>			<i>Parietal</i>		
Posterior Insula	13	(-41, 4, 6) (43, -2, 6)	Superior parietal	7	(-38, -62, 55) (35, -72, 49)
<i>Cerebellum</i>			Inferior parietal	40	(-38, -69, 45) (45, -52, 51)
VermisVIII		(0, -73, -26) (0, -73, -26)	Angular gyrus	40	(-42, -69, 45) (45, -55, 51)
(b) V network			Precuneus	7	(0, -69, 52) (0, -69, 52)
Names	BA	Talairach coordinates	<i>Temporal</i>		
<i>Occipital</i>			MT	21	(-57, -49, -3) (56, -51, -3)
Cuneus	19	(0, -83, 30) (0, -83, 30)	Inferior temporal	37	(-62, -48, -12) (55, -55, -12)
Calcarine	17	(-7, -90, 8) (7, -85, 7)	<i>Subcortical areas</i>		
Lingual	18	(-13, -51, 3) (15, -51, 2)	Caudate nucleus		(-14, 4, 13) (10, 11, 9)
Fusiform	19	(-27, -60, -9) (31, -63, -9)	Thalamus VL		(-10, -13, 10) (10, -13, 10)
Superior occipital	18	(-17, -94, 21) (18, -92, 21)	<i>Cerebellum</i>		
Middle occipital	19	(-42, -88, 4) (38, -89, 4)	Crus1		(-35, -66, -26) (31, -66, -26)
Inferior occipital	18	(-39, -86, 0) (39, -85, -2)	Crus2		(-7, -83, -19) (14, -83, -22)
<i>Cerebellum</i>			(e) vATT network		
Crus1		(-28, -79, -14) (35, -82, -14)	Names	BA	Talairach coordinates
(c) DM network			<i>Frontal</i>		
Names	BA	Talairach coordinates	preSMA	6	(0, 6, 45) (0, 6, 45)
<i>Frontal</i>			Ventral prefrontal	46	(—, —, —) (52, 38, 8)
Superior frontal	8	(-24, 36, 47) (24, 26, 47)	Dorsolateral prefrontal	9	(-35, 39, 34) (31, 39, 34)
Rostromedial frontal	10	(0, 53, 4) (0, 53, 4)	Inferior frontal opercule	43	(-44, 13, 4) (51, 15, 4)
Dorsolateral prefrontal	9	(-37, 17, 49) (36, 18, 51)	<i>Cingulate cortex</i>		
<i>Cingulate cortex</i>			MCC	24	(0, 12, 35) (0, 12, 35)
ACC	24/32	(0, 44, 4) (0, 44, 4)	<i>Parietal</i>		
MCC	24/31	(0, -30, 34) (0, -30, 34)	Inferior parietal	7/40	(-51, -50, 48) (53, -49, 48)
PCC	31	(0, -42, 31) (0, -42, 31)	Supramarginal	40	(-62, -32, 31) (59, -23, 26)
<i>Parietal</i>			Precuneus	7	(0, -61, 58) (0, -61, 58)
Angular gyrus	40	(-49, -62, 42) (42, -69, 45)	<i>Temporal</i>		
Precuneus	7	(0, -66, 36) (0, -66, 36)	MT		(—, —, —) (52, -34, -2)
<i>Occipital</i>			<i>Insula</i>		
Cuneus	18	(0, -70, 25) (0, -70, 25)	Insula	13	(-45, 0, -3) (38, 10, -1)
<i>Temporal</i>			<i>Subcortical areas</i>		
Anterior MT	21	(-59, -18, -14) (59, -11, -17)	Caudate		(-10, 1, 13) (14, -6, 16)
Posterior MT	39	(-55, -53, 19) (52, -57, 16)	Thalamus		(-5, -20, 7) (5, -20, 7)
PHG		(-25, -29, -14) (24, -30, -14)	<i>Cerebellum</i>		
Hippocampus		(-20, -25, -9) (24, -26, -9)	Crus1		(-45, -56, -24) (45, -56, -24)
<i>Subcortical areas</i>			VI		(-21, -65, -17) (28, -65, -17)
Caudate nucleus		(-7, 13, -4) (7, 10, -6)			
Dorsomedial Thalamus		(-3, -23, 8) (7, -23, 8)			
<i>Cerebellum</i>					
IX		(-3, -53, -36) (10, -49, -36)			

TABLE 2: Continued.

(f) EC network

Names	BA	Talairach coordinates
<i>Frontal</i>		
Medial superior frontal	8/9	(0, 43, 37) (0, 43, 37)
Lateral premotor	6/8	(−38, 10, 54) (45, 13, 48)
Ventrolateral prefrontal	47	(−49, 25, −7) (47, 25, −7)
Ventrolateral prefrontal	45	(−52, 21, 2) (55, 24, 5)
Dorsolateral prefrontal	9	(−21, 49, 36) (24, 52, 30)
<i>Cingulate cortex</i>		
MCC	24/31	(0, −18, 40) (0, −18, 40)
<i>Parietal</i>		
Angular gyrus	39	(−49, −60, 26) (49, −53, 32)
Precuneus	7	(0, −52, 38) (0, −52, 38)
<i>Temporal</i>		
Temporal pole	21	(−49, 9, −27) (52, 12, −27)
Anterior MT	20/21	(−57, −11, −19) (60, −11, −19)
Posterior MT	22/39	(−51, −59, 15) (55, −56, 15)
<i>Subcortical areas</i>		
Caudate nucleus		(−10, 3, 17) (12, 2, 17)
Dorsomedial Thalamus		(−3, −16, 14) (3, −16, 14)
Anterior Thalamus		(−6, −6, 12) (6, −6, 12)
<i>Cerebellum</i>		
Crus1		(−24, −76, −23) (28, −79, −23)
Crus2		(−21, −76, −29) (24, −83, −25)

one rather underlying language functions [100]. Networks are not exclusive from each other either. Mesulam [18] refers to transmodal nodes that connect various neurocognitive networks. For instance, activation of some fronto-parietal regions is observed during different cognitive tasks [101]; are these regions transmodal or part of a subnetwork that has a specific function? Similarly, the insular cortex is typically a multimodal association area that is not specifically activated by auditory stimuli. However, as reported in Section 4, recent papers have consistently classified it as belonging to a so-called auditory system. As evidenced by Figure 1, there are also some overlapping between networks, and voxels can be simultaneously classified as belonging to different networks. What is the function of such regions? Could this overlapping between networks be related to synchronization through distinct frequency-bands [35]—if such a phenomenon is indeed visible through fMRI BOLD imaging? Regarding the influence of a task on a network, an issue that has not received much attention yet, studies have shown that networks could indeed be influenced by the processing of a task, either during the task [86] or even after it [102]. It is hence not unrealistic to suspect that processing of a task might also modify the very structure of some networks.

Another cogent question is the relationship between networks as detected by fMRI data analyses and those mentioned in the literature. Networks extracted from fMRI are the consequence of the optimization of a mathematical criterion whose link to neuroscience is, at the very least, not obvious. While some results have been rather successfully related to the neurocognitive literature (e.g., attentional network), other results are more complex to interpret. Some

networks extracted seem to share commonalities with some of the subtypes described by Mesulam [18] (e.g., the motor network; cf. Section 2), while others seem to be rather related to Mesulam [18]’s neurocognitive networks (e.g., the attentional network). Besides, the union of all reported networks (e.g., by sICA) does not include the whole brain. Some brain regions are then excluded from the functional networks organization of the brain. Why so? Globally, the criterion used for network extraction might make the methods sensitive to some functions or types of connections. For instance, top-down and bottom-up influences have distinct features [25, 34, 36–38]. Can they be detected equally well by existing methods?

Apart from these difficulties, there has also been evidence of variability across healthy subjects [80, 103] that could be explained by many factors, such as development and/or age [104, 105], and, in general, all forms of plasticity [106, 107]. Pathologies, for example, stroke [108, 109] or tumors [110–113], render the issue even more complex. Some studies have shown that certain pathologies can have network-specific effects: behavioral deficits in spatial neglects for the fronto-parietal network [114]; epilepsy [115] and Alzheimer’s disease [116] for the default-mode network. Nonetheless, these results must be used with caution, for it is not clear yet whether they truly reflect a change in neuronal properties or, as, for example, in grade II glioma, a mere modification of the metabolic and vascular properties of the surrounding tissues.

5.2. BOLD fMRI imaging

Use of BOLD fMRI as a way to investigate large-scale networks relies on three successive assumptions, namely, that information exchanges between neurons is related to synchronies, synchronies to the BOLD contrast, and the BOLD contrast to the fMRI data effectively measured.

Synchronies are the blueprint of communication between regions [17, 39, 117–120] and, as such, should be strongly related to large-scale networks. A challenging issue is to determine the exact relationship between the spatial distribution and interaction pattern of regions within a large-scale network on the one hand and, on the other hand, the spatial and frequential distribution of oscillations.

Another issue is the connection between neuronal activity/synchrony and the appearance of a BOLD signal. While much still needs to be unraveled as to the connection between neuronal synchronies and the BOLD signal, it now seems more and more accepted that a sustained change in neuronal activity is likely to entail a relative change in the BOLD level [121–124], even though the exact relationship is expected to be rather complex [125].

Still, the BOLD signal is only a fraction of the total signal that is acquired in fMRI, a signal that is not exempt from many kinds of artifacts [126–128]. In particular, some physiological processes (e.g., cardiac, respiratory, or movement-related) induce spurious effects that contaminate the BOLD signal in the whole brain [129, 130]. Such artifacts are predominant in certain regions of the brain, such as the basal arteries for cardiac activity or the interfaces between

cerebrospinal fluid pools and brain tissue for breathing and head movements. This origin-dependent predilection implies a spatial structure of the noise. Some network detection algorithms may hence recognize voxels influenced by the same spatially structured artifact as meeting the requirement for strong temporal coherence and, hence, assign them to a common structure. This feature has been successfully used by ICA techniques to provide efficient noise separation and removal techniques [66, 131, 132]. Yet, the issue arises when structures induced by noise are wrongly interpreted as functional networks; their detection and removal is hence of very high importance. The fundamental question, while examining spatial structures with a similar temporal behavior, is “do we measure neurally induced signal or consequences of physiological processes [133]?” Even though our understanding of the potential artifacts that can contaminate the BOLD fMRI signal improves, the consequences of many potential sources of structured noise have barely been mentioned, let alone investigated. For instance, it is believed that some mechanisms related to the regulation of blood flow (e.g., through the level of CO₂ in the blood) could induce coherent changes in BOLD signal throughout the brain—giving birth to an effect likely to be identified as a functional network. In fact, such an effect has been used to explain the presence of the default-mode network in fMRI [134, 135]. Now, whether these regions are wrongfully classified as belonging to a common functional network because their voxels are corrupted by the same artifact, or whether they are actually regions that drive the physiological response is a matter that remains to be solved.

5.3. Data analysis

Many questions remain open regarding what methodologies to apply to extract functional networks. We here quickly discuss issues related to the choice of a model, the redundancy of fMRI signals, the necessity to provide both individual and group analyses, the importance of result representation, and the validation of fMRI results with other modalities.

Procedures used to investigate networks are usually based on mathematical methods that have been discovered independently of the field of fMRI data analysis. Their behavior is hence not guided by cognitive but mathematical considerations. While it can be accepted that most methods are general enough to be applied to a wide variety of problems, they still require a careful assessment of how best to adapt them to the issue at hand. We believe that the major point to cope with here is “how do methods code for segregation and integration? Does it make sense?” A relevant approach could be to try to derive out consistency requirements from cognitive consideration of what an “ideal” method should be able to do: quantify integration between voxels, regions, or networks using the same principled measure (such as the multiple correlation coefficient [136] or integration [7, 137]); differentiate between direct and indirect information exchanges (such as partial correlation [19, 72, 138–141]); discriminate causality from simple co-occurrence (such as Granger causality [138, 142–144]). Some methods are able

to deal with one aspect of the problem, but none has been proposed to answer all these questions simultaneously.

Besides, investigation of large-scale networks face a very interesting problem, namely that of determining the spatial precision under which data should be considered as segregated and over which they should be said to be integrated. While it is obvious that neighboring voxels share a great deal of information, methods that model and summarize the behavior of a whole network with one single time course clearly oversimplify the problem and discard a lot of cogent information. Bellec et al. [80] proposed a statistical model that provides a critical distance that separates segregation and integration. Voxel clustering is another attempt to deal with that issue. However, the parameters that characterize the clustering coarseness are set a priori, when they should be determined by the intrinsic properties of the data and allowed to vary across the brain (e.g., between subcortical and cortical structures, which have distinct characteristic spatial extents). This step allows one also to reduce the dimensionality of the data. At least for this reason, it is a crucial step, because network investigation requires multivariate analyses that are computationally very demanding (the computational burden roughly exponentially increase with the number of regions).

In neurocomputing, models investigating issues very similar to that of large-scale networks have already been developed [145–148]. However, most methods developed so far for effective connectivity, such as structural equation modeling (SEM) [149–152], dynamical causal modeling (DCM) [153–155], or generative models—including neural mass models [145, 156] and large-scale neural models [147, 157–159]—, have been of little use to the investigation of extended large-scale networks, since their intrinsic complexity prevent them from modeling systems with that many degrees of freedom (but see, [160]).

Methods originating from graph and/or network theories might prove more adapted to such problems [161–163], since they provide global quantification of structures that, besides from being ubiquitous [164, 165], are not unlike some models of brain networks. Using such methods, brain networks have been shown to exhibit small-world [70, 166–170] and scale-free [171, 172] features. The fact that networks simultaneously exhibit both properties has strong structural [104, 173] and functional [174, 175] implications.

Being able to devise methods that can deal with both individual and group analyses is also an important issue. At the individual level, it is essential to assess the significance of the different networks [80, 85, 176]. With procedures of increasing complexity, nonparametric resampling procedures [177], mostly used in the context of the GLM so far [178], might be appealing [179]. At the group level, one seeks to determine invariant networks across subjects. This has been done by either considering a model for the group [76] or solving the problem at an individual level and then performing clustering [79]. Validation of such methods have to be developed; a first step in this direction has been proposed by Calhoun et al. [180].

Once results have been produced, representing the results becomes a key issue. Consider for instance functional

connectivity as measured by marginal correlation. Though computationally tractable on a large-scale network of N units, even for N large, such a method generates $N(N - 1)/2$ correlation coefficients (e.g., 4950 for as few as 100 voxels/regions; 19900 for 200; 499 500 for 1000). Simply representing these on a graph as is commonly done [72, 140, 181] would prove impossible to read, let alone to interpret. Procedures that summarize the information have to be proposed; these can rely on PCA/MDS [71, 79, 182]; they could also use other representational techniques [183, 184].

Last, but not least, an essential point to validate and better understand the large-scale network approach in fMRI is the comparison with results from other imaging modalities or areas of neuroscience, such as electrophysiology [34–38], electroencephalography (EEG) or magnetoencephalography (MEG) [39, 125, 185, 186], and diffusion tensor imaging (DTI) [187–190]. To be able to efficiently compare results from different imaging modalities, it is essential to better understand how each modality images the activity of large-scale brain networks. In this perspective, providing a unified generative and/or statistical model for several of these modalities would be of the utmost importance, granting access to multimodal in vivo imaging of the brain in action.

ACKNOWLEDGMENTS

The authors would like to thank the guest editors for providing them with the opportunity to submit an invited paper to this special issue of the International Journal of Biomedical Imaging, as well as an anonymous referee for improving the quality of this manuscript. They are also grateful to Pierre Bellec, Jean Daunizeau, and Saâd Jbabdi for discussions regarding an early draft of this manuscript.

REFERENCES

- [1] W. Chen and S. Ogawa, “Principles of BOLD functional MRI,” in *Functional MRI*, C. Moonen and P. Bandettini, Eds., pp. 103–113, Springer, Berlin, Germany, 1999.
- [2] S. A. Huettel, A. W. Song, and G. McCarthy, *Functional Magnetic Resonance Imaging*, Sinauer Associates, Sunderland, Mass, USA, 2004.
- [3] K. J. Friston, A. P. Holmes, J.-B. Poline, et al., “Analysis of fMRI time-series revisited,” *NeuroImage*, vol. 2, no. 1, pp. 45–53, 1995.
- [4] K. J. Friston, A. P. Holmes, K. J. Worsley, J.-P. Poline, C. D. Frith, and R. S. J. Frackowiak, “Statistical parametric maps in functional imaging: a general linear approach,” *Human Brain Mapping*, vol. 2, no. 4, pp. 189–210, 1994.
- [5] K. J. Friston, P. Jezzard, and R. Turner, “Analysis of functional MRI time-series,” *Human Brain Mapping*, vol. 1, no. 2, pp. 153–171, 1993.
- [6] N. Picard and P. L. Strick, “Imaging the premotor areas,” *Current Opinion in Neurobiology*, vol. 11, no. 6, pp. 663–672, 2001.
- [7] G. Tononi, O. Sporns, and G. M. Edelman, “A measure for brain complexity: relating functional segregation and integration in the nervous system,” *Proceedings of the National Academy of Sciences of the United States of America*, vol. 91, no. 11, pp. 5033–5037, 1994.
- [8] S. Zeki and S. Shipp, “The functional logic of cortical connections,” *Nature*, vol. 335, no. 6188, pp. 311–317, 1988.
- [9] D. O. Hebb, *The Organization of Behavior: A Neurophysiological Theory*, John Wiley & Sons, New York, NY, USA, 1949.
- [10] A. R. Luria, “The functional organization of the brain,” *Scientific American*, vol. 222, no. 3, pp. 66–78, 1970.
- [11] F. Varela, J.-P. Lachaux, E. Rodriguez, and J. Martinerie, “The brainweb: phase synchronization and large-scale integration,” *Nature Reviews Neuroscience*, vol. 2, no. 4, pp. 229–239, 2001.
- [12] B. Biswal, F. Z. Yetkin, V. M. Haughton, and J. S. Hyde, “Functional connectivity in the motor cortex of resting human brain using echo-planar MRI,” *Magnetic Resonance in Medicine*, vol. 34, no. 4, pp. 537–541, 1995.
- [13] B. B. Biswal, J. Van Kylen, and J. S. Hyde, “Simultaneous assessment of flow and BOLD signals in resting-state functional connectivity maps,” *NMR in Biomedicine*, vol. 10, no. 4-5, pp. 165–170, 1997.
- [14] D. A. Gusnard and M. E. Raichle, “Searching for a baseline: functional imaging and the resting human brain,” *Nature Reviews Neuroscience*, vol. 2, no. 10, pp. 685–694, 2001.
- [15] M. E. Raichle and M. A. Mintun, “Brain work and brain imaging,” *Annual Review of Neuroscience*, vol. 29, pp. 449–476, 2006.
- [16] R. G. Shulman, D. L. Rothman, K. L. Behar, and F. Hyder, “Energetic basis of brain activity: implications for neuroimaging,” *Trends in Neurosciences*, vol. 27, no. 8, pp. 489–495, 2004.
- [17] S. L. Bressler and E. Tognoli, “Operational principles of neurocognitive networks,” *International Journal of Psychophysiology*, vol. 60, no. 2, pp. 139–148, 2006.
- [18] M.-M. Mesulam, “From sensation to cognition,” *Brain*, vol. 121, no. 6, pp. 1013–1052, 1998.
- [19] G. Marrelec, J. Daunizeau, M. Péligrini-Issac, J. Doyon, and H. Benali, “Conditional correlation as a measure of mediated interactivity in fMRI and MEG/EEG,” *IEEE Transactions on Signal Processing*, vol. 53, no. 9, pp. 3503–3516, 2005.
- [20] W. Kahle, *Atlas de Poche d’Anatomie. 3. Système nerveux et organes des sens*, Flammarion, Paris, France, 3rd edition, 2002.
- [21] K. Brodmann, *Vergleichende Lokalisationslehre der Großhirnrinde in ihren Prinzipien dargestellt auf Grund des Zellenbaues*, J. A. Barth, Leipzig, Germany, 1909.
- [22] M. F. Bear, B. W. Connors, and M. A. Paradiso, *Neuroscience: Exploring the Brain*, Lippincott Williams & Wilkins, Baltimore, Md, USA, 2nd edition, 2001.
- [23] R. A. Poldrack, “Can cognitive processes be inferred from neuroimaging data?” *Trends in Cognitive Sciences*, vol. 10, no. 2, pp. 59–63, 2006.
- [24] S. L. Bressler, “Large-scale cortical networks and cognition,” *Brain Research Reviews*, vol. 20, no. 3, pp. 288–304, 1995.
- [25] K. Friston, “Beyond phrenology: what can neuroimaging tell us about distributed circuitry?” *Annual Review of Neuroscience*, vol. 25, pp. 221–250, 2002.
- [26] D. J. Felleman and D. C. Van Essen, “Distributed hierarchical processing in the primate cerebral cortex,” *Cerebral Cortex*, vol. 1, no. 1, pp. 1–47, 1991.
- [27] R. Kötter and K. E. Stephan, “Network participation indices: characterizing component roles for information processing in neural networks,” *Neural Networks*, vol. 16, no. 9, pp. 1261–1275, 2003.
- [28] J. W. Scannell, G. A. P. C. Burns, C. C. Hilgetag, M. A. O’Neil, and M. P. Young, “The connectional organization of the

- cortico-thalamic system of the cat," *Cerebral Cortex*, vol. 9, no. 3, pp. 277–299, 1999.
- [29] O. Sporns, C. J. Honey, and R. Kötter, "Identification and classification of hubs in brain networks," *PLoS Biology*, vol. 2, no. 10, p. e1049, 2007.
- [30] M. P. Young, "Objective analysis of the topological organization of the primate cortical visual system," *Nature*, vol. 358, no. 6382, pp. 152–155, 1992.
- [31] E. Hoshi, L. Tremblay, J. Féger, P. L. Carras, and P. L. Strick, "The cerebellum communicates with the basal ganglia," *Nature Neuroscience*, vol. 8, no. 11, pp. 1491–1493, 2005.
- [32] H. Künzle, "An autoradiographic analysis of the efferent connections from premotor and adjacent prefrontal regions (areas 6 and 9) in macaca fascicularis," *Brain, Behavior and Evolution*, vol. 15, no. 3, pp. 185–234, 1978.
- [33] G. R. Leichnetz, "Afferent and efferent connections of the dorsolateral precentral gyrus (area 4, hand/arm region) in the macaque monkey, with comparisons to area 8," *Journal of Comparative Neurology*, vol. 254, no. 4, pp. 460–492, 1986.
- [34] T. J. Buschman and E. K. Miller, "Top-down versus bottom-up control of attention in the prefrontal and posterior parietal cortices," *Science*, vol. 315, no. 5820, pp. 1860–1864, 2007.
- [35] G. Buzsáki and A. Draguhn, "Neuronal oscillations in cortical networks," *Science*, vol. 304, no. 5679, pp. 1926–1929, 2004.
- [36] R. T. Knight, "Neural networks debunk phrenology," *Science*, vol. 316, no. 5831, pp. 1578–1579, 2007.
- [37] Y. B. Saalman, I. N. Pigarev, and T. R. Vidyasagar, "Neural mechanisms of visual attention: how top-down feedback highlights relevant locations," *Science*, vol. 316, no. 5831, pp. 1612–1615, 2007.
- [38] T. Womelsdorf, J.-M. Schoffelen, R. Oostenveld, et al., "Modulation of neuronal interactions through neuronal synchronization," *Science*, vol. 316, no. 5831, pp. 1609–1612, 2007.
- [39] E. Başar, C. Başar-Eroğlu, S. Karakaş, and M. Schürmann, "Gamma, alpha, delta, and theta oscillations govern cognitive processes," *International Journal of Psychophysiology*, vol. 39, no. 2–3, pp. 241–248, 2000.
- [40] M. E. Raichle, "Modern phrenology: maps of human cortical function," *Annals of the New York Academy of Sciences*, vol. 882, pp. 107–118, 1999.
- [41] D. Cordes, V. M. Haughton, K. Arfanakis, et al., "Mapping functionally related regions of brain with functional connectivity MR imaging," *American Journal of Neuroradiology*, vol. 21, no. 9, pp. 1636–1644, 2000.
- [42] M. D. Fox, M. Corbetta, A. Z. Snyder, J. L. Vincent, and M. E. Raichle, "Spontaneous neuronal activity distinguishes human dorsal and ventral attention systems," *Proceedings of the National Academy of Sciences of the United States of America*, vol. 103, no. 26, pp. 10046–10051, 2006.
- [43] M. Hampson, B. S. Peterson, P. Skudlarski, J. C. Gatenby, and J. C. Gore, "Detection of functional connectivity using temporal correlations in MR images," *Human Brain Mapping*, vol. 15, no. 4, pp. 247–262, 2002.
- [44] M. J. Lowe, B. J. Mock, and J. A. Sorenson, "Functional connectivity in single and multislice echoplanar imaging using resting-state fluctuations," *NeuroImage*, vol. 7, no. 2, pp. 119–132, 1998.
- [45] M. Quigley, D. Cordes, G. Wendt, et al., "Effect of focal and nonfocal cerebral lesions on functional connectivity studied with MR imaging," *American Journal of Neuroradiology*, vol. 22, no. 2, pp. 294–300, 2001.
- [46] J. L. Vincent, A. Z. Snyder, M. D. Fox, et al., "Coherent spontaneous activity identifies a hippocampal-parietal memory network," *Journal of Neurophysiology*, vol. 96, no. 6, pp. 3517–3531, 2006.
- [47] J. Xiong, L. M. Parsons, J.-H. Gao, and P. T. Fox, "Interregional connectivity to primary motor cortex revealed using MRI resting state images," *Human Brain Mapping*, vol. 8, no. 2–3, pp. 151–156, 1999.
- [48] F. T. Sun, L. M. Miller, and M. D'Esposito, "Measuring interregional functional connectivity using coherence and partial coherence analyses of fMRI data," *NeuroImage*, vol. 21, no. 2, pp. 647–658, 2004.
- [49] F. T. Sun, L. M. Miller, and M. D'Esposito, "Measuring temporal dynamics of functional networks using phase spectrum of fMRI data," *NeuroImage*, vol. 28, no. 1, pp. 227–237, 2005.
- [50] M. S. Gonçalves and D. A. Hall, "Connectivity analysis with structural equation modelling: an example of the effects of voxel selection," *NeuroImage*, vol. 20, no. 3, pp. 1455–1467, 2003.
- [51] J. L. Vincent, G. H. Patel, M. D. Fox, et al., "Intrinsic functional architecture in the anaesthetized monkey brain," *Nature*, vol. 447, no. 7140, pp. 83–86, 2007.
- [52] Y. M. Wang and J. Xia, "Functional interactivity in fMRI using multiple seeds' correlation analyses—novel methods and comparisons," in *Proceedings of the 20th International Conference on Information Processing in Medical Imaging (IPMI '07)*, N. Karssemeijer and B. P. F. Lelieveldt, Eds., vol. 4584 of *Lecture Notes in Computer*, pp. 147–159, Springer, Kerkrade, The Netherlands, July 2007.
- [53] A. H. Andersen, D. M. Gash, and M. J. Avison, "Principal component analysis of the dynamic response measured by fMRI: a generalized linear systems framework," *Magnetic Resonance Imaging*, vol. 17, no. 6, pp. 795–815, 1999.
- [54] R. Baumgartner, L. Ryner, W. Richter, R. Summers, M. Jarmasz, and R. Somorjai, "Comparison of two exploratory data analysis methods for fMRI: fuzzy clustering vs. principal component analysis," *Magnetic Resonance Imaging*, vol. 18, no. 1, pp. 89–94, 2000.
- [55] E. T. Bullmore, S. Rabe-Hesketh, R. G. Morris, et al., "Functional magnetic resonance image analysis of a large-scale neurocognitive network," *NeuroImage*, vol. 4, no. 1, pp. 16–33, 1996.
- [56] R. Baumgartner, C. Windischberger, and E. Moser, "Quantification in functional magnetic resonance imaging: fuzzy clustering vs. correlation analysis," *Magnetic Resonance Imaging*, vol. 16, no. 2, pp. 115–125, 1998.
- [57] R. Baumgartner, R. Somorjai, R. Summers, and W. Richter, "Assessment of cluster homogeneity in fMRI data using Kendall's coefficient of concordance," *Magnetic Resonance Imaging*, vol. 17, no. 10, pp. 1525–1532, 1999.
- [58] R. Baumgartner, R. Somorjai, R. Summers, W. Richter, and L. Ryner, "Correlator beware: correlation has limited selectivity for fMRI data analysis," *NeuroImage*, vol. 12, no. 2, pp. 240–243, 2000.
- [59] P. Filzmoser, R. Baumgartner, and E. Moser, "A hierarchical clustering method for analyzing functional MR images," *Magnetic Resonance Imaging*, vol. 17, no. 6, pp. 817–826, 1999.
- [60] C. Goutte, P. Toft, E. Rostrup, F. Å. Nielsen, and L. K. Hansen, "On clustering fMRI time series," *NeuroImage*, vol. 9, no. 3, pp. 298–310, 1999.

- [61] S. J. Peltier, T. A. Polk, and D. C. Noll, "Detecting low-frequency functional connectivity in fMRI using a self-organizing map (SOM) algorithm," *Human Brain Mapping*, vol. 20, no. 4, pp. 220–226, 2003.
- [62] K.-H. Chuang, M.-J. Chiu, C.-C. Lin, and J.-H. Chen, "Model-free functional MRI analysis using Kohonen clustering neural network and fuzzy C-means," *IEEE Transactions on Medical Imaging*, vol. 18, no. 12, pp. 1117–1128, 1999.
- [63] D. Cordes, V. Haughton, J. D. Carew, K. Arfanakis, and K. Maravilla, "Hierarchical clustering to measure connectivity in fMRI resting-state data," *Magnetic Resonance Imaging*, vol. 20, no. 4, pp. 305–317, 2002.
- [64] J. R. Foucher, P. Vidailhet, S. Chanraud, et al., "Functional integration in schizophrenia: too little or too much? Preliminary results on fMRI data," *NeuroImage*, vol. 26, no. 2, pp. 374–388, 2005.
- [65] G. Tononi, A. R. McIntosh, D. P. Russell, and G. M. Edelman, "Functional clustering: identifying strongly interactive brain regions in neuroimaging data," *NeuroImage*, vol. 7, no. 2, pp. 133–149, 1998.
- [66] M. J. McKeown, S. Makeig, G. G. Brown, et al., "Analysis of fMRI data by blind separation into independent spatial components," *Human Brain Mapping*, vol. 6, no. 3, pp. 160–188, 1998.
- [67] K. J. Friston and C. Büchel, "Functional connectivity: eigenimages and multivariate analysis," in *Human Brain Function*, pp. 999–1018, Elsevier, San Diego, Calif, USA, 2004.
- [68] C. Ecker, E. Reynaud, S. C. Williams, and M. J. Brammer, "Detecting functional nodes in large-scale cortical networks with functional magnetic resonance imaging: a principal component analysis of the human visual system," *Human Brain Mapping*, vol. 28, no. 9, pp. 817–834, 2007.
- [69] V. D. Calhoun, T. Adali, J. J. Pekar, and G. D. Pearlson, "Latency (in)sensitive ICA: group independent component analysis of fMRI data in the temporal frequency domain," *NeuroImage*, vol. 20, no. 3, pp. 1661–1669, 2003.
- [70] S. Achard, R. Salvador, B. Whitcher, J. Suckling, and E. Bullmore, "A resilient, low-frequency, small-world human brain functional network with highly connected association cortical hubs," *Journal of Neuroscience*, vol. 26, no. 1, pp. 63–72, 2006.
- [71] R. Salvador, J. Suckling, M. R. Coleman, J. D. Pickard, D. Menon, and E. Bullmore, "Neurophysiological architecture of functional magnetic resonance images of human brain," *Cerebral Cortex*, vol. 15, no. 9, pp. 1332–2342, 2005.
- [72] R. Salvador, J. Suckling, C. Schwarzbauer, and E. Bullmore, "Undirected graphs of frequency-dependent functional connectivity in whole brain networks," *Philosophical Transactions of the Royal Society of London Series B*, vol. 360, no. 1457, pp. 937–946, 2005.
- [73] V. D. Calhoun, T. Adali, V. B. McGinty, J. J. Pekar, T. D. Watson, and G. D. Pearlson, "fMRI activation in a visual-perception task: network of areas detected using the general linear model and independent components analysis," *NeuroImage*, vol. 14, no. 5, pp. 1080–1088, 2001.
- [74] V. D. Calhoun, T. Adali, G. D. Pearlson, and J. J. Pekar, "A method for making group inferences from functional MRI data using independent component analysis," *Human Brain Mapping*, vol. 14, no. 3, pp. 140–151, 2001.
- [75] V. G. van de Ven, E. Formisano, D. Prvulovic, C. H. Roeder, and D. E. J. Linden, "Functional connectivity as revealed by spatial independent component analysis of fMRI measurements during rest," *Human Brain Mapping*, vol. 22, no. 3, pp. 165–178, 2004.
- [76] C. F. Beckmann, M. DeLuca, J. T. Devlin, and S. M. Smith, "Investigations into resting-state connectivity using independent component analysis," *Philosophical Transactions of the Royal Society of London Series B*, vol. 360, no. 1457, pp. 1001–1013, 2005.
- [77] J. S. Damoiseaux, S. A. R. B. Rombouts, F. Barkhof, et al., "Consistent resting-state networks across healthy subjects," *Proceedings of the National Academy of Sciences of the United States of America*, vol. 103, no. 37, pp. 13848–13853, 2006.
- [78] M. De Luca, C. F. Beckmann, N. De Stefano, P. M. Matthews, and S. M. Smith, "fMRI resting state networks define distinct modes of long-distance interactions in the human brain," *NeuroImage*, vol. 29, no. 4, pp. 1359–1367, 2006.
- [79] F. Esposito, T. Scarabino, A. Hyvarinen, et al., "Independent component analysis of fMRI group studies by self-organizing clustering," *NeuroImage*, vol. 25, no. 1, pp. 193–205, 2005.
- [80] P. Bellec, V. Perlberg, S. Jbabdi, et al., "Identification of large-scale networks in the brain using fMRI," *NeuroImage*, vol. 29, no. 4, pp. 1231–1243, 2006.
- [81] N. Tzourio-Mazoyer, B. Landeau, D. Papathanassiou, et al., "Automated anatomical labeling of activations in SPM using a macroscopic anatomical parcellation of the MNI MRI single-subject brain," *NeuroImage*, vol. 15, no. 1, pp. 273–289, 2002.
- [82] Y. Lu, T. Jiang, and Y. Zang, "Region growing method for the analysis of functional MRI data," *NeuroImage*, vol. 20, no. 1, pp. 455–465, 2003.
- [83] P. Fransson, "Spontaneous low-frequency BOLD signal fluctuations: an fMRI investigation of the resting-state default mode of brain function hypothesis," *Human Brain Mapping*, vol. 26, no. 1, pp. 15–29, 2005.
- [84] P. Fransson, "How default is the default mode of brain function? Further evidence from intrinsic BOLD signal fluctuations," *Neuropsychologia*, vol. 44, no. 14, pp. 2836–2845, 2006.
- [85] M. D. Greicius, B. Krasnow, A. L. Reiss, and V. Menon, "Functional connectivity in the resting brain: a network analysis of the default mode hypothesis," *Proceedings of the National Academy of Sciences of the United States of America*, vol. 100, no. 1, pp. 253–258, 2003.
- [86] M. D. Greicius and V. Menon, "Default-mode activity during a passive sensory task: uncoupled from deactivation but impacting activation," *Journal of Cognitive Neuroscience*, vol. 16, no. 9, pp. 1484–1492, 2004.
- [87] M. D. Fox, A. Z. Snyder, J. L. Vincent, M. Corbetta, D. C. Van Essen, and M. E. Raichle, "The human brain is intrinsically organized into dynamic, anticorrelated functional networks," *Proceedings of the National Academy of Sciences of the United States of America*, vol. 102, no. 27, pp. 9673–9678, 2005.
- [88] T. Stein, C. Moritz, M. Quigley, D. Cordes, V. Haughton, and E. Meyerand, "Functional connectivity in the thalamus and hippocampus studied with functional MR imaging," *American Journal of Neuroradiology*, vol. 21, no. 8, pp. 1397–1401, 2000.
- [89] M. F. Mason, M. I. Norton, J. D. Van Horn, D. M. Wegner, S. T. Grafton, and C. N. Macrae, "Wandering minds: the default network and stimulus-independent thought," *Science*, vol. 315, no. 5810, pp. 393–395, 2007.
- [90] M. E. Raichle, "Neuroscience: the brain's dark energy," *Science*, vol. 314, no. 5803, pp. 1249–1250, 2006.
- [91] M. E. Raichle, A. M. MacLeod, A. Z. Snyder, W. J. Powers, D. A. Gusnard, and G. L. Shulman, "A default mode of brain function," *Proceedings of the National Academy of Sciences of the United States of America*, vol. 98, no. 2, pp. 676–682, 2001.

- [92] M. Corbetta and G. L. Shulman, "Control of goal-directed and stimulus-driven attention in the brain," *Nature Reviews Neuroscience*, vol. 3, no. 3, pp. 201–215, 2002.
- [93] L. G. Ungerleider and J. V. Haxby, "'What' and 'where' in the human brain," *Current Opinion in Neurobiology*, vol. 4, no. 2, pp. 157–165, 1994.
- [94] A. M. Achim and M. Lepage, "Neural correlates of memory for items and for associations: an event-related functional magnetic resonance imaging study," *Journal of Cognitive Neuroscience*, vol. 17, no. 4, pp. 652–667, 2005.
- [95] E. K. Miller and J. D. Cohen, "An integrative theory of prefrontal cortex function," *Annual Review of Neuroscience*, vol. 24, pp. 167–202, 2001.
- [96] L. G. Ungerleider, S. M. Courtney, and J. V. Haxby, "A neural system for human visual working memory," *Proceedings of the National Academy of Sciences of the United States of America*, vol. 95, no. 3, pp. 883–890, 1998.
- [97] J. Doyon and H. Benali, "Reorganization and plasticity in the adult brain during learning of motor skills," *Current Opinion in Neurobiology*, vol. 15, no. 2, pp. 161–167, 2005.
- [98] T. Taniwaki, A. Okayama, T. Yoshiura, et al., "Functional network of the basal ganglia and cerebellar motor loops in vivo: different activation patterns between self-initiated and externally triggered movements," *NeuroImage*, vol. 31, no. 2, pp. 745–753, 2006.
- [99] E. Awh, E. K. Vogel, and S.-H. Oh, "Interactions between attention and working memory," *Neuroscience*, vol. 139, no. 1, pp. 201–208, 2006.
- [100] O. Gruber and T. Goschke, "Executive control emerging from dynamic interactions between brain systems mediating language, working memory and attentional processes," *Acta Psychologica*, vol. 115, no. 2-3, pp. 105–121, 2004.
- [101] H. R. Naghavi and L. Nyberg, "Common fronto-parietal activity in attention, memory, and consciousness: shared demands on integration?" *Consciousness and Cognition*, vol. 14, no. 2, pp. 390–425, 2005.
- [102] A. B. Waites, A. Stanislavsky, D. F. Abbott, and G. D. Jackson, "Effect of prior cognitive state on resting state networks measured with functional connectivity," *Human Brain Mapping*, vol. 24, no. 1, pp. 59–68, 2005.
- [103] A. Mechelli, W. D. Penny, C. J. Price, D. R. Gitelman, and K. J. Friston, "Effective connectivity and intersubject variability: using a multisubject network to test differences and commonalities," *NeuroImage*, vol. 17, no. 3, pp. 1459–1469, 2002.
- [104] M. Kaiser and C. C. Hilgetag, "Modelling the development of cortical systems networks," *Neurocomputing*, vol. 58–60, pp. 297–302, 2004.
- [105] T. Wu, Y. Zang, L. Wang, et al., "Aging influence on functional connectivity of the motor network in the resting state," *Neuroscience Letters*, vol. 422, no. 3, pp. 164–168, 2007.
- [106] A. K. Majewska and M. Sur, "Plasticity and specificity of cortical processing networks," *Trends in Neurosciences*, vol. 29, no. 6, pp. 323–329, 2006.
- [107] R. A. Poldrack, "Imaging brain plasticity: conceptual and methodological issues—a theoretical review," *NeuroImage*, vol. 12, no. 1, pp. 1–13, 2000.
- [108] C. Calautti and J.-C. Baron, "Functional neuroimaging studies of motor recovery after stroke in adults: a review," *Stroke*, vol. 34, no. 6, pp. 1553–1566, 2003.
- [109] N. S. Ward, "Plasticity and the functional reorganization of the human brain," *International Journal of Psychophysiology*, vol. 58, no. 2-3, pp. 158–161, 2005.
- [110] H. Duffau, "Lessons from brain mapping in surgery for low-grade glioma: insights into associations between tumour and brain plasticity," *The Lancet Neurology*, vol. 4, no. 8, pp. 476–486, 2005.
- [111] A. Krainik, S. Lehericy, H. Duffau, et al., "Postoperative speech disorder after medial frontal surgery: role of the supplementary motor area," *Neurology*, vol. 60, no. 4, pp. 587–594, 2003.
- [112] A. Krainik, S. Lehericy, H. Duffau, et al., "Role of the supplementary motor area in motor deficit following medial frontal lobe surgery," *Neurology*, vol. 57, no. 5, pp. 871–878, 2001.
- [113] A. Thiel, K. Herholz, A. Koyuncu, et al., "Plasticity of language networks in patients with brain tumors: a positron emission tomography activation study," *Annals of Neurology*, vol. 50, no. 5, pp. 620–629, 2001.
- [114] B. J. He, A. Z. Snyder, J. L. Vincent, A. Epstein, G. L. Shulman, and M. Corbetta, "Breakdown of functional connectivity in frontoparietal networks underlies behavioral deficits in spatial neglect," *Neuron*, vol. 53, no. 6, pp. 905–918, 2007.
- [115] J. Gotman, C. Grova, A. Bagshaw, E. Kobayashi, Y. Aghakhani, and F. Dubeau, "Generalized epileptic discharges show thalamocortical activation and suspension of the default state of the brain," *Proceedings of the National Academy of Sciences of the United States of America*, vol. 102, no. 42, pp. 15236–15240, 2005.
- [116] R. L. Buckner, A. Z. Snyder, B. J. Shannon, et al., "Molecular, structural, and functional characterization of Alzheimer's disease: evidence for a relationship between default activity, amyloid, and memory," *Journal of Neuroscience*, vol. 25, no. 34, pp. 7709–7717, 2005.
- [117] E. Başar, C. Başar-Eroğlu, S. Karakaş, and M. Schürmann, "Are cognitive processes manifested in event-related gamma, alpha, theta and delta oscillations in the EEG?" *Neuroscience Letters*, vol. 259, no. 3, pp. 165–168, 1999.
- [118] E. Başar, M. Schürmann, and O. Sakowitz, "The selectively distributed theta system: functions," *International Journal of Psychophysiology*, vol. 39, no. 2-3, pp. 197–212, 2000.
- [119] S. Karakaş, C. Başar-Eroğlu, Ç. Özemi, H. Kafadar, and Ö. Ü. Erzenin, "Gamma response of the brain: a multifunctional oscillation that represents bottom-up with top-down processing," *International Journal of Psychophysiology*, vol. 39, no. 2-3, pp. 137–150, 2000.
- [120] M. Schürmann and E. Başar, "Functional aspects of alpha oscillations in the EEG," *International Journal of Psychophysiology*, vol. 39, no. 2-3, pp. 151–158, 2000.
- [121] D. A. Leopold, Y. Murayama, and N. K. Logothetis, "Very slow activity fluctuations in monkey visual cortex: implications for functional brain imaging," *Cerebral Cortex*, vol. 13, no. 4, pp. 422–433, 2003.
- [122] N. K. Logothetis, "The underpinnings of the BOLD functional magnetic resonance imaging signal," *Journal of Neuroscience*, vol. 23, no. 10, pp. 3963–3971, 2003.
- [123] N. K. Logothetis, J. Pauls, M. Augath, T. Trinath, and A. Oeltermann, "Neurophysiological investigation of the basis of the fMRI signal," *Nature*, vol. 412, no. 6843, pp. 150–157, 2001.
- [124] N. K. Logothetis and J. Pfeuffer, "On the nature of the BOLD fMRI contrast mechanism," *Magnetic Resonance Imaging*, vol. 22, no. 10, pp. 1517–1531, 2004.
- [125] G. Winterer, F. W. Carver, F. Musso, V. Mattay, D. R. Weinberger, and R. Coppola, "Complex relationship between BOLD signal and synchronization/desynchronization

- of human brain MEG oscillations,” *Human Brain Mapping*, vol. 28, no. 9, pp. 805–816, 2007.
- [126] K. J. Friston, S. Williams, R. Howard, R. S. J. Frackowiak, and R. Turner, “Movement-related effects in fMRI time-series,” *Magnetic Resonance in Medicine*, vol. 35, no. 3, pp. 346–355, 1996.
- [127] A. Gretton, A. Belitski, Y. Murayama, B. Schölkopf, and N. Logothetis, “The effect of artifacts on dependence measurement in fMRI,” *Magnetic Resonance Imaging*, vol. 24, no. 4, pp. 401–409, 2006.
- [128] G. Krüger and G. H. Glover, “Physiological noise in oxygenation-sensitive magnetic resonance imaging,” *Magnetic Resonance in Medicine*, vol. 46, no. 4, pp. 631–637, 2001.
- [129] M. S. Dagli, J. E. Ingeholm, and J. V. Haxby, “Localization of cardiac-induced signal change in fMRI,” *NeuroImage*, vol. 9, no. 4, pp. 407–415, 1999.
- [130] D. Raj, A. W. Anderson, and J. C. Gore, “Respiratory effects in human functional magnetic resonance imaging due to bulk susceptibility changes,” *Physics in Medicine and Biology*, vol. 46, no. 12, pp. 3331–3340, 2001.
- [131] V. Perlberg, P. Bellec, J.-L. Anton, M. Pélégrini-Issac, J. Doyon, and H. Benali, “CORSIKA: correction of structured noise in fMRI by automatic identification of ICA components,” *Magnetic Resonance Imaging*, vol. 25, no. 1, pp. 35–46, 2007.
- [132] C. G. Thomas, R. A. Harshman, and R. S. Menon, “Noise reduction in BOLD-based fMRI using component analysis,” *NeuroImage*, vol. 17, no. 3, pp. 1521–1537, 2002.
- [133] T. E. Lund and S.-J. Li, “fcMRI—mapping functional connectivity or correlating cardiac-induced noise?” *Magnetic Resonance in Medicine*, vol. 46, no. 3, pp. 628–628, 2001.
- [134] R. M. Birn, J. B. Diamond, M. A. Smith, and P. A. Bandettini, “Separating respiratory-variation-related fluctuations from neuronal-activity-related fluctuations in fMRI,” *NeuroImage*, vol. 31, no. 4, pp. 1536–1548, 2006.
- [135] R. G. Wise, K. Ide, M. J. Poulin, and I. Tracey, “Resting fluctuations in arterial carbon dioxide induce significant low frequency variations in BOLD signal,” *NeuroImage*, vol. 21, no. 4, pp. 1652–1664, 2004.
- [136] T. W. Anderson, *An Introduction to Multivariate Statistical Analysis*, Wiley Publications in Statistics, John Wiley & Sons, New York, NY, USA, 1958.
- [137] G. Marrelec, P. Bellec, H. Duffau, et al., “Regions, systems, and the brain: hierarchical measures of functional integration in fMRI,” to appear in *Medical Image Analysis*.
- [138] G. Marrelec, P. Bellec, and H. Benali, “Exploring large-scale brain networks in functional MRI,” *Journal of Physiology Paris*, vol. 100, no. 4, pp. 171–181, 2006.
- [139] G. Marrelec, B. Horwitz, J. Kim, M. Pélégrini-Issac, H. Benali, and J. Doyon, “Using partial correlation to enhance structural equation modeling of functional MRI data,” *Magnetic Resonance Imaging*, vol. 25, no. 8, pp. 1181–1189, 2007.
- [140] G. Marrelec, A. Krainik, H. Duffau, et al., “Partial correlation for functional brain interactivity investigation in functional MRI,” *NeuroImage*, vol. 32, no. 1, pp. 228–237, 2006.
- [141] G. Marrelec, J. Kim, J. Doyon, and B. Horwitz, “Large scale model validation of partial correlation analysis for effective connectivity investigation in functional MRI,” to appear in *Human Brain Mapping*.
- [142] B. Abler, A. Roebroeck, R. Goebel, et al., “Investigating directed influences between activated brain areas in a motor-response task using fMRI,” *Magnetic Resonance Imaging*, vol. 24, no. 2, pp. 181–185, 2006.
- [143] R. Goebel, A. Roebroeck, D.-S. Kim, and E. Formisano, “Investigating directed cortical interactions in time-resolved fMRI data using vector autoregressive modeling and Granger causality mapping,” *Magnetic Resonance Imaging*, vol. 21, no. 10, pp. 1251–1261, 2003.
- [144] A. Roebroeck, E. Formisano, and R. Goebel, “Mapping directed influence over the brain using Granger causality and fMRI,” *NeuroImage*, vol. 25, no. 1, pp. 230–242, 2005.
- [145] O. David and K. J. Friston, “A neural mass model for MEG/EEG: coupling and neuronal dynamics,” *NeuroImage*, vol. 20, no. 3, pp. 1743–1755, 2003.
- [146] R. Kötter and F. T. Sommer, “Global relationship between anatomical connectivity and activity propagation in the cerebral cortex,” *Philosophical Transactions of the Royal Society of London Series B*, vol. 355, no. 1393, pp. 127–134, 2000.
- [147] M.-A. Tagamets and B. Horwitz, “Integrating electrophysiological and anatomical experimental data to create a large-scale model that simulates a delayed match-to-sample human brain imaging study,” *Cerebral Cortex*, vol. 8, no. 4, pp. 310–320, 1998.
- [148] G. Tononi, O. Sporns, and G. M. Edelman, “Reentry and the problem of integrating multiple cortical areas: simulation of dynamic integration in the visual system,” *Cerebral Cortex*, vol. 2, no. 4, pp. 310–335, 1992.
- [149] C. Büchel and K. Friston, “Assessing interactions among neuronal systems using functional neuroimaging,” *Neural Networks*, vol. 13, no. 8-9, pp. 871–882, 2000.
- [150] A. R. McIntosh, “Towards a network theory of cognition,” *Neural Networks*, vol. 13, no. 8-9, pp. 861–870, 2000.
- [151] A. R. McIntosh and F. Gonzalez-Lima, “Structural equation modeling and its application to network analysis in functional brain imaging,” *Human Brain Mapping*, vol. 2, no. 1-2, pp. 2–22, 1994.
- [152] A. R. McIntosh, C. L. Grady, L. G. Ungerleider, J. V. Haxby, S. I. Rapoport, and B. Horwitz, “Network analysis of cortical visual pathways mapped with PET,” *Journal of Neuroscience*, vol. 14, no. 2, pp. 655–666, 1994.
- [153] K. J. Friston, L. Harrison, and W. Penny, “Dynamic causal modelling,” *NeuroImage*, vol. 19, no. 4, pp. 1273–1302, 2003.
- [154] W. D. Penny, K. E. Stephan, A. Mechelli, and K. J. Friston, “Comparing dynamic causal models,” *NeuroImage*, vol. 22, no. 3, pp. 1157–1172, 2004.
- [155] W. D. Penny, K. E. Stephan, A. Mechelli, and K. J. Friston, “Modelling functional integration: a comparison of structural equation and dynamic causal models,” *NeuroImage*, vol. 23, supplement 1, pp. S264–S274, 2004.
- [156] O. David, D. Cosmelli, and K. J. Friston, “Evaluation of different measures of functional connectivity using a neural mass model,” *NeuroImage*, vol. 21, no. 2, pp. 659–673, 2004.
- [157] B. Horwitz, “Relating fMRI and PET signals to neural activity by means of large-scale neural models,” *Neuroinformatics*, vol. 2, no. 2, pp. 251–266, 2004.
- [158] B. Horwitz and A. R. Braun, “Brain network interactions in auditory, visual and linguistic processing,” *Brain and Language*, vol. 89, no. 2, pp. 377–384, 2004.
- [159] F. T. Husain, M.-A. Tagamets, S. J. Fromm, A. R. Braun, and B. Horwitz, “Relating neuronal dynamics for auditory object processing to neuroimaging activity: a computational modeling and an fMRI study,” *NeuroImage*, vol. 21, no. 4, pp. 1701–1720, 2004.
- [160] C. J. Honey, R. Kötter, M. Breakspear, and O. Sporns, “Network structure of cerebral cortex shapes functional connectivity on multiple time scales,” *Proceedings of the*

- National Academy of Sciences of the United States of America*, vol. 104, no. 24, pp. 10240–10245, 2007.
- [161] N. Gupte, B. K. Singh, and T. M. Janaki, “Networks: structure, function and optimisation,” *Physica A*, vol. 346, no. 1-2, pp. 75–81, 2005.
- [162] M. E. J. Newman, “The structure and function of complex networks,” *SIAM Review*, vol. 45, no. 2, pp. 167–256, 2003.
- [163] S. H. Strogatz, “Exploring complex networks,” *Nature*, vol. 410, no. 6825, pp. 268–276, 2001.
- [164] R. Albert and A.-L. Barabási, “Statistical mechanics of complex networks,” *Reviews of Modern Physics*, vol. 74, no. 1, pp. 47–97, 2002.
- [165] A.-L. Barabási and R. Albert, “Emergence of scaring in random networks,” *Science*, vol. 286, no. 5439, pp. 509–512, 1999.
- [166] S. Achard and E. Bullmore, “Efficiency and cost of economical brain functional networks,” *PLoS Computational Biology*, vol. 3, no. 2, p. e17, 2007.
- [167] D. S. Bassett and E. Bullmore, “Small-world brain networks,” *The Neuroscientist*, vol. 12, no. 6, pp. 512–523, 2006.
- [168] D. S. Bassett, A. Meyer-Lindenberg, S. Achard, T. Duke, and E. Bullmore, “Adaptive reconfiguration of fractal small-world human brain functional networks,” *Proceedings of the National Academy of Sciences of the United States of America*, vol. 103, no. 51, pp. 19518–19523, 2006.
- [169] O. Sporns and J. D. Zwi, “The small world of the cerebral cortex,” *Neuroinformatics*, vol. 2, no. 2, pp. 145–162, 2004.
- [170] D. J. Watts and S. H. Strogatz, “Collective dynamics of ‘small-world’ networks,” *Nature*, vol. 393, no. 6684, pp. 440–442, 1998.
- [171] D. R. Chialvo, “Critical brain networks,” *Physica A*, vol. 340, no. 4, pp. 756–765, 2004.
- [172] V. M. Eguíluz, D. R. Chialvo, G. A. Cecchi, M. Baliki, and A. V. Apkarian, “Scale-free brain functional networks,” *Physical Review Letters*, vol. 94, no. 1, Article ID 018102, 4 pages, 2005.
- [173] M. Kaiser, R. Martin, P. Andras, and M. P. Young, “Simulation of robustness against lesions of cortical networks,” *European Journal of Neuroscience*, vol. 25, no. 10, pp. 3185–3192, 2007.
- [174] S. Micheloyannis, E. Pachou, C. J. Stam, et al., “Small-world networks and disturbed functional connectivity in schizophrenia,” *Schizophrenia Research*, vol. 87, no. 1–3, pp. 60–66, 2006.
- [175] C.-W. Shin and S. Kim, “Self-organized criticality and scale-free properties in emergent functional neural networks,” *Physical Review E*, vol. 74, no. 4, Article ID 045101, 4 pages, 2006.
- [176] C. F. Beckmann and S. M. Smith, “Probabilistic independent component analysis for functional magnetic resonance imaging,” *IEEE Transactions on Medical Imaging*, vol. 23, no. 2, pp. 137–152, 2004.
- [177] J. Himberg, A. Hyvärinen, and F. Esposito, “Validating the independent components of neuroimaging time series via clustering and visualization,” *NeuroImage*, vol. 22, no. 3, pp. 1214–1222, 2004.
- [178] O. Friman and C.-F. Westin, “Resampling fMRI time series,” *NeuroImage*, vol. 25, no. 3, pp. 859–867, 2005.
- [179] P. Bellec, G. Marrelec, and H. Benali, “A bootstrap test to investigate changes in brain connectivity for functional MRI,” to appear in *Statistica Sinica* <http://www3.stat.sinica.edu.tw/preprint/SS-07-138.1.pdf>.
- [180] V. D. Calhoun, T. Adali, and J. J. Pekar, “A method for comparing group fMRI data using independent component analysis: application to visual, motor and visuomotor tasks,” *Magnetic Resonance Imaging*, vol. 22, no. 9, pp. 1181–1191, 2004.
- [181] S. Dodel, N. Golestani, C. Pallier, V. ElKouby, D. Le Bihan, and J.-B. Poline, “Condition-dependent functional connectivity: syntax networks in bilinguals,” *Philosophical Transactions of the Royal Society of London Series B*, vol. 360, no. 1457, pp. 921–935, 2005.
- [182] K. J. Fristen, C. D. Frith, P. Fletcher, P. F. Liddle, and R. S. J. Frackowiak, “Functional topography: multidimensional scaling and functional connectivity in the brain,” *Cerebral Cortex*, vol. 6, no. 2, pp. 156–164, 1996.
- [183] R. Toro and Y. Burnod, “Geometric atlas: modeling the cortex as an organized surface,” *NeuroImage*, vol. 20, no. 3, pp. 1468–1484, 2003.
- [184] A. Unwin, M. Theus, and H. Hofmann, *Graphics of Large Datasets. Visualizing A Million*, Springer, New York, NY, USA, 2006.
- [185] H. Mizuhara, L.-Q. Wang, K. Kobayashi, and Y. Yamaguchi, “Long-range EEG phase synchronization during an arithmetic task indexes a coherent cortical network simultaneously measured by fMRI,” *NeuroImage*, vol. 27, no. 3, pp. 553–563, 2005.
- [186] L. A. Wheaton, G. Nolte, S. Bohlhalter, E. Fridman, and M. Hallett, “Synchronization of parietal and premotor areas during preparation and execution of praxis hand movements,” *Clinical Neurophysiology*, vol. 116, no. 6, pp. 1382–1390, 2005.
- [187] P. J. Basser, J. Mattiello, and D. LeBihan, “Estimation of the effective self-diffusion tensor from the NMR spin echo,” *Journal of Magnetic Resonance, Series B*, vol. 103, no. 3, pp. 247–254, 1994.
- [188] T. E. J. Behrens and H. Johansen-Berg, “Relating connective architecture to grey matter function using diffusion imaging,” *Philosophical Transactions of the Royal Society of London Series B*, vol. 360, no. 1457, pp. 903–911, 2005.
- [189] T. E. J. Behrens, H. Johansen-Berg, M. W. Woolrich, et al., “Non-invasive mapping of connections between human thalamus and cortex using diffusion imaging,” *Nature Neuroscience*, vol. 6, no. 7, pp. 750–757, 2003.
- [190] H. Johansen-Berg, T. E. J. Behrens, M. D. Robson, et al., “Changes in connectivity profiles define functionally distinct regions in human medial frontal cortex,” *Proceedings of the National Academy of Sciences of the United States of America*, vol. 101, no. 36, pp. 13335–13340, 2004.

Research Article

Resurrecting Brinley Plots for a Novel Use: Meta-Analyses of Functional Brain Imaging Data in Older Adults

Ann M. Peiffer, Joseph A. Maldjian, and Paul J. Laurienti

Department of Radiology, Wake Forest University School of Medicine, Medical Center Boulevard, PP1 - 7th Floor,
Winston-Salem, NC 27157, USA

Correspondence should be addressed to Ann M. Peiffer, apeiffer@wfubmc.edu

Received 29 March 2007; Accepted 25 August 2007

Recommended by Oury Monchi

By plotting response times of young and older adults across a variety of tasks, Brinley spurred investigation and debate into the theory of general cognitive slowing. Though controversial, Brinley plots can assess between-task differences, the impact of increasing task demand, and the relationship between responses in two groups of subjects. Since a relationship exists between response times and the blood-oxygen level dependent (BOLD) signal of functional MRI (fMRI), Brinley's plotting method could be applied as a meta-analysis tool in fMRI studies of aging. Here, fledgling "Peiffer plots" are discussed for their potential impact on understanding general cognitive brain activity in aging. Preliminary results suggest that general cognitive slowing may be localized at the sensorimotor transformation in the precentral gyrus. Although this meta-analysis method is naturally used with imaging studies of aging, theoretically it may be applied to other study pairs (e.g., schizophrenic versus normal) or imaging datasets (e.g., PET).

Copyright © 2008 Ann M. Peiffer et al. This is an open access article distributed under the Creative Commons Attribution License, which permits unrestricted use, distribution, and reproduction in any medium, provided the original work is properly cited.

1. INTRODUCTION

In the mid 1960s, Brinley presented a novel plotting method to consider the relationship between response times in young and older adults across a variety of tasks with varying levels of cognitive difficulty [1]. The average response times for both the young and older groups of adults on each task were placed on a scatter-plot, and a regression line was then fitted to the data using the operation of $y = mx + b$. In doing so, a relationship was realized between the behavior in young adults and its ability to predict behavior on the same task in older adults. The power of this method of data analysis is that it can be used across task types to pool data from multiple studies. Here we harvest the powerful aspects of the Brinley analysis method and apply them to functional magnetic resonance imaging (fMRI) data. Meta-analyses of fMRI data are typically hindered by differences in the types of tasks used across studies. The use of the Brinley method allows for a meta-analysis of fMRI data that actually takes advantage of multiple cognitive tasks. However, the remaining challenge is to carefully interpret the findings.

The history of Brinley plots is rife with debate and discussion on what the plot is measuring and what it means.

Feelings in opposing camps can even be so strong as to elicit T-shirts emblazoned with the No symbol over the word Brinley. Later researchers inferred that aspects of Brinley plots could provide information on general cognitive functioning in older adults since Brinley's data contained both task switching and nonswitching data subsets [2–7]. For example, if the slope for the fitted line of a group of tasks is 1, then there is equal change between tasks for younger and older adults. However, when the slope of the fitted line deviates and is greater than 1, there is an increased slowing in older adults associated with more cognitively demanding tasks (i.e., a general cognitive slowing deficit is evident in older adults regardless of task [e.g., [2]]). Other researchers have disagreed with this Brinley plot interpretation and suggest that the plot reflects a difference in response variability between the age groups rather than processing speed, per se [8]. Finally, current work in how aging affects processing speed questions the degree to which general cognitive slowing can be summarized with one linear function across all types of tasks [5, 9, 10].

In addition to describing the behavioral appearance of cognitive slowing, research has pursued localizing the phenomenon within the aging brain. Generalized cognitive

slowing has been thought to result from pervasive slowing of all cognitive brain functions in older adults. With this in mind, some researchers have proposed that the locus of general cognitive slowing occurs where sensory impulses transfer to a common site of motor generation for the response and that this sensorimotor dysregulation intensifies with more difficult tasks [11–13]. Yordanova and colleagues found evidence to support this hypothesis using event-related potentials, which are able to evaluate the timing and strength of cognitive processing in response to external stimuli [11]. However, when considering task-specific slowing impact, other researchers point to additional slowing in specific cognitive areas such as working memory, visual search and mental rotation [10, 14], which may occur in addition to or instead of the sensorimotor slowing.

After reviewing the body of research literature on general cognitive slowing in aging, we adopted the early Brinley method for plotting reaction times and applied it to the blood-oxygen level dependent (BOLD) signal from multiple fMRI studies. In doing so, an attempt is made to localize brain areas responsible for the deviant slope in the response time Brinley plot. Unlike reaction times, the BOLD signal has a legitimate negative value (i.e., deactivations) that occurs when contrasting activity during two different events. For example, certain brain areas are more active during baseline than during any particular task. These areas prominently include posterior cingulate cortex and inferior parietal lobe areas and are known as the default network [15]. In applying Brinley’s plotting method on the BOLD signal, we are able to construct novel Peiffer plots, a meta-analysis of fMRI data that is not limited to site locations of activation maxima and thus not skewed to evaluate only areas identified as statistically different within a study [see discussion in [16]]. Typical meta-analyses of fMRI data use location-centered approaches where the focus of peak activity is evaluated [16–20]. This can underestimate between-task differences because subthreshold activity differences are overlooked [see discussion in [16]]. Further, differences in task parameters and paradigm domain limit the tasks compared in many fMRI meta-analyses to a single type of task (e.g., Stroop interference task [16, 21]). With the novel method proposed here, a plot can be made across a variety of fMRI studies to evaluate two different population groups to identify areas showing between-task differences that may not necessarily be identified as deviant within an individual study comparison. Lastly, in using this method to compare young and older adults, we may be able to show localization of the areas that may in fact identify differences in age-related information processing that characterize general cognitive slowing.

2. METHODS

BOLD data and behavioral response times were obtained from 4 simple detection tasks (3 visual and 1 auditory). In order to plot a BOLD signal value for young and older adults in each study, original fMRI data was needed. The fMRI Data Center (<http://www.fmridc.org>) contributed a complete dataset from Buckner and colleagues (Accession no. 2-2000-1118W) for 2 points in the analysis (young = 14;

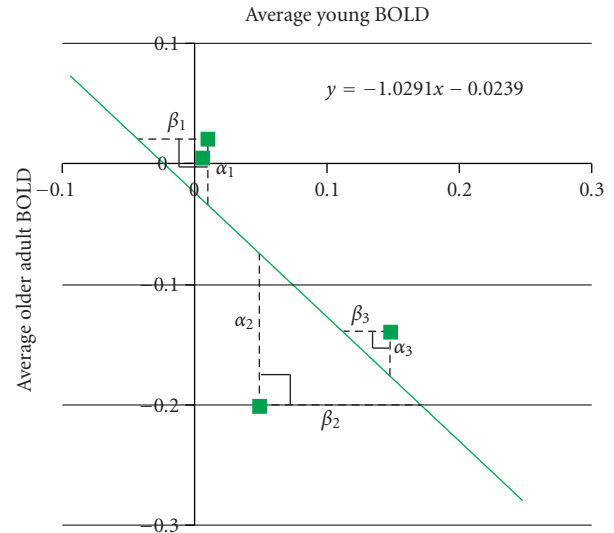


FIGURE 1: Representative voxel illustrating testing of the null hypothesis ($H_0 : m = 1$). To assess whether the null hypothesis is true in any given voxel, a t-test comparison of the α and β residual values was used. When $\alpha \neq \beta$, then the line was not significantly close to one and the voxel was considered to have a significant deviant slope. If the T value survived the correction for multiple comparison (3 contiguous voxels where FWE $P < .05$), the respective brain area was considered to be a loci for general cognitive slowing. A second analysis is needed to identify areas where voxels with slopes of -1 were eliminated in the residual analysis.

older adults = 14) [22]. These BOLD signal measurements related to responses associated with the presentation of a single or double flashing checkerboard. The other 2 points were from studies performed in our laboratory (young = 20; older adults = 20) [23]. These BOLD signal measurements were related to block activity during an auditory task where subjects needed to respond when they heard a target tone or in a visual task where they responded to the blurring of a flashing checkerboard. For all points in the meta-analysis, all fMRI comparisons were between task and baseline (i.e., fixation cross) and were preprocessed with global signal correction. Further, during the preprocessing of the data, it is spatially normalized to MNI template space. Normalized task specific “con” images reflecting the task-related BOLD activity change from baseline were computed with SPM99 for all individuals in each dataset. These individual “con” images were then averaged within age group for each study resulting in a total of 8 average BOLD activity maps (2 age groups over 4 tasks). This process emulated the construction of a traditional Brinley plot which averaged the response times for each task within each age group. Within the BOLD average signal maps, each voxel contains a value representing the age group’s average BOLD activity for that task at that standardized MNI x, y, z coordinate.

Using the 4 average young maps as observed x -values and the corresponding 4 average older adult maps as observed y -values, a linear regression analysis ($y = mx + b$) was calculated within each voxel that contained at least 3 x, y data points (see Figure 1 for a representative voxel). Individual

3D maps were computed that contained voxels with individual regression parameters of interest (e.g., slope, b-intercept, R-square, predicted y -value, etc.). Since the null hypothesis (H_0) in question was whether or not there was equivalent change between young and older adults across tasks, the slope value for H_0 was 1. To evaluate $H_0 : m = 1$, the absolute residual values were calculated at each data point in SPM2 ($\alpha = |y - \hat{y}|$ where $\hat{y} = mx + b$ and $\beta = |x - \hat{x}|$ where $\hat{x} = (y - b)/m$). The resulting 8 residual maps (2 age groups over 4 tasks) were then statistically compared using a t-test in SPM. When the n is large enough, theoretically, it would be more statistically correct to analyze the difference between these residuals with a paired t-test. If the null hypothesis was true, then the absolute residual values would be equal and not statistically different from each other ($\alpha = \beta$). If the slope was not equal to 1, then the voxel's t-test would be significant ($\alpha \neq \beta$). Multiple comparisons were controlled for by using FWE of $P < 0.05$ and an extent threshold of at least 3 consecutive voxels. The sign (+ or -) and value of the slope could then be assessed to determine how the two groups deviated in their BOLD signals across the tasks plotted in the analysis (e.g., one group activates an area more across tasks than the other group).

As graciously pointed out by an anonymous reviewer, slopes of -1 should not be considered as part of the null hypothesis, since the direction of activity across tasks for the age groups would actually be opposite (i.e., young adults activating across tasks while older adults deactivate). Therefore, it is also important to investigate areas where the slope is significantly negative, since the above "residual" analysis would not just eliminate slopes of $+1$ but also slopes which were not significantly different from -1 . An example of this can be seen in the plotted data of Figure 1 in which this particular voxel would not be significant in the above "residual" analysis, but still represents an interesting result. Significant voxels with a slope of -1 can be identified using the P -value of the regression used to fit the Peiffer plot (i.e., $P < .05$ for the slope to be different from zero). Three contiguous voxels with a significant regression P -value and a negative slope will be considered a cluster of interest as well.

To evaluate a significant voxel's b-intercept, the 95% confidence interval was assessed. If this interval contained zero, the voxel's b-intercept was considered not to deviate from zero. Again, b-intercept clusters were considered significant if they contained at least 3 contiguous voxels with significantly nonzero b-intercepts.

3. RESULTS

The traditional Brinley plot using average response times across the 4 tasks included in the fMRI meta-analysis showed the established differences between young and older adults (see Figure 2). The slope of 1.4 supports general cognitive slowing within the dataset even though relatively simple response time tasks were used, and although uninterpretable for response time data, the negative b-intercept is also typical. With a slope greater than one, older adults had greater differences between tasks in response time than younger adults.

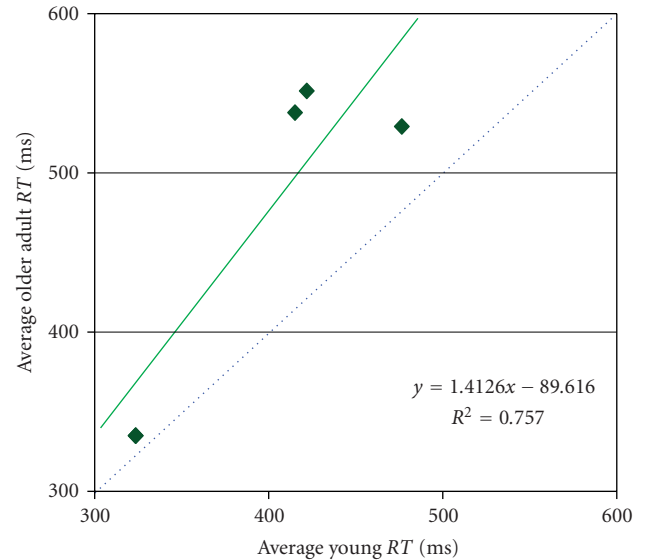


FIGURE 2: Traditional Brinley plot of response times for the 4 tasks used in the fMRI meta-analysis. If young and older adults showed equivalent between-task change in the speed of responses across these studies, the slope of the fitted line would be 1 (dotted blue line); however, results indicated that some general cognitive slowing is evident within the datasets since the slope of the fitted line was 1.4 (solid green line).

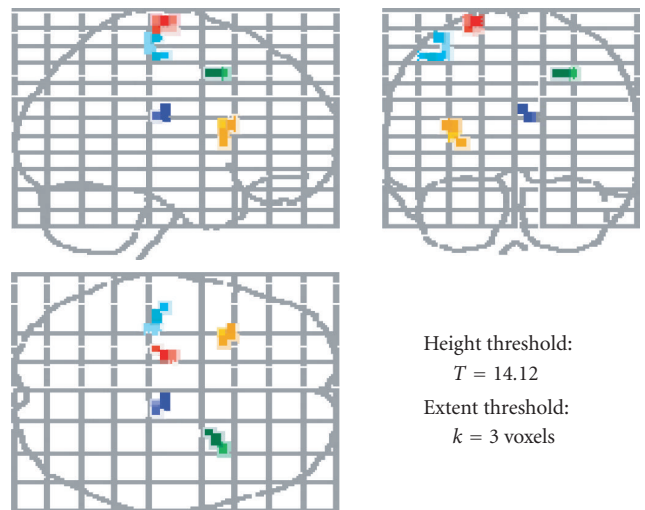


FIGURE 3: Contiguous clusters that survived FWE correction. These clusters had slopes that were not significantly equal to one (color-coded for clarity), and theoretically, they localized areas of differences in between-task BOLD signal change for older and younger adults.

For the fMRI meta-analysis, five distinct clusters survived the stringent correction applied for multiple comparisons. The location of these clusters is summarized visually in Figure 3 and details are given in Table 1. Clusters of interest to competing theories of general cognitive slowing were found within the left pre- and postcentral gyrus areas as well as within the right medial frontal gyrus. All clusters identified

TABLE 1: SPM volume summary

Cluster number	Talairach daemon label	Cluster size	FWE-corrected P -value	T	x, y, z (mm)
1	Left postcentral gyrus	7	.000	43.33	-44, -24, 55
2	Right thalamus	4	.000	41.35	8, -20, 20
3	Left precentral gyrus	6	.000	37.85	-20, -20, 75
4	Subgyral right MFG	3	.001	27.48	28, 8, 45
5	Subgyral/left insula	5	.003	22.91	-36, 16, 15

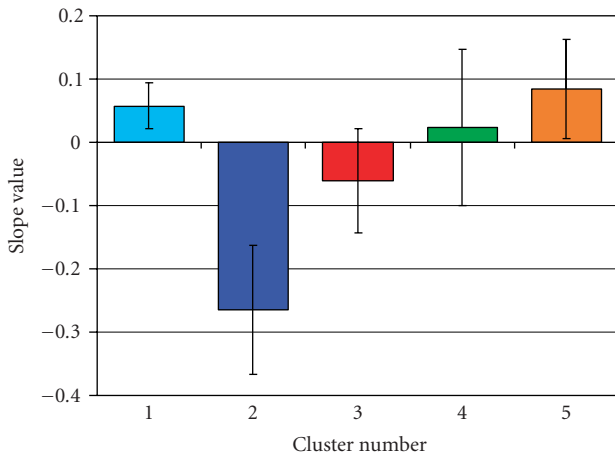


FIGURE 4: Average slope values for clusters with slopes significantly different from one. A total of 5 clusters (color-coded for clarity) survived and had average slope values less than 1 and greater than -1 . These slope values are the result of greater between-task BOLD signal change in the cohort of young adults than older adults.

in the analysis had, on average, a slope that was significantly less than one yet significantly greater than negative one (see Figure 4). This slope indicates that between these 4 tasks, younger adults had greater BOLD signal change than older adults in these brain areas. Notably, there is a lack of difference in between-task BOLD activity within primary sensory areas such as vision between older and younger adults, even though several studies have reported older adults having less activity than younger adults in sensory areas [24–26].

When the Peiffer plot was explored for 3 contiguous voxels with significantly negative slopes less than zero, 19 total clusters were identified. Nine of these clusters (47%) were located within the right middle and superior frontal gyri and included a total of 68 voxels (see Figure 5). Across these clusters older adults showed BOLD deactivation on tasks when younger adults tended to slightly activate and older adults had BOLD activation when younger adults were deactivating on a task (average slope -1.89 ± 0.21). These areas appear to be activating in opposition between the age groups and are contiguous to the right middle frontal gyrus area (cluster no. 4) identified in the “residual” analysis. Other clusters, showing similar activity differences were seen within left medial frontal gyrus (2 clusters; 6 voxels); left inferior parietal lobule (3 clusters; 10 voxels); cingulate gyrus (2 clus-

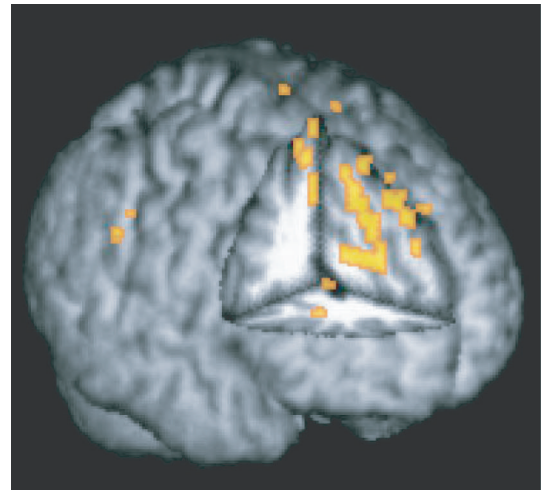


FIGURE 5: Contiguous clusters in right frontal cortex where the slope is -1 . Several clusters were identified in the secondary analysis to assess for areas where activity was opposite in younger and older adults. These areas within right frontal cortex tended to be active across tasks in younger adults and deactivated across task in older adults. Further, these areas correspond to regions involved in attention and task decisions, which have also been implicated in general cognitive slowing theories.

ters; 7 voxels); and single clusters within the basal ganglia (5 voxels), midbrain (3 voxels), and the left posterior lobe of the cerebellum (7 voxels). It is important to note, however, that these findings, unlike those from the “residual” analysis above, have not been stringently controlled for multiple comparisons aside from retaining the requirement for 3 contiguous voxels.

To assess whether these slope findings were dependent on age and not an epiphenomenon of the datasets, a randomization of the age groups was performed within each dataset. Individuals were randomized in two groups so that the average age of both groups was roughly equal (~ 51 years of age). When the Peiffer plot was constructed for these new groups, no significant clusters were identified where the null hypothesis ($H_0 : m = 1$) was false. Additionally, no significant areas were identified where the slope was -1 . These findings thus support the claim that the results of the original plot were not due to the dataset composition (i.e., scanner, site, or paradigm) but were dependent on separating the study populations by age.

Assessment of the b-intercept indicated that the lack of significant slopes within the primary sensory areas may be

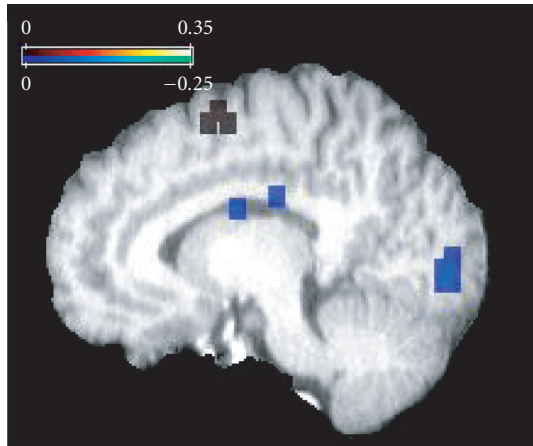


FIGURE 6: B-intercept map for Peiffer plot at $x = 10$ mm. Cool-colored voxels show negative b-intercept values where older adults have lower activity than younger adults. Note the large cluster within the occipital area. Warm-colored voxels indicate positive b-intercepts where older adults show greater activity than younger adults. Interestingly, several contiguous voxels were identified within right motor cortex and indicated increased bilateral activity in older relative to younger adults across the 4 detection tasks.

due to a baseline shift in activity between the age groups (see Figure 6). For example, within visual cortex, several areas were identified that had negative b-intercepts which indicated that across the tasks older adults tended to start from a lower BOLD activity level than young adults (if $x = 0$, then $y =$ a negative BOLD signal). This result is a continual within-task difference, which is also seen in the published literature [23–27]; however, since this reduced BOLD signal in older adults is constant across several tasks, it does not have a slope which deviates significantly from 1. In addition, an area within right motor cortex shows a positive b-intercept and thus greater activity in older adults relative to younger adults. As graciously pointed out by an anonymous reviewer, this result is consistent with the model hypothesis of hemispheric asymmetry in older adults (HAROLD). The HAROLD model states that there is reduced lateralization of brain activity in older adults relative to younger adults, which results from changes in neural architecture and not cognitive strategy [28, 29]. Due to the small number of data points used to construct these plots, the area included within the 95% confidence interval of the b-intercept is relatively large. Therefore, these early findings may underestimate the amount of brain activity which could be described as being affected by an age-related DC-shift and is thus an age-related BOLD signal difference that is independent of task.

Finally, an epiphenomenon of the method was revealed when evaluating the goodness of fit, as measured by the R-squared value. Areas where the slope was similar to one showed very high R-squared values (>0.8) suggesting a high predictability for older adults' BOLD signal in several brain regions; however, within the clusters identified as significantly deviant from one, R-squared values were lower and ranged between 0.1–0.46.

4. DISCUSSION

Here we report the preliminary use of a novel meta-analysis technique in studies on aging, which localizes one factor of general cognitive slowing to the sensorimotor transfer. These findings lend support to existing data from event-related potential work indicating that slowing occurs predominately during the time for generation of the response in older adults and not when evaluating incoming sensory material [11, 13]. Deviant slopes could be found in between-task BOLD activity values where younger adults have greater BOLD activity change than older adults in the sensorimotor transfer area in the left hemisphere. Additionally, right frontal areas were identified with slopes near -1 , indicating that older and younger adults were activating these attentional areas in opposite directions across the tasks. Not surprisingly, more attentionally demanding tasks have shown that older adults have differential patterns of activation within the frontal cortex in response to the task when compared to younger participants [30, 31].

An important caveat exists, however, since datasets within this analysis were obtained from relatively noncognitively demanding tasks. In other words, more brain areas may be involved as loci of general cognitive slowing and would emerge as more cognitively demanding datasets become available for assessment. Comparing our current datasets to the existing literature on Brinley plots of reaction times, simple discrimination tasks show the least amount of response time slowing; therefore, these BOLD signal findings presumably will only become stronger with the addition of datasets containing more cognitively demanding conditions (e.g., working memory). In addition, with more tasks requiring greater attentional demand, the negative slope found within right frontal cortex may steepen and be found within the residual analysis which can control for the multiple comparisons inherent within imaging data. Power analyses of these preliminary results suggest that roughly 9 datasets are needed to perform a meta-analysis with a paired t-test to achieve a power-level of 80%.

Interestingly, all significant clusters identified as deviant within the meta-analysis were separate from peak activity differences reported in any of the individual tasks used within the datasets. If traditional meta-analysis techniques were used [16–20], none of these areas would have been found. Utilizing this novel meta-analysis technique, it is possible to assess between-task differences in BOLD activity between groups regardless of paradigm design, task parameters, and location of the scan. While global signal correction was used to normalize the datasets within this study, the assessment method could also be performed using average group z-maps that would allow datasets from multiple fMRI processing software packages to be analyzed collectively. Additionally, this method may yield interesting findings in a variety of study groups where a clear “normal” group can be identified and used on the x -axis (e.g., schizophrenics versus normals; dyslexics versus normals; AD versus normal older adults). It is important to keep in mind that the use of this method is to determine between-task differences among two populations and not to differentiate the two groups within any one

paradigm of the analysis. Thus, differences in whether or not an area is identified as deviant come from how the BOLD signal responds across a wide array of tasks.

An existing disadvantage of this meta-analysis technique is that it requires access to raw fMRI data to obtain subjects' normalized contrast weighted BOLD activity maps (task - baseline) from multiple tasks. With the continued increase of complete data sets maintained in accessible repositories like the fMRI Data Center, this should hopefully become less burdensome in the near future.

Overall as a meta-analysis method in the fMRI field, this plotting addresses several limitations of existing analysis methods. Specifically, it allows the assessment of between-task differences regardless of a task's paradigm domain or baseline condition. Further, it can identify areas of sub-threshold effects in addition to the suprathreshold within-task differences that are identified by performing a meta-analysis on voxel quadrants identified in individual studies as the local maxima. Lastly, this method provides imaging researchers the ability to localize between-task differences in BOLD signal and apply that knowledge to existing behavioral evidence not only in aging but in other complex conditions (e.g., dyslexia, schizophrenia, Alzheimer's disease, etc.) as well.

ACKNOWLEDGMENTS

This research was funded by grants from NIH no. NS042568 and no. EB004673, the Dana Foundation, Wake Forest University's GCRC no. RR07122, and the Roena Kulynych Memory and Cognition Research Center. A portion of the data presented was obtained from The fMRI Data Center (Accession no. 2-2000-1118W) and was originally published by Buckner and colleagues [22]. Additionally, researchers would like to thank the Biomolecular Imaging Staff and ANSIR Lab personnel, especially Ms. Debra Hege, Ms. Kathy Pearson, Ms. Christina E. Hugenschmidt, Ms. Jennifer L. Mozolic, and Mr. Allen W. Elster Jr. for their assistance.

REFERENCES

- [1] J. F. Brinley, "Cognitive sets, speed and accuracy of performance in the elderly," in *Behavior, Aging, and the Nervous System*, A. T. Welford and J. E. Birren, Eds., pp. 114–149, Thomas, Springfield, Ill, USA, 1965.
- [2] J. Cerella, "Generalized slowing in Brinley plots," *Journals of Gerontology*, vol. 49, no. 2, pp. P65–P71, 1994.
- [3] J. Myerson, D. R. Adams, S. Hale, and L. Jenkins, "Analysis of group differences in processing speed: Brinley plots, Q-Q plots, and other conspiracies," *Psychonomic Bulletin & Review*, vol. 10, no. 1, pp. 224–237, 2003.
- [4] J. Myerson, D. Wagstaff, and S. Hale, "Brinley plots, explained variance, and the analysis of age differences in response latencies," *Journals of Gerontology*, vol. 49, no. 2, pp. P72–P80, 1994.
- [5] T. A. Salthouse, "The processing-speed theory of adult age differences in cognition," *Psychological Review*, vol. 103, no. 3, pp. 403–428, 1996.
- [6] T. A. Salthouse, "Aging and measures of processing speed," *Biological Psychology*, vol. 54, no. 1–3, pp. 35–54, 2000.
- [7] U. Lindenberger, U. Mayr, and R. Kliegl, "Speed and intelligence in old age," *Psychology and Aging*, vol. 8, no. 2, pp. 207–220, 1993.
- [8] R. Ratcliff, D. Spieler, and G. Mckoon, "Explicitly modeling the effects of aging on response time," *Psychonomic Bulletin & Review*, vol. 7, no. 1, pp. 1–25, 2000.
- [9] A. D. Fisk and D. L. Fisher, "Brinley plots and theories of aging: the explicit, muddled, and implicit debates," *Journals of Gerontology*, vol. 49, no. 2, pp. P81–P89, 1994.
- [10] M. J. Sliwinski and C. B. Hall, "Constraints on general slowing: a meta-analysis using hierarchical linear models with random coefficients," *Psychology and Aging*, vol. 13, no. 1, pp. 164–175, 1998.
- [11] J. Yordanova, V. Kolev, J. Hohnsbein, and M. Falkenstein, "Sensorimotor slowing with ageing is mediated by a functional dysregulation of motor-generation processes: evidence from high-resolution event-related potentials," *Brain*, vol. 127, no. 2, pp. 351–362, 2004.
- [12] R. H. van der Lubbe and R. Verleger, "Aging and the Simon task," *Psychophysiology*, vol. 39, no. 1, pp. 100–110, 2002.
- [13] V. Kolev, M. Falkenstein, and J. Yordanova, "Motor-response generation as a source of aging-related behavioural slowing in choice-reaction tasks," *Neurobiology of Aging*, vol. 27, no. 11, pp. 1719–1730, 2006.
- [14] N. Raz, S. D. Briggs, W. Marks, and J. D. Acker, "Age-related deficits in generation and manipulation of mental images: II. The role of dorsolateral prefrontal cortex," *Psychology and Aging*, vol. 14, no. 3, pp. 436–444, 1999.
- [15] M. D. Greicius, G. Srivastava, A. L. Reiss, and V. Menon, "Default-mode network activity distinguishes Alzheimer's disease from healthy aging: evidence from functional MRI," *Proceedings of the National Academy of Sciences of the United States of America*, vol. 101, no. 13, pp. 4637–4642, 2004.
- [16] J. Derrfuss, M. Brass, J. Neumann, and D. Y. von Cramon, "Involvement of the inferior frontal junction in cognitive control: meta-analyses of switching and Stroop studies," *Human Brain Mapping*, vol. 25, no. 1, pp. 22–34, 2005.
- [17] S. R. Arnott, M. A. Binns, C. L. Grady, and C. Alain, "Assessing the auditory dual-pathway model in humans," *NeuroImage*, vol. 22, no. 1, pp. 401–408, 2004.
- [18] J. M. Chein and W. Schneider, "Neuroimaging studies of practice-related change: fMRI and meta-analytic evidence of a domain-general control network for learning," *Cognitive Brain Research*, vol. 25, no. 3, pp. 607–623, 2005.
- [19] P. E. Turkeltaub, G. F. Eden, K. M. Jones, and T. A. Zeffiro, "Meta-analysis of the functional neuroanatomy of single-word reading: method and validation," *NeuroImage*, vol. 16, no. 3, part 1, pp. 765–780, 2002.
- [20] T. D. Wager, J. Jonides, and S. Reading, "Neuroimaging studies of shifting attention: a meta-analysis," *NeuroImage*, vol. 22, no. 4, pp. 1679–1693, 2004.
- [21] J. Neumann, G. Lohmann, J. Derrfuss, and D. Y. von Cramon, "Meta-analysis of functional imaging data using replicator dynamics," *Human Brain Mapping*, vol. 25, no. 1, pp. 165–173, 2005.
- [22] R. L. Buckner, A. Z. Snyder, A. L. Sanders, M. E. Raichle, and J. C. Morris, "Functional brain imaging of young, nondemented, and demented older adults," *Journal of Cognitive Neuroscience*, vol. 12, supplement 2, pp. 24–34, 2000.
- [23] A. M. Peiffer, C. E. Hugenschmidt, J. A. Maldjian, et al., "Aging and the interaction of sensory cortices," in *Human Brain Mapping*, in press.
- [24] M. D'Esposito, E. Zarahn, G. K. Aguirre, and B. Rypma, "The effect of normal aging on the coupling of neural activity to the

- bold hemodynamic response,” *NeuroImage*, vol. 10, no. 1, pp. 6–14, 1999.
- [25] B. K. Levine, L. L. Beason-Held, K. P. Purpura, et al., “Age-related differences in visual perception: a PET study,” *Neurobiology of Aging*, vol. 21, no. 4, pp. 577–584, 2000.
- [26] M. H. Ross, D. A. Yurgelun-Todd, P. F. Renshaw, et al., “Age-related reduction in functional MRI response to photic stimulation,” *Neurology*, vol. 48, no. 1, pp. 173–176, 1997.
- [27] S. C. Johnson, A. J. Saykin, L. C. Baxter, et al., “The relationship between fMRI activation and cerebral atrophy: comparison of normal aging and Alzheimer disease,” *NeuroImage*, vol. 11, no. 3, pp. 179–187, 2000.
- [28] R. Cabeza, “Hemispheric asymmetry reduction in older adults: the HAROLD model,” *Psychology and Aging*, vol. 17, no. 1, pp. 85–100, 2002.
- [29] F. Dolcos, H. J. Rice, and R. Cabeza, “Hemispheric asymmetry and aging: right hemisphere decline or asymmetry reduction,” *Neuroscience & Biobehavioral Reviews*, vol. 26, no. 7, pp. 819–825, 2002.
- [30] R. Cabeza, S. M. Daselaar, F. Dolcos, S. E. Prince, M. Budde, and L. Nyberg, “Task-independent and task-specific age effects on brain activity during working memory, visual attention and episodic retrieval,” *Cerebral Cortex*, vol. 14, no. 4, pp. 364–375, 2004.
- [31] M. P. Milham, K. I. Erickson, M. T. Banich, et al., “Attentional control in the aging brain: insights from an fMRI study of the Stroop task,” *Brain and Cognition*, vol. 49, no. 3, pp. 277–296, 2002.

Review Article

The Role of Noninvasive Techniques in Stroke Therapy

Daniel Maxwell Bernad^{1,2} and Julien Doyon³

¹ Institute of Biotechnology, University of Cambridge, Tennis Court Road, Cambridge CB2 3HU, UK

² Department of Medicine, University of Ottawa, 451 Smyth Road, Ottawa, Ontario, Canada K1H 8M5

³ Functional Neuroimaging Unit, University of Montreal Geriatric Institute, 4565, Queen-Mary Street, Montreal, Quebec, Canada H3W 1W5

Correspondence should be addressed to Daniel Maxwell Bernad, db366@cam.ac.uk

Received 3 May 2007; Accepted 25 September 2007

Recommended by Oury Monchi

Noninvasive techniques such as functional magnetic resonance imaging (fMRI) and transcranial magnetic stimulation (TMS) have provided insight into understanding how neural connections are altered in consequence to cerebrovascular injury. The first part of this review will briefly survey some of the methodological issues and limitations related to noninvasive poststroke motor recovery studies. The second section will investigate some of the different neural mechanisms that underlie neurorehabilitation in stroke patients. The third part will explore our current understanding of motor memory processing, describe the neural structures that subserve motor memory consolidation, and discuss the current literature related to memory reconsolidation in healthy adults. Lastly, this paper will suggest the potential therapeutic applications of integrating noninvasive tools with memory consolidation and reconsolidation theories to enhance motor recovery. The overall objective of this work is to demonstrate how noninvasive technologies have been utilized in the multidisciplinary field of clinical behavioral neuroscience and to highlight their potential to be employed as clinical tools to promote individualized motor recovery in stroke patients.

Copyright © 2008 D. M. Bernad and J. Doyon. This is an open access article distributed under the Creative Commons Attribution License, which permits unrestricted use, distribution, and reproduction in any medium, provided the original work is properly cited.

1. INTRODUCTION AND OUTLINE

Stroke is a debilitating disorder that has the potential to cause substantial sensory, motor, and cognitive impairment. Roughly half of all stroke victims will have some degree of residual motor impairment [1], becoming partially dependent for performing activities of daily living [2]. Acute stroke onset, usually defined as the first six to twelve hours following the interruption of blood supply to neurons, results in a core of dead neurons surrounded by a penumbra where neural tissue remains dysfunctional. If blood flow is not reinstated, the neurons within the penumbra will die and clinical deficits will tend to stabilize. Research efforts have focused on understanding the mechanisms that subserve plasticity or functional modifications in consequence to neuronal damage. Modifications in neural connections and networks are believed to result from cellular or synaptic changes in neuronal functioning following injury. To this extent, a framework describing neurorehabilitation can be conceptualized from a cellular, systems, and behavioral perspective [3]. For example, changes that occur at a cellular level can initiate

different molecular mechanisms such as engaging remyelination. Adaptation that arises at a systems level can involve the recruitment of new neural regions, which can activate the same final output pathway. In addition, behavioral level changes can result from enhanced motivation or altered cognitive strategies to regain function by completing a particular motor task [3]. Diagnostic tools that can detect early stroke onset is crucial for neuronal survival and provides clinicians and rehabilitation specialists with a wider range of treatment options, which ultimately is more effective in helping patients recover motor function.

Recent advances in noninvasive imaging techniques have enabled physicians to diagnose stroke at an earlier point in time and have provided greater comprehension of the changes in neural activity that transpire after stroke [3]. In particular, the application of functional magnetic imaging (fMRI) and transcranial magnetic stimulation (TMS) has provided a better understanding of the neural substrates that subserve recovery. The first part of this review article will briefly survey some of the methodological issues and limitations related to noninvasive poststroke motor recovery

studies. The second section will investigate some of the different mechanisms that underlie neurorehabilitation in recovering stroke patients. The third part will explore our current understanding of procedural memory processing and explore some of the neural regions that subservise motor memory consolidation and recent studies on reconsolidation in human subjects. Lastly, this article will explore some of the potential applications of integrating noninvasive tools with memory consolidation and reconsolidation theories to promote motor recovery. The overall objective of this work is to provide a better understanding of the compensatory mechanisms that are involved in poststroke motor recovery and neural regions engaged in motor memory formation in healthy adults, to demonstrate how noninvasive technologies have been utilized in the multidisciplinary field of clinical behavioral neuroscience, and to highlight their potential to be employed as clinical tools to promote individualized motor recovery in stroke patients.

2. PATIENT-RELATED LIMITATIONS ASSOCIATED WITH IMAGING TECHNIQUES

There are many important patient-related limitations to consider when using MRI. For example, in addition to general MRI contraindications (e. g., pacemaker, metallic implants, etc.), acute stroke (i.e., stroke onset within 24 hours) patients are more easily agitated, are medically unstable in consequence to underlying haemodynamic issues, are more likely to have a diminished level of consciousness associated with vomiting (i.e., increased risk of aspiration), and usually have other coexisting medical problems [4, 5]. In consequence to these issues and in order to investigate the neural mechanisms that drive recovery over and above the spontaneous time-dependent process, most fMRI studies are performed on the chronic (i.e., at least three months after stroke onset) stroke patient population and thus generalization may be limited to this cohort.

Another important patient-related methodological issue to consider is that fMRI studies may be confounded because when patients with vascular lesions are compared with normal controls, the blood oxygenation-level-dependent (BOLD) signal may reflect the underlying diseased hemodynamics and not differences in cortical activation. For example, the BOLD signal captured in recovering stroke patients is typically delayed and lower in amplitude, which could reflect disruptions in neurovascular coupling due to diffuse vascular disease [6].

3. fMRI METHODOLOGICAL ISSUES

Despite such limitations related to the patient population, fMRI offers excellent spatial (i.e., few millimeters) and temporal (i.e., few seconds) resolution [7–9]. In addition, early poststroke motor recovery fMRI studies have been designed as cross-sectional experiments that compared neural changes in fully recovered stroke patients and normal controls at a single point in time [7–9]. Such experiments have been limited because they do not show changes in neural activity throughout the duration of the recovery process. Recently,

longitudinal studies have been designed to investigate neural activity in patients recovering from stroke over an extended period of time [7–9]. Such studies have allowed investigators to correlate changes in neural activation with specific motor gains during the recovery process.

Most studies have used a block design, whereby data is acquired in correlation to a distinct cognitive state (i.e., during a behavioral task) and then compared to a control period [7]. However, recent experiments have employed event-related design, whereby data is acquired during the repetition of discrete stimuli or responses (i.e., finger tapping task). In comparison to block design, the event-related paradigm has a longer acquisition time, but has certain advantages such as providing the option of using either periodic or randomized stimuli. Both block- and event-related designs enable continuous data collection usually with a repeat time of 2–5 seconds [7]. Such parameters must be taken into consideration in order to optimize data acquisition and derive meaningful results.

4. TMS METHODOLOGICAL ISSUES

TMS uses a strong but transient magnetic field that induces an electric current in the underlying cortical tissue [10, 12, 13]. Repetitive TMS involves repeated stimuli at intervals of 1–50 Hz for periods that range from 1–30 minutes [10, 12, 13]. Regular stimulation at low frequencies (up to 1 Hz) can inhibit cortical activation, whereas higher frequencies can stimulate cortical activity. TMS has been used to map functional cortical regions and inhibit or stimulate neural activity [10, 12, 13]. TMS is an excellent noninvasive instrument because it is of low cost, multifunctional, and relatively safe to the patient [10, 12, 13].

5. NEURAL SUBSTRATES THAT UNDERLIE COMPENSATORY MECHANISMS

Through the implementation of noninvasive techniques such as fMRI, investigators have been able to explore the neural regions that subservise compensatory mechanisms in recovering stroke patients. One important observation is that the integrity of the corticospinal tract, the main pathway from the cortical motor regions through the spinal cord to the muscles, correlates with functional motor recovery [14]. For example, Heald et al. [15] conducted a longitudinal study to evaluate the neurophysiological measurements of central motor conduction time (CMCT) immediately after stroke onset. They showed that normal or delayed CMCT correlated with a higher probability of survival and motor recovery. In addition, they found that patients with the poorest functional recovery at twelve months and greatest probability of stroke-related death responded least to initial cortical stimulation. In corroboration, Fujii and Nakada [16] demonstrated that the integrity of the ipsilesional sensorimotor cortex and corticospinal tract play an important role in motor recovery. They conducted an fMRI study in which they demonstrated that the rate of motor recovery, but not the absolute level of motor function, correlated with patterns of activation that were observed after subcortical stroke.

Patients that recovered quickly, defined as within one month poststroke, showed similar patterns of activation in comparison to controls. However, patients that recovered more slowly, defined as within the end of the third month poststroke, showed greater activation in contralesional sensorimotor and supplementary motor areas. These studies suggest that patients with sufficient ipsilesional sensorimotor cortex and corticospinal tract integrity regain motor function more rapidly in comparison to patients with significant lesions.

There is also evidence that secondary cortical motor networks may play an important role in motor recovery. It has been suggested that motor function may be facilitated by projections from secondary motor regions and neural fibers originating in the primary motor region (M1), premotor cortex (PM), and supplementary motor area (SMA), which constitute parallel-independent motor networks with separate projections to spinal cord motor neurons and cortical regions [8, 17]. This implies that parallel motor networks could compensate for one another in consequence to neural damage [8]. In addition, Johansen-Berg et al. [20] illustrated through constraint-induced movement therapy (CIMT) that improvement in hand function correlated with increased fMRI activity in the ipsilesional premotor and somatosensory cortex; and Miyai et al. [21] reported increased ipsilesional premotor cortical (PM) activity in correlation with therapy-induced improvement in gait function.

Although such work does not directly prove that secondary motor regions subserve motor recovery, the application of TMS has been used to address this hypothesis more directly. Fridman et al. [22] applied TMS to four chronic stroke patients with focal subcortical lesions and showed that inhibition of the ipsilesional dorsal PM resulted in delays in a simple reaction time task, whereas TMS targeted to the contralesional dorsal PM of patients or in normal controls did not. In addition, Johansen-Berg et al. [23] showed that transient interference of the dorsal PM with TMS was more disruptive in patients with greater injury. In corroboration of both studies, Ward et al. [24] demonstrated that impaired functional integrity of the corticospinal system is associated with recruitment of bilateral secondary motor networks. Together, such work suggests that both secondary motor regions may also represent a compensatory pathway in motor recovery.

It is well established that the ipsilesional primary motor cortex plays an important role in motor recovery. The evidence surrounding the role of contralesional motor cortex remains controversial; however Chen et al. [25] demonstrated that temporarily inhibiting the contralesional M1 results in errors in both complex and simple motor tasks, suggesting that this region may play a role in planning and organizing motor movements [20]. In contrast, Johansen-Berg et al. [20] showed that disruption of the contralesional M1 using TMS does not impair performance in simple motor task, hence raising questions whether it subserves recovery after stroke. They also found that patients with moderate or poor outcome activate unaffected contralesional cortical motor regions more than those who recovered better. Furthermore, Murase et al. [26] has proposed that contralesional M1 may impair recovering motor function in patients with

small subcortical stroke through interhemispheric inhibitory projections on ipsilesional M1 during attempted voluntary movement of the affected hand. More work is still needed, however, to better understand the role of the contralesional M1 in motor recovery.

Longitudinal studies have been designed to investigate the dynamic changes in neural regions in correlation to motor recovery. Calautti et al. [27] found that patients had greater bilateral activation in the sensorimotor region during paretic hand movement early after stroke onset in comparison to normal controls, but this pattern normalized in association with regained motor function (~ 8 months poststroke). In addition, Feydy et al. [28] demonstrated patterns of activation correlated with location of stroke-induced lesions. They showed that after initial recruitment of bilateral areas, activation gradually shifted towards the ipsilesional sensorimotor cortex. Ward et al. [29] showed that patterns of activation increased in the sensorimotor area in stroke patients during paretic hand movement early after stroke onset, but this trend decreased toward a normal pattern in correlation with motor recovery. In addition, Zemke et al. [30] used fMRI to study recovering subcortical stroke patients while they performed a hand-grip task over six months. They found an initial overactivation within the primary and secondary motor regions, and characterized a focusing of task-related brain activation towards a more “normal” lateralized pattern. Taken together, these studies suggest that normalization of activation in the sensorimotor network, following early increased activation, also correlates with better motor recovery after stroke.

Other quantitative indices have demonstrated changes in neural activity in correlation to motor recovery. For example, Cramer et al. [31] showed that recovered stroke patients had a significantly lower laterality index (LI) = $(C-I)/(C+I)$, where C = contralesional and I = ipsilesional regions, in comparison to controls. The LI can range from +1, which is exclusively ipsilesional, to -1, which is exclusively contralesional. Other studies have also shown that normalization in the LI shifts towards the ipsilesional sensorimotor networks in correlation with motor recovery after stroke [6, 32]. In addition, Marshall et al. [33] demonstrated the laterality of activation in primary sensorimotor cortex during paretic hand movement shifted towards the contralesional hemisphere within the first week of stroke onset but returned back to the ipsilesional hemisphere in correlation to good motor recovery (\sim three to six months after stroke onset). Jang et al. [34] showed that motor recovery (5–15 months poststroke) is correlated with a shift in laterality of primary sensorimotor cortex activation during paretic hand movement from nearly bilateral to strongly ipsilesional. These studies suggest that normalization of sensorimotor cortex laterality is again linked to good recovery of motor function after stroke.

6. NEURAL SUBSTRATES OF MOTOR MEMORY FORMATION

Neural regions that are re-engaged after injury afford an evolutionarily adaptive process to provide a pathway for continued motor output. Similar functional plasticity is also

observed in the procedural memory system. For example, after learning a sequence of finger movements (i.e., finger-to-thumb opposition task), the motor trace is believed to be processed offline, characterized by at least two distinct stages; an initial (i.e., within a single training session) fast learning stage measured by significant improvements in task performance, followed by a slower stage where further gains transpires over several sessions [35–38]. Within 6–8 hours an initially labile motor trace becomes resistant to interference from various amnesic agents (i.e., learning another motor sequence task) and eventually persists despite periods without practice. The process by which newly learned motor information is transformed from a labile state into a robust memory trace is referred to as consolidation and is subserved by specific neural structures and networks [35–38].

Noninvasive imaging techniques have been used to investigate the neural regions that participate in motor memory processing and consolidation. For example, Karni et al. used fMRI to study the changes in BOLD signals underlying motor skill learning [38]. They showed that after weeks of practicing finger-to-thumb sequences within a brief period of time, there was a noticeable enhancement of activation of the M1 region, which persisted for several months, and further suggests that motor sequence learning is subserved by a slowly evolving long-term experience dependent reorganization of the primary motor cortex. In addition, Shadmehr and Holcomb used fMRI to study the underlying neuroanatomical correlates of short-term motor skill learning [39]. They showed that during the earlier stages of motor learning there is a shift from prefrontal cortical regions to the premotor cortex, posterior parietal, and cerebellar structures. Both studies highlight that motor memory processing is subserved by functional reorganization of neural regions.

It has also been proposed that procedural memories can undergo a higher level memory formation process, referred to as system consolidation, whereby over longer periods of time, which can range from days to years pending on memory system, newly learned information is transferred from one neural processing region to another location for long-term storage [40]. For example, Doyon and Ungerleider [41] proposed that during the fast-learning stage, defined as a noticeable improvement in performance within a single training session, the corticocerebellar (CC) and corticostriatal (CS) systems are engaged pending on the motor skill learning task. However, when a motor sequence or adaptation task is well learned, the neural representations are thought to be distributed in one of two circuits, whereby the CS pathway supports the new motor sequence trace and the CC subserves motor adaptation [41, 42]. This theory was recently revised to incorporate findings that suggest that cerebral functional plasticity exists within the striatum and cerebellum in the later stages of motor sequence learning and motor adaptation, respectively [35]. For example, a 3T fMRI study that tracked motor sequence learning within the basal ganglia circuitry and motor-related structures showed improvements in task performance correlated with a change in signal from the associative to sensori-motor regions within the putamen, which suggests that this switch or transfer of information is functionally important for a motor memory trace to persist

with time [43]. Understanding the neural regions that are engaged in motor memory formation may provide further insight into ways to enhance motor recovery in stroke patients.

Although noninvasive imaging techniques have provided much insight into the neural regions that underlie memory consolidation, our overall assumption that this process is permanent has been challenged [44–46, 49]. Misanin et al. used electroconvulsive shock treatments (ECST) to show that memory could be disrupted when in transition from a stored to an active state [45]. The process by which consolidated memories become labile and require stabilization after reactivation is now referred to as reconsolidation [44]. More recently, Nader et al. showed that the reactivation of a consolidated fear memory requires *de novo* protein synthesis in order for such information to persist with time [46]. Debiec et al. further expanded on these findings by demonstrating that hippocampal-dependent memories undergo both reconsolidation within the hippocampus, referred to as cellular reconsolidation, and at a second level of processing termed systems reconsolidation [47].

Whereas most work characterizing the reconsolidation of reactivated, once well consolidated, memories have been performed mostly on animals, there are ample publications showing the reconsolidation effect in human subjects. For example, Rubin reported that all twenty-eight psychiatric patients that received ECST after recall or recurrence of their psychiatric symptoms dramatically improved, some being symptom free when interviewed ten years after treatment [48]. In addition, Walker et al. utilized a motor skill finger tapping paradigm to show that overnight improvements in accuracy were significantly lost when a second interference trace (i.e., from a competing sequence task) was learned immediately after reactivating the first motor trace [49]. They showed that reactivating that trace one day after learning brought the trace back into a labile state that became sensitive to disruption from the interference trace. Although they failed to show the effect on their main dependent variable (i.e., the speed at which sequences are executed in a 30-second period), this study provides the first evidence that the reactivation of a stable and well-consolidated motor memory brings certain components back again into a labile state. More recently, Hupbach et al. showed in a group of college students that providing subjects with a reminder enhanced recall twenty-four hours after the reactivation of a consolidated list of items [50]. The latter finding suggests that reconsolidation may have a constructive effect on episodic memory processing. Although more work is necessary to further characterize and identify the boundary conditions associated with reconsolidation, it may be feasible to apply reconsolidation theory to enhance neurorehabilitation in stroke patients undergoing physical therapy.

7. FUTURE IMPLICATIONS FOR NOVEL THERAPY

How can our understanding of the neural substrates that subserves post-stroke compensatory mechanisms and procedural memory formation in healthy adults assist in clinical therapy? To a certain extent, most neurorehabilitation therapies consist of training patients how to perform previously

learned tasks in a different way [3]. For example, arm ability training was developed for patients with mild hemiparesis and maximizes the retention and generalization of what is learned during the rehabilitation session through varying the difficulty of repetitive motor tasks [51, 52]. In addition, another behavioural therapy mentioned previously is CIMT, which has two components that are administered over two weeks. For example, the patient overcomes learned nonuse of the less functional extremity by practicing motor tasks for six hours per day while simultaneously restraining the use of the more functional extremity for 90% of the patient's waking hours [52].

In both of these training protocols, success relies on learning novel ways to regain lost motor functions, which requires learning new procedural movements that are mediated by similar neural regions that drive procedural memory formation. Therefore, it is plausible that manipulation of these regions may enhance neurorehabilitation. For example, it has been proposed that the application of TMS to the nonaffected hemisphere could be employed to disrupt the interhemispheric inhibition that has previously been described [52–56]. In addition, TMS could also be used to target the affected hemisphere in order to stimulate regions that are damaged or enhance the neural substrates that underlie motor memory formation [52]. Although speculative, it is conceivable that inhibiting the reconsolidation of a nonfunctional motor memory trace via TMS may help a patient learn how to use a corresponding unaffected limb. Moreover, this may be facilitated through simultaneously enhancing the underlying neural substrates that promote forming functional motor memory traces via TMS. These procedures could be used in concert with other neurorehabilitation therapies in order to reprogram novel motor movements.

Numerous variables such as the neuroanatomical regions affected, the period of time since injury, and the patients' previous experiences will all influence the neural substrates that are engaged after stroke [3, 8]. Thus, another potential application of fMRI could be used as a clinical tool to identify a patient's specific *type* of neurocompensatory mechanism. This could enable physicians and rehabilitation specialists to tailor their treatment strategy to more accurately address their patient's individual needs and requirements.

8. CONCLUSION

This review surveyed some of the literature which has examined the application of fMRI and TMS to study the neural substrates that underlie compensatory mechanisms in both stroke recovery and the neural regions that drive procedural memory formation in healthy adults. Although more work is necessary to further understand the mechanisms that subserve neural plasticity, the current literature suggests that specific neuroanatomical regions can be identified with fMRI and be stimulated or inhibited with TMS to cause functional changes in motor output. Such noninvasive tools may one day be more routinely applied to promote neurorehabilitation to benefit patients recovering from poststroke motor impairments.

ACKNOWLEDGMENTS

This work would not have been possible without the support of Dr. Anna Kempinska who proofread and formatted this document. D. M. Bernad is funded through the Cambridge overseas trusts.

REFERENCES

- [1] H. T. Hendricks, J. van Limbeek, A. C. Geurts, and M. J. Zwarts, "Motor recovery after stroke: a systematic review of the literature," *Archives of Physical Medicine and Rehabilitation*, vol. 83, no. 11, pp. 1629–1637, 2002.
- [2] G. E. Gresham, P. W. Duncan, W. B. Stason, et al., "Post-stroke rehabilitation," Clinical practice guideline no. 16. Department of Health and Human Services, Public Health Service, Agency for Health Care Policy and Research, Rockville, Md, USA, May 1995.
- [3] P. M. Matthews, H. Johansen-Berg, and H. Reddy, "Non-invasive mapping of brain functions and brain recovery: applying lessons from cognitive neuroscience to neurorehabilitation," *Restorative Neurology and Neuroscience*, vol. 22, no. 3–4, pp. 245–260, 2004.
- [4] P. J. Hand, J. M. Wardlaw, A. M. Rowat, J. A. Haisma, R. I. Lindley, and M. S. Dennis, "Magnetic resonance brain imaging in patients with acute stroke: feasibility and patient related difficulties," *Journal of Neurology, Neurosurgery and Psychiatry*, vol. 76, no. 11, pp. 1525–1527, 2005.
- [5] O. C. Singer, M. Sitzer, R. du Mesnil de Rochemont, and T. Neumann-Haefelin, "Practical limitations of acute stroke MRI due to patient-related problems," *Neurology*, vol. 62, no. 10, pp. 1848–1849, 2004.
- [6] R. Pineiro, S. Pendlebury, H. Johansen-Berg, and P. M. Matthews, "Altered hemodynamic responses in patients after subcortical stroke measured by functional MRI," *Stroke*, vol. 33, no. 1, pp. 103–109, 2002.
- [7] P. M. Matthews and P. Jezzard, "Functional magnetic resonance imaging," *Journal of Neurology, Neurosurgery and Psychiatry*, vol. 75, no. 1, pp. 6–12, 2004.
- [8] N. S. Ward, "The neural substrates of motor recovery after focal damage to the central nervous system," *Archives of Physical Medicine and Rehabilitation*, vol. 87, no. 12, supplement 1, pp. 30–35, 2006.
- [9] C. Calautti and J.-C. Baron, "Functional neuroimaging studies of motor recovery after stroke in adults: a review," *Stroke*, vol. 34, no. 6, pp. 1553–1566, 2003.
- [10] J. C. Rothwell, "Techniques and mechanisms of action of transcranial stimulation of the human motor cortex," *Journal of Neuroscience Methods*, vol. 74, no. 2, pp. 113–122, 1997.
- [11] H. Johansen-berg, "Functional imaging of stroke recovery: what have we learnt and where do we go from here?" *International Journal of Stroke*, vol. 2, no. 1, pp. 7–16, 2007.
- [12] P. Tallelli and J. Rothwell, "Does brain stimulation after stroke have a future?" *Current Opinion in Neurology*, vol. 19, no. 6, pp. 543–550, 2006.
- [13] J. Grafman and E. Wassermann, "Transcranial magnetic stimulation can measure and modulate learning and memory," *Neuropsychologia*, vol. 37, no. 2, pp. 159–167, 1998.
- [14] F. Binkofski, R. J. Seitz, S. Arnold, J. Classen, R. Benecke, and H.-J. Freund, "Thalamic metabolism and corticospinal tract integrity determine motor recovery in stroke," *Annals of Neurology*, vol. 39, no. 4, pp. 460–470, 1996.
- [15] A. Heald, D. Bates, N. E. F. Cartlidge, J. M. French, and S. Miller, "Longitudinal study of central motor conduction

- time following stroke: 2. Central motor conduction measured within 72 h after stroke as a predictor of functional outcome at 12 months,” *Brain*, vol. 116, no. 6, pp. 1371–1385, 1993.
- [16] Y. Fujii and T. Nakada, “Cortical reorganization in patients with subcortical hemiparesis: neural mechanisms of functional recovery and prognostic implication,” *Journal of Neurosurgery*, vol. 98, no. 1, pp. 64–73, 2003.
- [17] P. L. Strick, “Anatomical organization of multiple motor areas in the frontal lobe: implications for recovery of function,” *Advances in Neurology*, vol. 47, pp. 293–312, 1988.
- [18] R. P. Dum and P. L. Strick, “Spinal cord terminations of the medial wall motor areas in macaque monkeys,” *Journal of Neuroscience*, vol. 16, no. 20, pp. 6513–6525, 1996.
- [19] E. M. Rouiller, “Evidence for direct connections between the hand region of the supplementary motor area and cervical motoneurons in the macaque monkey,” *European Journal of Neuroscience*, vol. 8, no. 5, pp. 1055–1059, 1996.
- [20] H. Johansen-Berg, H. Dawes, C. Guy, S. M. Smith, D. T. Wade, and P. M. Matthews, “Correlation between motor improvements and altered fMRI activity after rehabilitative therapy,” *Brain*, vol. 125, no. 12, pp. 2731–2742, 2002.
- [21] I. Miyai, H. Yagura, M. Hatakenaka, I. Oda, I. Konishi, and K. Kubota, “Longitudinal optical imaging study for locomotor recovery after stroke,” *Stroke*, vol. 34, no. 12, pp. 2866–2870, 2003.
- [22] E. A. Fridman, T. Hanakawa, M. Chung, F. Hummel, R. C. Leiguarda, and L. G. Cohen, “Reorganization of the human ipsilesional premotor cortex after stroke,” *Brain*, vol. 127, no. 4, pp. 747–758, 2004.
- [23] H. Johansen-Berg, M. E. S. Rushworth, M. D. Bogdanovic, U. Kischka, S. Wimalaratna, and P. M. Matthews, “The role of ipsilateral premotor cortex in hand movement after stroke,” *Proceedings of the National Academy of Sciences of the United States of America*, vol. 99, no. 22, pp. 14518–14523, 2002.
- [24] N. S. Ward, J. M. Newton, O. B. C. Swayne, et al., “Motor system activation after subcortical stroke depends on corticospinal system integrity,” *Brain*, vol. 129, no. 3, pp. 809–819, 2006.
- [25] R. Chen, J. Classen, C. Gerloff, et al., “Depression of motor cortex excitability by low-frequency transcranial magnetic stimulation,” *Neurology*, vol. 48, no. 5, pp. 1398–1403, 1997.
- [26] N. Murase, J. Duque, R. Mazzocchio, and L. G. Cohen, “Influence of interhemispheric interactions on motor function in chronic stroke,” *Annals of Neurology*, vol. 55, no. 3, pp. 400–409, 2004.
- [27] C. Calautti, F. Leroy, J.-Y. Guinestrestre, and J.-C. Baron, “Dynamics of motor network overactivation after striatocapsular stroke: a longitudinal PET study using a fixed-performance paradigm,” *Stroke*, vol. 32, no. 11, pp. 2534–2542, 2001.
- [28] A. Feydy, R. Carlier, A. Roby-Brami, et al., “Longitudinal study of motor recovery after stroke: recruitment and focusing of brain activation,” *Stroke*, vol. 33, no. 6, pp. 1610–1617, 2002.
- [29] N. S. Ward, M. M. Brown, A. J. Thompson, and R. S. J. Frackowiak, “Neural correlates of motor recovery after stroke: a longitudinal fMRI study,” *Brain*, vol. 126, no. 11, pp. 2476–2496, 2003.
- [30] A. C. Zemke, P. J. Heagerty, C. Lee, and S. C. Cramer, “Motor cortex organization after stroke is related to side of stroke and level of recovery,” *Stroke*, vol. 34, no. 5, pp. e23–e26, 2003.
- [31] S. C. Cramer, G. Nelles, R. R. Benson, et al., “A functional MRI study of subjects recovered from hemiparetic stroke,” *Stroke*, vol. 28, no. 12, pp. 2518–2527, 1997.
- [32] J. R. Carey, T. J. Kimberley, S. M. Lewis, et al., “Analysis of fMRI and finger tracking training in subjects with chronic stroke,” *Brain*, vol. 125, no. 4, pp. 773–788, 2002.
- [33] R. S. Marshall, G. M. Perera, R. M. Lazar, J. W. Krakauer, R. C. Constantine, and R. L. DeLaPaz, “Evolution of cortical activation during recovery from corticospinal tract infarction,” *Stroke*, vol. 31, no. 3, pp. 656–661, 2000.
- [34] S. H. Jang, Y.-H. Kim, S.-H. Cho, J.-H. Lee, J.-W. Park, and Y.-H. Kwon, “Cortical reorganization induced by task-oriented training in chronic hemiplegic stroke patients,” *NeuroReport*, vol. 14, no. 1, pp. 137–141, 2003.
- [35] J. Doyon and H. Benali, “Reorganization and plasticity in the adult brain during learning of motor skills,” *Current Opinion in Neurobiology*, vol. 15, no. 2, pp. 161–167, 2005.
- [36] O. Hikosaka, K. Sakai, X. Lu, et al., “Parallel neural networks for learning sequential procedures,” *Trends in Neurosciences*, vol. 22, no. 10, pp. 464–471, 1999.
- [37] A. Karni and D. Sagi, “The time course of learning a visual skill,” *Nature*, vol. 365, no. 6443, pp. 250–252, 1993.
- [38] A. Karni, G. Meyer, P. Jezard, M. M. Adams, R. Turner, and L. G. Ungerleider, “Functional MRI evidence for adult motor cortex plasticity during motor skill learning,” *Nature*, vol. 377, no. 6545, pp. 155–158, 1995.
- [39] R. Shadmehr and H. H. Holcomb, “Neural correlates of motor memory consolidation,” *Science*, vol. 277, no. 5327, pp. 821–825, 1997.
- [40] Y. Dudai, “The neurobiology of consolidations, or, how stable is the engram?” *Annual Review of Psychology*, vol. 55, pp. 51–86, 2004.
- [41] J. Doyon and L. G. Ungerleider, “Functional anatomy of motor skill learning,” in *Neuropsychology of Memory*, pp. 225–238, Guilford Press, New York, NY, USA, 3rd edition, 2002.
- [42] J. Doyon, V. Penhune, and L. G. Ungerleider, “Distinct contribution of the cortico-striatal and cortico-cerebellar systems to motor skill learning,” *Neuropsychologia*, vol. 41, no. 3, pp. 252–262, 2003.
- [43] S. Lehericy, H. Benali, and P.-F. van de Moortele, “Distinct basal ganglia territories are engaged in early and advanced motor sequence learning,” *Proceedings of the National Academy of Sciences of the United States of America*, vol. 102, no. 35, pp. 12566–12571, 2005.
- [44] K. Nader, “Memory traces unbound,” *Trends in Neurosciences*, vol. 26, no. 2, pp. 65–72, 2003.
- [45] J. R. Misanin, R. R. Miller, and D. J. Lewis, “Retrograde amnesia produced by electroconvulsive shock after reactivation of a consolidated memory trace,” *Science*, vol. 160, no. 827, pp. 554–555, 1968.
- [46] K. Hader, G. E. Schafe, and J. E. Le Doux, “Fear memories require protein synthesis in the amygdala for reconsolidation after retrieval,” *Nature*, vol. 406, no. 6797, pp. 722–726, 2000.
- [47] J. Debiec, J. E. LeDoux, and K. Nader, “Cellular and systems reconsolidation in the hippocampus,” *Neuron*, vol. 36, no. 3, pp. 527–538, 2002.
- [48] R. D. Rubin, “Clinical use of retrograde amnesia produced by electroconvulsive shock: a conditioning hypothesis,” *Canadian Psychiatric Association Journal*, vol. 21, no. 2, pp. 87–90, 1976.
- [49] M. P. Walker, T. Brakefield, J. A. Hobson, and R. Stickgold, “Dissociable stages of human memory consolidation and reconsolidation,” *Nature*, vol. 425, no. 6958, pp. 616–620, 2003.
- [50] A. Hupbach, R. Gomez, O. Hardt, and L. Nadel, “Reconsolidation of episodic memories: a subtle reminder triggers integration of new information,” *Learning & Memory*, vol. 14, no. 1, pp. 47–53, 2007.
- [51] T. Platz, T. Winter, N. Muller, C. Pinkowski, C. Eickhof, and K.-H. Mauritz, “Arm ability training for stroke and traumatic brain injury patients with mild arm paresis: a single-blind,

- randomized, controlled trial,” *Archives of Physical Medicine and Rehabilitation*, vol. 82, no. 7, pp. 961–968, 2001.
- [52] J. W. Krakauer, “Motor learning: its relevance to stroke recovery and neurorehabilitation,” *Current Opinion in Neurology*, vol. 19, no. 1, pp. 84–90, 2006.
- [53] C. G. Mansur, F. Fregni, P. S. Boggio, et al., “A sham stimulation-controlled trial of rTMS of the unaffected hemisphere in stroke patients,” *Neurology*, vol. 64, no. 10, pp. 1802–1804, 2005.
- [54] E. M. Khedr, M. A. Ahmed, N. Fathy, and J. C. Rothwell, “Therapeutic trial of repetitive transcranial magnetic stimulation after acute ischemic stroke,” *Neurology*, vol. 65, no. 3, pp. 466–468, 2005.
- [55] F. Fregni, P. S. Boggio, A. C. Valle, et al., “A sham-controlled trial of a 5-day course of repetitive transcranial magnetic stimulation of the unaffected hemisphere in stroke patients,” *Stroke*, vol. 37, no. 8, pp. 2115–2122, 2006.
- [56] E. M. Khedr, M. A. Ahmed, N. Fathy, and J. C. Rothwell, “Therapeutic trial of repetitive transcranial magnetic stimulation after acute ischemic stroke,” *Neurology*, vol. 65, no. 3, pp. 466–468, 2005.